

**ADAPTING EXTRUSION DEPOSITION ADDITIVE
MANUFACTURING FOR CARBON/CARBON COMPOSITES**

by

Edwin Sebastian Romero

A Dissertation

Submitted to the Faculty of Purdue University

In Partial Fulfillment of the Requirements for the degree of

Doctor of Philosophy



School of Materials Engineering

West Lafayette, Indiana

March 2024

THE PURDUE UNIVERSITY GRADUATE SCHOOL
STATEMENT OF COMMITTEE APPROVAL

Dr. Rodney W. Trice, Chair

School of Materials Engineering

Dr. Eduardo Barocio Vaca

School of Mechanical Engineering

Dr. R. Byron Pipes

School of Materials Engineering

Dr. Kevin P. Trumble

School of Materials Engineering

Approved by:

Dr. David F. Bahr

ACKNOWLEDGMENTS

I would like to thank Prof. Rod Trice, Prof. R. Byron Pipes, and Prof. Eduardo Barocio for thinking of me when this research opportunity surfaced in late 2020. I was just a few days away from leaving Purdue when they contacted me about participating in this project and now thinking back on these last three years, I am profoundly grateful that they extended the offer. I have learned so much during my Ph.D. program, and I know the skills they have helped me develop will become my technical foundation for decades to come. This research truly could not have been possible without their perennial support guiding me and motivating me.

I would also like to thank Prof. Chelsea Davis and Prof. Kevin Trumble for the insightful discussions we had and for outlining better ways to analyze my results.

Thank you to the Air Force Research Lab (AFRL) for sponsoring this research as well as Prof. Jonathan Poggie for facilitating discussions with AFRL.

A special thank you to Dr. Ashley Hilmas and Bryant Burton for helping me perform computer-aided tomography scans at AFRL. Without their support, I would not have gained valuable insight into the densification process or completed a significant chapter of my thesis.

Lastly, I would like to thank all my lab mates, including Olivia Brandt, Averyonna Kimery, Rodrigo Orta Guerra, Sushrut Karmarkar, Abdullah Saad, Dawson Smith, Nicole Franklin, Tess Marconie, and Matt Thompson, for training me on some of the equipment I used for this research and for being especially patient with me while I figured out a way to safely process my material.

TABLE OF CONTENTS

LIST OF TABLES	6
LIST OF FIGURES	8
ABSTRACT	12
1. EVALUATING EXTRUSION-BASED ADDITIVELY MANUFACTURED SHORT FIBER-REINFORCED THERMOPLASTIC POLYMERS AS CARBON/CARBON PREFORMS	13
1.1 Introduction	13
1.2 Experimental Procedure	17
1.2.1 Materials Investigated	17
1.2.2 Thermogravimetric Analysis	18
1.2.3 Additive Manufacturing of Coupons	19
1.2.4 Coupon Distortion Tests	23
1.3 Results and Discussion	23
1.3.1 Thermogravimetric Results	23
1.3.2 Coupon Distortion and Density Results	27
1.3.3 Distortion Results of a 3D Printed Nozzle Preform	31
1.4 Conclusion	35
2. 4D IMAGING OF ADDITIVELY MANUFACTURED SHORT FIBER-REINFORCED CARBON/CARBON COMPOSITES THROUGH POLYMER INFILTRATION AND PYROLYSIS PROCESSING	38
2.1 Introduction	38
2.2 Experimental Procedure	40
2.2.1 Manufacturing the 3D Printed C/C Coupon	40
2.2.2 Polymer Infiltration and Pyrolysis Processing with Phenolic Resin	43
2.2.3 X-ray Micro-Computed Tomography Scans	46
2.2.4 Iterative Mass Conservation Analysis	48
2.3 Results and Discussion	50
2.3.1 Pore Type and Evolution Throughout PIP Processing	50
2.3.2 Pore Shape and Orientation	55
2.3.3 Spatial Evolution of the Pores Throughout PIP Processing	60

2.4	Conclusion.....	62
3.	POPULATING THE ORTHOTROPIC STIFFNESS TENSOR OF ADDITIVELY MANUFACTURED SHORT FIBER-REINFORCED CARBON/CARBON COMPOSITES ...	64
3.1	Introduction	64
3.2	Experimental Procedure	65
3.2.1	Manufacturing the 3D Printed C/C Coupons	65
3.2.2	Polymer Infiltration and Pyrolysis Processing with Phenolic Resin.....	66
3.2.3	Mechanical Testing	69
3.2.4	Multi-Scale Modeling of C/C Coupons Throughout PIP Processing	77
3.3	Results and Discussion	81
3.3.1	Evolution of Elastic Constants <i>E</i>1 and <i>G</i>23 Through Densification.....	81
3.3.2	Tensile and Double-Notched Shear Test Results	86
3.3.3	Digimat-MF Predictions of Elastic Constant Evolutions	93
3.3.4	Comparison of Mechanical Properties to Literature Results.....	97
3.4	Conclusion.....	103
4.	CONCLUSIONS AND FUTURE WORK	104
	APPENDIX A. CHAPTER 1 MATERIAL PROPERTIES AND SCRIPTS	106
	APPENDIX B. CHAPTER 2 MATERIAL PROPERTIES AND SCRIPTS	107
	APPENDIX C. CHAPTER 3 MATERIAL PROPERTIES AND SCRIPTS	116
	REFERENCES	146
	PUBLICATION	159

LIST OF TABLES

Table 1.1 Material descriptions.....	18
Table 1.2 Extrusion system parameters.	21
Table 1.3 Elastic constants of some of the materials analyzed in this study.	22
Table 1.4 Constituent char yields and polymer onsets of decomposition.....	25
Table 1.5 Initial lengths and average strains of the carbonized coupons.....	30
Table 1.6 Coupon densities before and after pyrolysis at $5^{\circ}\text{C}/\text{min}$ and $1^{\circ}\text{C}/\text{min}$	30
Table 2.1 Coupon dimensions for the different steps shown in Figure 2.2.	42
Table 2.2 Weights of the CT coupon used in the mass conservation analysis equations shown below. Note that the weight after pyrolysis during PIP0 was the weight after machining the orientation marker into the coupon as in Figure 2.2.	46
Table 2.3 X-ray micro-computed tomography scan parameters used after each PIP cycle.	47
Table 2.4 Iterative mass conservation analysis equations used to calculate the evolution of pore volume fraction and density from weight data during PIP processing.	49
Table 2.5 Density, pore volume fraction, and percent open & closed porosity evolution data in the ROI.....	55
Table 2.6 Percent of closed pores with lengths below $10\mu\text{m}$, $100\mu\text{m}$, and $1000\mu\text{m}$	57
Table 2.7 Radial distribution data shown in Figure 2.15.....	61
Table 3.1 Dimensions of C/C composite coupons shown in Figure 3.1.....	66
Table 3.2 Weights of the 5 C/C coupons at every process step used to calculate the density and pore volume fraction evolution data.	67
Table 3.3 Density and pore volume fraction evolution data shown in Figure 3.2.....	69
Table 3.4 Dimensions of the tension-loaded C/C coupons shown in Figure 3.4.....	73
Table 3.5 Dimensions of the compression-loaded double-notched C/C coupons shown in Figure 3.5.....	75
Table 3.6 Summary of test cases used to vary the Digimat-MF predictions.	80

Table 3.7 Elastic constant inputs for Digimat-MF. The values shown for PyC were calculated with the Mathematica® 13 script in Appendix Table C.3.	81
Table 3.8 Elastic constant evolution data shown in Figure 3.13.	86
Table 3.9 Fracture loads and ultimate stress/strain data for the tensile and double-notched shear tests.	89
Table 3.10 Total error between the predicted and experimental curve for each test case in Figure 3.18.....	94
Table 3.11 Mechanical properties of C/C composites reported in literature by references [99] to [103].	99
Table 3.12 Mechanical properties of C/C composites reported in literature by references [103] to [108].	100
Table 3.13 Mechanical properties of C/C composites reported in literature by references [108] to [112].	101
Table 3.14 Mechanical properties of C/C composites reported in literature by references [22], [108] to [112], and [140].	102

LIST OF FIGURES

Figure 1.1 Methodology chart for the current study.....	17
Figure 1.2 Computer-aided design (CAD) of additively manufactured vertical panels used to generate coupons for pyrolysis processing, with the 1-direction as the print direction.....	22
Figure 1.3 Fractional weight loss versus time at $5^{\circ}\text{C}/\text{min}$ showing the neat fiber char yield and composite char yields.....	24
Figure 1.4 Fractional weight loss rates versus temperature for the composite pellets tested at $5^{\circ}\text{C}/\text{min}$ showing the peak weight loss rate and the decomposition temperature at the peak.....	26
Figure 1.5 Distortion results of several additively manufactured coupons at $5^{\circ}\text{C}/\text{min}$ (a-d) and $1^{\circ}\text{C}/\text{min}$ (e-h) from 25°C to 900°C showing the effect of heating rate and fiber orientation on dimensional stability.....	28
Figure 1.6 Distortion results of 40CF-PPS and 40CF-PEI at $5^{\circ}\text{C}/\text{min}$ (a-b) and $1^{\circ}\text{C}/\text{min}$ (c-d) from 25°C to 900°C showing that PEI thermally expanded more than PPS.	29
Figure 1.7 Nozzle computer-aided design (CAD) dimensions in millimeter (left) and the test piece cut from the CD nozzle preform (right).....	32
Figure 1.8 The pre- and post- pyrolysis states for the test pieces (a) and the cracks in the top layer of the cylinder test piece due to removable internal support.	34
Figure 1.9 Deviation analysis results in millimeters for the outer surfaces of the nozzle (a) and cylinder (b) test pieces.	35
Figure 2.1 Manufacturing procedure showing (a) the 3D hollow square, (b) the 50CF-PPS wall/panel extracted from the hollow square, (c) the two 8.15 mm bead widths (w) constituting the panel thickness, (d) the as-printed panel surface, and (e) the smooth surface achieved after passing the panel through the planer. Figure 2.1e also shows the two orientations used to produce tensile and shear coupons with predominant fiber alignments in the 3-direction and 1-direction (print direction) for orientation A and orientation B, respectively. The red region in Figure 2.1e represents the bottom-most layers of the geometry, which were avoided since these layers did not print with a constant width.....	41
Figure 2.2 50CF-PPS coupon (a) before and (b) after pyrolysis showing the in-plane swelling perpendicular to the fibers, and (c) machining of an orientation marker to distinguish between the coupon faces during tomography.....	42

Figure 2.3 The infiltration process used in this study including (a) vacuuming the air from the pores, (b) debagging the coupon while submerged in phenolic resin, (c) applying a pressure of 551 <i>kPa</i> in a pressure pot to push the resin in to the pores, (d) vacuum bagging with 2 layers of breather cloth + 1 layer of perforated release film on each side, (e) curing the resin an autoclave with 137 <i>kPa</i> external pressure, and (f) debagging the coupon to load in a tube furnace.	44
Figure 2.4 The cure cycle used for the resole phenolic resin.....	45
Figure 2.5 CAD model of coupon dimensions (<i>mm</i>)/local coordinate system and region of interest (ROI) analyzed.....	47
Figure 2.6 Open and closed porosity on a circular cross-section in the region of interest (ROI) during PIP0.	51
Figure 2.7 Evolution of the porosity visible on the ROI outer surface.....	52
Figure 2.8 The evolution of percent closed porosity in the ROI	53
Figure 2.9 The graphical representation of density and total pore volume fraction evolutions results in Table 2.5.	54
Figure 2.10 Aspect ratio distribution evolution for the open and closed pores throughout PIP processing displayed using a bin width of 1.	56
Figure 2.11 Length distribution of the closed pores throughout PIP processing.....	57
Figure 2.12 Cross-sections of the C/C coupon after initial pyrolysis processing showing the preferred orientation of the pores along the fiber direction (1-direction).....	58
Figure 2.13. Moving from back face to front face in the 1-3 plane of the C/C CT coupon during PIP0 to show the preferred alignment of the pores in the fiber direction (vertical direction).	59
Figure 2.14 Sectioning the ROI into zone 1, 2, 3 with radius $R/3$, $2R/3$, $3R/3$, respectively. ..	61
Figure 2.15 Radial distribution evolution of the percent open and closed porosity throughout PIP processing.	62
Figure 3.1 C/C composite coupons after initial pyrolysis processing, showing cracks aligned dominantly with the print direction (1-direction).	65
Figure 3.2 Density and pore volume fraction evolution data after 5 PIP cycles for coupons 1-5 through. Note that GS in plots refers to the green state (3D printed).	68
Figure 3.3 Impulse excitation test setup for the (a) flexural and (b) torsional vibrational test modes, in which parallel and cross-shaped nodal supports were used, respectively.	70

Figure 3.4 (a) CAD model with local/material coordinate system & reference dimensions, (b) isometric view, (c) and side view showing the bead interface noted in Figure 2.1c of the tension-loaded C/C coupons.	72
Figure 3.5 (a) CAD model with local/material coordinate system & reference dimensions, (b) isometric view, and (c) side view of the compression-loaded double-notched C/C coupons.	74
Figure 3.6 Tensile (a-b) and double-notched shear (c-d) test setups according to ASTM C1275 and ASTM C1292/D3846, respectively.	76
Figure 3.7 Two-step homogenization scheme in Digimat-MF illustrating (a) the real representative volume element (RVE) decomposed into two phase pseudo-grains with aligned and identical inclusions (b) the homogenization of each pseudo-grain via M-T model, and (c) the homogenization and computed effective response of the set of pseudo-grains via the Voigt model.	77
Figure 3.8 Flowchart of example input parameters fed into 1 st order Mori-Tanaka model in Digimat-MF.	78
Figure 3.9 Graphical representation of the (a) fiber orientation tensor, (b) fiber orientation tensor + void orientation tensor, and (c) the porous carbon matrix microstructure. These representations were generated in Digimat-FE but the analysis was performed in Digimat-MF.	80
Figure 3.10 Raw amplitude oscillation decay for C/C composite coupon 1 throughout PIP processing.	82
Figure 3.11 Evolution of fast Fourier transform for C/C composite coupon 1 throughout PIP processing.	83
Figure 3.12 Evolution of damping coefficients for the first two harmonic frequencies shown in Figure 3.11.	84
Figure 3.13 Impulse excitation evolution of E_1 and G_{23} after 5 PIP cycles for coupons 1-5. Note that GS in plots refers to the green state (3D printed).	85
Figure 3.14 Force vs displacement curves showing the fracture load from the tension and double-notched shear tests.	87
Figure 3.15 Stress vs strain curves showing the strengths measured by the tension and double-notched shear tests.	88
Figure 3.16 Cracks generated in the C/C coupons during (a) tension and (b) double-notched shear tests.	90
Figure 3.17 Scanning electron micrographs showing (a) fiber pull-out/splitting, and (b) inter-pore ligament splitting as possible failure modes during tension and double-notched shear tests.	92

Figure 3.18 Digimat-MF predictions for the evolution of $E1$ and $G23$ through densification for test cases 1-4 as described in Table 3.6.	94
Figure 3.19 Evolution predictions of $E2$, $E3$, $G12$, and $G13$ by Digimat-MF for test cases 1-4 in Table 3.6.	95
Figure 3.20 Evolution predictions of the Poisson's ratios by Digimat-MF for test cases 1-4 in Table 3.6.....	96
Figure 3.21 Fiber architectures reported in literature by the references listed in Table 3.11 to Table 3.14.....	98

ABSTRACT

Carbon/carbon composites are attractive for hypersonic flight applications because of their low coefficient of thermal expansion and high specific strength at temperatures above 3000 °C in non-oxidizing atmospheres, but the conventional manufacturing methods used for shaping this material into structural components with oriented fibers can increase costs. The use of molds/tooling surfaces and lack of automation via filament winding, resin transfer molding, autoclave processing, and textile processing (e.g. braiding, stitching, knitting, weaving) for manufacturing certain geometries introduces scalability issues and high labor costs during carbon/carbon preform production. As a result, this study explored the practicality of extrusion deposition additive manufacturing (EDAM) for producing complex-shaped carbon/carbon composites. Compared to other additive manufacturing methods, EDAM can both orient fibers and be scaled to produce large dimensionally stable structures. The investigations began with a comparison of the size- and shape- preserving-pyrolysis-processing capability of several fiber-reinforced thermoplastic polymers to identify the most dimensionally stable material, followed by X-ray micro-computed tomography scans to observe porosity changes during densification. After several phenolic resin densification cycles, the mechanical properties were measured via impulse, tension, and double-notched shear tests to gain better insight into the performance of carbon/carbon composites prepared from 3D printed preforms.

1. EVALUATING EXTRUSION-BASED ADDITIVELY MANUFACTURED SHORT FIBER-REINFORCED THERMOPLASTIC POLYMERS AS CARBON/CARBON PREFORMS

The content in this chapter has been published in Applied Composite Materials:

Romero, E.S., Barocio, E. & Trice, R.W. Evaluating Extrusion Deposited Additively Manufactured Fiber-Reinforced Thermoplastic Polymers as Carbon/Carbon Preforms. *Applied Composite Materials* (2023). <https://doi.org/10.1007/s10443-023-10176-y>

1.1 Introduction

Hypersonic vehicle development is one emerging technology where development of hot structures, particularly composite structures, is critical [1,2]. At Mach 5 and greater speeds, the convective heat from the potentially chemically reacting flow sheathing the vehicle surface can generate wall temperatures in excess of 1800°C [3]. This harsh aerothermodynamic environment can not only be difficult to model and replicate in ground test facilities [4], necessitating demand for expensive flight tests to obtain experimental data, but also introduces several thermo-structural challenges to cool the vehicle from the intense heating, including mitigating strain mismatch of multi-material assemblies arising from temperature gradients in the thermal protection system. The type of thermal protection system (TPS) used to cool the vehicle largely depends on the heat flux conditions, and becomes increasingly more complex as exposure times to higher heat fluxes increases [5,6]. Although active TPS are ideal for managing high heat fluxes over long periods of time and can improve the flight envelope and subsequently the performance of the vehicle [7], it is the most expensive, requiring complex internal geometries to flow a working fluid to carry away heat that would otherwise damage the structure [5,6]. Because TPS are manufactured with high temperature materials such as ceramic matrix composites (CMCs) and carbon/carbon (C/C) composites, developing cheaper ways to manufacture these materials into complex geometries can be an effective way of reducing hypersonic technology costs.

Carbon/carbon (C/C) composites, or carbon matrices reinforced with carbon fibers, are an attractive class of materials for hypersonic flight applications due to their low coefficient of thermal expansion and high specific strength at temperatures above 3000°C in non-oxidizing atmospheres [6,8]. First developed in the 1950s for ablative use and for special aerospace

applications including rocket nozzles and atmospheric reentry vehicles [5], C/C composites are also used in the aviation, automotive, power generation, and furnace construction industries for production of brake discs & brake pads, high-temperature racks, heating elements, high-temperature fasteners, and furnace liners [9,10]. The C/C composite manufacturing process starts with the preform production step, where a one- or multi- directional carbon fiber-reinforced polymer (CFRP) is manufactured into a geometry and thermally decomposed in a non-oxidizing environment near 1000 °C (pyrolysis) for polymer conversion to carbon. Because pyrolysis processing results in weight loss and the formation of a porous carbon matrix, the C/C composite is taken through several infiltration and pyrolysis cycles with either a carbonaceous polymer (polymer infiltration and pyrolysis, PIP) or vapor (chemical vapor infiltration, CVI) to reduce porosity and obtain dense parts, followed by graphitization to increase the degree of covalent bond alignment, and further improve the thermomechanical properties of the material [11,12]. While the manufacturing costs associated with multiple densification cycles and long furnace residence times of C/C composites have been reduced with the development of high char-yielding polymers such as polyarylacetylene and bis-ortho-diynylarene (BODA) [13,14], the manufacturing costs associated with fiber orientation and part geometry during preform production remain current challenges. Fiber orientation is an important parameter in meeting strength and shape requirements for high temperature composites, since it dictates many of the engineering properties in the composite including transport and mechanical properties. CFRPs or preforms are conventionally manufactured via filament winding, resin transfer molding, and autoclave curing [15]. Hand layups and textile techniques such as braiding, stitching, knitting, and weaving have also been conventional manufacturing methods of multi-directional fiber-reinforced preforms for decades, but their laboriousness/complexity in preform processing and lack of automation can hinder fabrication of highly customized preforms for experimental research and in-service applications [16–18].

Many fabrication challenges associated with the geometry of C/C composites, as well as CMCs, can be addressed with additive manufacturing (AM). AM is a novel manufacturing approach whereby components are made layer-by-layer according to a CAD model, enabling greater design flexibility in creating near-net shape parts that minimize component assembly/post-processing machining, cost reductions for small batch manufacturing, material waste savings, and designs for more engineering-efficient structures [19,20]. Several AM methods have been used to

manufacture CMCs and C/C composites with complex geometries, including selective laser sintering (SLS), stereolithography (SLA), and direct ink writing (DIW) [21], but present challenges for orienting fibers and/or scaling. SLS is a method used to selectively sinter powders into parts and while its main advantages include fast build speeds, dimensional accuracy, and direct manufacture of high-temperature composites, achieving uniform dispersions via mixing of the carbon fibers with ceramic powder or carbon matrix powder precursors followed by rolling to prepare the material for sintering makes it difficult to preferentially orient fibers in load-critical directions [22–24]. SLA is another AM method that provides high resolution and dimensional accuracy of printed parts but differs from SLS in that it uses a light source, typically in the ultraviolet (UV) wavelength range, to cure a photopolymerizable monomer into complex shapes [25]. But like SLS, SLA also relies on mixing techniques to disperse carbon fibers, and because of their absorption and light scattering properties, the fibers can reduce the UV cure depth during manufacturing [26,27], making it difficult to manufacture thick-walled parts and prolonging manufacturing times for large-scale structures. Automated tape layup (ATL) and automated fiber placement (AFP) are two AM methods that have become widely adopted in industry, developed initially in the 1980s as a means of automating the traditional hand layup process [15,28]. ATL/AFP are well-suited for orienting carbon fibers and differ primarily in the width of the material that is laid down, with AFP utilizing tows instead of the wider tapes used in ATL, and which facilitates layup of more complex shapes. Despite being relatively mature processes, the use of molds by ATL/AFP introduces scalability issues compared to mold-free AM methods and limits their ability to manufacture certain geometries, such as lattice-type structures [29]. Extrusion-based methods such as DIW and extrusion deposition additive manufacturing (EDAM) are by contrast, mold-free methods and can readily orient fibers by controlling deposition conditions of fiber-reinforced viscoelastic materials, making them attractive for tailoring the microstructure and mechanical properties of composite materials [30–32]. DIW differs from EDAM in that it can achieve material extrusion at room temperature, relying more on the rheological properties than heat to flow and deposit material [30]. Because of its fabrication approach, DIW depends considerably on the yield stress of engineering thermoplastic polymers to control layer deformation [33]. This can make DIW difficult to scale, since the self-weight of large geometries can generate internal stresses in the layers that exceed the polymer yield stress and increase part susceptibility to sagging [34]. By comparison, the EDAM process uses high performance

thermoplastic polymers to create free-standing structures, and has steadily advanced for commercial use, most noticeably with the development of the large-scale additive manufacturing (LSAM) and the big area additive manufacturing (BAAM) systems by Thermwood© Incorporated and Oak Ridge National Laboratory, respectively [35]. The high-performance polymers used by EDAM differ from standard and engineering thermoplastic polymers in their superior temperature stability, mechanical properties, and chemical resistance [36]. The replacement of aliphatic backbones with aromatic backbones in high-performance thermoplastics increases intermolecular forces and yields thermomechanical properties and solvent resistances that often exceed thermosets [36]. Because of their thermoviscoelastic properties, EDAM employs heat to extrude high-performance thermoplastic polymers, which can lead to undesirable residual stresses and part deformation during solidification, but which has also been successfully modeled and simulated to produce parts with high dimensional accuracies [37,38]. Whereas DIW has been used to manufacture high temperature composites [39,40], EDAM has not.

As a result, the goal of this study was to determine whether carbon fiber-reinforced thermoplastic composites manufactured via EDAM could provide a novel approach to manufacturing complex-shaped C/C composites. The EDAM process passes pelletized feedstock material consisting of compounded fiber-reinforced high-performance thermoplastic polymers through a single-screw extruder, where the polymer is melted dominantly by viscous heat losses [41]. The melted material then flows into a melt pump that provides precise flow rate control during printing. As the melted material flows through the nozzle, the suspended short fibers in the flow are dominantly oriented along the print direction via shear flow [42,43]. By following a prescribed print path and speed set via computer software, the 3D printer can deposit molten feedstock material with oriented fibers on a print bed layer by layer to form complex geometries [35]. Prior studies on additively manufactured high-performance thermoplastic polymers for TPS development revealed the difficulty in processing these materials for hot structure applications. Ablation experiments on polyetherimide (PEI), polyetheretherketone (PEEK), and polyetherketoneketone (PEKK) with carbon fiber, glass microsphere, and nano-clay additives showed the composites had char yields comparable to other carbonaceous polymers used for C/C composite processing, such as phenolic resin (~55 wt.%) [14], but exhibited intumescent or swelling behavior after 60 *sec* of ablation, causing significant distortion of the printed geometries [44–46]. Partially motivated by these results, this study investigated the post-pyrolysis char yield

and dimensional stabilities of a broader range of thermoplastic polymers including polyphenylene sulfide (PPS), polysulfone (PSU), polyetheretherketone (PEEK), polyethersulfone (PESU), and polyetherimide (PEI) to determine if the controlled deposition of oriented fibers in any of these polymers could aid in reducing the distortion of printed geometries during thermal decomposition. The methodology for this study was summarized in Figure 1.1.

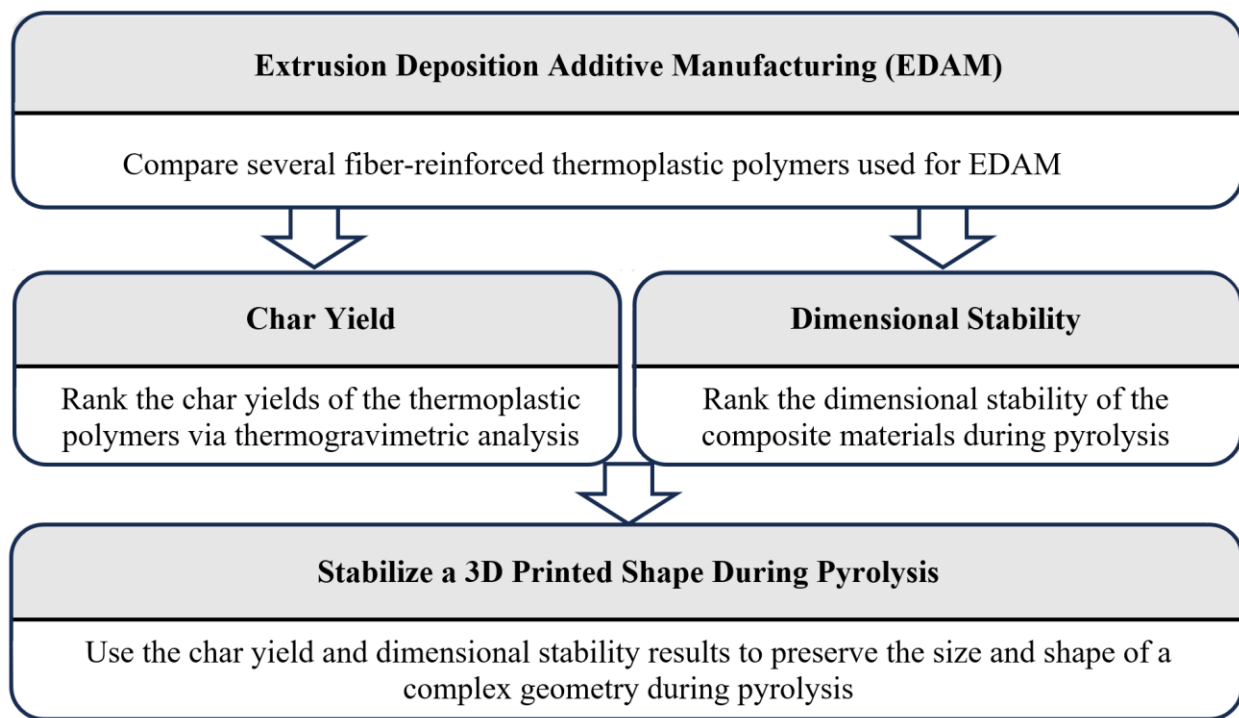


Figure 1.1 Methodology chart for the current study.

1.2 Experimental Procedure

1.2.1 Materials Investigated

Table 1.1 lists the abbreviations and suppliers for the commercially-available materials analyzed in this study, likely polyacrylonitrile (PAN) -based short carbon fiber systems. Whereas polyphenylene sulfide (PPS) and polyetheretherketone (PEEK) are semicrystalline thermoplastics, polyetherimide (PEI), polysulfone (PSU), and polyethersulfone (PESU) are amorphous thermoplastics. We note that because of the proprietary blend of additives (e.g. stabilizers, plasticizers, flame retardants, etc.) in these compounded materials to tailor the rheological and

thermal properties of the base polymer for extrusion, the only additive known in the feedstock materials was the fiber loading.

Table 1.1 Material descriptions.

Carbon Fiber Loading/ Thermoplastic Polymer	Report Abbreviation	Material Supplier	Material Supplier Description
Neat Fiber	Neat Fiber	Hexcel	AS4-GP3K
50 wt.% fiber loaded PPS	50CF-PPS	Techmer	Electrafil PPS CF50 HS DP
50 wt.% fiber loaded PPS	50CF-PPS_C	Celanese	Celstran PPS-CF 50-01
40 wt.% fiber loaded PPS	40CF-PPS	Techmer	Electrafil PPS CF40 HS DP
40 wt.% fiber loaded PPS	40CF-PPS_C	Celanese	Celstran PPS-CF 40-01
40 wt.% fiber loaded PEI	40CF-PEI	Sabir	LNP Thermocomp AM Compound EC008APQ
30 wt.% fiber loaded PEEK	30CF-PEEK	Evonik	Vestakeep 2000 CF30
25 wt.% fiber loaded PSU	25CF-PSU	Techmer	Electrafil PSU CF25 HS 3DP
25 wt.% fiber loaded PESU	25CF-PESU	Techmer	Electrafil PESU CF25 HS 3DP
20 wt.% fiber loaded PEI	20CF-PEI	Sabir	LNP Thermocomp AM Compound EC004EXAR1

1.2.2 Thermogravimetric Analysis

The goal for the thermogravimetric analysis tests was to determine which thermally decomposed polymer had the highest char yield, since a higher char yield would indicate less resulting porosity. To distinguish between the fiber char yields and polymer char yields in the pellets, a thermogravimetric analysis (TGA) was also conducted on a tow segment of neat fiber for an estimate of the weight loss from the fibers and/or fiber sizing in the pellets. A 500 μL alumina sample pan and a thermogravimetric analyzer model Q500 (TA Instruments, New Castle, Delaware) were used together with high purity nitrogen for these experiments. The sample masses during TGA were $76 \pm 1 \text{ mg}$ for all materials. For the temperature program, the TGA furnace was equilibrated at 120°C in an air atmosphere and held isothermally for 60 min to evaporate any absorbed moisture. The furnace temperature was then decreased to 25°C where a gas switch to nitrogen was made at a flow rate of 10 mL/min . To simulate pyrolysis using the TGA, the furnace was ramped at 5°C/ min from 25°C to 900°C in a nitrogen atmosphere then decreased back down to 25°C. Because of the number of materials tested, the thermogravimetric analyzer was again ramped at 5°C/ min to 200°C in an air atmosphere to ensure the thermocouple reading was accurate

for the following test. Equation (1.1) was used to calculate the polymer char yields from the composite pellet char yields,

$$Y_m = \frac{Y_c - \mathcal{W}_{f,i} Y_f}{\mathcal{W}_{m,i}} \quad (1.1)$$

where Y_m (%) was the polymer char yield, Y_c (%) was the composite pellet char yield, $\mathcal{W}_{f,i}$ (%) was the initial fiber weight fraction, Y_f (%) was the fiber char yield, and $\mathcal{W}_{m,i}$ (%) was the initial polymer matrix weight fraction. This equation was derived using the principle of mass conservation. In this equation, the initial weight fractions of fiber and polymer were known while the char yield values, Y_c and Y_f , were found after thermogravimetric analysis. The data was analyzed using Universal Analysis software.

1.2.3 Additive Manufacturing of Coupons

The composite additive manufacturing research instrument (CAMRI) at the Indiana Manufacturing Institute [35,37,38,41], was the extrusion deposition system used for 3D printing. The process parameters used such as drying time, screw zone temperatures, extruder nozzle temperatures, and print bed temperatures were set according to the material manufacturers process sheets, and are summarized in Table 1.2. The screw length/diameter ratio, extruder nozzle diameter, print bed speed, and bead dimensions used for printing the coupons were also listed. For each material, two coupons with approximately 25.4 mm x 25.4 mm cross-sections were cut out from additively manufactured vertical panels, as Figure 1.2 shows. In this context, the term “bead” refers to the extrudate material once it has been deposited on the print bed. We note that varying processing parameters can induce different microstructures that change the viscoelastic behavior, thermo-elastic properties, and strengths of the printed part. Because of the no-slip condition along the inner walls of the extruder nozzle, the fiber orientation distribution in the molten flow follows a core-shell mapping, where short fibers in the shell are more aligned in the print direction than in the core. This fiber orientation distribution and fiber loading influences the rheology of the extrudate, and as it turns 90° after exiting the nozzle and begins to cool on the print bed, several deformation mechanisms can further modify the fiber orientation distribution, changing again the rheology and consequently the bead geometry, which together with its cooling rate, determines the conductive and radiative heat transfer rates of the bead to the surrounding environment. During

deposition, the hot extrudate wets or reheats the deposited layer beneath it, determining the contact area between beads and promoting the interdiffusion of polymer chains through the interface [35]. Since the wetting process is influenced by the bead viscosity transverse to the print direction and is highly temperature-dependent, the viscosity limits the temperature regime for forming a bond between layers. While higher temperatures facilitate diffusion-based fusion between beads, lower temperatures reduce polymer chain mobility and fusion between layers. To prevent the layers from solidifying too quickly, then, the print bed is heated so that the layers can be successfully bonded together. The results by Pibulchinda et. al [32] show that the processing parameters that induce deformation on the extrudate as it exits the nozzle, including the height of the nozzle above the print bed (NH) and the print bed speed/extrusion speed ratio (V_b/V_e), change the bead morphology from a semi-circular edged parallelogram cross-section (high bead aspect ratio, w/h) to a round ovular-shaped cross-section (low bead aspect ratio, w/h) and increase the in-plane anisotropy of the reinforcing phase (more fibers aligned in the print direction) as NH and V_b/V_e are increased, respectively. The processing parameters that affect the bead aspect ratio (w/h) and subsequently the bead to nozzle area ratio (A_b/A_n), also influence the elastic properties and strengths of the printed part. The results by Thomas et. al [47] showed that while increasing w/h increased the Poisson's ratio (ν_{13}), Young's modulus (E_1) and strength (X_1) in the print direction, increasing A_b/A_n increased ν_{13} but decreased E_1 and X_1 . The coordinate system defined in Figure 1.2 can be used as a reference for these properties. Because of their influence on the microstructure, the processing parameters in Table 1.2 were kept constant for all composite materials during the manufacturing of the vertical panels, as an effort to obtain the same fiber orientation distribution in the printed coupons for the different materials. However, because of the different fiber loadings and inherent thermo-elastic properties of the polymer in each material, the thermo-elastic properties of the composite materials differ. The orthotropic elastic properties of only some of the composite materials analyzed in this study have been investigated and reported in literature [48,49], and are summarized in Table 1.3. These values can be used as a reference for the mechanical properties of the corresponding coupons, since they were experimentally measured from additively manufactured vertical panels with the same bead aspect ratio (w/h), bead to nozzle area ratio (A_b/A_n), and process temperatures reported in Table 1.2.

Table 1.2 Extrusion system parameters.

Composite Material	Screw Zone 1, 2, 3 Temperature ($^{\circ}\text{C}$)	Extruder Nozzle Temperature ($^{\circ}\text{C}$)	Print Bed Temperature ($^{\circ}\text{C}$)
50CF-PPS	276, 293, 301	300	120
50CF-PPS_C	326, 387, 387	300	140
40CF-PPS	276, 293, 301	300	120
40CF-PPS_C	326, 387, 387	300	140
40CF-PEI	370, 380, 390	395	150
30CF-PEEK	360, 390, 390	390	140
25CF-PSU	288, 316, 354	357	140
25CF-PESU	305, 330, 360	360	120
20CF-PEI	305, 330, 360	360	140
Property		Value	
Screw Diameter		25.4 mm	
Screw Length/Diameter ratio		24	
Extruder Nozzle Diameter		4 mm	
Print Bed Speed, $V_b = V_{nozzle}$		5000 mm/min	
Nozzle Height Above Print Bed, NH		6.15 mm	
Bead Width, w		6.15 mm	
Bead Height, h		1.5 mm	
Bead Area, A_b		8.742 mm ²	
Bead Aspect Ratio, w/h		4.1	
Bead to Nozzle Area Ratio, A_b/A_n		0.695	

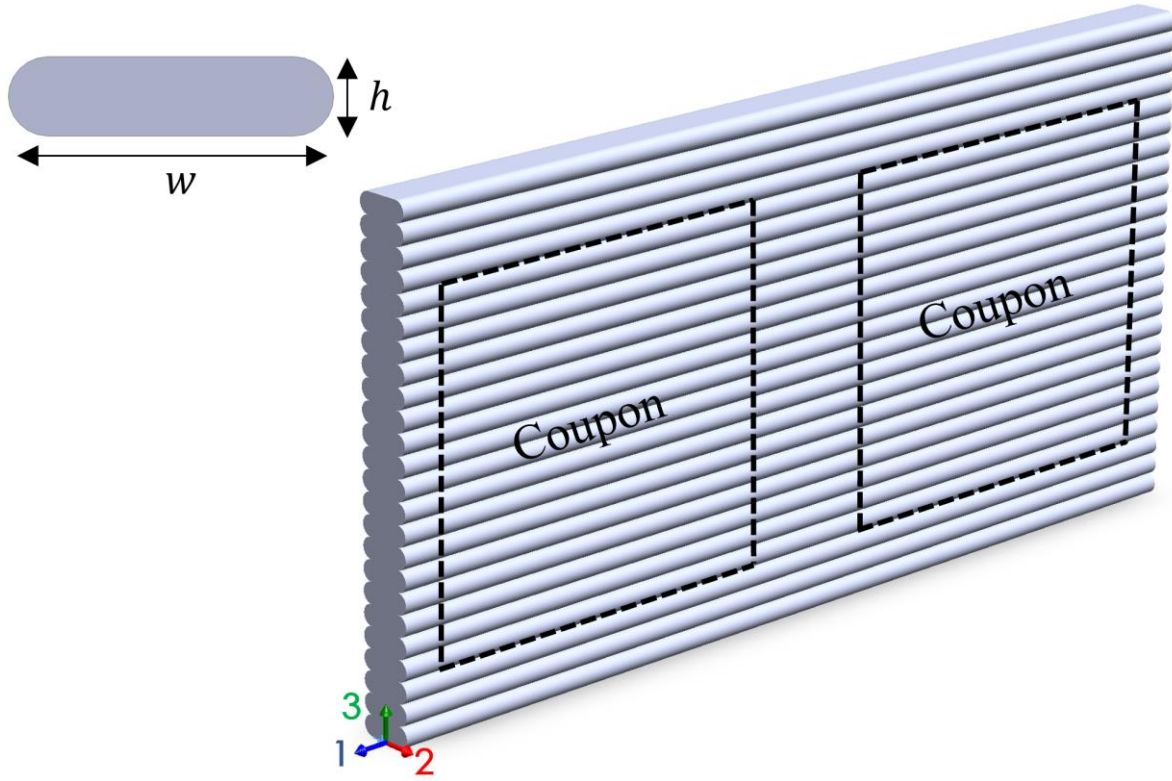


Figure 1.2 Computer-aided design (CAD) of additively manufactured vertical panels used to generate coupons for pyrolysis processing, with the 1-direction as the print direction.

Table 1.3 Elastic constants of some of the materials analyzed in this study.

Composite Material	E_1 (GPa)	E_2 (GPa)	E_3 (GPa)	G_{23} (GPa)	G_{13} (GPa)	G_{12} (GPa)	ν_{23}	ν_{13}	ν_{12}
50CF-PPS [48]	23.51	8.46	5.19	2.31	3.01	4.92	0.39	0.36	0.40
25CF-PSU [48]	15.78	4.59	3.87	1.46	1.95	2.54	0.44	0.38	0.42
25CF-PESU [48]	10.55	5.52	3.84	1.54	1.84	2.75	0.44	0.40	0.38
20CF-PEI [49]	15.42	5.14	4.12	1.53 *	2.55	2.52 *	0.45 *	0.35	0.18

Note: values reported with an asterisk (*) were inferred, not measured experimentally.

1.2.4 Coupon Distortion Tests

The goal for the coupon distortion tests was to determine if any composite material(s) in Table 1.1 could maintain their size and shape during pyrolysis processing despite thermal decomposition. The coupons were placed on an alumina dee tube (Advalue Technologies, Tuscon, Arizona) sprayed with a boron nitride coating (Materion, Mayfield, Ohio) to prevent coupon adhesion with the tool surface. Constant heating rates of $1^{\circ}\text{C}/\text{min}$ and $5^{\circ}\text{C}/\text{min}$ were used from 25°C to 900°C , and a heating rate of $1^{\circ}\text{C}/\text{min}$ was used from 900°C to 25°C . High purity nitrogen was run through a Lindberg Sola Basic 54552 tube furnace rated for 1200°C at a rate of $10\text{ mL}/\text{min}$, where the furnace temperatures inside were monitored using a type K high-temperature quick disconnect thermocouple (Omega Engineering, Norwalk, Connecticut). The alumina tube had an inner diameter of 92 mm and an outer diameter of 101.6 mm . Equation (1.2) was used to calculate the strains of the coupons after carbonization,

$$\varepsilon = \frac{\Delta L}{L_0} \quad (1.2)$$

where ΔL (mm) was the change in length of the coupons after pyrolysis, and L_0 (mm) was the initial length of the coupons before pyrolysis. The coupon densities before and after pyrolysis were found via equation (1.3),

$$\rho = \frac{m}{V} \quad (1.3)$$

where ρ (g/cm^3) was the coupon density, m (g) was the coupon mass, and V (cm^3) was the coupon volume.

1.3 Results and Discussion

1.3.1 Thermogravimetric Results

Figure 1.3 shows the fractional weight loss versus time for the neat fiber and each of the composite pellets. Note that the temperature program, plotted on the second y-axis with no symbol marker, deviates from the temperature program outlined in section 1.2.4 at the beginning and end of the nitrogen region. The furnace temperature at these times never reached 25°C because of a delay in chamber cooling. This occurred for all the material tests but was thought not to influence results. The neat fibers showed a small weight loss of 1.6% during pyrolysis, suggesting a fiber

char yield of 98.4%. The weight loss from the neat fiber test was assumed for the short fibers in each of the composite pellets. Substituting the neat fiber char yield, Y_f , and the composite pellet char yields, Y_c , from Figure 1.3 into equation (1.1) showed that all the polymer char yields, Y_m , were below 60%. This process is summarized in Table 1.4. Using equation (1.1) on weight loss results from previous findings [50–57], showed that the Y_m values in Table 1.4 were consistent. PEI had the highest char yield between 54.1–56.9%, followed by PEEK which had a char yield of 50.6%. Char yield results for PPS varied between material suppliers Techmer and Celanese with yields of 42.9–49.1% and 33.9–44.9% respectively, likely due to different additives used in the formulation of the polymer. PESU and PSU had the lowest char yields, with 40.3% and 35.6%, respectively. Since the carbon fibers were already carbonized prior to extrusion and were unaffected during polymer conversion to carbon, as the low weight loss showed, the onset of decomposition temperatures in Figure 1.4 and Table 1.4 reflected the polymer thermal stabilities. The onset temperature was defined as the intersection between the baseline and the tangent at the point of the highest slope for the weight fraction curve. Ranking the polymers based on their char yields, $PEI > PEEK > PPS > PESU > PSU$, revealed that PEI and PEEK were better polymer precursors for carbon/carbon composite processing than PPS, PESU, and PSU because of their superior char yield.

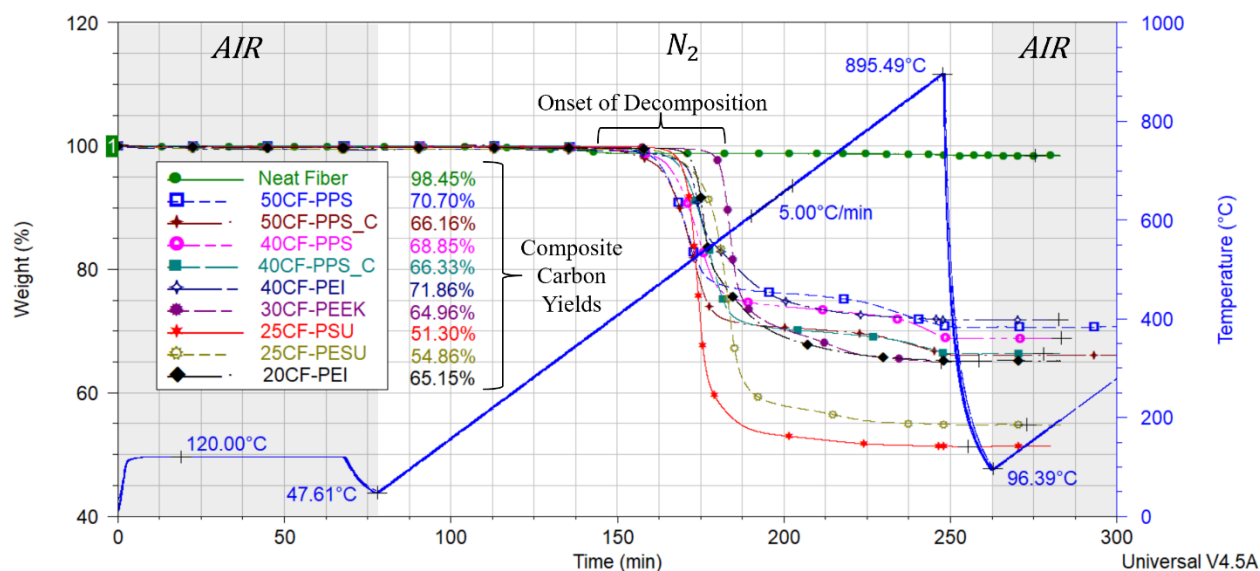


Figure 1.3 Fractional weight loss versus time at 5°C/min showing the neat fiber char yield and composite char yields.

Table 1.4 Constituent char yields and polymer onsets of decomposition

Composite Material	Composite Pellet Char Yield, Y_c (%)	Fiber Char Yield, Y_f (%)	Polymer Char Yield, Y_m (%)	Temperature at Onset of Decomposition ($^{\circ}\text{C}$)
50CF-PPS	70.6	98.4	42.9	472.0
50CF-PPS_C	66.1	98.4	33.9	477.7
40CF-PPS	68.8	98.4	49.1	484.6
40CF-PPS_C	66.3	98.4	44.9	505.7
40CF-PEI	71.8	98.4	54.1	512.9
30CF-PEEK	64.9	98.4	50.6	564.1
25CF-PSU	51.3	98.4	35.6	511.4
25CF-PESU	54.8	98.4	40.3	543.6
20CF-PEI	65.2	98.4	56.9	522.9

Figure 1.4 shows the fractional weight loss rates versus temperature for the composite pellets tested in Figure 1.3. The shape of these curves revealed autocatalytic behavior for all the polymers, accelerating to a maximum due to the production of gaseous by-products acting as catalysts for subsequent chemical reactions and then decelerating as a result of depleting amounts of polymer converting to carbon. For the heating rate and temperature range tested, all the polymers in this study demonstrated multi-step degradation kinetics, with only the PPS-based composite materials continuing to degrade from 750-900 $^{\circ}\text{C}$. The materials with the highest carbon fiber loadings (50CF-PPS, 50CF-PPS_C, 40CF-PPS, 40CF-PPS_C, 40CF-PEI) had the lowest peak weight loss rates, due to a smaller starting amount of unreacted polymer compared to the other feedstock materials. Because of the law of mass action, the increase in carbon fiber loading from 20CF-PEI to 40CF-PEI had a suppressive effect on the degradation kinetics, shifting the curve down and to the left, lowering the peak weight loss rate and onset of decomposition temperature. This was also seen for 40CF-PPS and 50CF-PPS, as well as for 40CF-PPS_C and 50CF-PPS_C. The peak weight loss rate, however, was not in general proportional to the fiber loading, with 30CF-PEEK and 25CF-PSU having higher peak weight loss rates than 25CF-PESU and 20CF-PEI.

Compared to PSU, PEI, and PEEK, PESU and PPS exhibited slower accelerations during degradation, with larger differences between their onset of decomposition temperature and peak decomposition temperature. The differences in degradation kinetics can be partially attributed to different thermal stabilities for different functional groups in the polymer. A pyrolysis gas

chromatography/mass spectrometry (Py-GC/MS) analysis by Perng et. al on variations of PPS, PEEK, PESU/PSU, and PEI showed that the most abundant pyrolysis products during initial degradation were H_2S & benzenethiol, $CO + CO_2$ & phenol, SO_2 & phenol, and $CO + CO_2$ & phenol + benzonitrile, due to thermally unstable sulfide groups, ether & carbonyl groups, sulfone & ether groups, and imide, isopropylene, & ether groups, respectively [51,53,55,57]. Perng et. al noted that decomposition mechanisms responsible for the evolution of gaseous by-products detected were depolymerization from thermally unstable chain ends and chain branches at lower decomposition temperatures followed by random main chain scission of unstable carbonized residue at higher temperatures, promoting the release of additional moieties and the recombination of adjacent radicals. Because these commercially available short carbon fiber-reinforced thermoplastic polymers contain a proprietary blend of additives (e.g. stabilizers, plasticizers, flame retardants, etc.) to tailor the rheological and thermal properties of the base polymer for extrusion, the degradation kinetics models reported in literature [58–61] may not accurately capture the decomposition behavior in these compounded materials.

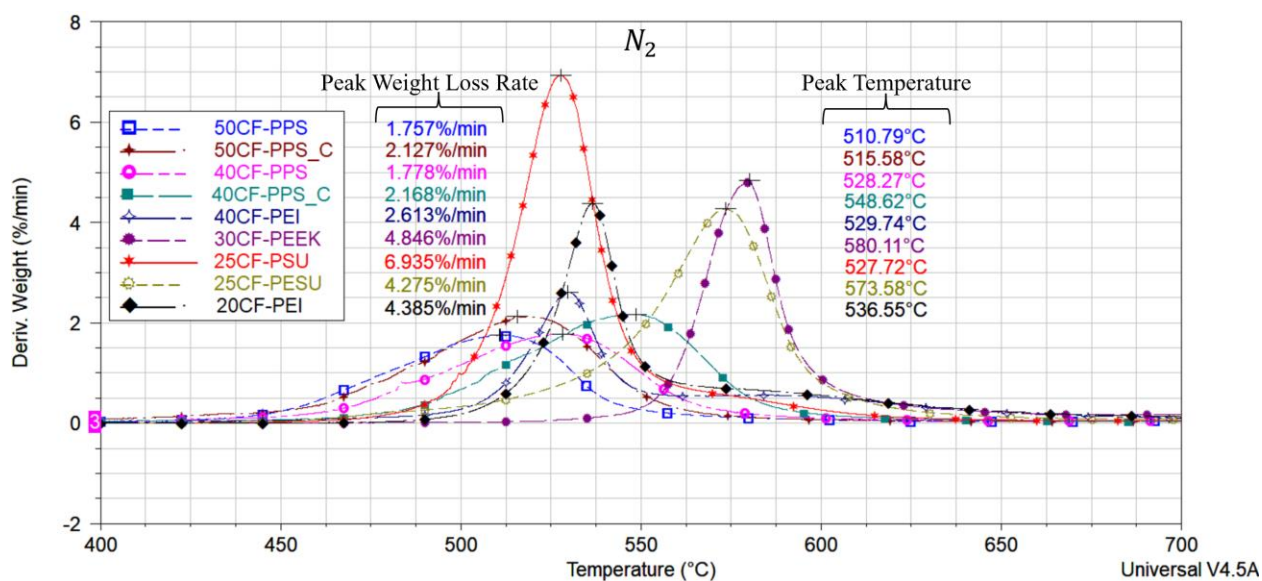


Figure 1.4 Fractional weight loss rates versus temperature for the composite pellets tested at 5°C/min showing the peak weight loss rate and the decomposition temperature at the peak.

1.3.2 Coupon Distortion and Density Results

Figure 1.5 and Table 1.5 showed that as the heating rate was decreased, the distortion of all materials decreased. The distortion for all the composite coupons was justifiably less along the print direction, due to the predominant alignment of carbon fibers in this direction and the resulting low coefficient of thermal expansion. All the coupons were placed on the crucible such that print direction was parallel to the 1-direction, except for 20CF-PEI in Figure 1.5a and Figure 1.5b, which was accidentally rotated 90° and had its print direction parallel to the 3-direction noted in the figure. We note that coupons for 50CF-PPS_C and 40CF-PPS_C were not tested since 50CF-PPS and 40CF-PPS had higher char yields.

For the same heating rate, polymer degradation distinctly varied between materials. Despite having similar carbon fiber loadings, 25CF-PSU and 20CF-PEI degraded into a foam structure at 5°C/min while 25CF-PESU swelled with no visible porosity. The foamability of thermoplastic polymers has been shown to depend on several factors, including their rheological and morphological characteristics. Banerjee and Ray [62] note that higher extensional and shear viscosities reduce foamability by increasing the polymer melt strength, suppressing bubble coalescence/growth as well as the loss of gas from the polymer to its surroundings. The stability of the bubbles that comprise the foam structure has also been shown to depend on fillers, which when present in higher quantities can lower the volumetric expansion ratio (ratio of nonfoam material density to foam density) and physically slow desorption [62]. Both 25CF-PSU and 20CF-PEI had highly, visibly porous surfaces, showing the polymer melt viscosities and their enhancement via fiber loadings were sufficiently high for promoting a moderate cell density but not high enough to provide good cell stabilization and prevent dimensionally unstable cell coalescence/growth during degradation. PESU was also a polymer tested with a low fiber loading, but its foamability may have been affected more by its slower production rate of volatile species (as noted in Figure 1.4), with slower desorption/bubble growth possibly decelerating scission-induced stress relaxation and causing swelling. The weight loss was characterized for all the coupons and was in close agreement with the thermogravimetric results of the composite pellets. Although the TGA results indicated that PEI and PEEK were the best polymer precursors due to their high char yields, the coupon distortion results showed that 50CF-PPS was the most dimensionally stable. At 1°C/min, 50CF-PPS exhibited very little distortion, indicating this

material and this heating rate as a potential processing route for carbon/carbon composite manufacturing.

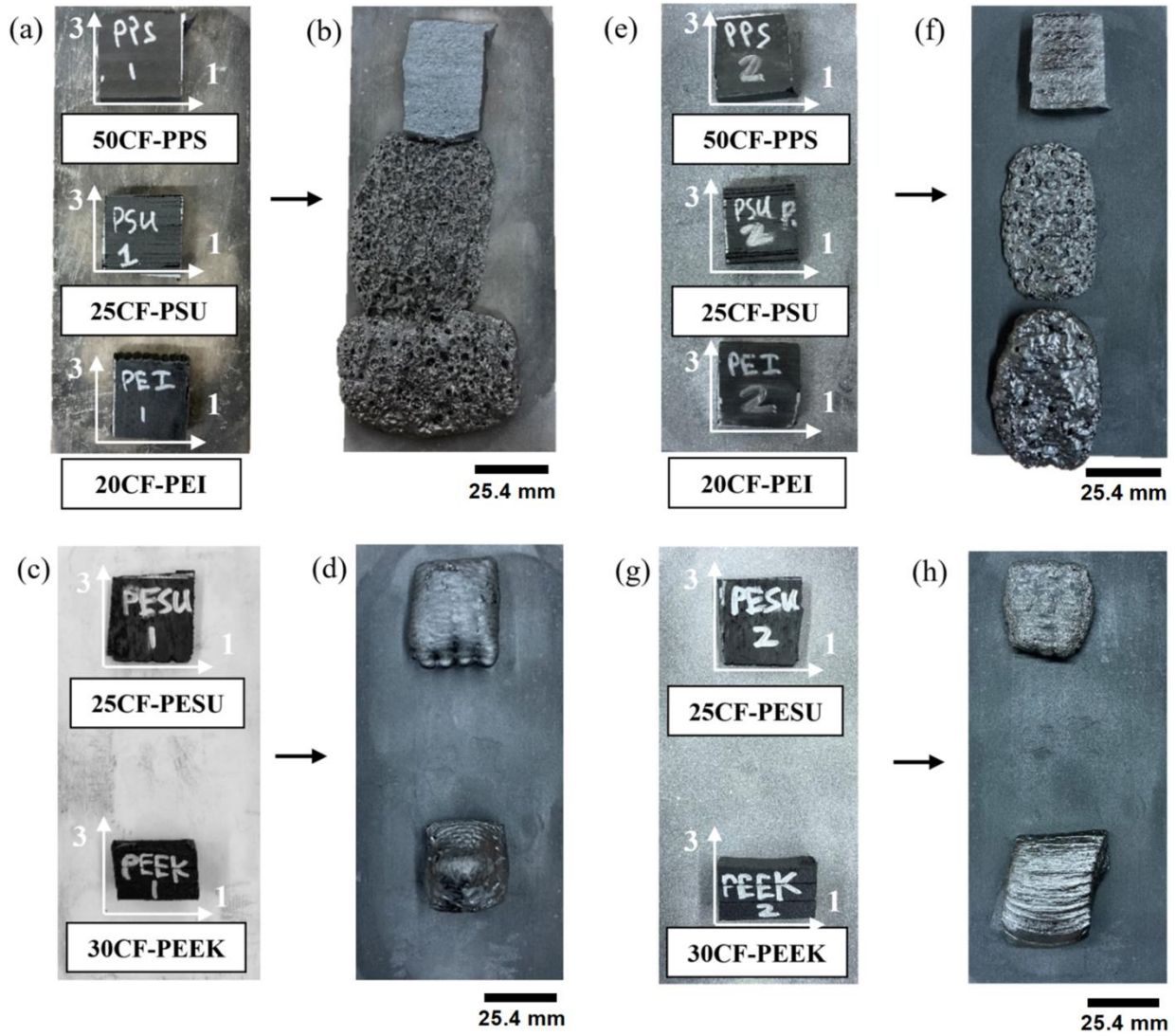


Figure 1.5 Distortion results of several additively manufactured coupons at $5^{\circ}\text{C}/\text{min}$ (a-d) and $1^{\circ}\text{C}/\text{min}$ (e-h) from 25°C to 900°C showing the effect of heating rate and fiber orientation on dimensional stability.

Ideally however, PEI would be used to manufacture carbon/carbon (C/C) composites because of its superior char yield. The dimensional stability of 20CF-PEI was inadequate for manufacturing structural C/C shapes but it was not clear if it was worse than 50CF-PPS because of the fiber loading or because of the polymer. To better assess the dimensional stability between PPS and PEI, the carbon fiber loading was fixed at 40 wt. %. As Figure 1.6 and Table 1.5 showed,

PEI had larger average carbonized strains than PPS in the 1-3 plane for the same fiber loading, fiber orientation, and heating rate, further encouraging the use of 50CF-PPS for shape- and size-preserving pyrolysis processing of more complex geometries. Notably, 40CF-PEI did not foam like 20CF-PEI did at higher heating rates, reflecting the suppressive effects of fiber loading on degradation kinetics and the fiber loading influence on rheology and cell stabilization during pyrolysis. The large strains of 40CF-PEI relative to 50CF-PPS revealed the need for PEI with fiber loadings >40 wt. % to further improve the viability of PEI for C/C composite processing, but PEI-based feedstock material with fiber loadings >40 wt. % is currently not available from any material suppliers. The availability of feedstock materials with higher fiber loadings is related to the processability of the material during extrusion. As the fiber loading and therefore viscosity of the molten flow are increased, the increase in process temperatures needed to suitably flow the material can start to approach the polymer onset of decomposition temperature, which can undesirably lead to material decomposition in, and clogging of, the 3D printing system.

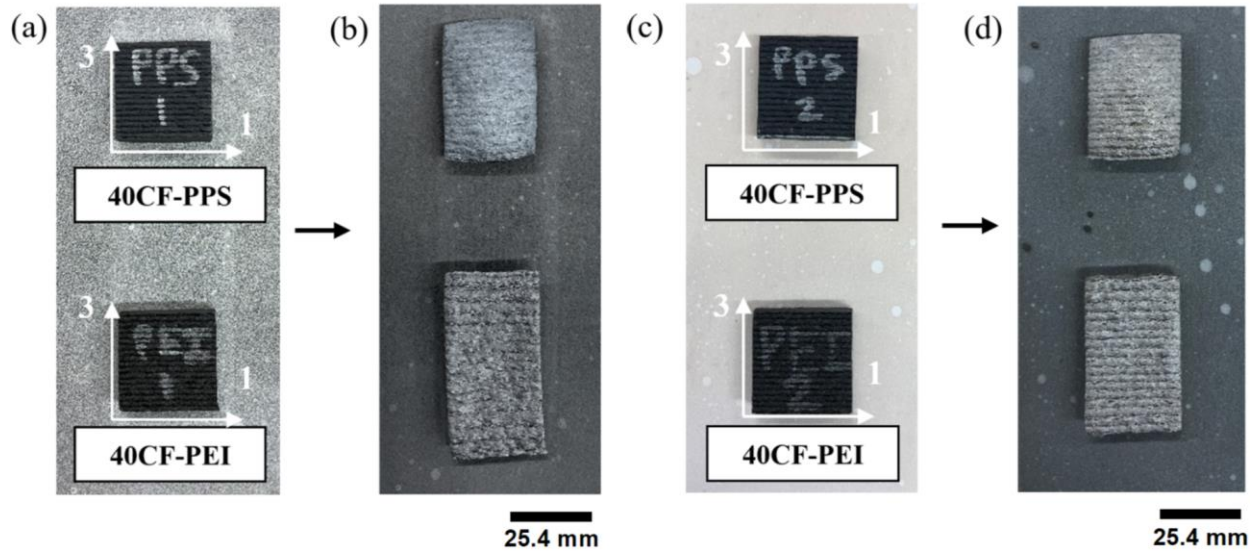


Figure 1.6 Distortion results of 40CF-PPS and 40CF-PEI at $5^{\circ}\text{C}/\text{min}$ (a-b) and $1^{\circ}\text{C}/\text{min}$ (c-d) from 25°C to 900°C showing that PEI thermally expanded more than PPS.

Table 1.5 Initial lengths and average strains of the carbonized coupons.

Composite Material	Initial Length, L_0 (mm)			
	Average Carbonized Strain, ϵ (mm/mm)			
	Along 1-Direction		Along 3-Direction	
	At $5^\circ\text{C}/\text{min}$	At $1^\circ\text{C}/\text{min}$	At $5^\circ\text{C}/\text{min}$	At $1^\circ\text{C}/\text{min}$
50CF-PPS	27.60 -4.09×10^{-2}	26.47 -4.18×10^{-2}	27.22 3.88×10^{-1}	26.62 1.82×10^{-1}
40CF-PPS	26.2 -2.19×10^{-2}	26.23 -3.55×10^{-2}	27.84 4.08×10^{-1}	27.50 2.62×10^{-1}
40CF-PEI	27.15 -1.55×10^{-2}	26.73 -2.52×10^{-2}	27.33 8.73×10^{-1}	27.48 5.82×10^{-1}
30CF-PEEK	25.86 1.06×10^{-2}	26.14 2.17×10^{-1}	14.99 9.17×10^{-1}	14.61 1.33×10^0
25CF-PSU	25.71 7.85×10^{-1}	24.43 2.88×10^{-1}	26.88 1.23×10^0	25.10 1.05×10^0
25CF-PESU	26.02 8.08×10^{-2}	28.12 1.09×10^{-1}	27.50 1.96×10^{-1}	25.29 9.31×10^{-2}
20CF-PEI	25.96 5.87×10^{-1}	27.62 3.19×10^{-1}	24.18 1.46×10^0	28.19 8.92×10^{-1}

Table 1.6 showed the coupon densities also varied with heating rate, just like the average carbonized strains in Table 1.5, being denser at slower heating rates as a result of smaller thermal expansions. Since the distortion of the coupons was highly anisotropic, three measurements along each coordinate axis were taken to calculate the volume and subsequently, density after pyrolysis.

Table 1.6 Coupon densities before and after pyrolysis at $5^\circ\text{C}/\text{min}$ and $1^\circ\text{C}/\text{min}$.

Composite Material	Density (g/cm^3)		
	Before Pyrolysis	After Pyrolysis at $5^\circ\text{C}/\text{min}$	After Pyrolysis at $1^\circ\text{C}/\text{min}$
50CF-PPS	1.51	0.67	0.81
40CF-PPS	1.47	0.63	0.72
40CF-PEI	1.43	0.56	0.67
30CF-PEEK	1.40	0.49	0.51
25CF-PSU	1.39	0.18	0.27
25CF-PESU	1.46	0.59	0.64
20CF-PEI	1.34	0.22	0.35

1.3.3 Distortion Results of a 3D Printed Nozzle Preform

Because of the promising results from the coupon distortion tests, a part with a more complex geometry was 3D printed to determine if the size and shape could be preserved during pyrolysis. As a tribute to one of the first applications of C/C composites, the shape chosen was a converging-diverging (CD) nozzle, additively manufactured with the 50CF-PPS feedstock material. To fabricate the CD nozzle preform, the CAMRI system processing parameters were the same as those listed in Table 1.2, except for the print bed speed (V_b), which was set to 1500 *mm/min*. Because the extruder nozzle of the CAMRI system momentarily stops for the print bed to drop one bead height before depositing a new layer, the 4 *mm* diameter extruder nozzle was programmed to follow a spiral print path to ensure a continuous print and avoid possible irregularities in the symmetry of the geometry. Despite this, the layers deposited just before and after the nozzle throat region were not perfectly concentric, as Figure 1.7 showed, causing the gradual change of the surface near the throat region to deviate from the CAD model. The source of this deviation was attributed to a constant print bed speed at every layer height, shortening the time taken for the extruder nozzle to travel the circumference as the CD nozzle diameter decreased, and not allowing enough time for the previous layer to sufficiently cool and solidify before a new layer was deposited. Since the 92 *mm* inner diameter tube furnace was too small to fit the entire geometry, the CD nozzle was cut into a cylinder test piece and a nozzle test piece, as noted in Figure 1.7.

layers, the localized cracking noted in Figure 1.8b was attributed to tensile stresses generated from constrained expansion with the insulation, since cracking was not seen in any of the other layers. To quantify the distortion of the layers, a deviation analysis was performed. A FARO® edge laser scan arm with an LLP 19121 probe was used to create a point cloud of the outer surfaces before and after pyrolysis with the FARO CAM2® Measure 10™ software. A grid-type scanning filter with the finest grid size and a point scan filter of 0.100 mm were the parameters used to generate the point clouds. The point clouds were converted into a mesh using the built-in 500K density filter meshing algorithm feature and were imported into Geomagic Wrap 2015 to heal the mesh and perform the deviation analyses. The results in Figure 1.9a showed that the throat region deformed asymmetrically, expanding significantly on one side and contracting on the other. The distortion of the layers near the base in Figure 1.9a however, were more symmetric, just like many of the layers seen in Figure 1.9b. The outer diameter at the bottom of the cylinder test piece was 63.1 mm before pyrolysis and 64.12 mm after pyrolysis, resulting in a total carbonized strain of 1.61×10^{-2} in the radial direction. This value was very close to the 3-direction strain measured for the 50CF-PPS coupon tested at $1^\circ\text{C}/\text{min}$. In addition to the print quality, several testing conditions may have contributed to the uneven expansion of some of the layers shown in the deviation analysis results. The surrounding environment was not much larger than the test pieces, and the furnace had heating elements only along the bottom half of the ceramic tube, potentially generating thermal gradients along the layer stacking direction despite the slow heating rate used. Although the carbonized test pieces deviated from their initial geometries, the results showed the distortion of the geometries was highly dependent on the print quality of the layers, distorting <1.5 mm in regions where layers were successfully deposited. A variable print bed speed can be programmed to improve print quality and several processing parameters could also be modified to obtain a less anisotropic fiber orientation distribution, including the bead aspect ratio and print bed speed/extrusion speed ratio, to further reduce the distortion of the layers during pyrolysis processing.

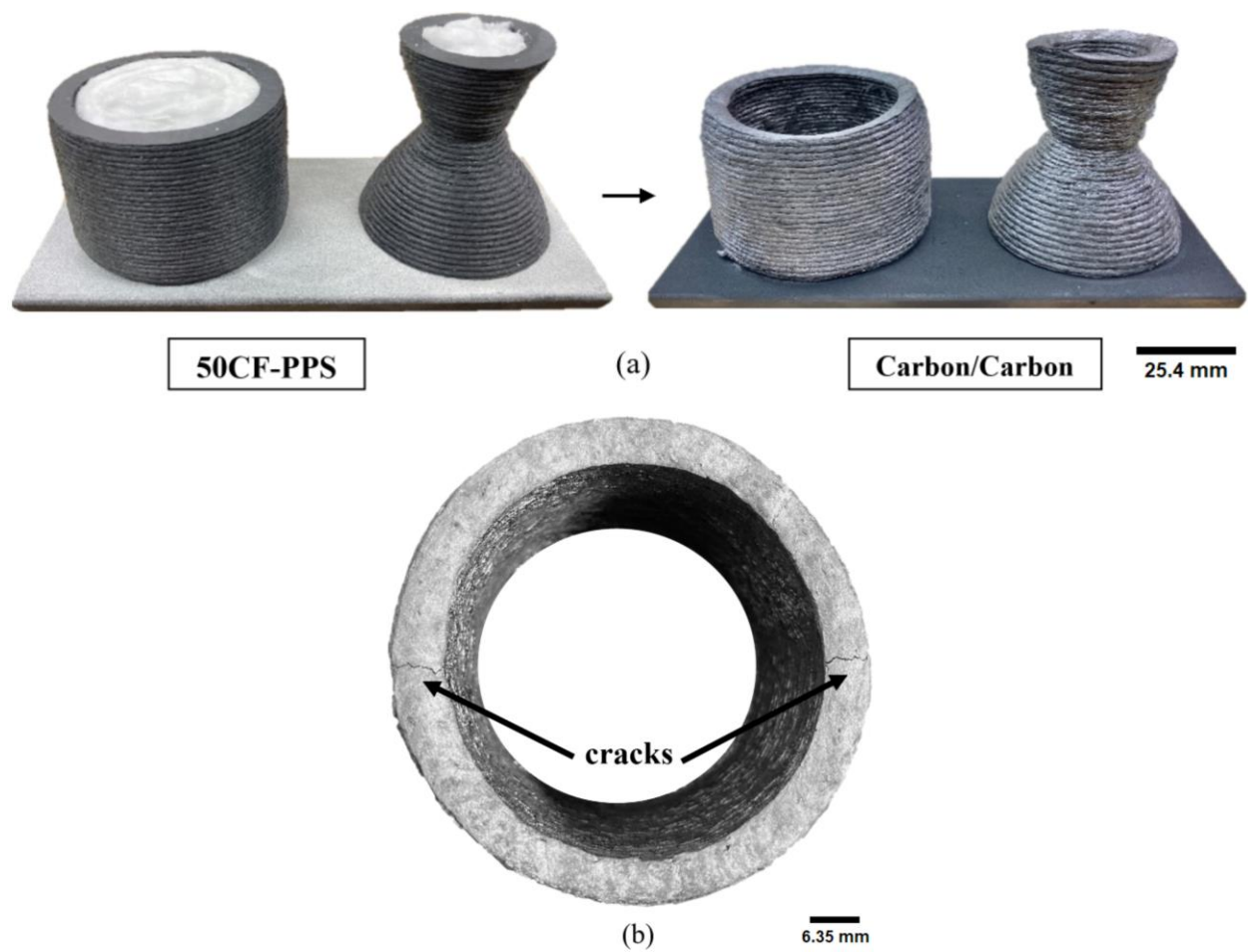


Figure 1.8 The pre- and post- pyrolysis states for the test pieces (a) and the cracks in the top layer of the cylinder test piece due to removable internal support.

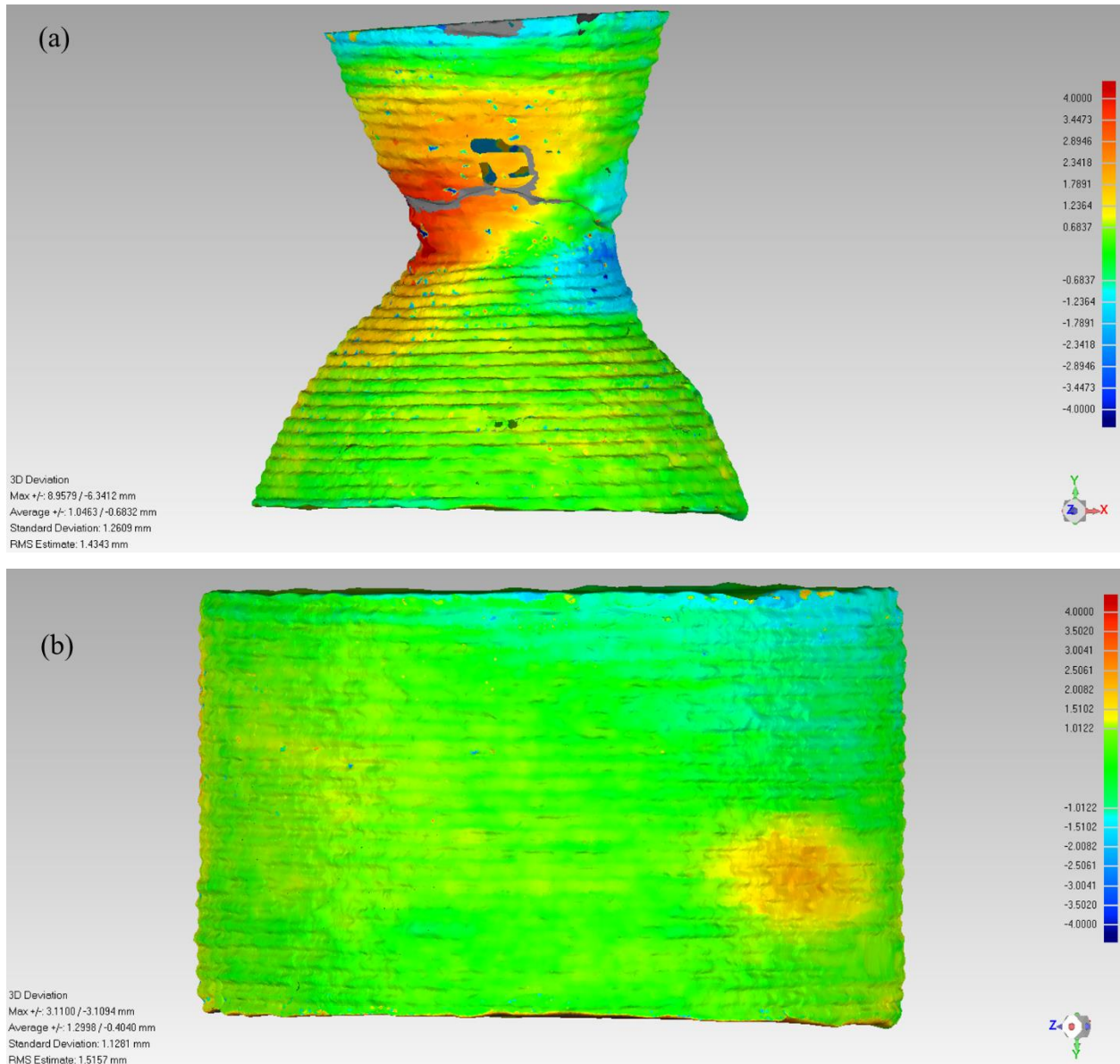


Figure 1.9 Deviation analysis results in millimeters for the outer surfaces of the nozzle (a) and cylinder (b) test pieces.

1.4 Conclusion

The polymer char yields and dimensional stabilities of several short carbon fiber-reinforced thermoplastic polymers, including polyetherimide (PEI), polysulfone (PSU), polyethersulfone (PESU), polyetheretherketone (PEEK), and polyphenylene sulfide (PPS), were investigated to determine if extrusion deposition additive manufacturing (EDAM) could be a practical approach for manufacturing complex-shaped carbon/carbon (C/C) composites. The thermogravimetric

analysis and coupon distortion results of nine different feedstock materials in this study showed several findings:

- PEI was the polymer with the highest char yield (wt. %): PEI (57) > PEEK (50) > PPS (43) > PESU (40) > PSU (36).
- Slower heating rates reduced weight loss rates and improved dimensional stability during pyrolysis.
- Higher fiber loadings reduced weight loss rates and improved dimensional stability during pyrolysis.
- The anisotropy of the reinforcing phase caused anisotropic distortions in the fiber-reinforced thermoplastic polymers.
- For the same heating rate, fiber loading, and approximate fiber orientation distribution, polyphenylene sulfide (PPS) was more dimensionally stable than polyetherimide (PEI) during pyrolysis.
- The distortion results of a cylinder and converging-diverging nozzle test piece showed that 50 wt. % carbon fiber-loaded polyphenylene sulfide (50CF-PPS) could be used to manufacture complex-shaped C/C composites.
- Several processing parameters of the extrusion process are suggested to change the fiber orientation distribution in the layers and continue improving the dimensional stability of more complex shapes.

The results also motivate improvements in several areas. All thermoplastic polymers tested in this study had char yields <60%, much less than some commercially available thermosetting resins (>85%). Therefore, densification will likely be the main driver of costs for EDAM C/C composites and will require infiltration with a high char-yielding secondary polymer to keep costs low, unless higher char-yielding thermoplastic binders can be developed for 3D printing. The ability to orient short fibers and locally modify crack deflection paths for increased fracture toughness, for example, in a carbonized matrix microstructure is a potential benefit of EDAM. However, 3D printing preforms with continuous fibers will also be important for meeting strength demands of hypersonic and other high-temperature applications. Lastly, while the

thermomechanical properties of C/C composites can be experimentally measured, it has yet to be seen whether an extension of 3D printing simulation tools/workflows that can model degradation kinetics and thermomechanical changes in material properties during pyrolysis could be developed as a predictive tool for EDAM C/C composites.

2. 4D IMAGING OF ADDITIVELY MANUFACTURED SHORT FIBER-REINFORCED CARBON/CARBON COMPOSITES THROUGH POLYMER INFILTRATION AND PYROLYSIS PROCESSING

2.1 Introduction

The results from chapter 1 showed that complex-shaped carbon/carbon (C/C) composites could be fabricated using additive manufacturing thermoplastic technology but the porosity generated during initial pyrolysis processing renders the C/C composites unsuitable for hot structure applications. To obtain dense C/C composites with improved heat and load transfer capabilities, the porous preforms must be densified.

Densification with either a carbonaceous vapor (chemical vapor infiltration) or a carbonaceous polymer (polymer infiltration and pyrolysis) have been reported in literature [63], [64]. By modifying the pressure, temperature, and concentration of pure or mixed gas during chemical vapor infiltration (CVI), various morphologies, crystal structures, crystal orientations, and resultant matrix properties can be obtained [64], [65], [11]. Two chemical vapor infiltration methods used for densifying C/C composites are the more popular isothermal (ICVI) and less popular thermal gradient (TGCVI) methods, which differ primarily in the temperatures used at the vapor entrance surface. Unlike ICVI, TGCVI achieves diffusion or forced flow of gaseous reactants through a cooled entrance surface, which avoids sealing of the entrance surface via crust formation resulting from higher reactant concentrations and residual carbon build-up that would otherwise require intermittent machining to remove [66]. Although TGCVI facilitates densification of thick-walled porous preforms and improved furnace residence times compared to ICVI, the inductively heated mandrel and/or active cooling system used to develop through-thickness temperature gradients in the preforms must be customized to fit the part geometry, increasing costs, and limiting practical use to moderately simple shapes [66]. Compared to CVI methods, polymer infiltration and pyrolysis (PIP) processing with either a thermosetting or thermoplastic polymer is a simpler and more economical way of densifying C/C composites, since rapid liquid infiltration of any complex-shaped porous composite can be performed at lower temperatures with either pressure- or vacuum- assisted resin transfer molding. Whereas thermoplastic polymers must be heated into their liquid state to infiltrate porous preforms and undergo liquid-state pyrolysis within a positively pressurized environment to minimize

oozing/exudation [67], [68], [69], thermosetting polymers can be pushed or pulled through porous preforms via a pressure differential at room temperature and undergo solid-state pyrolysis near atmospheric pressures post-cure [70], [71]. Conversion of these polymers to carbon forms a carbon build-up on pore walls that increases the carbon matrix density, but partial gasification of the polymer precursor leaves residual porosity behind, requiring that porous preforms undergo several cycles of PIP to obtain bulk fractional densities >90%.

Because defects such as pores and cracks critically influence the thermomechanical performance of high-temperature composites such as C/C and ceramic matrix composites (CMCs) [72], [73], researchers have aimed to observe defect evolution via X-ray micro-computed tomography (μ CT) to gain a better understanding of the structure-processing-property relationships in these materials [74–82]. Two notable papers by Bale et. al [79] and Creveling et. al [82] marked the first time 3D imaging of CMCs was used to characterize in-situ damage evolution during high-temperature testing and pore evolution after each PIP manufacturing step, respectively. Creveling et. al [82] analyzed two separate regions of interest (ROI) in a woven CMC laminate and noted that the percent of open pores were 83% and 87% after initial pyrolysis processing but decreased to 25% and 47% after 5 PIP cycles, concluding that the decreasing rate was constant for both ROIs but that the decreasing rate in one ROI was much faster due to higher capillarity helping to infiltrate smaller pores. Creveling et. al noted that for woven CMCs manufactured via PIP, pores tended to form in between fiber tows and in interstitial regions, and that the shrinkage cracks were like those found in unidirectional fiber tow CMCs. The correlation between fiber packing and crack structural features (i.e. crack shapes, sizes, locations, etc.) generated during initial pyrolysis processing was noted previously by Larson et. al [80], who developed a taxonomy of crack geometries after in-situ X-ray μ CT tests of 140 different crack structures in a SiC/SiC-based polymer precursor. Larson and Zok found that all primary (first to form) cracks that grew parallel to the continuous fibers (alternating and wavy crack structures) and perpendicular to fibers (perimural crack structures) emanated from fiber-matrix interfaces during initial pyrolysis processing and were bounded by fibers, showing how fiber packing and fiber architectures influenced the type of crack/void structures that formed.

Motivated by previous findings, the goal of this study was to investigate how a short carbon fiber architecture oriented via extrusion processing influenced the network of ingress pathways generated during initial pyrolysis processing and subsequent PIP cycles. A short fiber C/C preform

was manufactured by extruding fiber-reinforced polyphenylene sulfide feedstock material, followed by carbonization and densification with phenolic resin. The porosity formed after each PIP cycle was analyzed by quantifying the type, shape, and spatial location evolution of pores via X-ray μ CT. The X-ray μ CT results were additionally compared to mass conservation analysis results to qualify the data.

2.2 Experimental Procedure

2.2.1 Manufacturing the 3D Printed C/C Coupon

The composite additive manufacturing research instrument (CAMRI) at the Indiana Manufacturing Institute was used to extrude 50 wt.% carbon fiber loaded polyphenylene sulfide (Techmer, Clinton, Tennessee), or 50CF-PPS feedstock material, into a 3D hollow square. The extrusion system processing parameters were the same as those listed in Table 1.2, except the bead width was increased from 6.15 *mm* to 8.15 *mm* to eliminate gaps between layers. The height and side length of the hollow square geometry were set to 160 *mm* and 279.4 *mm*, respectively, while the walls were manufactured two bead widths thick, continuously printed along the perimeter starting with the inner layer first at every layer height. After extracting one of the walls of the printed geometry, the wall/panel was passed through a 15" spiral cutterhead planer (Grizzly Industrial, Bellingham, Washington) to reduce the wall thickness from 16.3 *mm* to 10.92 *mm* and obtain a smooth surface. This was accomplished by removing material symmetrically from each face at a rate of 0.5 *mm/pass* until the 10.92 *mm* thickness was reached. A coupon was then extracted for pyrolysis processing. This procedure is shown in Figure 2.1. The 50CF-PPS coupon was then pyrolyzed in a Carbolite Gero 16/180 tube furnace (Verder Scientific, Newton, Pennsylvania) at 1/2°C/*min* from 25°C to 1000°C and 1°C/*min* from 1000°C to 25°C. This is shown in Figure 2.2.

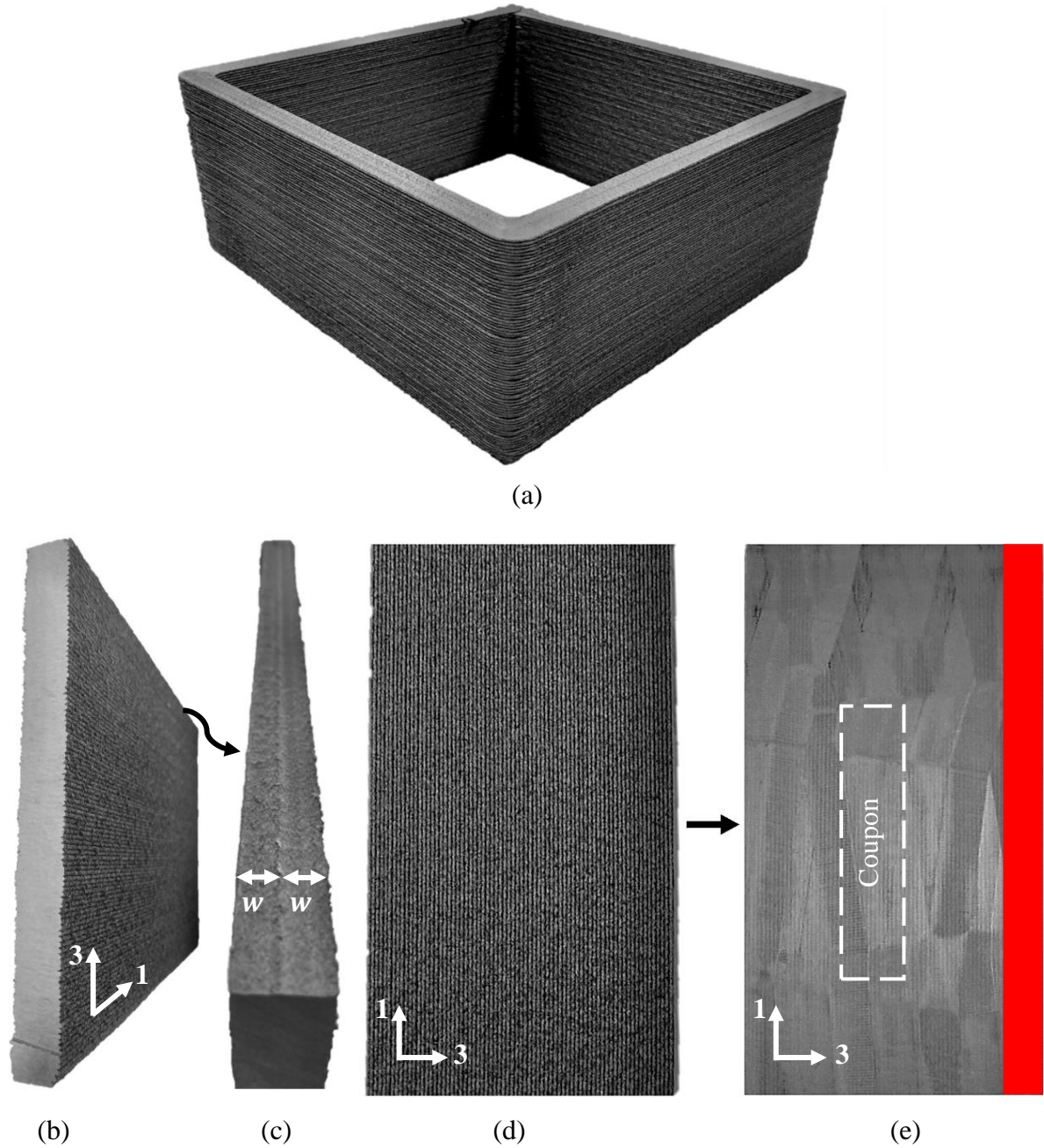


Figure 2.1 Manufacturing procedure showing (a) the 3D hollow square, (b) the 50CF-PPS wall/panel extracted from the hollow square, (c) the two 8.15 mm bead widths (w) constituting the panel thickness, (d) the as-printed panel surface, and (e) the smooth surface achieved after passing the panel through the planer. Figure 2.1e also shows the two orientations used to produce tensile and shear coupons with predominant fiber alignments in the 3-direction and 1-direction (print direction) for orientation A and orientation B, respectively. The red region in Figure 2.1e represents the bottom-most layers of the geometry, which were avoided since these layers did not print with a constant width.

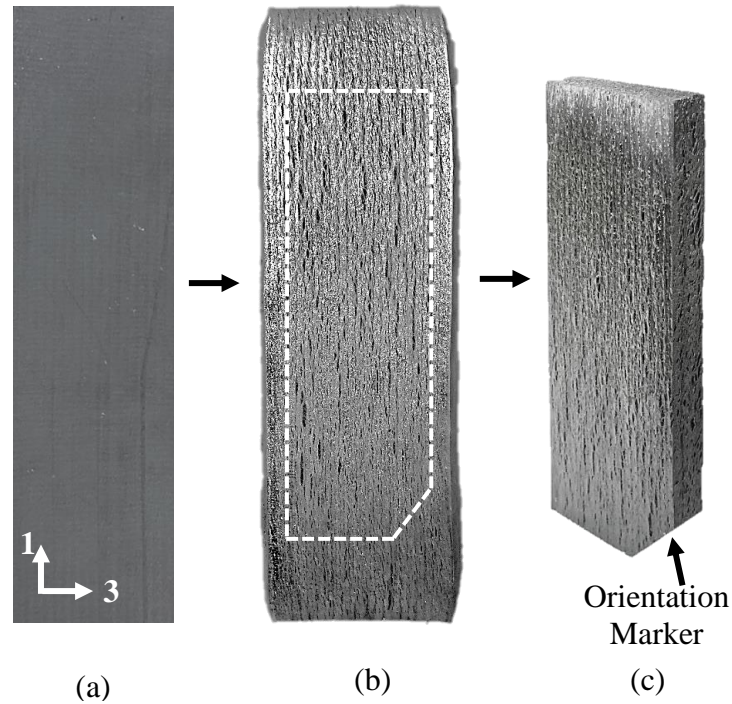


Figure 2.2 50CF-PPS coupon (a) before and (b) after pyrolysis showing the in-plane swelling perpendicular to the fibers, and (c) machining of an orientation marker to distinguish between the coupon faces during tomography.

Table 2.1 Coupon dimensions for the different steps shown in Figure 2.2.

Dimension (mm)	Coupon		
	Before Pyrolysis	After Pyrolysis	After Machining
Length 1	134.99	134.23	99.38
Length 2	134.97	134.54	99.58
Length 3	134.95	134.34	99.32
Average Length, L	134.97	134.37	99.43
Width 1	33.58	42.25	34.59
Width 2	33.65	43.1	34.72
Width 3	33.73	43.69	34.74
Average Width, W	33.65	43.01	34.68
Thickness 1	10.88	10.88	10.88
Thickness 2	10.96	11.35	11.35
Thickness 3	10.94	11.22	11.22
Average Thickness, T	10.93	11.15	11.15
Average Volume (cm^3)	49.63	64.44	38.44

2.2.2 Polymer Infiltration and Pyrolysis Processing with Phenolic Resin

For infiltration, the C/C coupon was vacuum bagged for 30 *min* to remove air from the pores and then debugged while submerged in a Pyrex container filled with room-temperature resole phenol formaldehyde (PF) (phenolic) resin (Plenco, Sheboygan, Wisconsin). The Pyrex container was placed inside a 10-gallon pressure pot (California Air Tools, San Diego, California) and slowly pressurized to 551 *kPa* to push the resin into the vacuumed pores. After 1 *hr*, the pressure pot was depressurized, the C/C coupon was flipped, and the pressure pot was slowly pressurized again to 551 *kPa* for 1 *hr* to ensure pressure gradients through the coupon thickness would not inhibit infiltration. The infiltration process is shown in Figure 2.3.

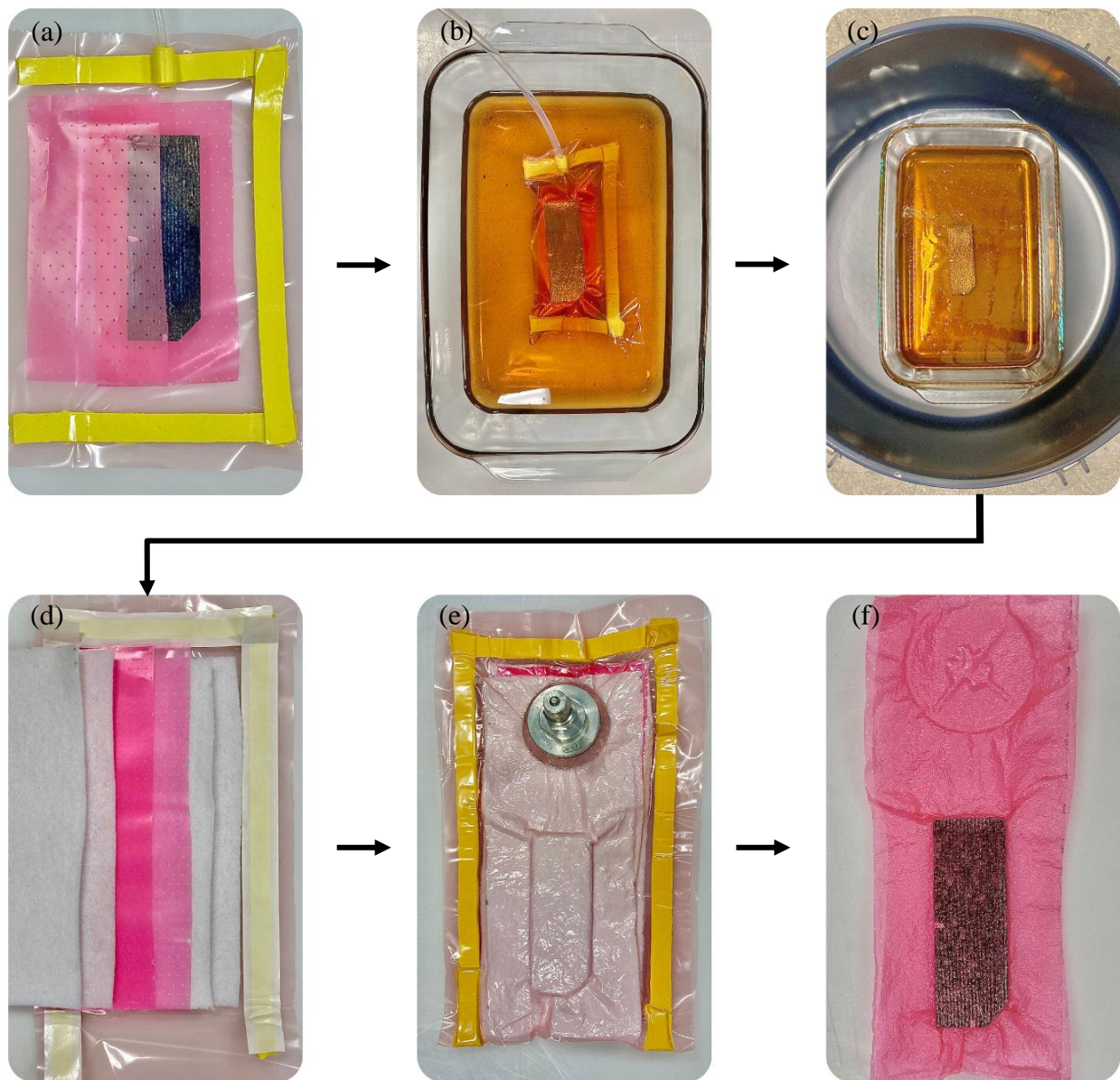


Figure 2.3 The infiltration process used in this study including (a) vacuuming the air from the pores, (b) debagging the coupon while submerged in phenolic resin, (c) applying a pressure of 551 *kPa* in a pressure pot to push the resin in to the pores, (d) vacuum bagging with 2 layers of breather cloth + 1 layer of perforated release film on each side, (e) curing the resin an autoclave with 137 *kPa* external pressure, and (f) debagging the coupon to load in a tube furnace.

To cure the infiltrated resin, the C/C coupon was placed in a vacuum bag with perforated release film, illustrated in Figure 2.3d-e, to minimize excess surface resin and provide an exit pathway for the condensation curing reaction-produced steam. Figure 2.4 shows the cure cycle programmed into the autoclave (Baron Blakeslee, Williamstown, West Virginia). A maximum

positive pressure of 137 kPa (20 psi) was applied to prevent the resin from foaming and a vacuum of 91 kPa (27 inHg) was held throughout the cure cycle, plotted in Figure 2.4 as positive. The temperature profile employed a ramp rate of 5°C/min to reach gelation and cure temperatures of 105°C and 150°C, which were held for 90 min and 60 min, respectively. A discovery HR-2 hybrid rheometer (TA Instruments, New Castle, Delaware) was used to justify the 90 min hold, where an oscillating stress with an angular frequency of 10 rad/s was applied between 40 mm aluminum parallel plates spaced with a 1 mm gap as the temperature was ramped at 5°C/min to the desired temperatures. The reader is referred to Figure B.1 and Figure B.2 for rheometer results. Once the resin in the coupon was cured, the coupon was re-carbonized at a rate of 2°C/min from 25°C to 1000°C and 2°C/min from 1000°C to 25°C. The coupon was taken through several PIP cycles until the weight-gain relative to the previous step was negligible. A summary of the coupon weights after every infiltration and pyrolysis processing step is shown in Table 2.2.

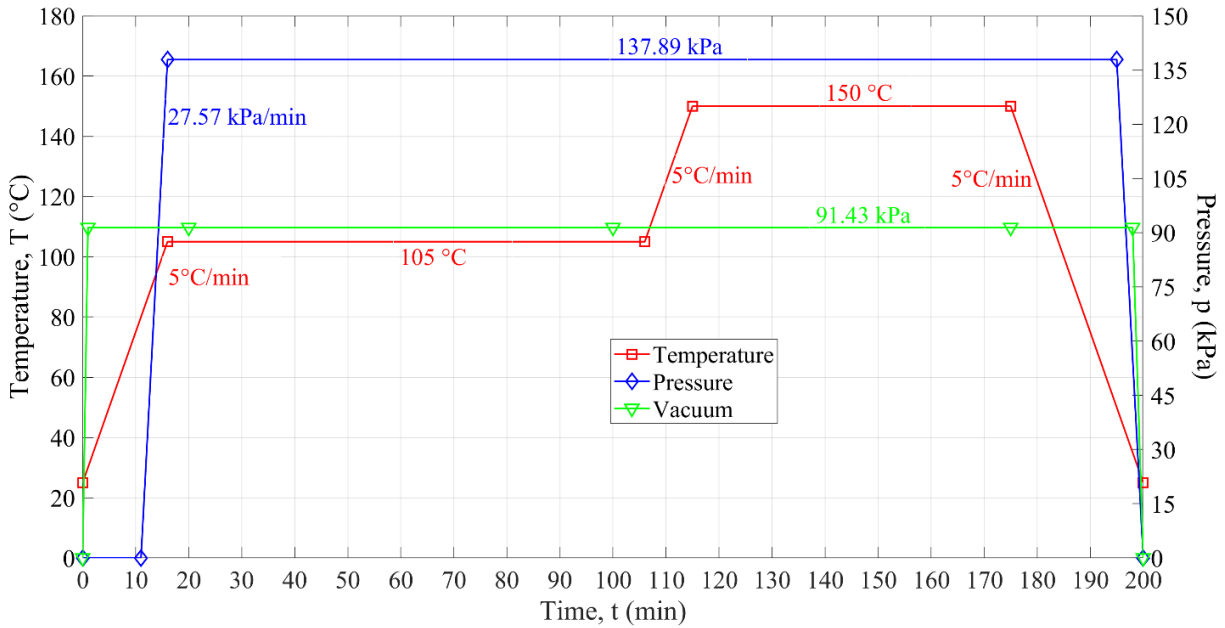


Figure 2.4 The cure cycle used for the resole phenolic resin.

Table 2.2 Weights of the CT coupon used in the mass conservation analysis equations shown below. Note that the weight after pyrolysis during PIP0 was the weight after machining the orientation marker into the coupon as in Figure 2.2.

PIP Cycle	Process Step	CT Coupon (<i>g</i>)
0	3D Printed	64.31
	Pyrolysis	28.31
1	Infiltration	35.94
	Pyrolysis	32.49
2	Infiltration	39.22
	Pyrolysis	35.93
3	Infiltration	41.1
	Pyrolysis	38.45
4	Infiltration	40.78
	Pyrolysis	39.47
5	Infiltration	40.49
	Pyrolysis	39.83

2.2.3 X-ray Micro-Computed Tomography Scans

A 10 *mm* diameter, 10 *mm* tall cylindrical region of interest (ROI) in the coupon was scanned with a Carl Zeiss Xradia Versa 520 & 620 X-ray μCT at the Air Force Research Laboratory (Dayton, Ohio). Scans were performed in between each PIP cycle with the scan parameters shown in Table 2.3. Dragonfly software was used to collect the data of interest including (1) percent open and closed porosity evolution throughout PIP processing, (2) pore shape and orientation, and (3) spatial evolution of the pores throughout PIP processing.

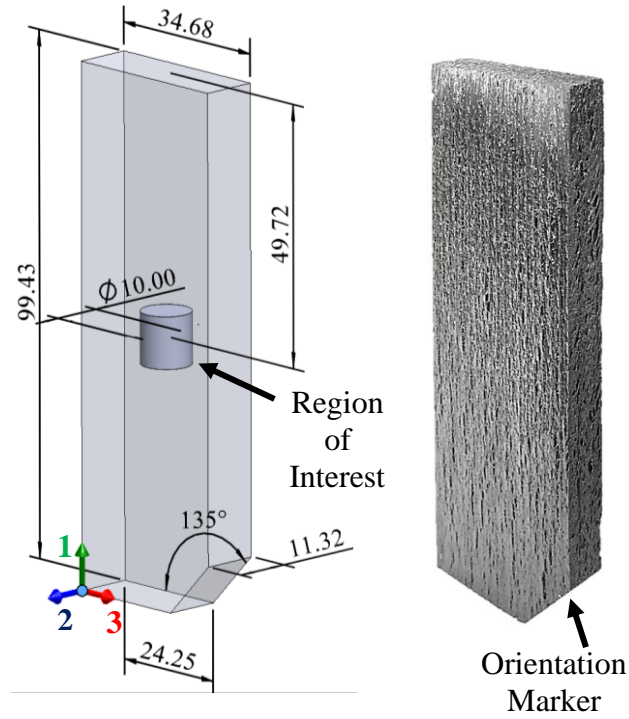


Figure 2.5 CAD model of coupon dimensions (*mm*)/local coordinate system and region of interest (ROI) analyzed.

Table 2.3 X-ray micro-computed tomography scan parameters used after each PIP cycle.

Parameter	Process Step					
	PIP0	PIP1	PIP2	PIP3	PIP4	PIP5
Objective	0.4x	0.4x	0.4x	0.4x	0.4x	0.4x
Voltage	50 <i>kV</i>	50 <i>kV</i>	50 <i>kV</i>	50 <i>kV</i>	50 <i>kV</i>	50 <i>kV</i>
Power	3 <i>W</i>	3 <i>W</i>	3 <i>W</i>	3 <i>W</i>	3 <i>W</i>	3 <i>W</i>
Bin Number	1	1	1	1	1	1
Projections	3201	3201	3201	3201	3201	3201
Resolution	5 μm	5 μm	5 μm	5 μm	5 μm	5 μm
Field of View	10 <i>mm</i> x 10 <i>mm</i>	10 <i>mm</i> x 10 <i>mm</i>	10 <i>mm</i> x 10 <i>mm</i>	10 <i>mm</i> x 10 <i>mm</i>	10 <i>mm</i> x 10 <i>mm</i>	10 <i>mm</i> x 10 <i>mm</i>
Exposure Time	18 <i>sec</i>	35 <i>sec</i>	18 <i>sec</i>	18 <i>sec</i>	35 <i>sec</i>	20 <i>sec</i>
CT Machine	Xradia 620 Versa	Xradia 520 Versa	Xradia 620 Versa	Xradia 620 Versa	Xradia 520 Versa	Xradia 620 Versa

2.2.4 Iterative Mass Conservation Analysis

The X-ray μCT results were verified with a mass conservation analysis, which used only weight data to calculate the density and pore volume fraction evolution during PIP processing. Given the 50% weight fractions of fiber and matrix for the 3D printed 50CF-PPS coupon, equations (2.1) to (2.17) in Table 2.4 were used, where \mathcal{W} (%) represents the weight fraction, W (g) represents the weight, V (g) represents the volume, \mathcal{V} (%) represents the volume fraction, ρ (g/cm³) represents the density, Y (%) represents the char yield, and where the subscripts $f, PPS, C, C/C, PyC, p, PF, RTM$ refer to properties for the short carbon fibers, PPS matrix, 50CF-PPS composite coupon, C/C composite coupon, pyrolytic carbon matrix, pores, phenol formaldehyde (PF) (phenolic) resin, and resin transfer molding results, respectively. Superscripts $GS, 0, \# \in [1, 5]$ were used to refer to properties for the composite material during the green state (3D printed 50CF-PPS), after initial pyrolysis processing, and after PIP cycles 0-5, respectively. Due to material distortion during initial pyrolysis processing, $V_{C/C}^0$ was taken to be the C/C coupon volume after machining into a rectangular shape again (as shown in Figure 2.2). This was done to facilitate volume calculations. The assumptions associated with certain equations are listed in Table 2.4. Because of the thermogravimetric analysis weight loss data in Table 1.4, the short carbon fibers were assumed to lose weight during initial pyrolysis processing ($Y_f = 98.4\%$), but not after. For every PIP cycle 0-5, the resin was assumed to fill in approximately all the pores. Because Ko et. al [83] and Zhang et. al [84] showed the density of phenolic resin and pyrolytic carbon to be approximately 1.55 g/cm³ at 1000 °C and range between 1.4 – 2.1 g/cm³, respectively, an average density value of $\rho_{PyC} = 1.65$ g/cm³ was used for the carbon matrix in this analysis. The reader is referred to Appendix Table B. 1 for the MATLAB® 2021a script used to automate density and pore volume fraction evolution calculations.

Table 2.4 Iterative mass conservation analysis equations used to calculate the evolution of pore volume fraction and density from weight data during PIP processing.

Process Step	Property	Equation	Assumption
Green State (3D Printed)	Weight Fractions	$\mathcal{W}_f^{GS} + \mathcal{W}_{PPS}^{GS} = \mathcal{W}_C^{GS}$ (2.1)	--
	Constituent Weights	$W_f^{GS} + W_{PPS}^{GS} = W_C^{GS}$ (2.2)	--
	Fiber Volume	$V_f^{GS} = W_f^{GS} / \rho_f$ (2.3)	$\rho_f = 1.78g/cm^3$
	Fiber Volume Fraction	$\mathcal{V}_f^{GS} = V_f^{GS} / V_C^{GS}$ (2.4)	--
	Volume Fractions	$\mathcal{V}_f^{GS} + \mathcal{V}_{PPS}^{GS} = \mathcal{V}_C^{GS}$ (2.5)	--
PIP Cycle 0-5	C/C Char Yield	$Y_{C/C} = W_{C/C}^0 / W_C^{GS}$ (2.6)	--
	Fiber Weight	$W_f^0 = Y_f * W_f^{GS}$ (2.7)	Fibers lose weight during pyrolysis
	Constituent Weights	$W_f^0 + W_{PyC}^0 = W_{C/C}^0$ (2.8)	--
	C/C coupon Volume	$V_{C/C}^0 = a * b * c \neq V_C^{GS}$ (2.9)	--
	Fiber Volume	$V_f^0 = W_f^0 / \rho_f$ (2.10)	--
	PyC Matrix Volume	$V_{PyC}^0 = W_{PyC}^0 / \rho_{PyC}$ (2.11)	$\rho_{PyC} = 1.65g/cm^3$
	Volume Fractions	$\mathcal{V}_f^0 + \mathcal{V}_{PyC}^0 + \mathcal{V}_p^0 = \mathcal{V}_{C/C}^0$ (2.12)	--
	PF Resin Weight	$W_{PF}^{\#} = W_{RTM}^{\#} - W_{C/C}^{\#-1}$ (2.13)	--
	Constituent Weights	$W_f^{\#-1} + (W_{PyC}^{\#-1} + Y_{PF} W_{PF}^{\#}) = W_{C/C}^{\#}$ (2.14)	--
	PyC Matrix Volume	$V_{PyC}^{\#} = \frac{W_{PyC}^{\#-1} + Y_{PF} W_{PF}^{\#}}{\rho_{PyC}}$ (2.15)	--
	Volume Fractions	$\mathcal{V}_f^0 + \mathcal{V}_{PyC}^{\#} + \mathcal{V}_p^{\#} = \mathcal{V}_{C/C}^0$ (2.16)	--

2.3 Results and Discussion

2.3.1 Pore Type and Evolution Throughout PIP Processing

Figure 2.6 shows a 2D representation of a 3D dimensional phenomenon performed in the Dragonfly software, distinguishing between open and closed porosity. Pores were classified as either an open pore or closed pore based on whether the pore was connected to the ROI outer surface in any of the three spatial dimensions. Figure 2.8, Figure 2.9, and Table 2.5 revealed that many of the internal pores that were initially accessible to the phenolic resin (open porosity) gradually became inaccessible to the phenolic resin (closed porosity) with each PIP cycle as greater amounts of closed porosity formed in the microstructure. The total porosity in the ROI was measured to be 40.93% after PIP0 and 21.04% after PIP5 via X-ray μCT . The mass conservation analysis results, however, calculated the total porosity to be 59.47% after PIP0 and 39.38% after PIP5. The measurements between the two methods, shown graphically in Figure 2.9, both revealed a non-linear decreasing trend in the total porosity but were lower for the tomography data most likely because of the resolution used. The $5\ \mu m$ resolution during X-ray μCT meant that the smallest objects that could be quantified in the tomographic images were pores with volumes $\geq 125\ \mu m^3$. As a result, many of the micron-sized pores were not captured, quantified, and included in the total pore volume fraction calculations. Because the Dragonfly software could not classify open and closed pores that shared a voxel in the 3D tomographic images, these pores were omitted from the pore volume fraction estimates. The resolution used and the voxels shared between pores made it difficult to determine whether the microstructure of the carbonized PPS was highly interconnected or not. Assuming the 20% porosity not accounted for was inaccessible, then 36.66% of the porosity would have been inaccessible from the start, potentially explaining the 39.38% porosity remaining after 5 PIP cycles. Density was not an attribute supported by the Dragonfly software, so density data could not be plotted and compared with the mass conservation analysis results. The density evolution calculated via the mass conservation analysis, however, showed that the C/C coupon density initially dropped from $1.51\ g/cm^3$ to $0.70\ g/cm^3$ and eventually plateaued to $1.04\ g/cm^3$ after ~20% of the porosity was infiltrated with phenolic resin. Note that the ROI generated after process step PIP1 appears cut off in Figure 2.7 due to empty space being included in the ROI. The flat face seen in this ROI was the coupon surface, even

though the ROI surface for all other PIP cycles was positioned 0.66 mm from each coupon face along the 2-direction, as Figure 2.5 illustrates.

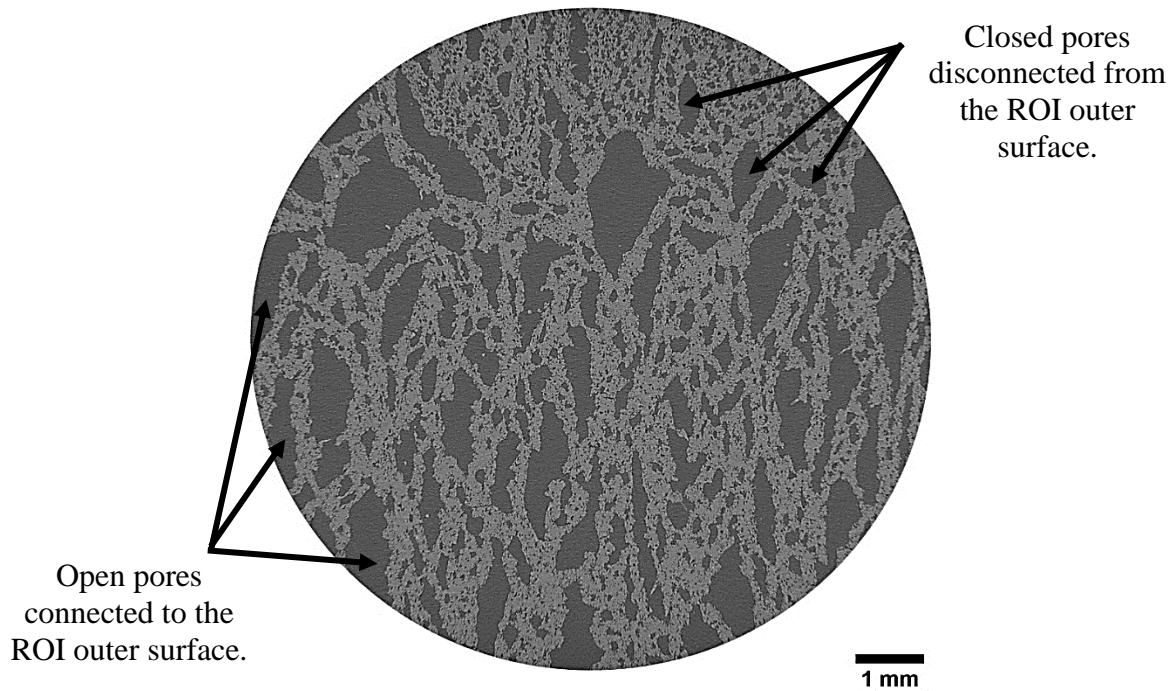


Figure 2.6 Open and closed porosity on a circular cross-section in the region of interest (ROI) during PIP0.

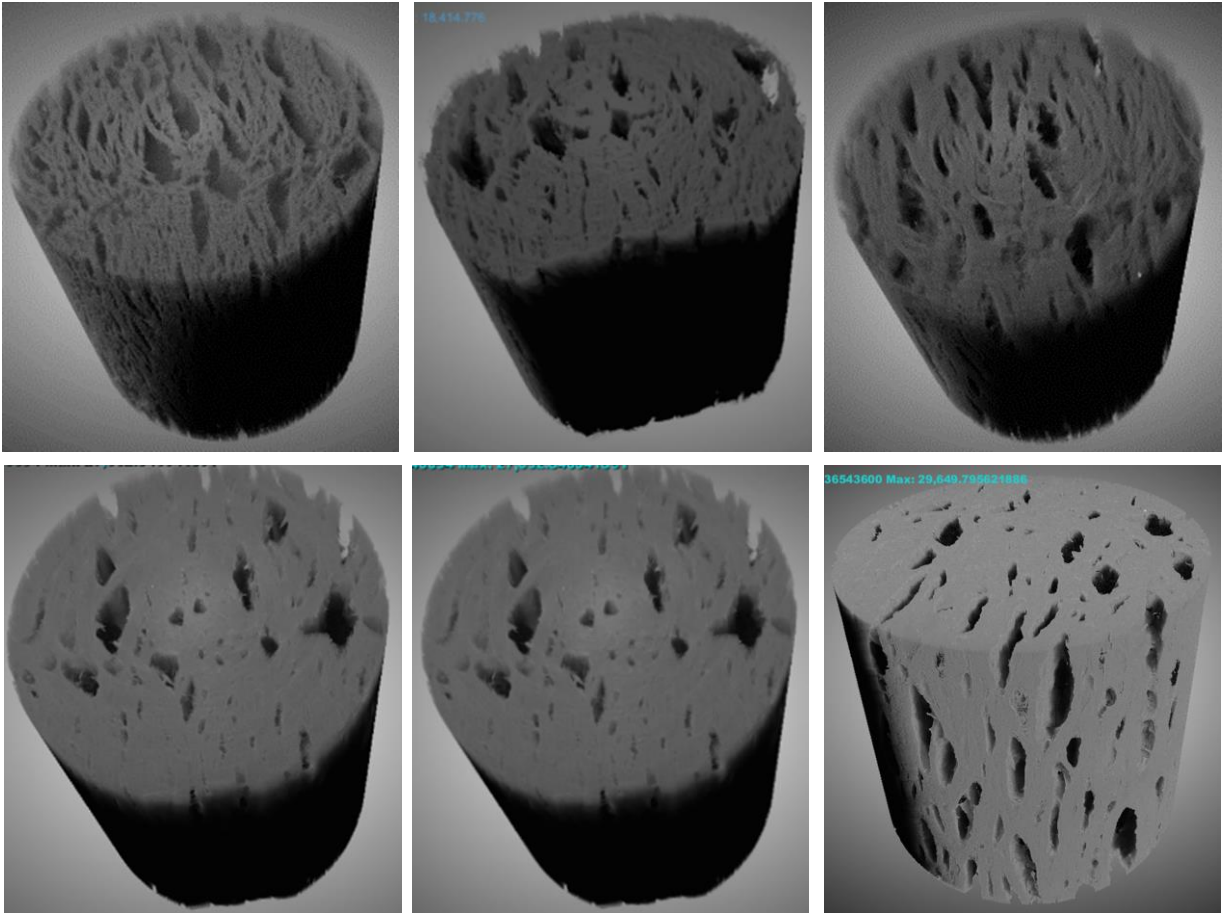
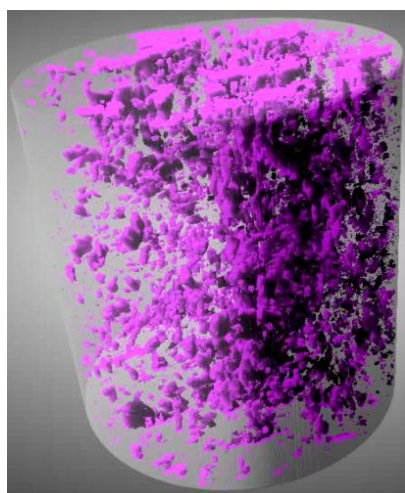
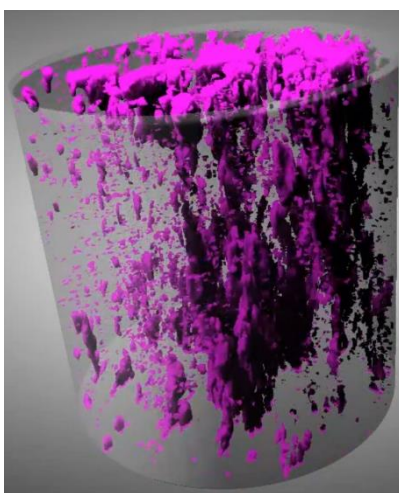


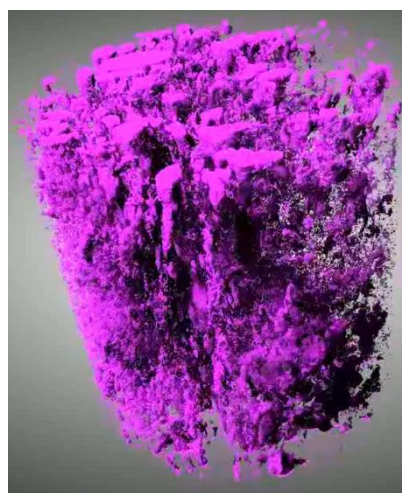
Figure 2.7 Evolution of the porosity visible on the ROI outer surface.



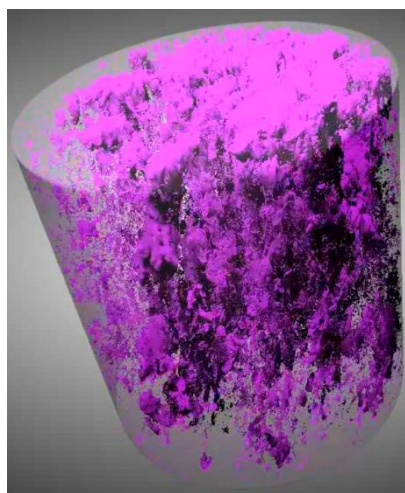
PIP0



PIP1



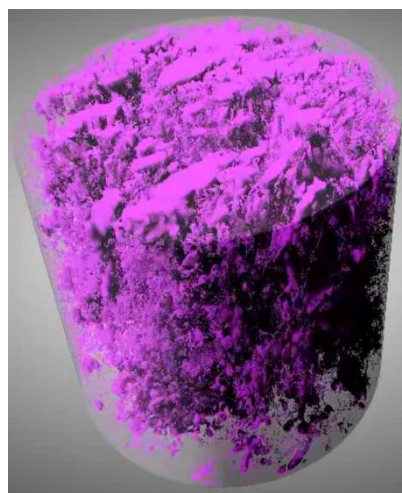
PIP2



PIP3



PIP4



PIP5

Figure 2.8 The evolution of percent closed porosity in the ROI

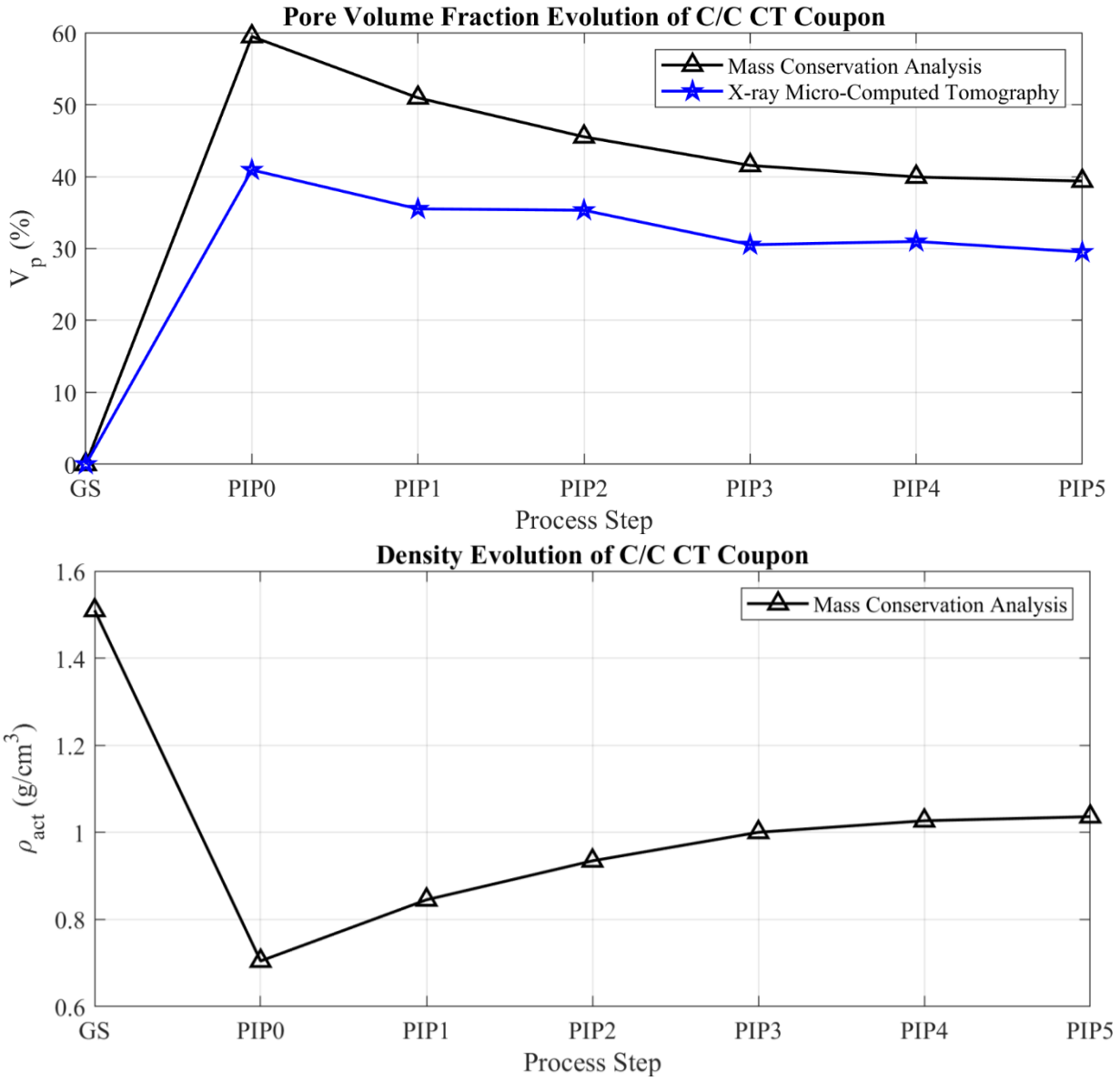


Figure 2.9 The graphical representation of density and total pore volume fraction evolutions results in Table 2.5.

Table 2.5 Density, pore volume fraction, and percent open & closed porosity evolution data in the ROI.

Method	Process Step						
	GS	PIP0	PIP1	PIP2	PIP3	PIP4	PIP5
Percent Closed Porosity (%)							
Micro-computed Tomography	0	2.85	4.59	2.11	5.7	6.04	8.47
Percent Open Porosity (%)							
Micro-computed Tomography	0	38.08	30.92	33.21	24.83	24.95	21.04
Total Pore Volume Fraction, \mathcal{V}_p (%)							
Micro-computed Tomography	0	40.93	35.51	35.32	30.53	30.98	29.51
Mass Conservation Analysis	0	59.47	50.95	45.53	41.56	39.95	39.38
Density, ρ_{act} (g/cm^3)							
Mass Conservation Analysis	1.51	0.70	0.84	0.93	1.00	1.03	1.04
Fiber Volume Fraction, \mathcal{V}_f (%)							
Mass Conservation Analysis	36.40	27.58	27.58	27.58	27.58	27.58	27.58

2.3.2 Pore Shape and Orientation

To determine the shape of the open and closed porosity, a length-to-diameter aspect ratio, $AR = L/D$, was calculated for each pore. The aspect ratio was determined by defining a circle with the same area and in the same plane as the pore's smallest cross-sectional area, and then using the direction normal to that plane to measure the pore's length. The results in Figure 2.10, Figure 2.12, and Figure 2.14 illustrated that the closed pores could be characterized by a prolate spheroidal shape ($AR > 1$) and were predominantly oriented in the print direction. The number of closed pores clearly increased with every PIP cycle, except for PIP1, which appeared to have a lesser number of closed pores than PIP0 but which in fact was the result of an incomplete scan of the microstructure, as Figure 2.7 showed. The aspect ratio parameter was not effective in describing

the open porosity because of its irregular shape but the orientation of the open pores was also mostly in the 1-direction.

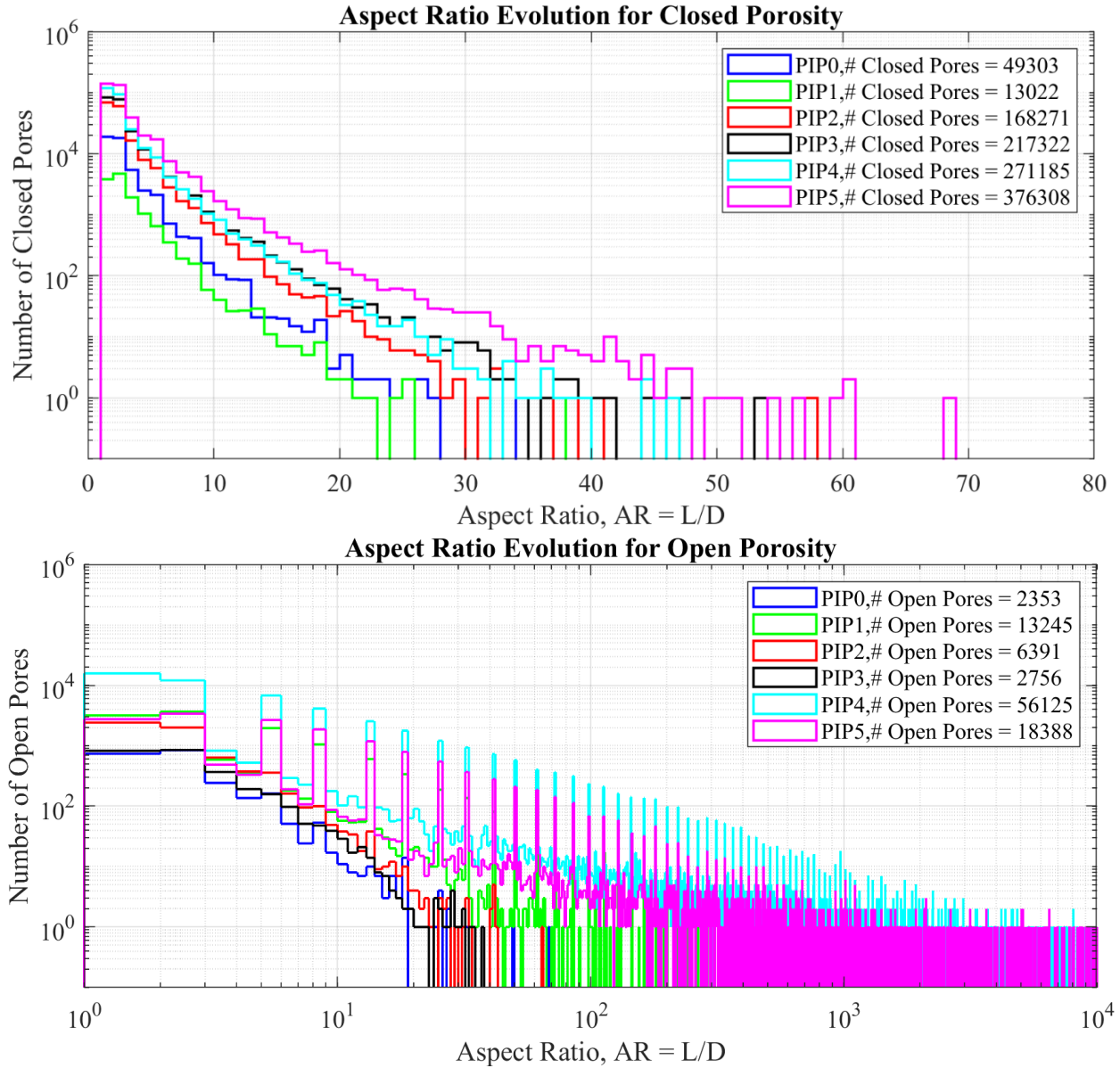


Figure 2.10 Aspect ratio distribution evolution for the open and closed pores throughout PIP processing displayed using a bin width of 1.

Rewriting the formula for a cylinder volume in terms of an aspect ratio, L/D , the length of the closed pores was plotted in Figure 2.11, illustrating that most of the pores were $5 - 8 \mu\text{m}$ long

but with many between $10 - 100\mu m$ long. The percentage of pores with lengths below $10\mu m$, $100\mu m$, and $1000\mu m$ is summarized in Table 2.6.

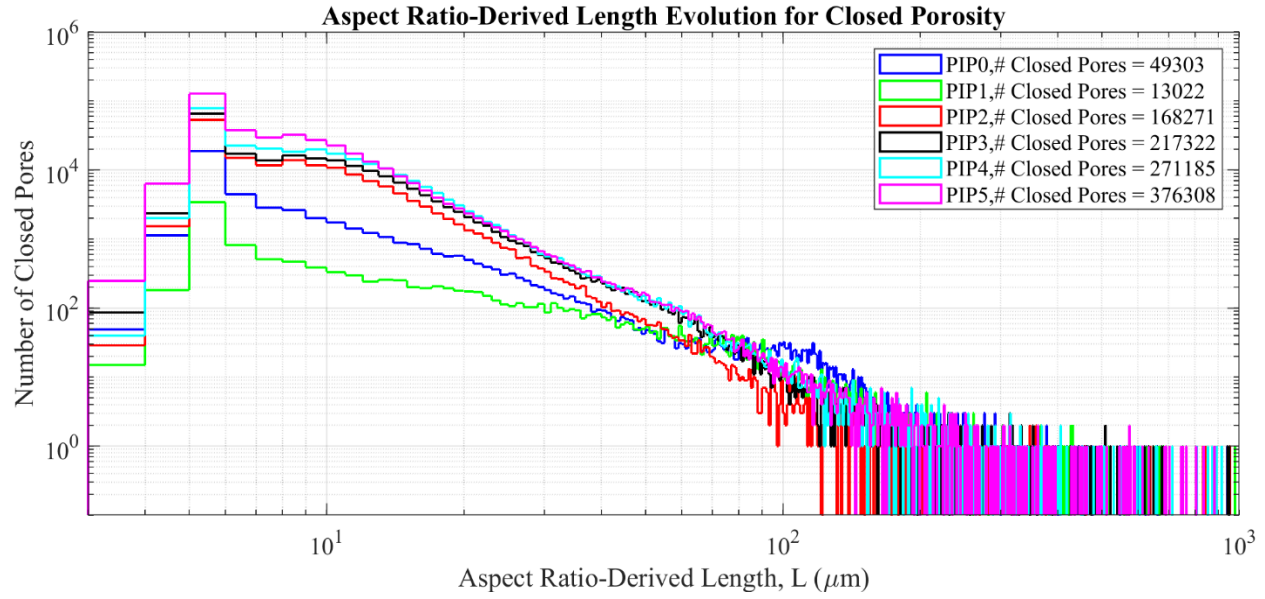


Figure 2.11 Length distribution of the closed pores throughout PIP processing.

Table 2.6 Percent of closed pores with lengths below $10\mu m$, $100\mu m$, and $1000\mu m$.

Length	Process Step					
	PIP0	PIP1	PIP2	PIP3	PIP4	PIP5
$< 10\mu m$ (%)	64.79	44.43	63.68	59.73	59.65	69.24
$< 100\mu m$ (%)	33.07	51.13	36.18	40.06	40.14	30.60
$< 1000\mu m$ (%)	2.14	0.16	0.13	0.21	0.21	0.16

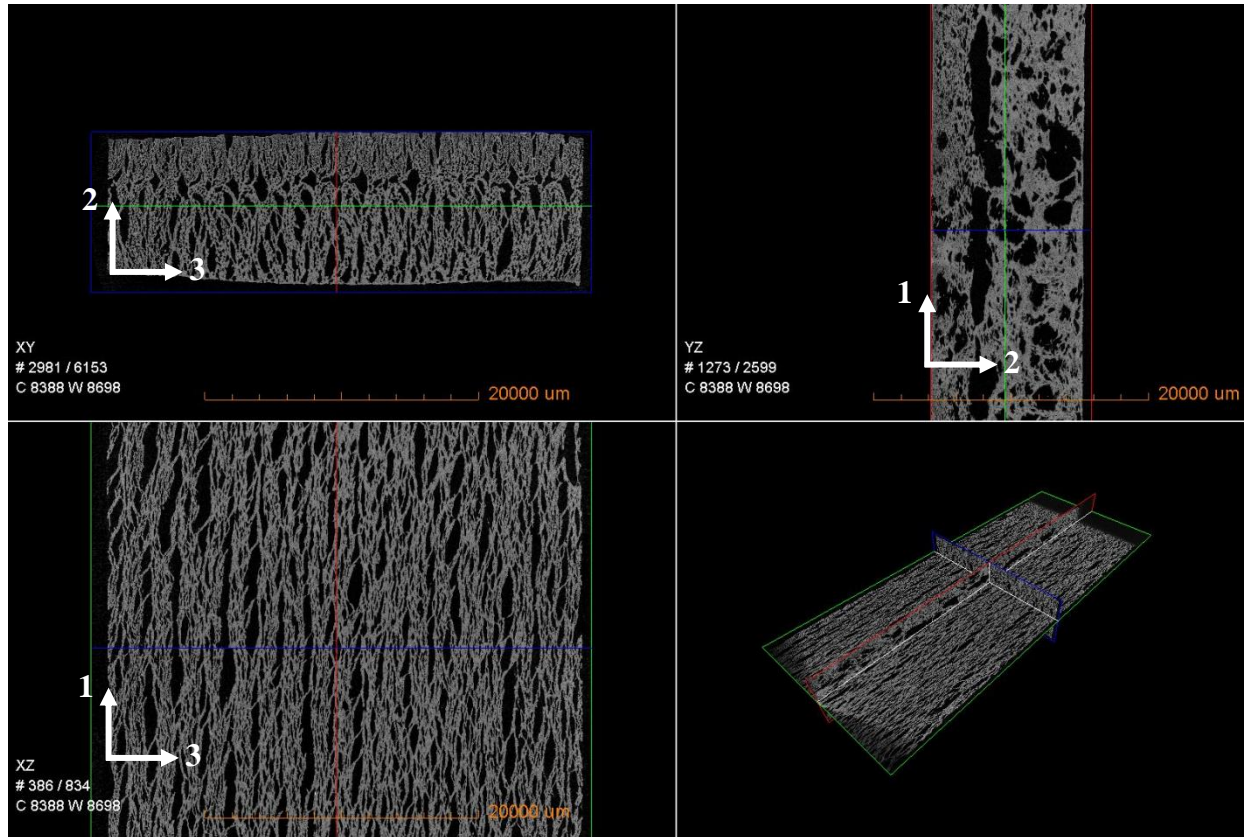


Figure 2.12 Cross-sections of the C/C coupon after initial pyrolysis processing showing the preferred orientation of the pores along the fiber direction (1-direction).

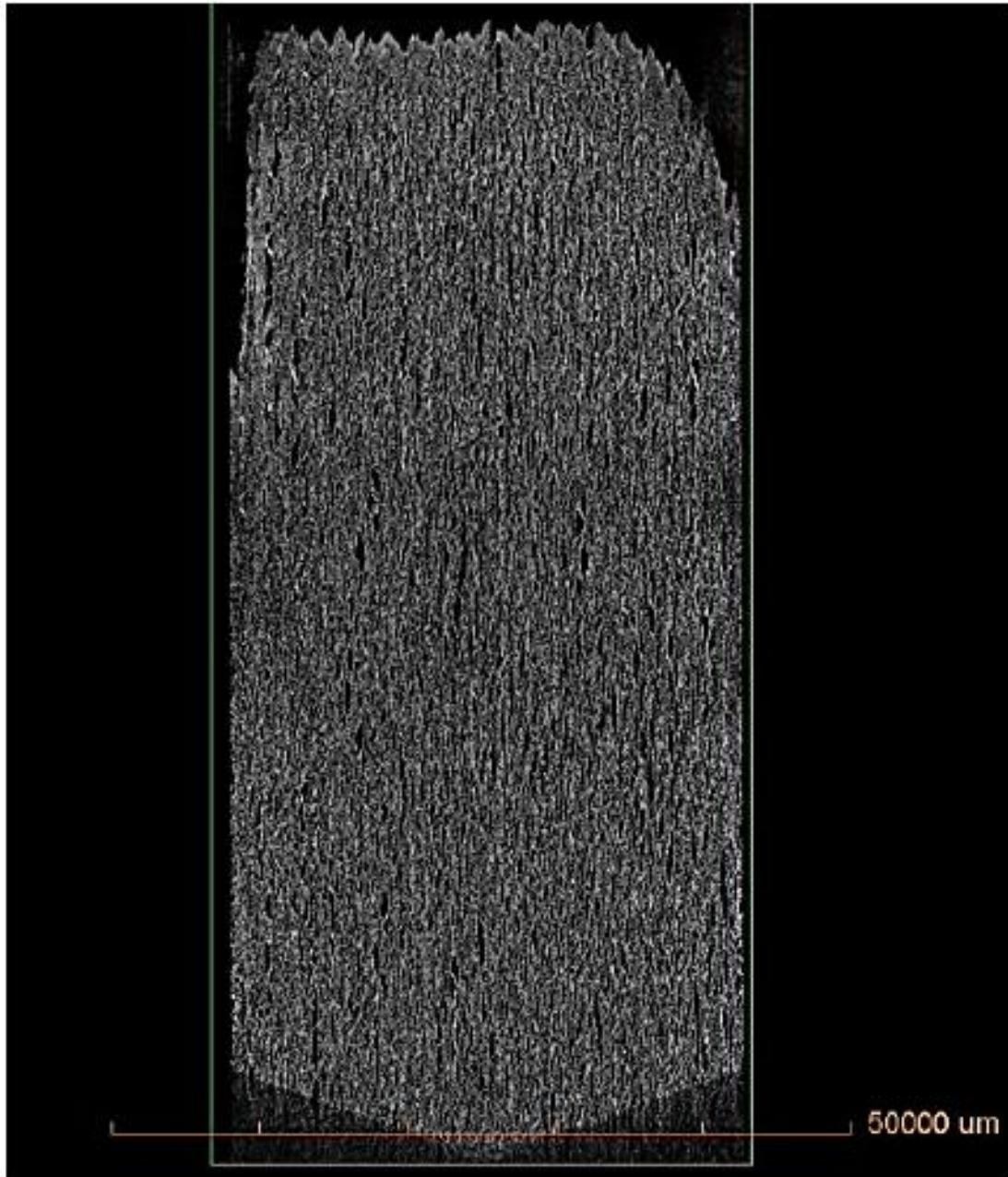


Figure 2.13. Moving from back face to front face in the 1-3 plane of the C/C CT coupon during PIP0 to show the preferred alignment of the pores in the fiber direction (vertical direction).

The ellipsoidal shape and orientation of the pores along the fiber direction (1-direction) in the C/C coupon after pyrolysis can be traced back to the foaming characteristics of the 50CF-PPS material noted in Chapter 1. While the higher viscosity of 50F-PPS reduced its foamability relative to other fiber-reinforced thermoplastic polymers tested, the cellular microstructure seen via X-ray microtomography suggested that the gas bubbles in the polymer melt-gas mixture were biaxially

stretched by shear forces during thermal decomposition. The ratio of shear forces to surface forces in a polymer melt-gas mixture are commonly described with the Weber (We) number:

$$We = \frac{\dot{\gamma} d_b \eta_p}{2\sigma} \left(\frac{19 \left[\frac{\eta_g}{\eta_p} + 16 \right]}{16 \left[\frac{\eta_g}{\eta_p} + 16 \right]} \right) \quad (2.17)$$

where $\dot{\gamma}(1/s)$ is the shear rate, $d_b(m)$ is the disintegrated bubble size, $\eta_p(Pa \cdot s)$ is the polymer viscosity, $\eta_g(Pa \cdot s)$ is the viscosity of the gas in the bubble, and $\sigma (N/m)$ is the surface tension [85,86]. As the low-molecular weight species diffused into the polymer melt, the decomposing 50CF-PPS coupon swelled initially along directions transverse to the fibers because of Brownian motion and the fiber-matrix coefficient of thermal expansion (CTE) mismatch until the compounding vapors preferentially escaped along the fiber direction, due to the anisotropic permeability in the 3D printed material. Park and Suh [85] experimentally measured higher bubble stretching ratios in higher viscosity fluids for the same shearing rates, indicating that higher fiber loadings in PPS with the same anisotropic fiber orientation would result in more needle-like porosity.

2.3.3 Spatial Evolution of the Pores Throughout PIP Processing

The spatial evolution of the open and closed pores was also analyzed, primarily to determine if a core-shell structure had formed where the outer surfaces were denser than the core. The results in Figure 2.15 show that within the core (zone 1) of the C/C coupon, the open pore volume fraction significantly decreased while the closed pore volume fraction significantly increased after 5 densification cycles. Within the shell region (zone 3), both the percent open and closed porosity were below 3% and seemed to fluctuate throughout PIP processing, easier to see in Table 2.7 than the plots. That the total pore volume fractions were lower in the shell region than the core indicated that the coupon did in fact have a core-shell microstructure, reaffirming the plateau behavior seen in the density and total pore volume fraction evolution plots. Notably, the total pore volume fraction estimates for the open and closed porosity differed from those values reported in Table 2.5 as a result of segmentation issues at the zone boundaries. Those pores intersecting the surfaces shared between zones were discounted from the analysis, but pores

sharing a common voxel within the zones were not, explaining why the pore volume fraction estimates shown were higher.

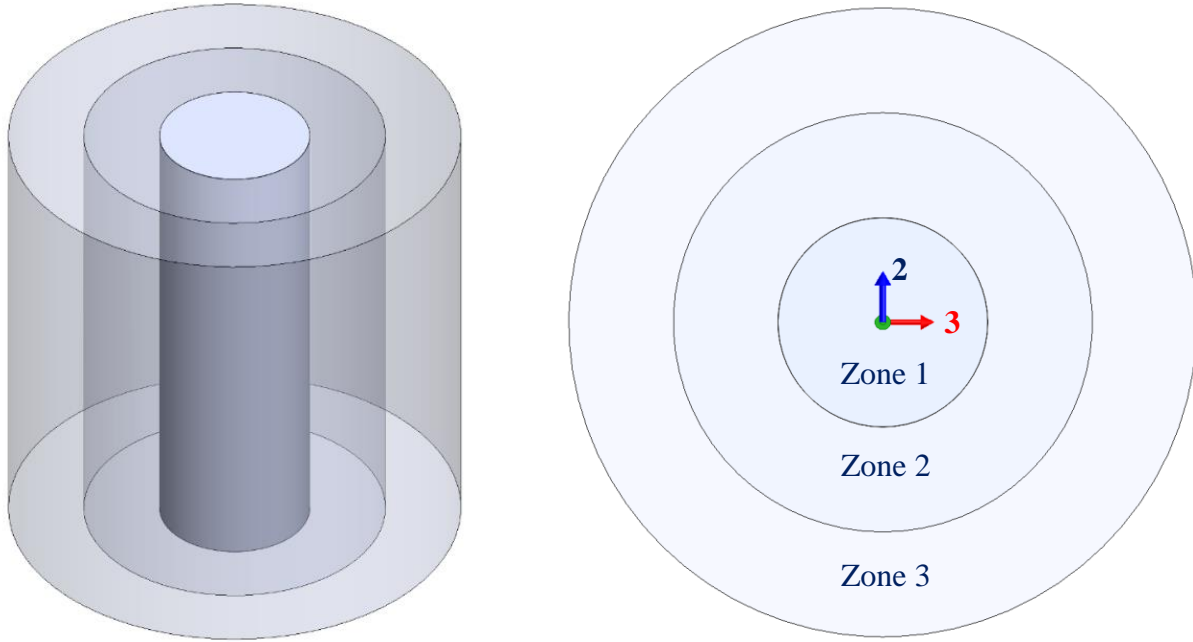


Figure 2.14 Sectioning the ROI into zone 1, 2, 3 with radius $R/3$, $2R/3$, $3R/3$, respectively.

Table 2.7 Radial distribution data shown in Figure 2.15.

Radial Location	Process Step					
	PIP0	PIP1	PIP2	PIP3	PIP4	PIP5
Percent Open Porosity, V_p (%)						
$R/3$	28.569	21.48	24.69	18.54	18.62	16.09
$2R/3$	12.56	9.72	11.29	7.20	7.56	5.74
$3R/3$	2.84	2.17	2.67	1.94	1.89	1.71
Total	43.97	33.37	38.66	27.69	28.08	23.54
Percent Closed Porosity, V_p (%)						
$R/3$	2.14	3.19	1.42	4.25	4.51	6.22
$2R/3$	1.27	2.33	0.87	3.07	2.69	4.17
$3R/3$	0.48	0.89	0.29	0.66	0.59	0.67
Total	3.89	6.41	2.59	7.99	7.79	11.06

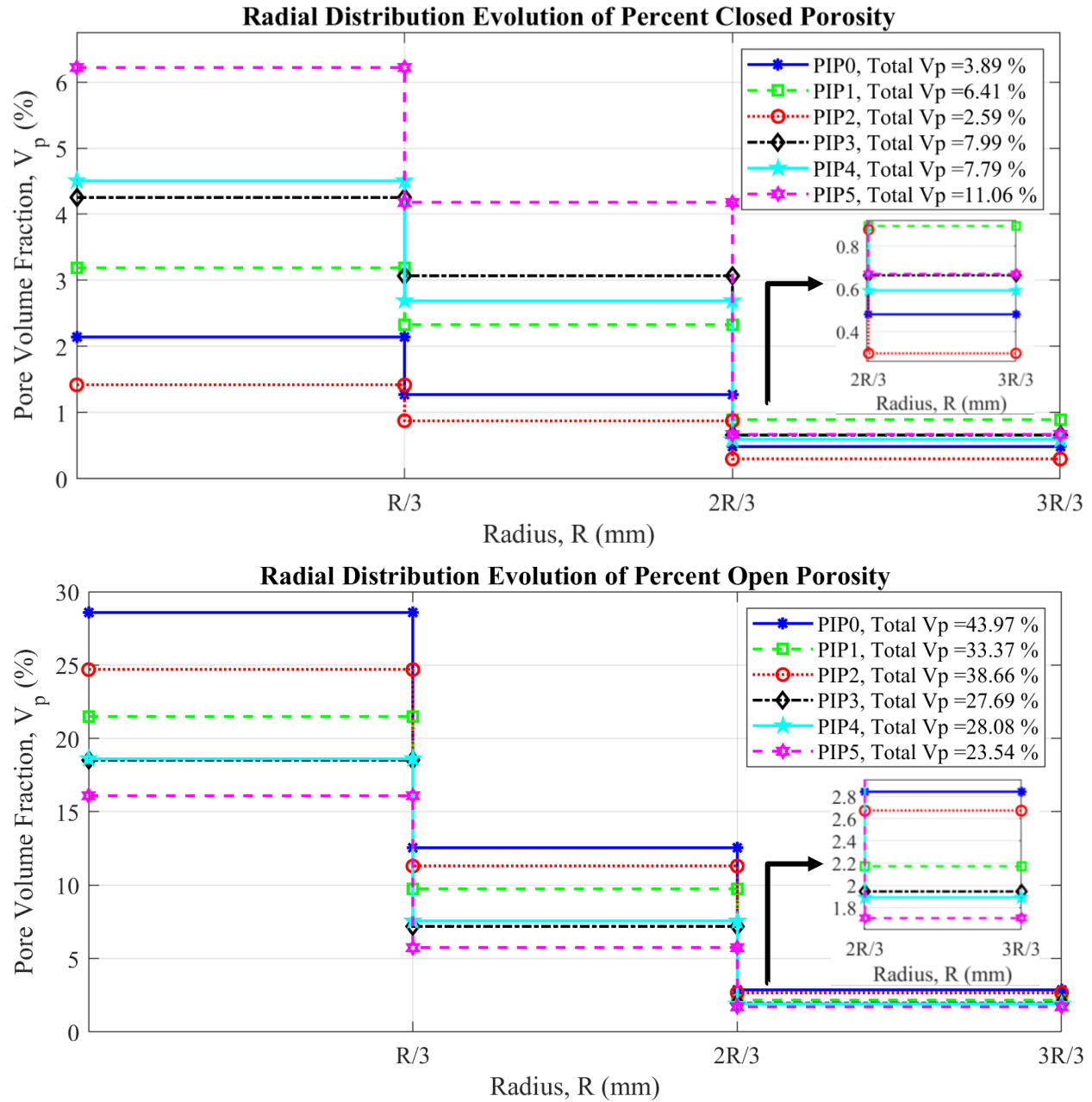


Figure 2.15 Radial distribution evolution of the percent open and closed porosity throughout PIP processing.

2.4 Conclusion

The X-ray micro-computed tomography scans were used to analyze the microstructure of a 50 wt. % short carbon fiber-reinforced polyphenylene sulfide-derived 3D printed C/C composite during repeated polymer infiltration and pyrolysis cycles to 1000°C. The results showed that the carbon fibers did not bound the pores as Larson et. al [80] noted for composites with continuous

fibers but did influence the preferential orientation of the pores. The anisotropic viscosities and permeabilities in the composite material above its melt temperature resulting from the anisotropic fiber orientation aligned the major axis of the pores in the fiber direction. The C/C coupon density dropped from 1.51 g/cm^3 to 0.7 g/cm^3 after initial pyrolysis processing and had a percent open & closed porosity of approximately 38.08% and 2.85%, although the $5\text{ }\mu\text{m}$ resolution and segmentation issues encountered may have omitted 19% of the starting porosity from the analysis, as the mass conservation measurements suggested. After five polymer infiltration and pyrolysis cycles with phenolic resin, the density, percent open and percent closed porosity plateaued to 1.04 g/cm^3 , 21.0%, and 8.5%, respectively. The density of the 3D printed C/C coupon was low and was attributed to the low pressures used to push the phenolic resin into the pores. A spatial evolution analysis showed a core-shell structure formed, where approximately 16.0% and 6.2% of the percent open and closed porosity was still in the core region of the coupon, while 1.7% and 0.67% open and closed porosity was present near the coupon surfaces.

3. POPULATING THE ORTHOTROPIC STIFFNESS TENSOR OF ADDITIVELY MANUFACTURED SHORT FIBER-REINFORCED CARBON/CARBON COMPOSITES

3.1 Introduction

While there is a growing body of literature for mechanical properties of additively manufactured ceramic matrix composites (CMCs) like SiC_f/SiC [87], C_f/SiC [88], [89], [90], C_f/C-SiC [91], [92], C_f/ZrB₂-SiC [93], and SiC_f/ZrB₂-SiC [94], publications surrounding additively manufactured carbon/carbon (C/C) composites and their resultant mechanical properties are less abundant. The susceptibility to oxidation of C/C composites at temperatures as low as 500°C discourages its use for a variety of high temperature applications [95], but its lower density relative to CMCs [96] makes it an excellent substrate for weight-critical hot structures >3000°C when ultra-high temperature ceramic coatings (e.g. ZrC, HfC, TaC, and ZrB₂) are applied [97], [98]. The ability to additively manufacture C/C composites with extrusion deposition additive manufacturing (EDAM) was shown in Chapter 1, since compared to other 3D printing methods, large-scale structures with fibers oriented in load-critical directions can be manufactured without the use of molds/tooling surfaces. However, the mechanical properties resulting from this processing route were not explored.

The mechanical properties of traditionally manufactured C/C composites have been reported for various fiber volume fractions, pore volume fractions, infiltration methods (either by chemical vapor infiltration (CVI) or polymer infiltration and pyrolysis (PIP)), heat treatment temperatures, and fiber architectures [99–119], with densities, tensile, compressive, and Iosipescu shear strengths ranging from 1.4 – 1.9 g/cm³, 100 – 400 MPa, 8 – 230 MPa, and 15 – 45 MPa, respectively. The infiltration-dependent evolution results in Chapter 2 showed that for an extrusion-based additively manufactured C/C composite with a fiber volume fraction of 27.58%, the pore volume fraction and bulk density plateaued to 39.38% and 1.04 g/cm³ after 5 PIP cycles with phenolic resin, not as reinforced or as dense, and alluding to lower mechanical properties, than traditionally manufactured C/C composites.

However, because the flow and fiber orientation are mutually dependent during the extrusion process, and can be tailored to meet different loading conditions for a given structure, an investigation of the mechanical properties of EDAM C/C composites was conducted to provide a

baseline for future investigations, if and when the extrusion processing parameters and the method of infiltration are varied to induce different microstructures, orthotropic thermo-elastic properties, and strengths in a 3D printed C/C composite. Mechanical property characterization via impulse tests, tensile tests, and double-notched shear tests were performed to find the elastic constant evolutions of additively manufactured C/C composites taken through 5 PIP cycles with phenolic resin as well as find two strength parameters. Since not all elastic constants were determined experimentally, the remaining elastic constants were obtained numerically via multi-scale material modeling with Digimat-MF® to fully populate the compliance/stiffness tensor. The results of the fully dense C/C composites were then compared to literature results of traditionally manufactured C/C composites to quantify the difference in mechanical properties.

3.2 Experimental Procedure

3.2.1 Manufacturing the 3D Printed C/C Coupons

The 5 C/C coupons prepared for mechanical testing were manufactured in the same way as described in section 2.2.1, where care was taken to ensure the coupons had a length-to-thickness ratio, $\frac{L}{T} \approx 3$, per the requirement specified in ASTM E1876.

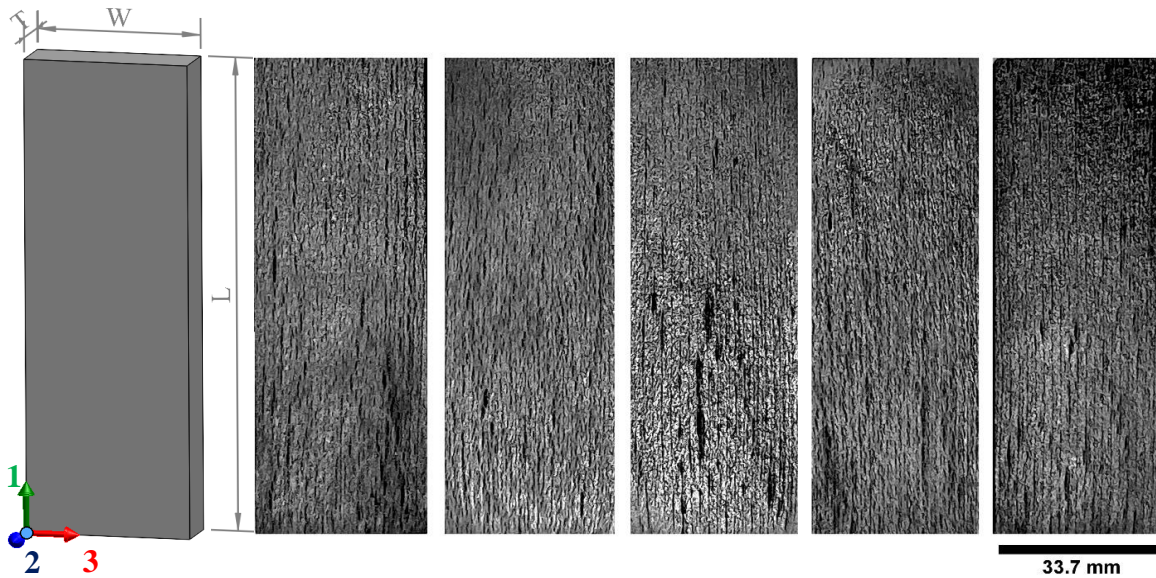


Figure 3.1 C/C composite coupons after initial pyrolysis processing, showing cracks aligned dominantly with the print direction (1-direction).

Table 3.1 Dimensions of C/C composite coupons shown in Figure 3.1.

Dimension (mm)	C/C Composite Coupon				
	1	2	3	4	5
Length 1	100.81	100.98	100.88	100.95	100.22
Length 2	100.89	100.94	101	101.12	100.36
Length 3	100.83	100.98	100.93	100.86	100.48
Average Length, L	100.84	100.97	100.94	100.98	100.35
Gage Width 1	33.97	33.7	33.43	33.26	33.25
Gage Width 2	33.82	33.78	33.84	33.59	33.5
Gage Width 3	33.68	33.87	33.82	33.6	33.25
Average Gage Width, W	33.82	33.78	33.70	33.48	33.33
Gage Thickness 1	11.51	11.57	11.17	11.32	11.41
Gage Thickness 2	11.38	11.63	11.3	11.12	11.31
Gage Thickness 3	11.03	11.39	11.28	11.03	11.03
Average Gage Thickness, T	11.31	11.53	11.25	11.16	11.25

3.2.2 Polymer Infiltration and Pyrolysis Processing with Phenolic Resin

The 5 C/C coupons were infiltrated in the same manner as outlined in section 2.2.2, and then re-carbonized at $2^{\circ}\text{C}/\text{min}$ from 25°C to 1000°C and $2^{\circ}\text{C}/\text{min}$ from 1000°C to 25°C . Table 3.2 shows all the coupon weights throughout PIP processing. The spread in density and pore volume fraction evolution data between the 5 C/C coupons in Figure 3.2 indicated variations in the microstructure, which may have resulted from small furnace deviations during heating/cooling. Comparing data between Table 2.5 and Table 3.3, the density and pore volume fraction evolution results of the 5 C/C coupons were on average 3.26% less porous and $0.05 \text{ g}/\text{cm}^3$ denser than the C/C CT coupon after 5 PIP cycles. The higher pore volume fraction and lower density in the C/C CT coupon was apparent even during PIP0 and was therefore attributed to the orientation marker, introduced during machining, facilitating egress of gaseous by-products by decreasing the diffusion distance for the radical species. The reader is referred to Appendix Table C.1 for more details on how the plots in Figure 3.2 were produced.

Table 3.2 Weights of the 5 C/C coupons at every process step used to calculate the density and pore volume fraction evolution data.

PIP Cycle	Process Step	Coupon 1 (<i>g</i>)	Coupon 2 (<i>g</i>)	Coupon 3 (<i>g</i>)	Coupon 4 (<i>g</i>)	Coupon 5 (<i>g</i>)
0	3D Printed	63.85	64.8	62.36	63.14	63.87
	Pyrolysis (post-machining)	29.27	29.43	30.05	28.65	30.07
1	Infiltration	41.96	41.79	39.65	39.63	40.91
	Pyrolysis	35.77	35.61	34.72	33.93	35.14
2	Infiltration	40.45	39.98	42.07	37.96	40.79
	Pyrolysis	38.16	37.95	38.39	36.14	38.29
3	Infiltration	43.63	42.82	44.06	39.11	43.76
	Pyrolysis	40.9	40.03	41.26	37.71	41.19
4	Infiltration	43.08	43.31	44.06	39.04	42.99
	Pyrolysis	41.97	41.59	42.51	38.38	42.08
5	Infiltration	42.77	42.43	43.21	39.15	43.08
	Pyrolysis	42.33	41.98	42.77	38.72	42.55

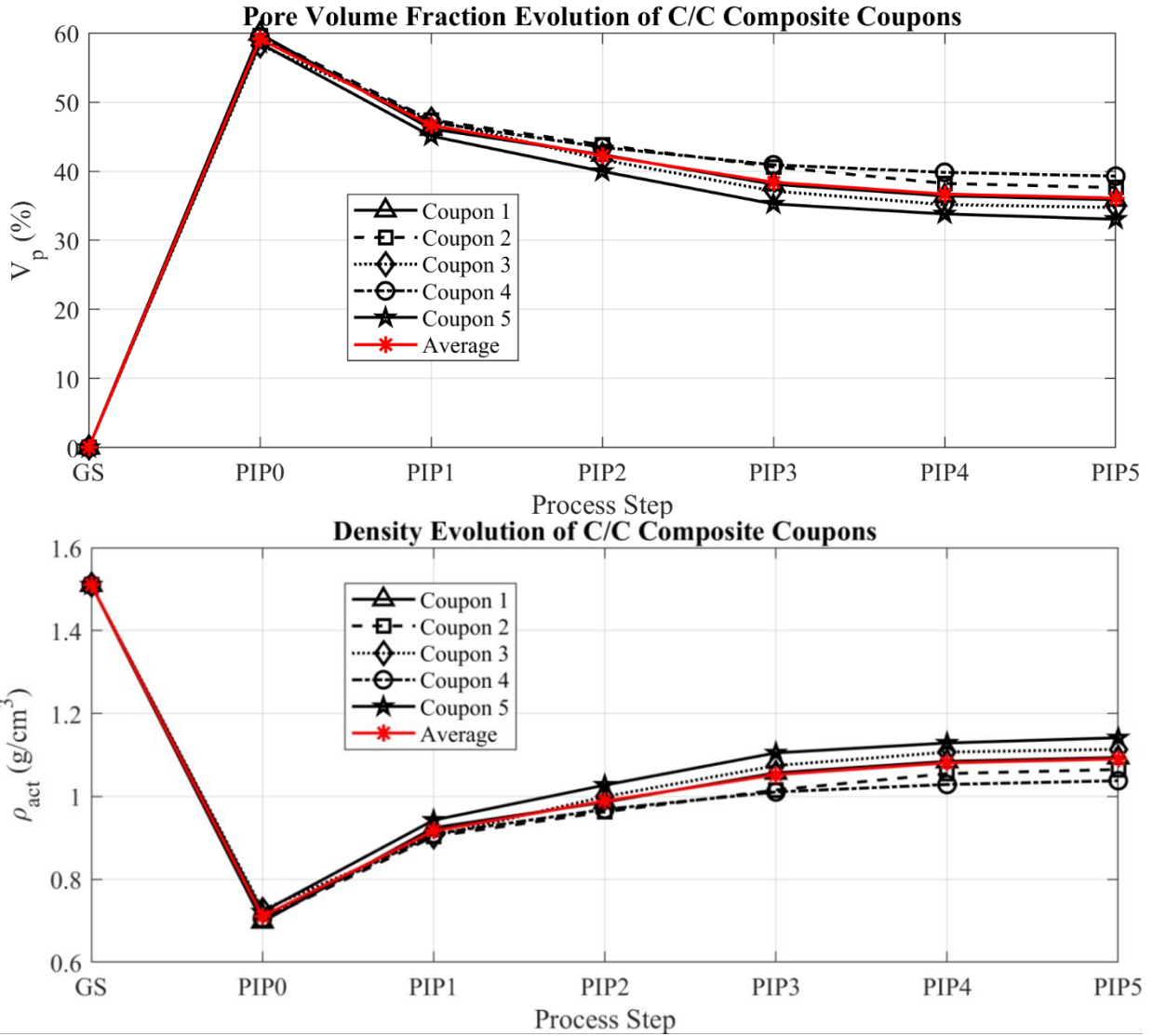


Figure 3.2 Density and pore volume fraction evolution data after 5 PIP cycles for coupons 1-5 through. Note that GS in plots refers to the green state (3D printed).

Table 3.3 Density and pore volume fraction evolution data shown in Figure 3.2.

C/C Coupon	Process Step						
	GS	PIP0	PIP1	PIP2	PIP3	PIP4	PIP5
Total Pore Volume Fraction, \mathcal{V}_p (%)							
1	0	59.87	46.14	42.39	38.10	36.43	35.86
2	0	59.64	47.42	43.83	40.63	38.23	37.63
3	0	58.22	47.45	41.66	37.13	35.16	34.75
4	0	59.41	47.06	43.47	40.92	39.83	39.28
5	0	58.52	45.09	39.98	35.26	33.81	33.05
Average	0	59.13	46.64	42.27	38.41	36.69	36.12
Density, ρ_{act} (g/cm^3)							
1	1.51	0.69	0.92	0.99	1.06	1.08	1.09
2	1.52	0.70	0.90	0.96	1.02	1.05	1.06
3	1.50	0.72	0.90	1.00	1.07	1.11	1.11
4	1.51	0.71	0.91	0.97	1.01	1.03	1.04
5	1.51	0.72	0.94	1.03	1.10	1.13	1.14
Average	1.51	0.71	0.92	0.99	1.05	1.08	1.09
Fiber Volume Fraction, \mathcal{V}_f (%)							
1	36.22	27.31	27.31	27.31	27.31	27.31	27.31
2	36.19	27.47	27.47	27.47	27.47	27.47	27.47
3	35.89	28.43	28.43	28.43	28.43	28.43	28.43
4	35.93	27.63	27.63	27.63	27.63	27.63	27.63
5	35.83	28.23	28.23	28.23	28.23	28.23	28.23
Average	36.01	27.81	27.81	27.81	27.81	27.81	27.81

3.2.3 Mechanical Testing

Impulse excitation tests were performed according to ASTM E1876 on 5 C/C coupons by impacting the coupons with a stainless-steel ball hammer while on foam nodal supports and exciting the flexural and vibrational modes, as in Figure 3.3. An acoustic microphone was connected to a GrindoSonic® MK7 data acquisition device (GrindoSonic, Leuven, Belgium) to pick up the stress wave signal. Each coupon was impacted approximately 10 times after each PIP cycle. Neither ASTM C1259, the carbon material specific standard ASTM C747, nor ASTM E1876 (which is employed by the GrindoSonic® MK7 device software) are applicable to anisotropic materials, but the development and validation of mixed numerical experimental techniques (MNET) by Lauwagie et. al [120], [121] with an orthotropic brass beam showed that the first 5 vibrational mode shapes were dominantly sensitive to changes in the young's modulus parallel to the beam axis and in-plane shear modulus perpendicular to the beam cross-section, respectively. As a result, the GrindoSonic® data was considered approximately valid for elastic

constant evolution measurements of E_1 & G_{23} . Because the impulse tests generated both elastic longitudinal and shear waves during impact, the corrugated surface produced after extrusion was smoothed, as in Figure 2.1, so that any attenuation in the data could be attributed solely to the porosity and heterogeneity of the material [122,123]. A Poisson's ratio, $\nu = 0.3$, was assumed constant throughout PIP processing for all coupons tested.

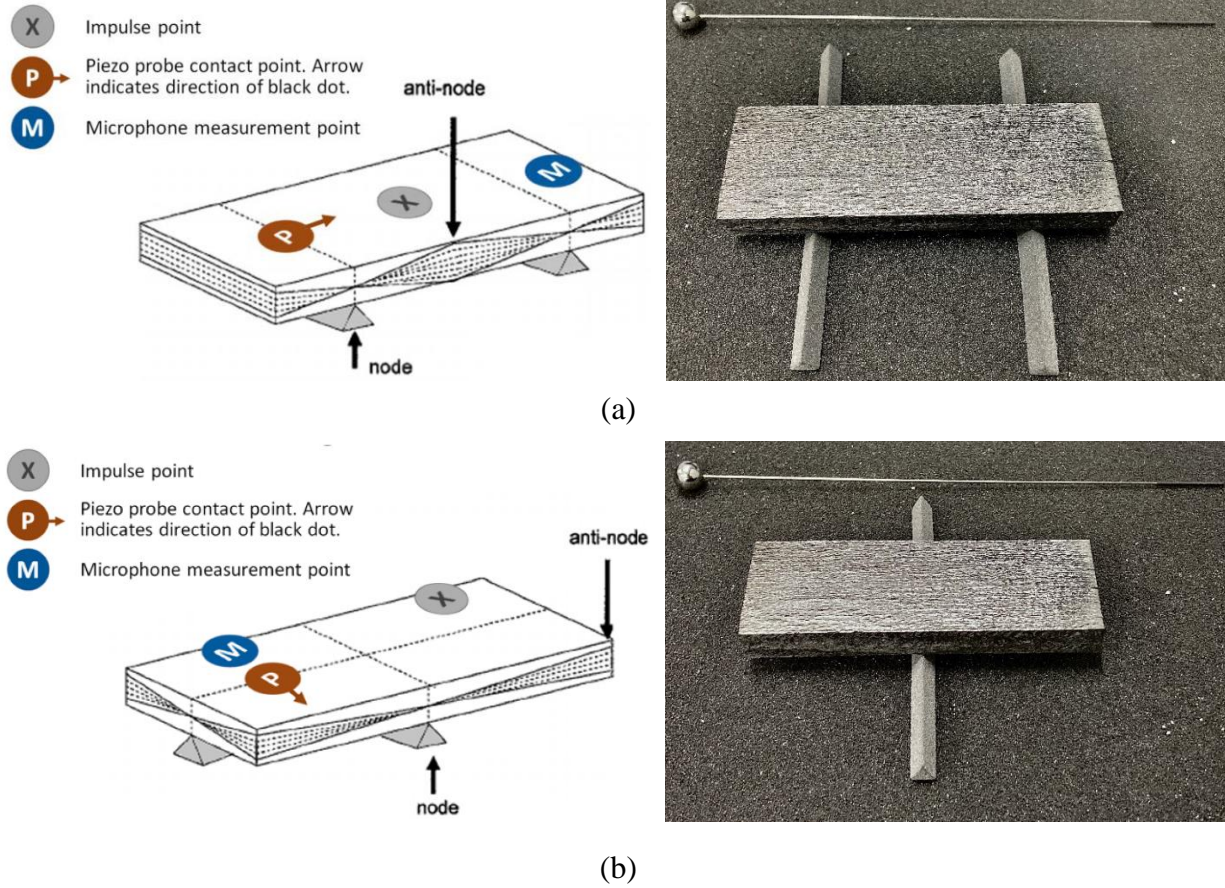


Figure 3.3 Impulse excitation test setup for the (a) flexural and (b) torsional vibrational test modes, in which parallel and cross-shaped nodal supports were used, respectively.

Tensile tests were performed in room-temperature ambient air according to ASTM C1275 on 4 C/C coupons, shown in Figure 3.4, laterally loaded with hydraulic finely serrated active grips using a 22 Kip load machine (MTS, Eden Prairie, Minnesota) (at the Indiana Manufacturing Institute) and a crosshead displacement rate of 0.01 mm/s to determine the tensile strengths of the C/C material. The grip pressure used for the 4 C/C coupons was 2757.90 kPa (400 psi), since the test coupon used to align the crossheads crushed when a grip pressure of

3447.38 *kPa* (500 *psi*) was used. This is shown in Appendix Figure C.10. It should be noted that the tensile coupons were the same coupons used for impulse testing but were machined to have the dimensions shown in Table 3.4, since the impulse excitation coupons had thickness tolerances outside the ± 0.1 *mm* range specified in ASTM C1275. To obtain the thicknesses reported in Table 3.4, the impulse excitation coupons were surface grinded (Kent USA, Tustin, California) with a 320-grit diamond wheel at a stock removal rate of 0.01 *mm/pass* using Rustlick G-25J synthetic grinding fluid. Because of the low interlaminar shear strength relative to the tensile strength in C/C composites [106], the straight-sided coupons were tested using beveled red fiberglass circuit board end tabs adhesively bonded with Lord 310 A/B epoxy (Parker Lord, Cary, North Carolina) to encourage failure in the gage section. The end tabs were clamped until the epoxy reached full strength (24 *hrs*). Because the tensile coupons were manufactured from the impulse excitation coupons, the mass conservation analysis results in Table 3.3 applied; the C/C tensile coupons had a fiber volume fraction of approximately 27.81%, an average bulk density of 1.09 ± 0.05 *g/cm*³ and an average pore volume fraction of 36.12 ± 3 %. The engineering stress, engineering strain, tensile strength, strain at tensile strength, and elastic modulus, E_1 , were calculated from the resulting data for each coupon. While surface strain measurements were initially planned during tensile tests to obtain Poisson's ratio, ν_{13} , data via digital image correlation (DIC) with VIC-snap® (acquisition) & VIC-3D® software (analysis) (Correlated Solution, Irmo, South Carolina), a speckle pattern could not be created on the tensile coupons because of surface porosity. The gage section was still spray painted white however, to provide a contrasting background for fractography studies, as Figure 3.6a shows.

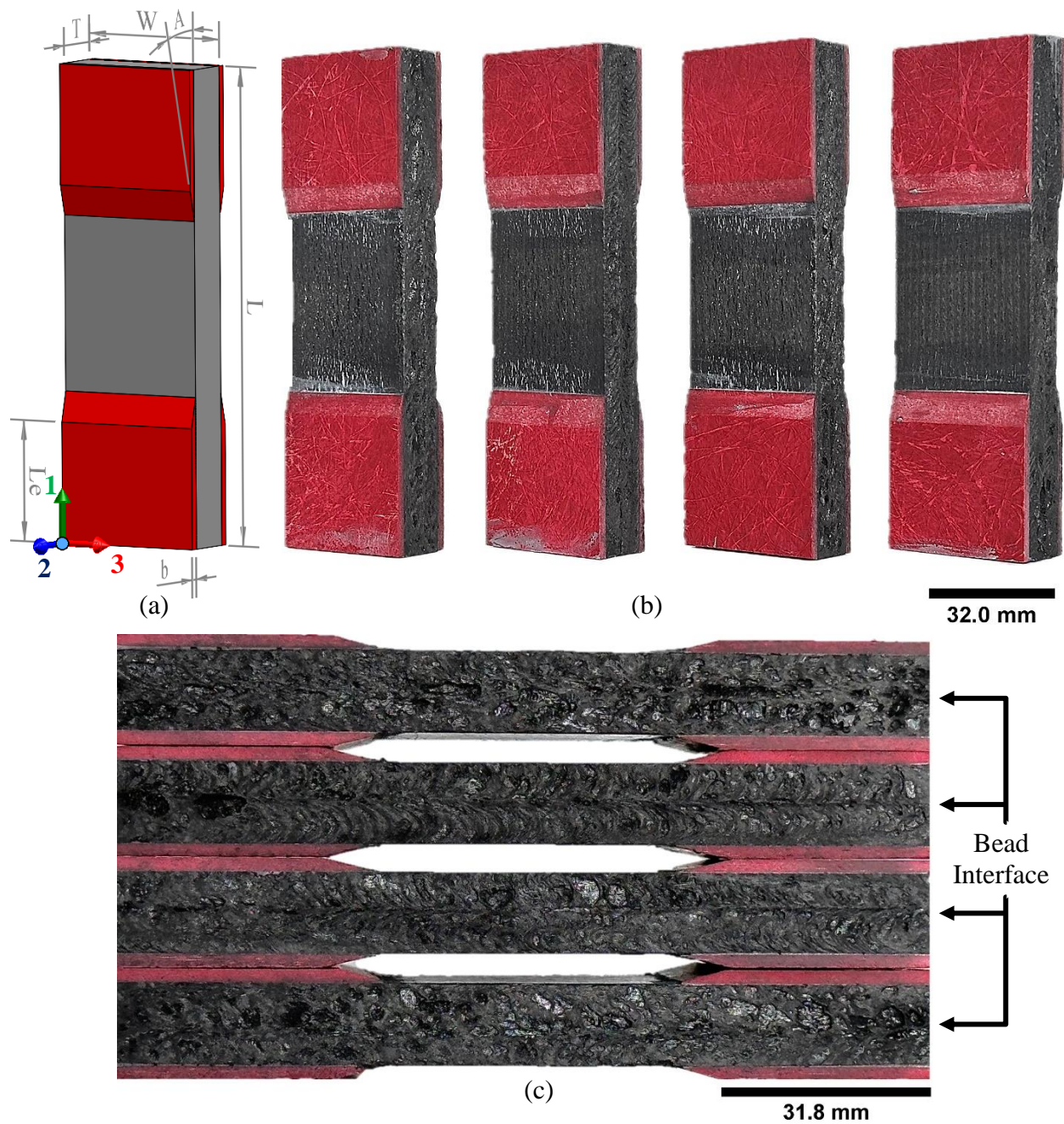


Figure 3.4 (a) CAD model with local/material coordinate system & reference dimensions, (b) isometric view, (c) and side view showing the bead interface noted in Figure 2.1c of the tension-loaded C/C coupons.

Table 3.4 Dimensions of the tension-loaded C/C coupons shown in Figure 3.4.

Dimension (<i>mm</i>)	Tension-loaded C/C Coupon			
	1	2	3	4
Length 1	101.19	101.03	100.59	101.38
Length 2	101.07	101.21	100.69	101.3
Length 3	101.24	101.16	100.64	101.11
Average Length, <i>L</i>	101.16	101.13	100.64	101.26
Gage Width 1	32.05	32.05	32	32.05
Gage Width 2	32.05	31.93	32.02	32.09
Gage Width 3	32.05	32.07	32.03	32.08
Average Gage Width, <i>W</i>	32.05	32.02	32.01	32.07
Gage Thickness 1	10.06	10.09	10.05	9.94
Gage Thickness 2	10.08	10.03	10.01	9.94
Gage Thickness 3	10.04	10.09	10.03	9.94
Average Gage Thickness, <i>T</i>	10.06	10.07	10.03	9.94
Tab Thickness, <i>b</i>	1.6	1.59	1.61	1.59
Bevel Angle, <i>A</i> (°)	14.2	14.3	14.5	14.4
Tab Length, <i>Le</i>	31.87	31.84	31.85	31.86

Double-notched shear tests of compression-loaded double-notched C/C coupons was performed in room temperature ambient air according to ASTM C1292 on 4 coupons using a 22 Kip load machine (MTS, Eden Prairie, Minnesota) (at the Indiana Manufacturing Institute) and a crosshead displacement rate of 0.01 *mm/s* to determine the shear strength of the C/C material. The disadvantage of the double-notched shear test method are the stress concentrations resulting from the corners of the notches, but the advantage is the shear strengths measured are more conservative than those measured via the Iosipescu shear test method [124]. Just like the tension-loaded C/C coupons, the compression-loaded C/C coupons were also the same coupons from impulse testing and were reduced in thickness to 10.0 ± 0.1 *mm* with a 320-grit diamond wheel at a stock removal rate of 0.01 *mm/pass* using Rustlick G-25J synthetic grinding fluid. It should be noted that the thickness specified by ASTM C1292, which referenced ASTM D3846 and required a thickness of 6.4 ± 0.1 *mm*, was not followed since this would have significantly changed the microstructure introduced after 5 PIP cycles. The dimensions of the coupons as well as the notch dimensions were summarized in Table 3.5. The C/C coupons prepared for double-

notched shear tests also had a fiber volume fraction of approximately 27.81%, an average bulk density of $1.09 \pm 0.05 \text{ g/cm}^3$ and an average pore volume fraction of $36.12 \pm 3 \%$. The engineering stress, engineering strain, shear strength, and shear modulus, G_{13} , were calculated from the resulting data for each coupon.

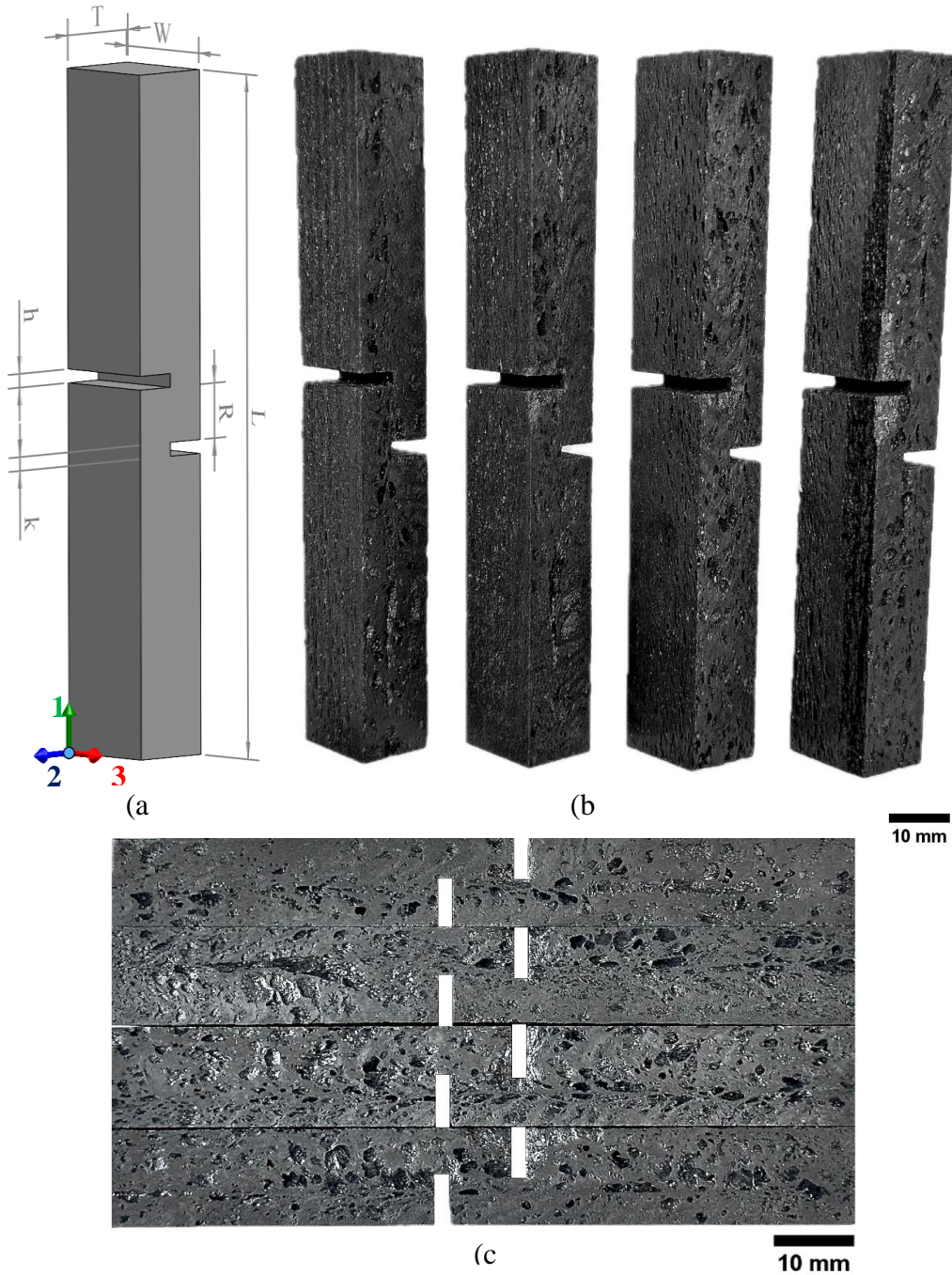


Figure 3.5 (a) CAD model with local/material coordinate system & reference dimensions, (b) isometric view, and (c) side view of the compression-loaded double-notched C/C coupons.

Table 3.5 Dimensions of the compression-loaded double-notched C/C coupons shown in Figure 3.5.

Dimension (mm)	Compression-loaded C/C Coupon			
	1	2	3	4
Length 1	79.52	79.53	79.51	79.12
Length 2	79.53	79.53	79.56	79.13
Length 3	79.53	79.53	79.55	79.14
Average Length, L	79.52	79.53	79.54	79.13
Gage Width 1	12.75	12.78	12.79	12.74
Gage Width 2	12.76	12.76	12.78	12.74
Gage Width 3	12.76	12.77	12.77	12.75
Average Gage Width, W	12.75	12.77	12.78	12.74
Gage Thickness 1	10.02	10.06	10.08	9.79
Gage Thickness 2	9.97	10.06	10.07	9.77
Gage Thickness 3	10.05	10.06	10.07	9.02
Average Gage Thickness, T	10.01	10.06	10.07	9.52
Notch Width 1 (Side 1)	1.55	1.52	1.54	1.53
Notch Width 2 (Side 1)	1.54	1.51	1.51	1.53
Notch Width 3 (Side 1)	1.55	1.53	1.51	1.52
Average Notch Width (Side 1), h	1.54	1.52	1.52	1.52
Notch Width 1 (Side 2)	1.52	1.65	1.61	1.64
Notch Width 2 (Side 2)	1.53	1.52	1.51	1.53
Notch Width 3 (Side 2)	1.54	1.51	1.51	1.53
Average Notch Width (Side 2), k	1.53	1.56	1.54	1.56
Notch Spacing 1	6.44	6.5	6.51	6.49
Notch Spacing 2	6.52	6.49	6.49	6.5
Notch Spacing 3	6.45	6.48	6.46	6.49
Average Notch Spacing, R	6.47	6.49	6.48	6.49

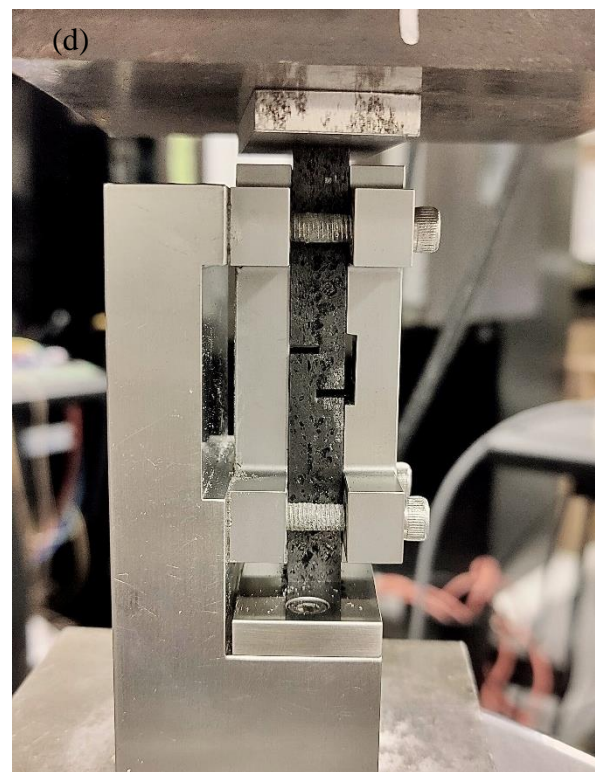
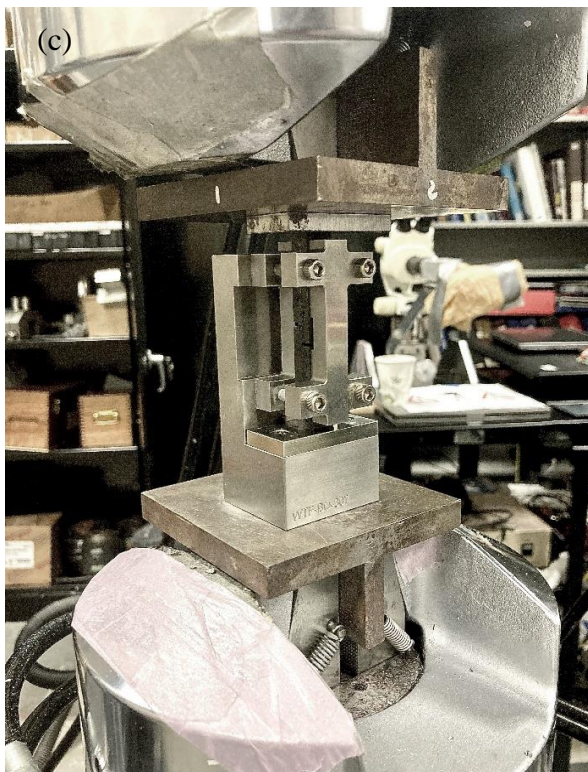
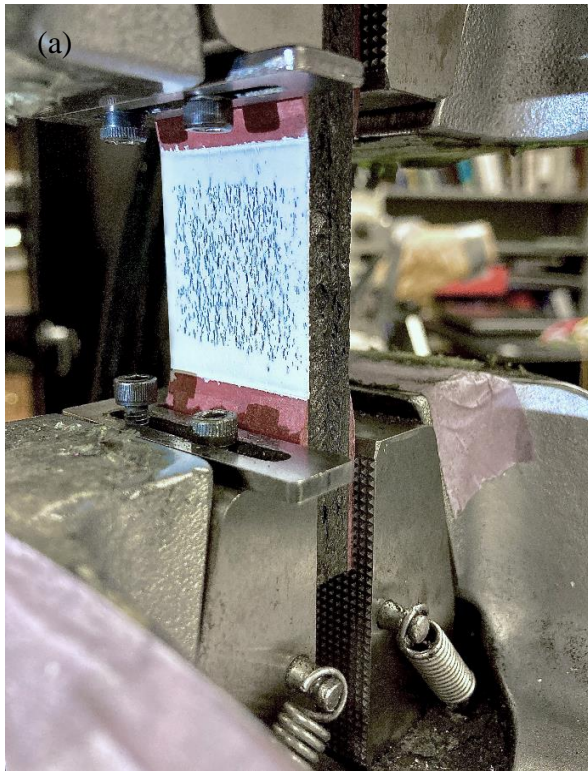


Figure 3.6 Tensile (a-b) and double-notched shear (c-d) test setups according to ASTM C1275 and ASTM C1292/D3846, respectively.

3.2.4 Multi-Scale Modeling of C/C Coupons Throughout PIP Processing

To better understand key parameters driving constitutive behavioral changes during densification, and ultimately determine the remaining elastic constants in the additively manufactured C/C composites, a 1st-order Mori-Tanaka (M-T) mean field homogenization model was used, because of its success in predicting effective properties for two-phase and multi-phase composites [125,126]. While the Voigt and Reuss models assume constant strain and stress in the inclusion and matrix phase of a composite, respectively, the M-T model extends Eshelby's analytical solution of the uniform strain developed in an ellipsoidal inclusion (i.e. fiber) to many inclusions (fibers) by multiplying the volume averaged matrix strain with a strain concentration tensor containing information about the inclusion shapes and orientations, matrix elasticity tensor, and inclusion elasticity tensor. The M-T model is limited to dilute suspensions with fiber volume fractions, $V_f = 25\%$, and so was deemed appropriate for modeling the porous C/C composites. The M-T model was available via the Digimat-MF software as part of a two-step homogenization scheme, shown below.

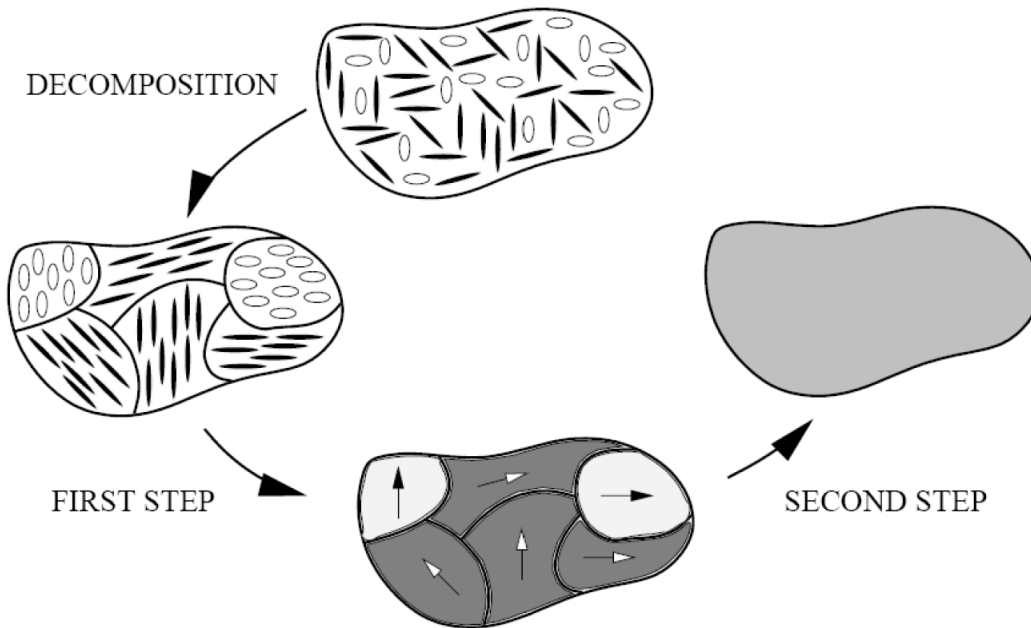


Figure 3.7 Two-step homogenization scheme in Digimat-MF illustrating (a) the real representative volume element (RVE) decomposed into two phase pseudo-grains with aligned and identical inclusions (b) the homogenization of each pseudo-grain via M-T model, and (c) the homogenization and computed effective response of the set of pseudo-grains via the Voigt model.

To run the Digimat-MF software, several input parameters were defined according to literature results while others were driven by results obtained in previous sections, including the X-ray micro-computed tomography scans in section 2.3 and the mass conservation analysis results in section 3.2.2, as illustrated in Figure 3.8.

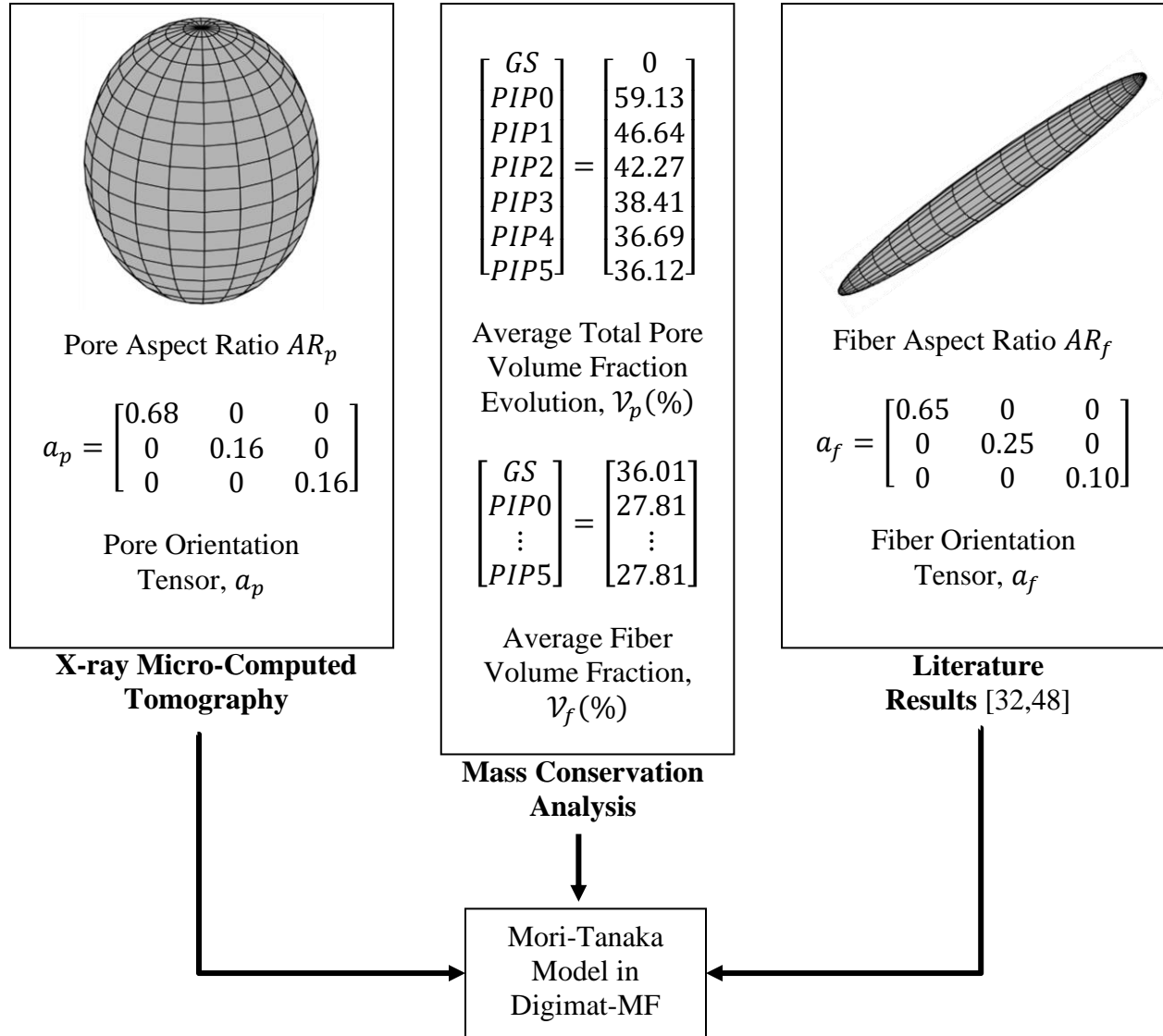


Figure 3.8 Flowchart of example input parameters fed into 1st order Mori-Tanaka model in Digimat-MF.

Note that for a given fiber aspect ratio AR_f , pore aspect ratio AR_p , fiber orientation tensor, a_f , pore orientation tensor, a_p , and fiber volume fraction, \mathcal{V}_f , pore volume fractions of 59.13%, 46.64%, 42.27%, 38.41%, 36.69%, and 36.12% were defined for PIP cycles 0-5 to model

densification, based on results in Table 3.3. For every pore volume fraction, a representative volume element (RVE) was generated, as in Figure 3.9. Because some of the input parameters were not known, their influence was explored via several test cases by varying them, as summarized with Table 3.6. Test case 1 served as an initial guess, where the fiber aspect ratio and orientation tensor were defined to be 28 and $a_{11} = 65.47\%$, $a_{22} = 24.55$, $a_{33} = 9.98\%$, respectively, since these values accurately predicted the effective properties in the green states and came close to results reported in literature [32,48]. For this test case, the porosity was assumed to be perfectly spherical and randomly oriented. Test case 2 updated the fiber orientation tensor values, since the walls of the 3D printed hollow square were passed through a planer, which removed bead edges along with many oriented fibers in the print direction (1-direction). Test cases 3 and 4 updated the pore orientation tensor and aspect ratio to more closely match the results seen in Chapter 2 via X-ray micro-computed tomography.

In addition to the input parameters above, the elastic constants for each phase in the green state and in the carbonized state were defined, as summarized in Table 3.7. Elastic constants for the carbon fibers were taken from Tanaka et. al [127] while the fiber orientation tensor and PPS elastic constants were determined using the machine learning approach developed by Thomas et.al [128], [49]. Since the degree of covalent bond alignment (graphitization) in C/C increases with heat treatment temperature, the elastic constants were defined for the C/C material based on highly textured pyrolytic carbon (PyC) heated to 1100°C [129], [130]. The PPS polymer was modeled as isotropic while the fibers and PyC matrix were modeled as transversely isotropic. The elastic constants for PyC in Table 3.7 were obtained after transforming the elasticity tensor populated by Gebert et. al [130], since they defined the $x_1 - x_2$ plane as the symmetry plane and because the $x_2 - x_3$ plane is the default symmetry plane in Digimat-MF. The reader is referred to Appendix Table C.2 for transformation details.

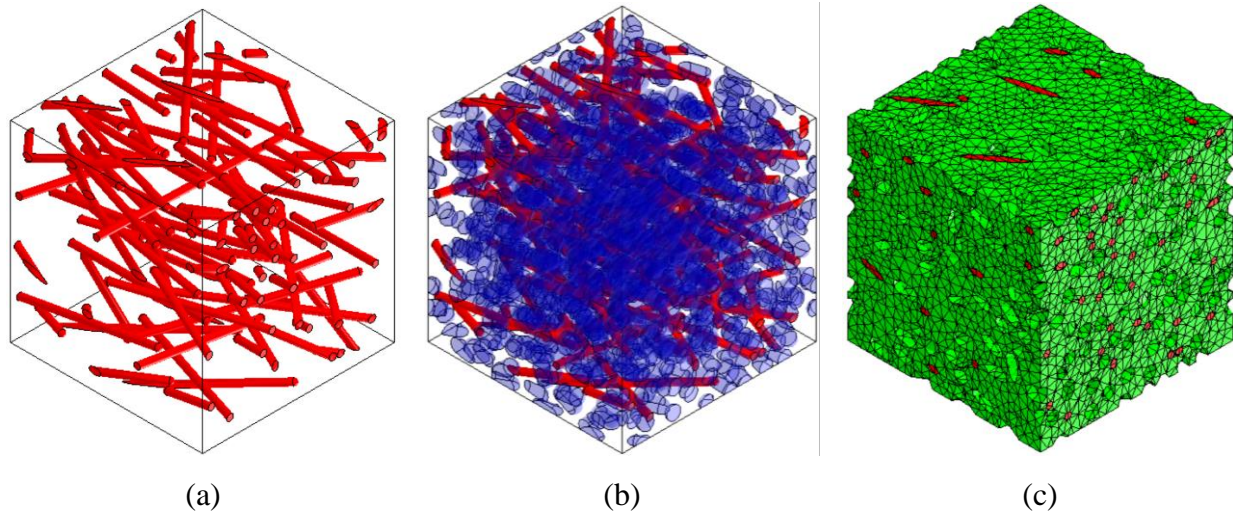


Figure 3.9 Graphical representation of the (a) fiber orientation tensor, (b) fiber orientation tensor + void orientation tensor, and (c) the porous carbon matrix microstructure. These representations were generated in Digimat-FE but the analysis was performed in Digimat-MF.

Table 3.6 Summary of test cases used to vary the Digimat-MF predictions.

Test Case	Digimat-MF Input Parameters								
	Fiber volume fraction $\mathcal{V}_f(\%)$	Fiber Aspect Ratio AR_f	Fiber Orientation Tensor $a_f = \begin{bmatrix} a_{11} & 0 & 0 \\ 0 & a_{22} & 0 \\ 0 & 0 & a_{33} \end{bmatrix}$			Pore Aspect Ratio AR_p	Pore Orientation Tensor $a_p = \begin{bmatrix} a_{11} & 0 & 0 \\ 0 & a_{22} & 0 \\ 0 & 0 & a_{33} \end{bmatrix}$		
			a_{11}	a_{22}	a_{33}		a_{11}	a_{22}	a_{33}
1	27.81	28	0.6547	0.2455	0.0998	1	0.33	0.33	0.33
2	27.81	28	0.6047	0.2955	0.0998	1	0.33	0.33	0.33
3	27.81	28	0.6047	0.2955	0.0998	1.5	0.68	0.16	0.16
4	27.81	28	0.6047	0.2955	0.0998	1.5	0.6	0.2	0.2

Table 3.7 Elastic constant inputs for Digimat-MF. The values shown for PyC were calculated with the Mathematica® 13 script in Appendix Table C.3.

Material	Phase	E_1 (MPa)	E_2 (MPa)	ν_{12}	ν_{23}	G_{23} (MPa)	ρ (kg/m ³)
50CF-PPS	Carbon Fiber [127]	220000	12000	0.25	0.2	28000	1800
	PPS Matrix [49,128]	1708	--	0.3412	--	--	1070
C/C	Carbon Fiber [127]	220000	12000	0.25	0.2	28000	1800
	PyC Matrix [130]	12800	27100	0.214	0.355	10000	2178

3.3 Results and Discussion

3.3.1 Evolution of Elastic Constants E_1 and G_{23} Through Densification

Figure 3.10 and Figure 3.11 show the time and frequency domain waveform data obtained by the MK7 GrindoSonic acquisition device for C/C composite coupon 1. The raw amplitude oscillation versus time data illustrated that the decay of the stress wave propagating through the C/C coupon was slower for each subsequent PIP cycle for both flexural and torsional excitations, owing to the decreasing porosity with densification. The stress wave took approximately 40 ms to decay for torsional excitation during PIP0, twice as long as it did for flexural excitation, since the higher harmonics generated during flexural excitation were more sensitive to attenuation. This can be seen in the Fast Fourier transform (FFT) graphs of Figure 3.11, where two peaks were observed for both vibrational modes but in which the second peak was higher than the first for flexural excitations in general. Like the trends seen in Figure 3.10, the FFT graphs illustrated that the first two harmonic frequencies shifted right with each PIP cycle, because of an increase in the coupon stiffness. The evolution of damping coefficients associated with each harmonic frequency in the FFT graphs are plotted in Figure 3.12, but did not show decreasing trends throughout PIP

processing because of the large scatter in damping data for the 10 impulse tests performed on every coupon. In addition to fiber-matrix interfaces, the shape, size, and orientation distribution of the pores may have been responsible for scatter in the data. In the interest of space, the results for coupons 2-5 are shown in Appendix Figure C.1 to Figure C.9. The amplitude oscillation decay results were very different, especially for PIP4 to PIP5, likely due to microstructural variations between coupons.

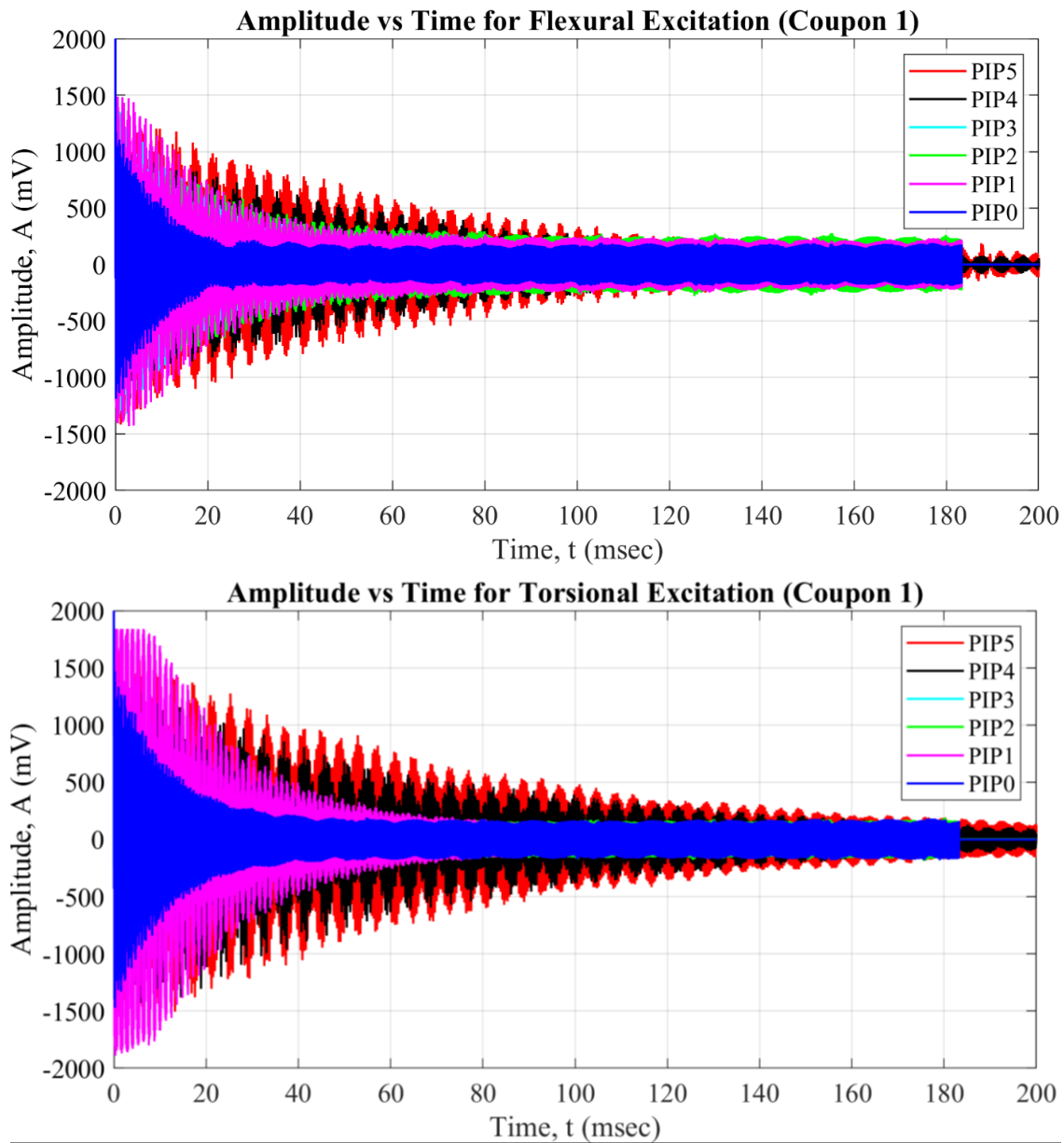


Figure 3.10 Raw amplitude oscillation decay for C/C composite coupon 1 throughout PIP processing.

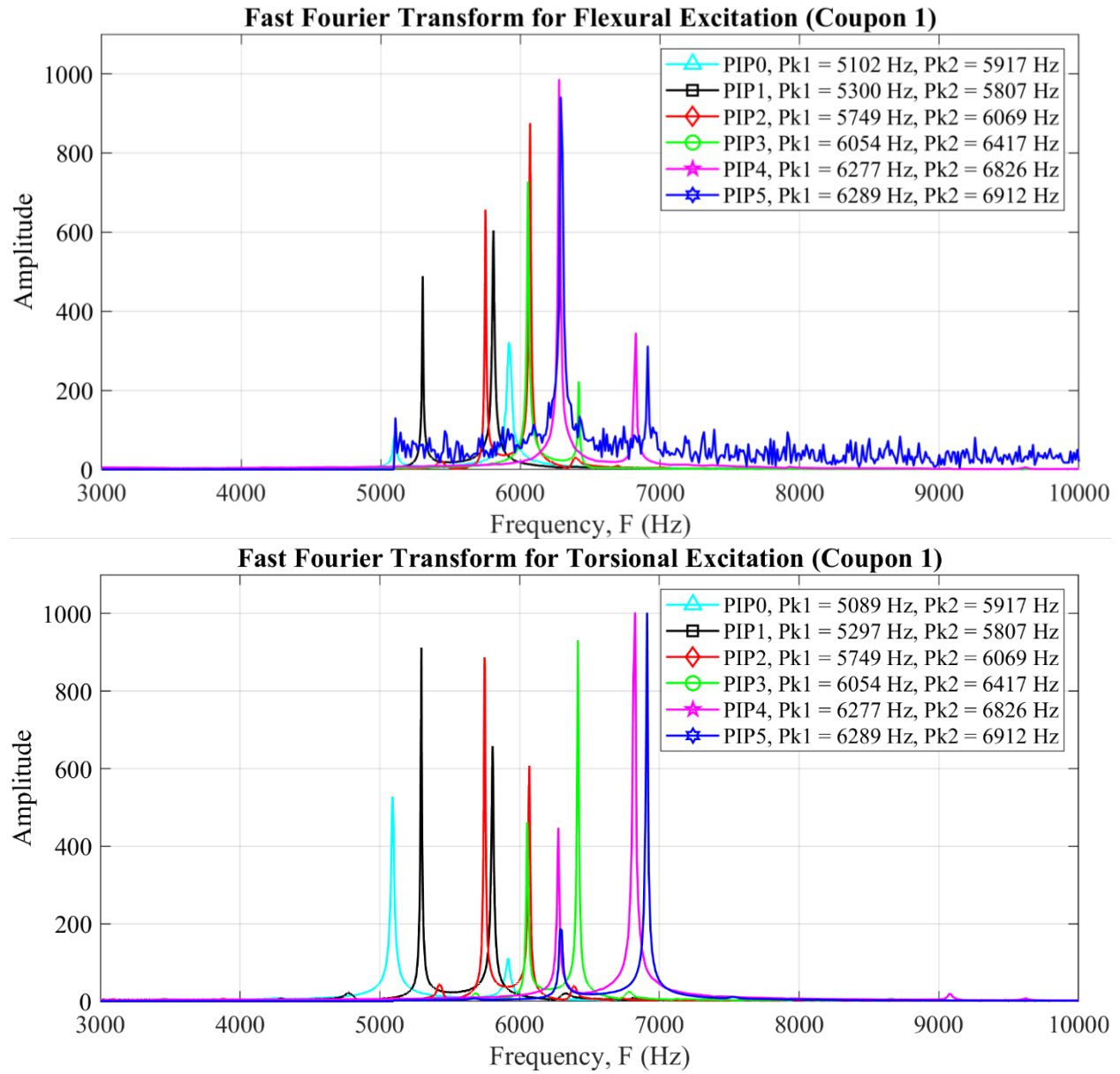


Figure 3.11 Evolution of fast Fourier transform for C/C composite coupon 1 throughout PIP processing.

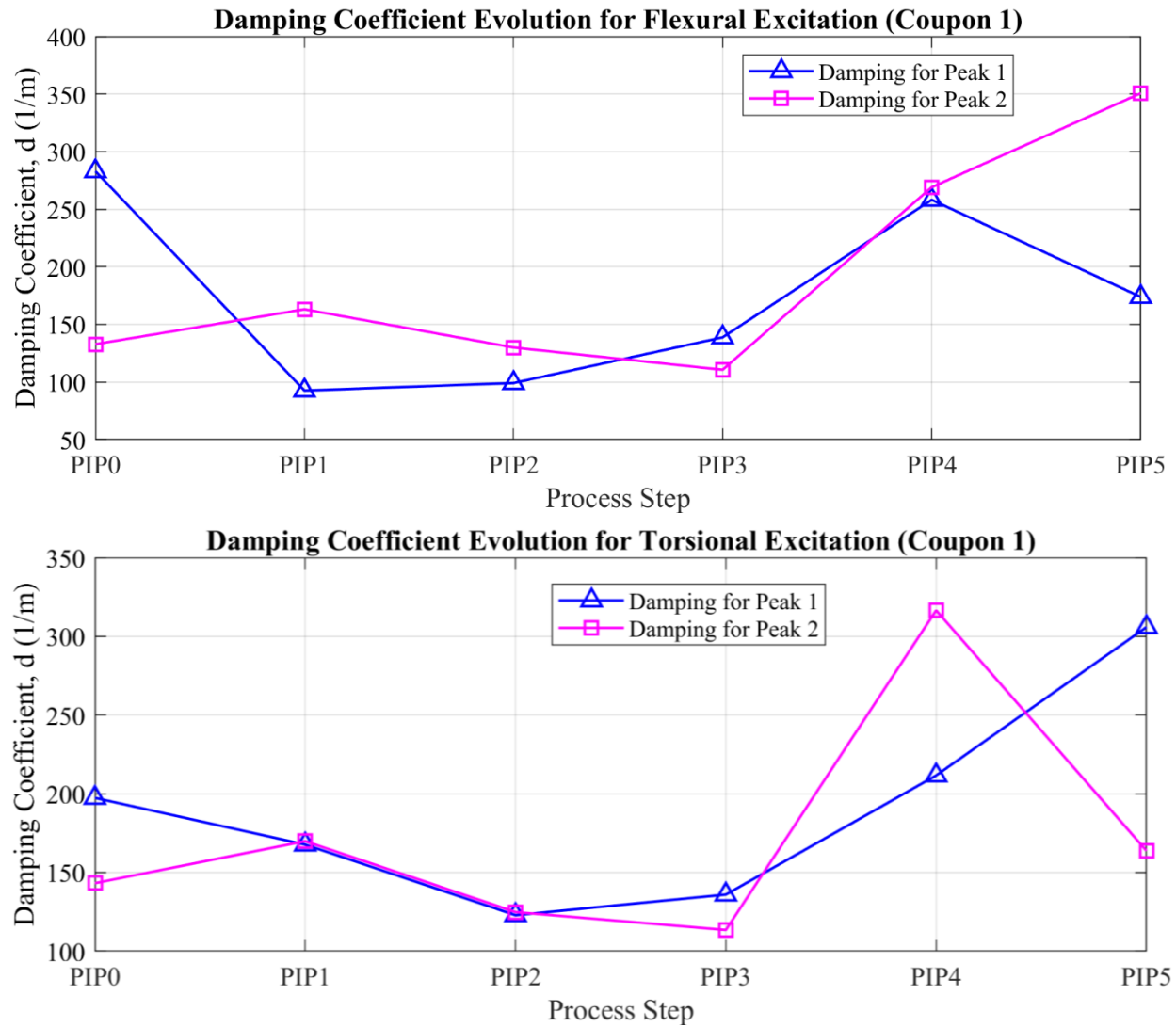


Figure 3.12 Evolution of damping coefficients for the first two harmonic frequencies shown in Figure 3.11.

Despite the scatter in amplitude decay and damping coefficient data, Figure 3.13 showed the evolution of elastic constants E_1 and G_{23} measured via impulse testing were consistent between coupons throughout PIP processing and followed the same trend as the density and pore volume fraction evolution data, increasing much more during the first 2 PIP cycles until eventually plateauing to a constant value at PIP cycle 5. The 3D printed 50CF-PPS (green state) E_1 value measured via impulse testing in the green state (GS) was 22.5 GPa, which came within ± 1 GPa with values reported by other researchers for 50CF-PPS (23.59 GPa & 21.56 GPa) [48,131], but the G_{23} value measured (3.04 GPa) was not as close (2.31 GPa) [48]. The discrepancy between

the values may be the result of planer processing, which may have changed the fiber orientation distribution by removing many fibers oriented in the print direction (1-direction).

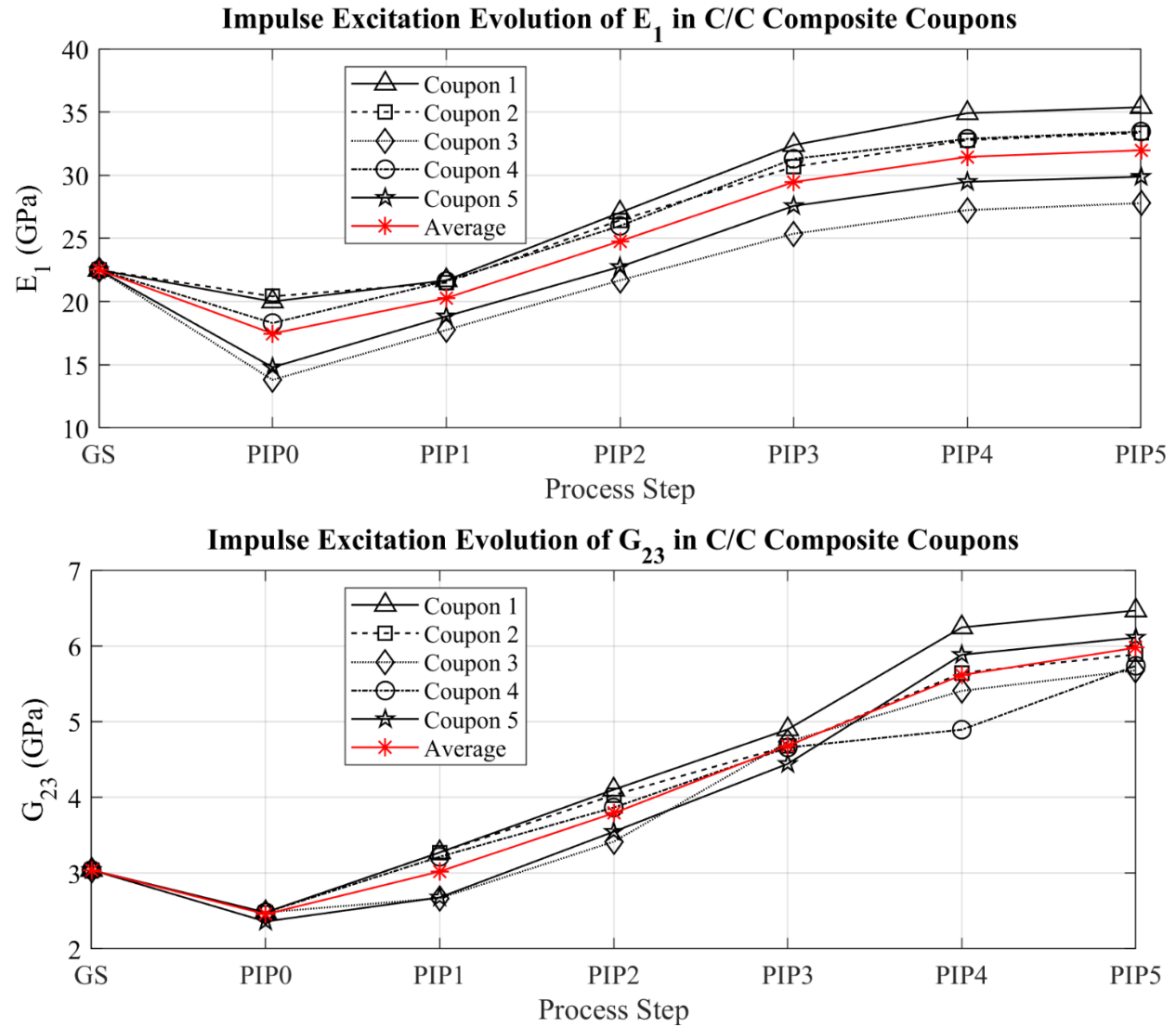


Figure 3.13 Impulse excitation evolution of E_1 and G_{23} after 5 PIP cycles for coupons 1-5. Note that GS in plots refers to the green state (3D printed).

Table 3.8 Elastic constant evolution data shown in Figure 3.13.

C/C Coupon	Process Step						
	GS	PIP0	PIP1	PIP2	PIP3	PIP4	PIP5
E_1 (GPa)							
1	22.5	20.00	21.68	27.04	32.39	34.91	35.39
2	22.5	20.41	21.49	26.44	30.67	32.78	33.36
3	22.5	13.80	17.75	21.68	25.37	27.24	27.79
4	22.5	18.30	21.62	25.99	31.30	32.88	33.46
5	22.5	14.80	18.83	22.75	27.57	29.48	29.88
Average	22.5	17.46	20.27	24.78	29.46	31.46	31.98
G_{23} (GPa)							
1	3.04	2.48	3.27	4.10	4.89	6.24	6.46
2	3.04	2.48	3.27	4.03	4.67	5.64	5.88
3	3.04	2.48	2.67	3.41	4.73	5.41	5.68
4	3.04	2.48	3.21	3.86	4.69	4.89	5.74
5	3.04	2.36	2.67	3.55	4.44	5.88	6.11
Average	3.04	2.46	3.02	3.79	4.68	5.61	5.97

3.3.2 Tensile and Double-Notched Shear Test Results

Processing the raw load vs displacement data from tensile and double-notched shear testing with a moving average, an ever-increasing filter, and x-/y- offset gave the fracture loads noted in Figure 3.14. The reader is referred to Appendix Figure C.11 and Table C.4 for the filters and MATLAB code used to process the raw data. The average ultimate strengths for the C/C coupons were 12.7 ± 1.26 MPa and 11.29 ± 3.56 MPa, respectively, as Figure 3.15 and Table 3.9 illustrate, and exhibited nonlinear behavior throughout the entire loading history. Pore-crack linking, or progressive crack growth between pores due to stress intensities in the inter-pore ligament regions, has been observed experimentally and numerically in cellular ceramics [132,133], and might explain the nonlinear behavior seen in the stress-strain curves. The tension-loaded and compression-loaded C/C coupons all failed as intended upon reaching the fracture

loads, within the gage section and in the 1-3 plane between notches, respectively, as Figure 3.16 illustrates.

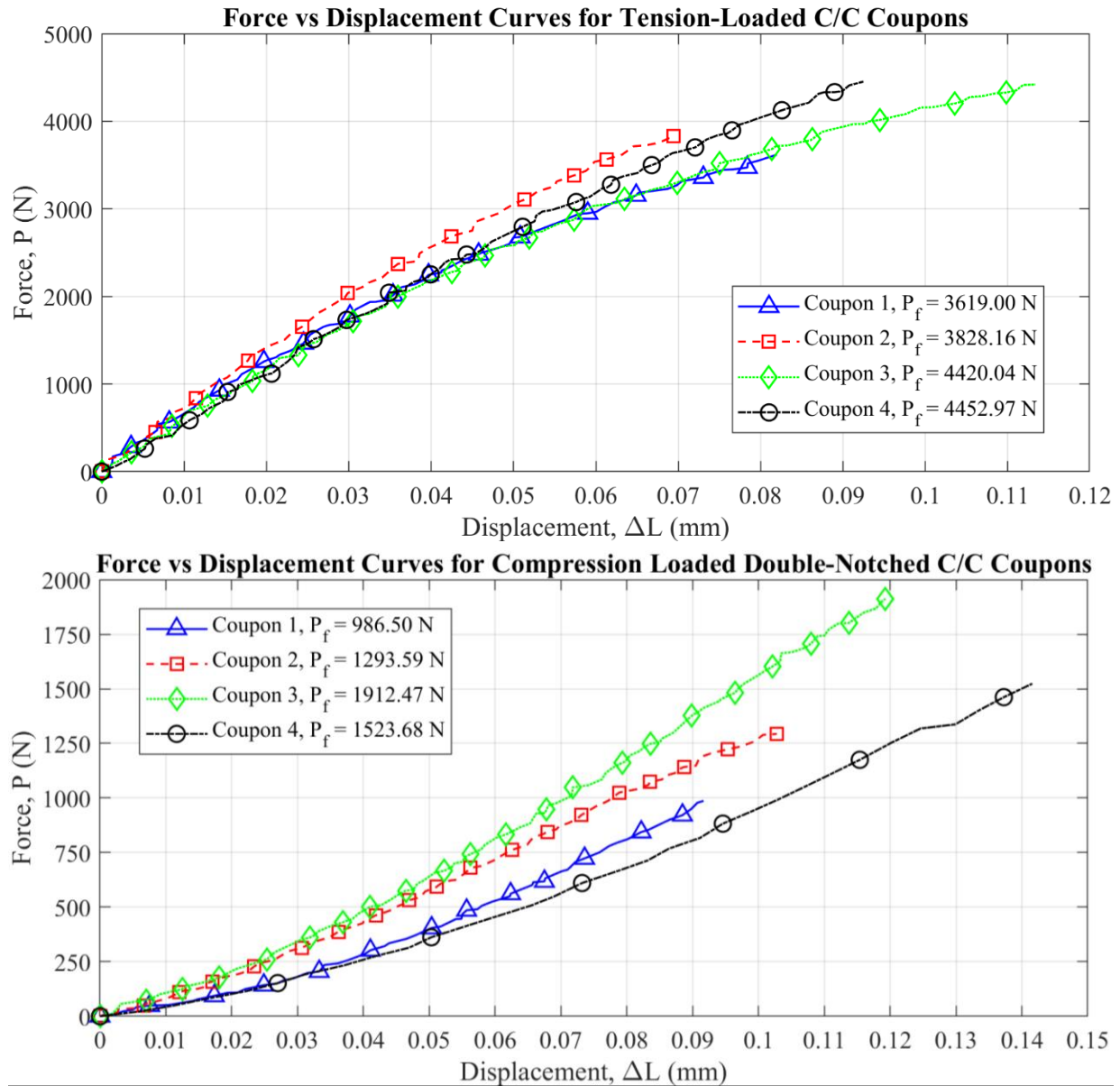


Figure 3.14 Force vs displacement curves showing the fracture load from the tension and double-notched shear tests.

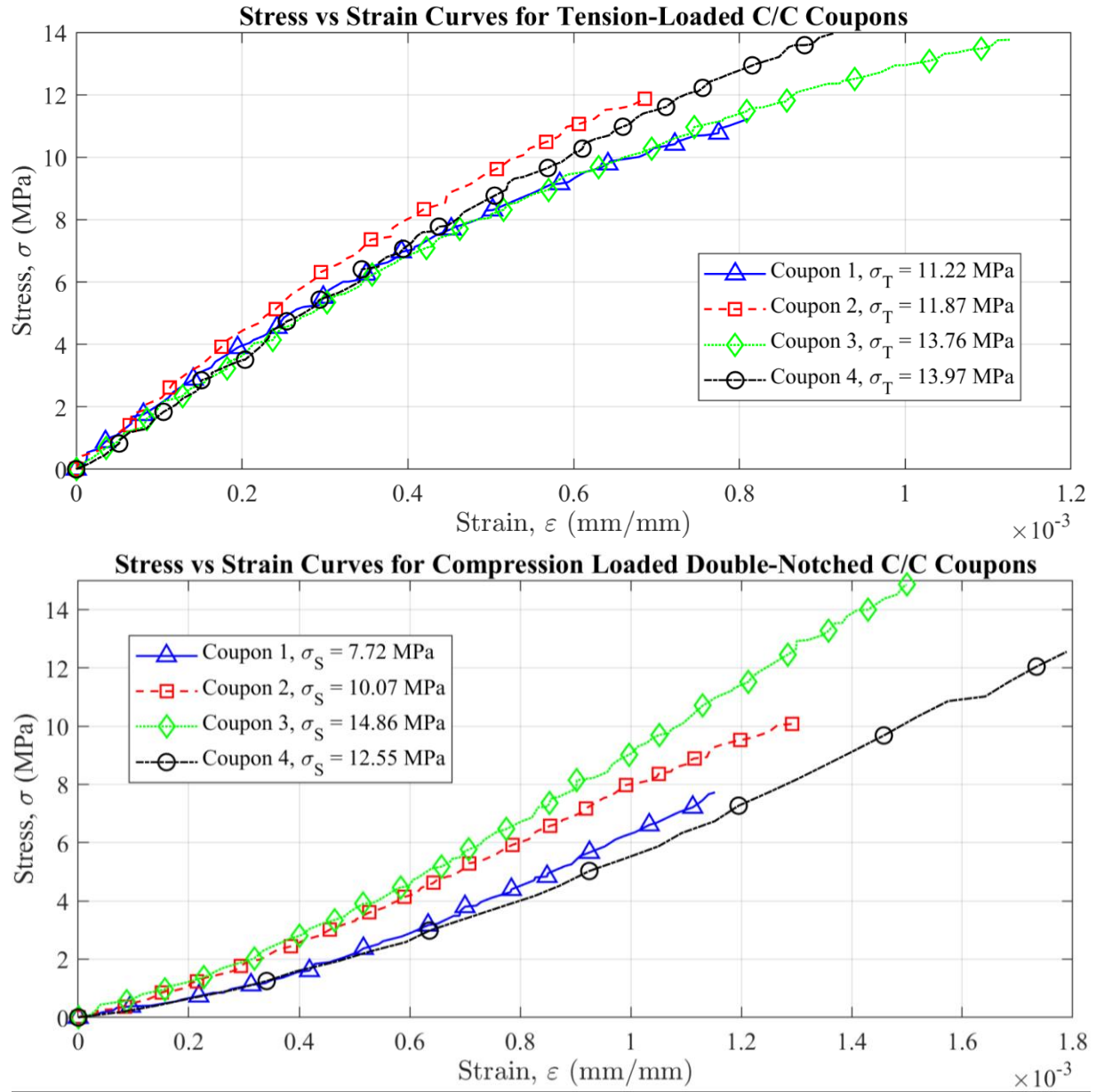
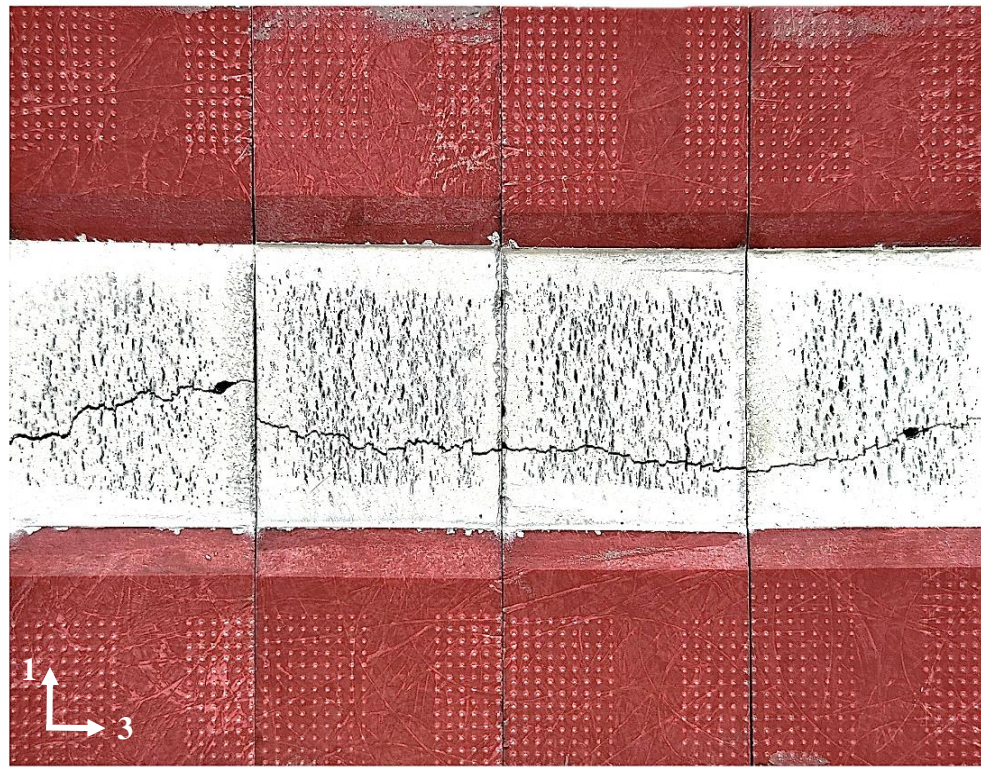


Figure 3.15 Stress vs strain curves showing the strengths measured by the tension and double-notched shear tests.

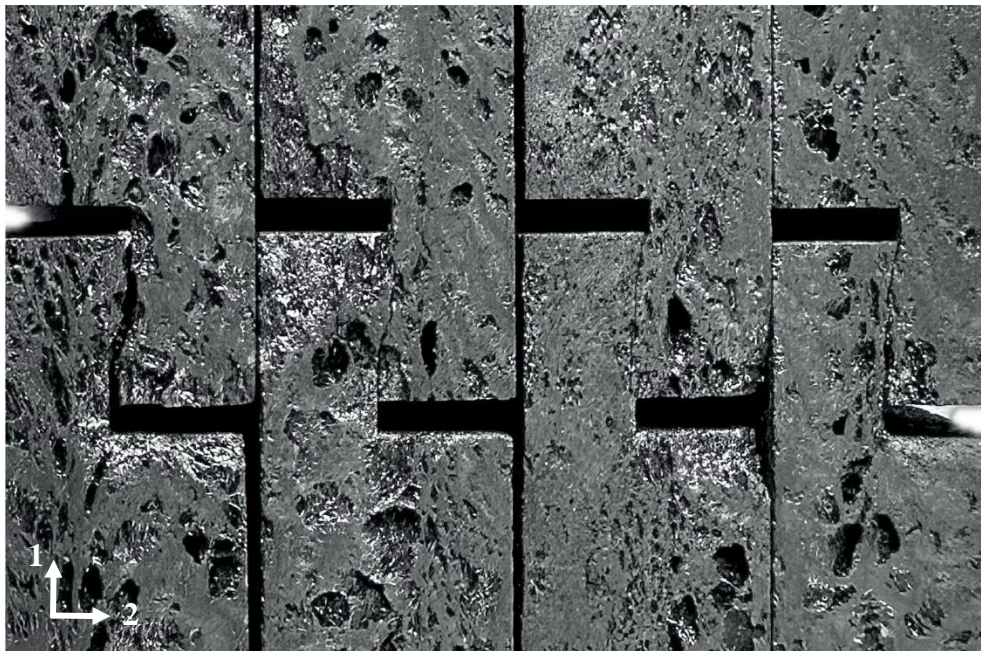
Table 3.9 Fracture loads and ultimate stress/strain data for the tensile and double-notched shear tests.

Property	C/C Coupon				
	1	2	3	4	Average
Tension					
Fracture Load, P_f (N)	3619.00	3828.16	4420.04	4452.97	4080.04
Ultimate Tensile Strain, ε_u	0.8×10^{-3}	0.7×10^{-3}	1.1×10^{-3}	0.9×10^{-3}	0.88×10^{-3}
Tensile Strength, σ_T (MPa)	11.22	11.87	13.76	13.97	12.71
Double-Notched Shear					
Fracture Load, P_f (N)	986.50	1293.59	1912.47	1523.68	2858.12
Ultimate Shear Strain, ε_u	1.2×10^{-3}	1.3×10^{-3}	1.5×10^{-3}	1.8×10^{-3}	1.4×10^{-3}
Shear Strength, σ_s (MPa)	7.72	10.07	14.85	12.55	11.29



(a)

32.0 mm

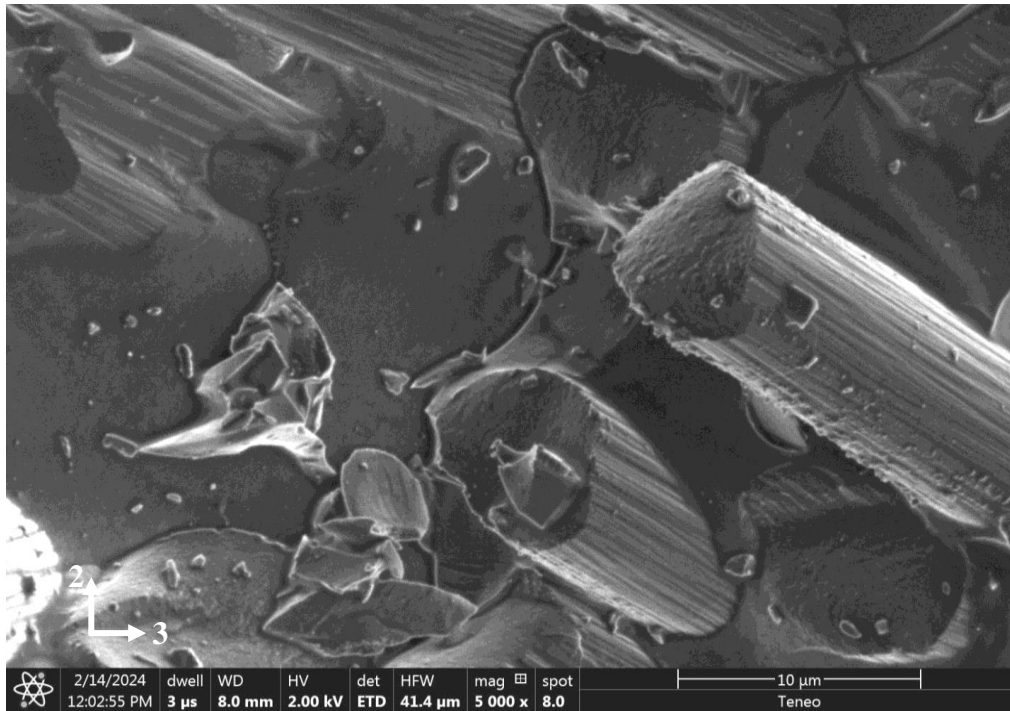


(b)

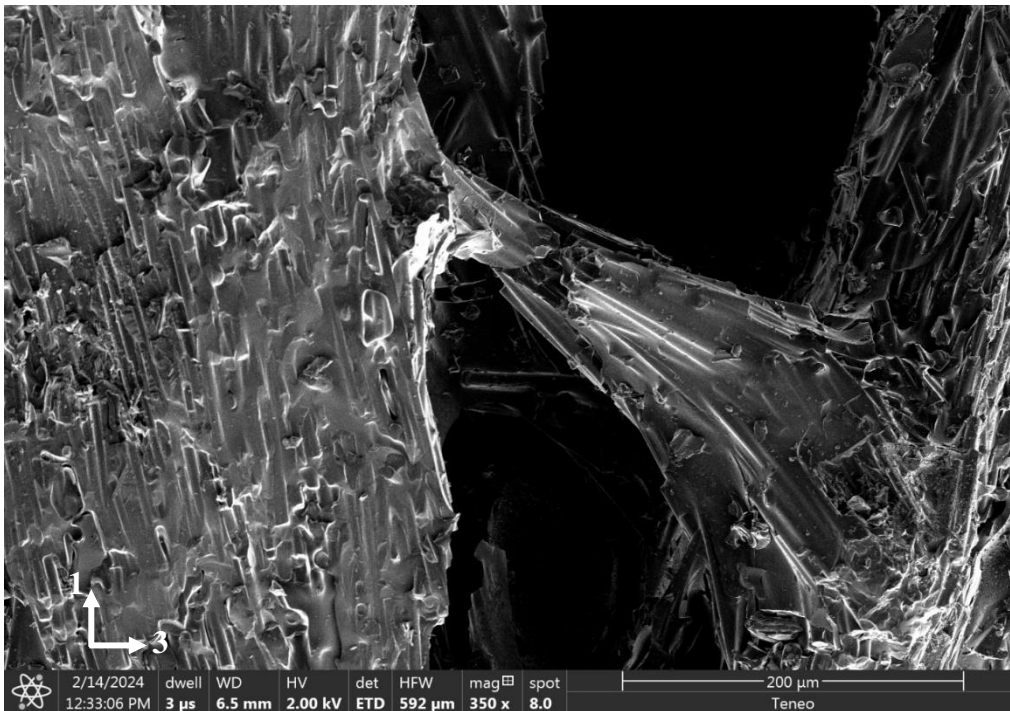
10.0 mm

Figure 3.16 Cracks generated in the C/C coupons during (a) tension and (b) double-notched shear tests.

Scanning electron micrographs of the fractured surfaces in Figure 3.16 illustrated that fiber pullout/splitting and interpore ligament/cohesive matrix fracture occurred during tension and double-notched shear tests. Note that the surfaces shown in Figure 3.17 are the 2-3 plane and 1-3 planes in the local/material coordinate system. The crack passing behind the two fibers in Figure 3.17a may have been a microcrack resulting from the branching of an initial crack as it passed through pores in the microstructure, a phenomenon noted by Bussiba et. al [100] in isobaric chemical vapor infiltrated carbon fiber felts with 15% and 30% porosity via acoustic emission data. The fiber pullout seen in the SEM image is indicative of weak fiber-matrix bonding [134], as other researchers have noted for carbon with turbostratic structures heat treated $<1200^{\circ}\text{C}$ [135,136], but which could be improved for polyphenylene sulfide-derived bulk carbon by heat treating to higher temperatures because of its graphitic nature [137,138]. The carbon fiber cross-sections in the fractured surfaces did not have an onion-ring texture [139], ruling out the possibility that the fibers used in the feedstock material were pitch-based. Most of the fibers during double-notched shear tests (Figure 3.17b) remained embedded in the pyrolytic carbon matrix, suggesting cohesive matrix failure was responsible for the unloading history seen in the force-displacement curves while the interpore ligament fractures likely contributed to the plastic consolidation and nonlinearity during loading.



(a)



(b)

Figure 3.17 Scanning electron micrographs showing (a) fiber pull-out/splitting, and (b) inter-pore ligament splitting as possible failure modes during tension and double-notched shear tests.

3.3.3 Digimat-MF Predictions of Elastic Constant Evolutions

The Digimat-MF predictions of the elastic constant E_1 and G_{23} evolutions for the different test cases were plotted in Figure 3.18 along with the impulse excitation averages in Table 3.8. Test case 1 came very close to predicting E_1 at PIP5 but did not agree with experimental results in the green state (GS) and up to PIP3, with a total error of 25 between the predicted and experimental curves, as noted in Table 3.10. Compared to test case 1, the decrease in anisotropy of the fiber phase for test case 2 reduced the error with the impulse excitation results for both E_1 and G_{23} . Increasing the pore aspect ratio as well as the anisotropy of the porosity as in test case 3 and 4, however, increased the total error with impulse test results to 69.32 and 52.1, respectively, suggesting aligned and ellipsoidal voids were less accurate in capturing the elastic constant evolutions than a random orientation of spherical voids. This was unexpected since the aspect ratios and preferred orientation of the pores in test cases 3 and 4 were an attempt to model the microstructural results in section 2.3.2. One reason for the discrepancies between predicted and experimental results was that a fixed aspect ratio was defined for the pores instead of an aspect ratio distribution, excluding the effect of various pore shapes on the effective properties in the homogenized RVE. A closer look showed that the higher fixed aspect ratio used in test case 3 & 4 decreased the number of pores generated in the model RVE and the total pore volume fraction from the inputted value. This was also noted by Chao et. al [102] during modeling of felt C/C composites. The model RVE was also simpler than the real RVE in that only closed pores were modeled, and not irregularly shaped open pores. The predictions had the most error with experimental values from PIP1 to PIP2 but came closer to the experimental values as the percent closed porosity increased and the model RVE started to approach the real RVE. Despite the pseudo-realistic model RVE generated, the predictions during test case 2 captured the overall shape of the experimental curve suitably, coming within 2 *GPa* at PIP5. The predictions for the remaining elastic constants were also plotted, seen in Figure 3.19 and Figure 3.20. The reader is referred to Appendix Table C.6 to Table C.9 for the values obtained for each test case.

Table 3.10 Total error between the predicted and experimental curve for each test case in Figure 3.18.

Test Case	#1	#2	#3	#4
Error				
E_1 Plot	21.01	10.84	61.05	39.21
G_{23} Plot	3.99	3.89	8.27	12.89
Total	25	14.73	69.32	52.1

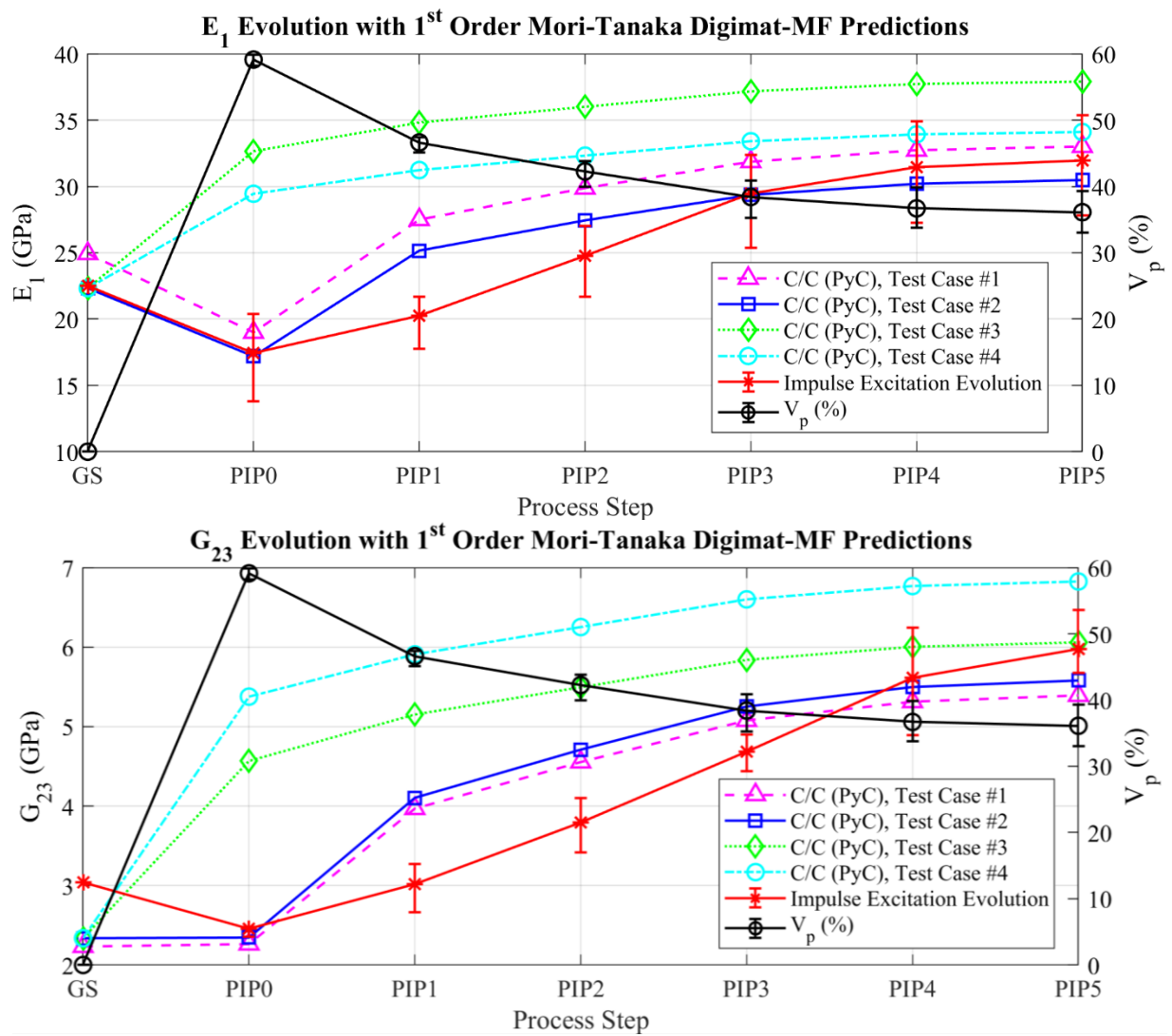


Figure 3.18 Digimat-MF predictions for the evolution of E_1 and G_{23} through densification for test cases 1-4 as described in Table 3.6.

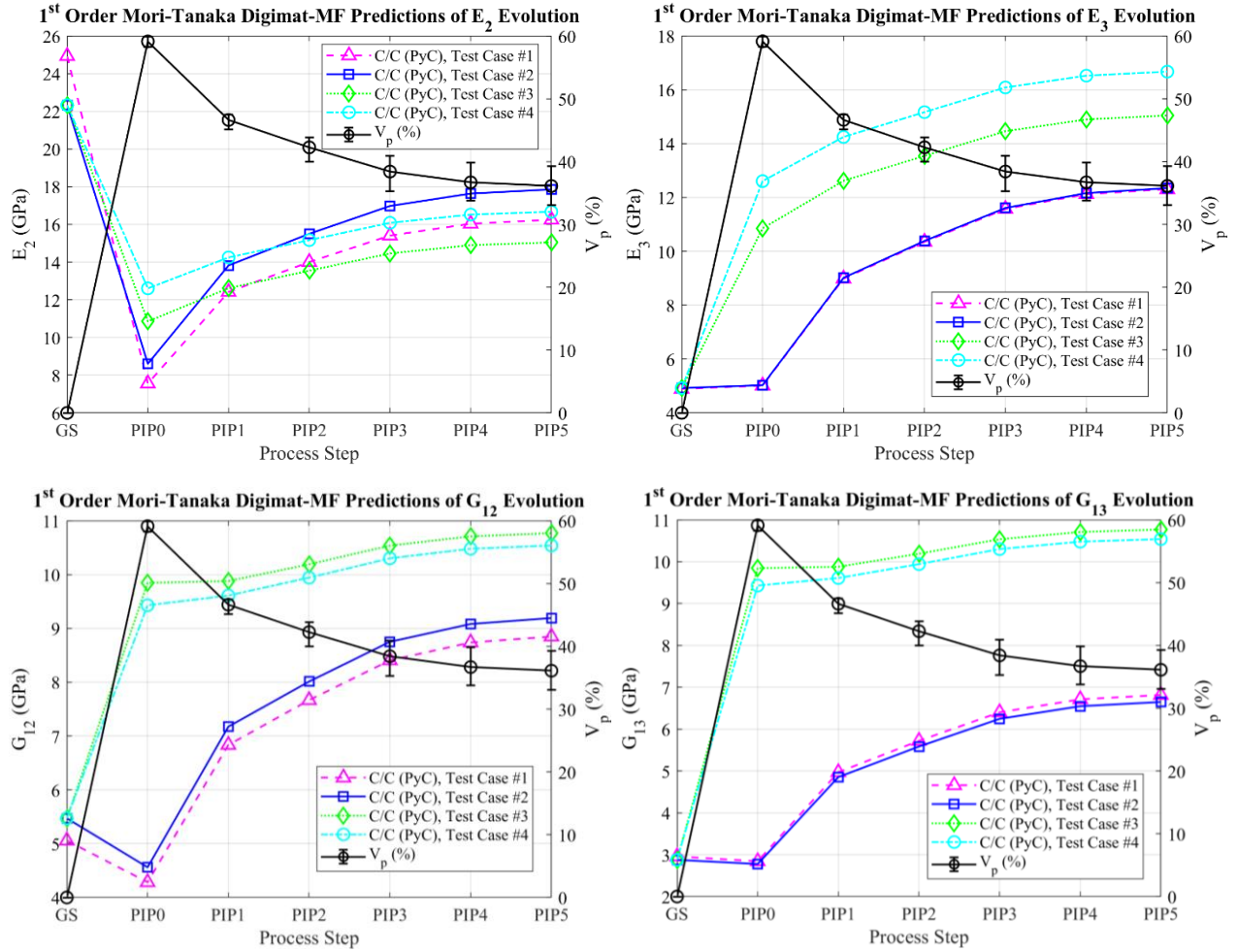


Figure 3.19 Evolution predictions of E_2 , E_3 , G_{12} , and G_{13} by Digimat-MF for test cases 1-4 in Table 3.6.

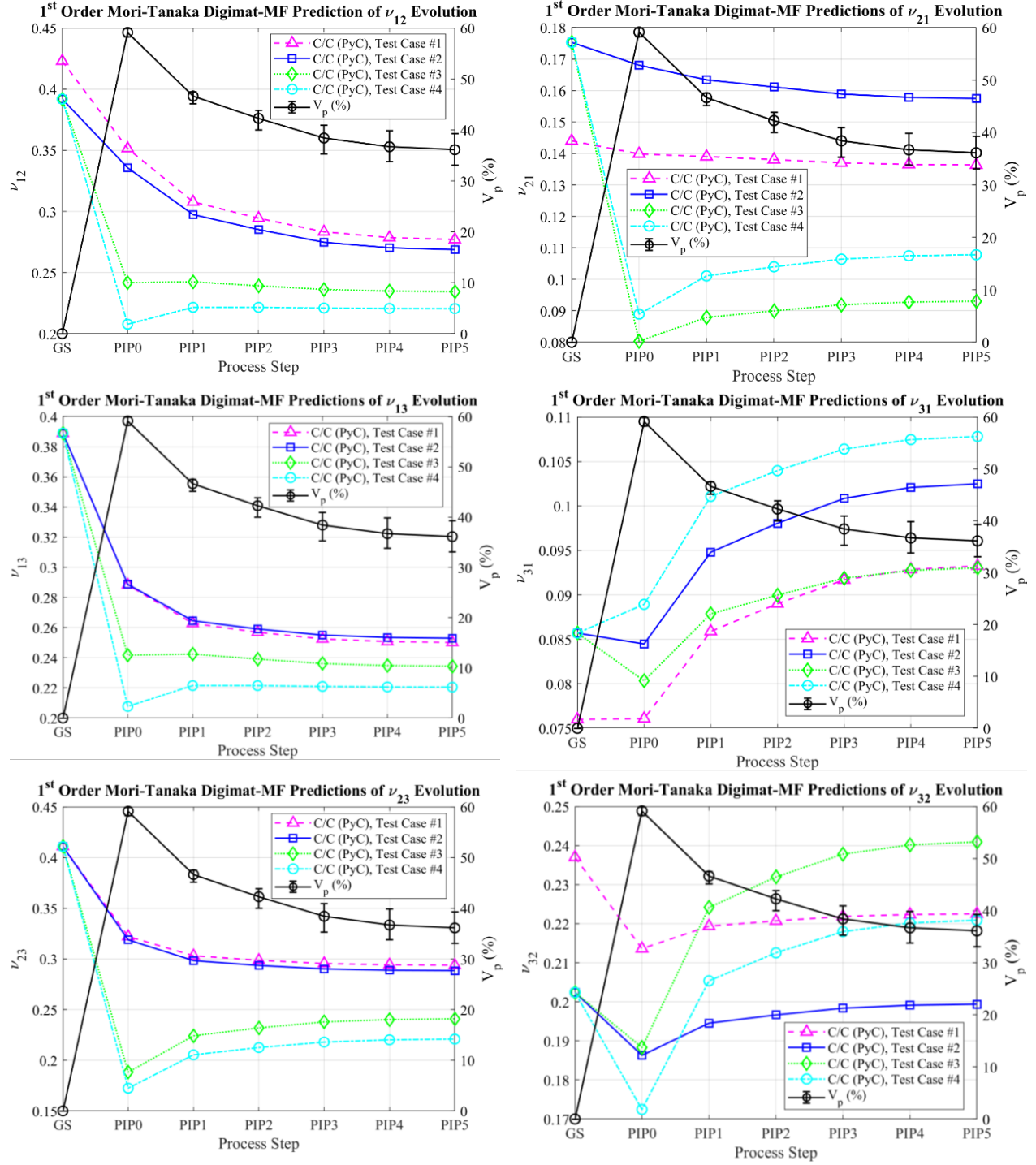


Figure 3.20 Evolution predictions of the Poisson's ratios by Digimat-MF for test cases 1-4 in Table 3.6.

3.3.4 Comparison of Mechanical Properties to Literature Results

The elastic constants for test case 2 and strengths measured via tension and double-notched shear tests for the 3D printed C/C coupons were summarized in Table 3.11 (Fiber architecture A) alongside values reported for traditionally manufactured C/C composites in Table 3.11 to Table 3.14 (Fiber Architecture B-O). In these tables, the 3-direction was defined as the stacking direction, T_{max} refers to the maximum processing temperature during densification/graphitization of the composite (not the fibers themselves), \mathcal{W}_f is the fiber weight fraction, \mathcal{V}_f is the fiber volume fraction, \mathcal{V}_p is the pore volume fraction, σ_T is the tensile strength, σ_C is the compressive strength, σ^{IPSS} refers to Iosipescu shear strengths, σ^{DNS} refers to double-notched shear strengths, σ_f refers to flexural strengths, E_f refers to the flexural modulus, and where the values entered in the cells were for room temperature quasi-static loading, although some articles reported values at elevated temperatures. The results were limited to polyacrylonitrile (PAN)-based fibers since these fibers were used in the EDAM C/C coupons, but few articles reported C/C composite properties with high modulus (pitch-based) fibers. The method was included in the tables to differentiate between data that was obtained experimentally (“Ex”) from data that was obtained numerically (“Nu”). A comparison with the table values showed the double-notched shear strength of EDAM C/C composites was approximately the same as the double-notched shear strength for felt- and woven-based C/C composites. However, the pore volume fraction was not reported by the authors for the corresponding references. The tensile strength was an order of magnitude smaller than woven C/C, owing to the short fibers and porosity in the 3D printed C/C material. The tables showed that a comparison of strengths and elastic constants is difficult to make, since the maximum heat treatment temperatures, densities, and porosities were different even for C/C composites with the same fiber architectures. In general, the mechanical properties increased from 2D felt, to 2D woven, and to 3D orthogonal fiber architectures.

A	= 3D Orthotropic Short Fibers
B	= 2D Felt
C	= 2D Needle-punched Felt
D	= 2D 0° Continuous Fibers Needled to Cross-Laid Felt Core
E	= 2D 0°/90° Non-woven Continuous Fibers with Felt Core
F	= 2D 0°/90° Non-woven Continuous Fibers Needled to Cross-Laid Felt Core
G	= 2D 0° Continuous Fibers
H	= 2D 0°/90° Non-woven Continuous Fibers
I	= 2D 0°/90° Woven Continuous Fibers
J	= 2.5D Needle-punched 0°/90° Woven Continuous Fibers
K	= 3D Isotropic Short Fibers
L	= 3D Fabric
M	= 3D Orthogonal Continuous Fibers
N	= 3D Orthotropic Continuous Fibers
O	= 4D In-plane Continuous Fibers

Figure 3.21 Fiber architectures reported in literature by the references listed in Table 3.11 to Table 3.14

Table 3.11 Mechanical properties of C/C composites reported in literature by references [99] to [103].

Method	Ex	Ex	Ex	Ex	Ex	Ex	Ex/Nu	Ex	Ex
Fiber Precursor	PAN	PAN	PAN	PAN	PAN	PAN	PAN	PAN	PAN
Fiber Architecture	A	B	B	B	B	B	B	C	D
Reference	--	[99]	[100]	[100]	[101]	[101]	[102]	[101]	[103]
$T_{max}(^{\circ}C)$	1000	1100	1095	1095	2100	2300	1050	2300	--
$\rho (g/cm^3)$	1.09	1.72			1.64	1.64	--	1.61	1.89
$\mathcal{W}_f(wt. \%)$	67.67	--	--	--	--	--	--	--	--
$\mathcal{V}_f(vol. \%)$	25.96	--			--	--	14.5	--	20
$\mathcal{V}_p(vol. \%)$	36.12	15	15	30	--	--	12.1	--	--
$\sigma_T(MPa)$	12.71	--	--	--	--	--	--	--	--
$\sigma_c(MPa)$	--	--	--	--	--	--	--	--	--
$\sigma_s^{IPSS} (MPa)$	--	--	--	--	--	--	--	--	41
$\sigma_s^{DNS} (MPa)$	11.29	--	--	--	6.5	6.8	--	11.1	--
$\sigma_f(MPa)$	--	47.75	63.25	38.75	60.3	44.1	--	147.3	--
$E_f(GPa)$	--	--	16.65	12.45	12.9	8.5	--	15.9	--
$E_1(GPa)$	30.48	--	--	--	--	--	34.8	--	--
$E_2(GPa)$	17.86	--	--	--	--	--	--	--	--
$E_3(GPa)$	12.34	--	--	--	--	--	--	--	--
ν_{12}	0.269	--	--	--	--	--	--	--	--
ν_{21}	0.157	--	--	--	--	--	--	--	--
ν_{13}	0.253	--	--	--	--	--	--	--	--
ν_{31}	0.102	--	--	--	--	--	--	--	--
ν_{23}	0.288	--	--	--	--	--	--	--	--
ν_{32}	0.199	--	--	--	--	--	--	--	--
$G_{12}(GPa)$	9.19	--	--	--	--	--	--	--	6.2
$G_{23}(GPa)$	5.58	--	--	--	--	--	--	--	1.1
$G_{13}(GPa)$	6.64	--	--	--	--	--	--	--	2.1

Table 3.12 Mechanical properties of C/C composites reported in literature by references [103] to [108].

Method	Ex	Ex	Ex	Ex/Nu	Ex	Ex	Ex	Ex	Ex	Ex/Nu
Fiber Precursor	PAN	PAN	PAN	PAN	PAN	PAN	PAN	PAN	PAN	PAN
Fiber Architecture	E	E	F	F	G	G	G	G	G	G
Reference	[104]	[105]	[103]	[106]	[107]	[107]	[107]	[108]	[108]	[102]
$T_{max}(^{\circ}C)$	1600	25	--	2300	1400	1400	1400	--	--	1050
$\rho (g/cm^3)$	1.5	1.5	1.81	1.75	1.38	1.41	1.41	--	--	--
$\mathcal{W}_f(wt. \%)$	--	--	--	--	--	--	--	--	--	--
$\mathcal{V}_f(vol. \%)$	25	25	20	35	--	--	--	46	58	40
$\mathcal{V}_p(vol. \%)$	17	17	--	8	25.20	14.48	5.88	--	--	13.2
$\sigma_T(MPa)$	--	--	--	--	--	--	--	337	383	--
$\sigma_c(MPa)$	--	--	--	--	--	--	--	--	--	--
$\sigma_s^{IPSS}(MPa)$	--	--	34	--	--	--	--	33	28	--
$\sigma_s^{DNS}(MPa)$	53.1	45	--	--	--	--	--	115	10.5	--
$\sigma_f(MPa)$	--	--	--	--	201	287	459	--	--	--
$E_f(GPa)$	--	--	--	--	68	109	126	--	--	--
$E_1(GPa)$	--	--	--	--	--	--	--	155	200	--
$E_2(GPa)$	--	--	--	--	--	--	--	--	--	13.5
$E_3(GPa)$	--	--	--	--	--	--	--	--	--	13.5
ν_{12}	--	--	--	--	--	--	--	--	--	--
ν_{21}	--	--	--	--	--	--	--	--	--	--
ν_{13}	--	--	--	--	--	--	--	--	--	--
ν_{31}	--	--	--	--	--	--	--	--	--	--
ν_{23}	--	--	--	--	--	--	--	--	--	--
ν_{32}	--	--	--	--	--	--	--	--	--	--
$G_{12}(GPa)$	--	--	6.4	--	--	--	--	5.5	6.5	--
$G_{23}(GPa)$	--	--	--	--	--	--	--	--	--	--
$G_{13}(GPa)$	--	--	1.4	10.52	--	--	--	--	--	--

Table 3.13 Mechanical properties of C/C composites reported in literature by references [108] to [112].

Method	Nu	Ex	Ex	Nu	Ex	Ex	Ex	Ex	Ex	Ex
Fiber Precursor	PAN	PAN	PAN	PAN	PAN	PAN	PAN	PAN	PAN	PAN
Fiber Architecture	G	H	H	H	H	I	I	I	I	I
Reference	[109]	[108]	[110]	[111]	[111]	[112]	[112]	[112]	[108]	[110]
$T_{max}(^{\circ}C)$	--	--	2000	1100	1100	800	800	1700	--	1500
$\rho (g/cm^3)$	--	--	1.7	--	--	1.65	1.68	1.67	--	1.5
$\mathcal{W}_f(wt. \%)$	--	--	--	--	--	--	--	--	--	--
$\mathcal{V}_f(vol. \%)$	72	56	40	40	40	57.5	57.5	57.5	56	50
$\mathcal{V}_p(vol. \%)$	--	--	--	0	12	--	--	--	--	--
$\sigma_T(MPa)$	--	230	129.2	422.36	--	--	--	--	242	161.1
$\sigma_c(MPa)$	-	--	--	8.26	--	143	145	144.5	--	--
$\sigma_s^{IPSS} (MPa)$	--	35.0	43.9	17.9	--	16	17	15	27	31.4
$\sigma_s^{DNS} (MPa)$	--	10.7	--	--	--	5.5	6	5.7	12.4	--
$\sigma_f(MPa)$	--	--	--	238	124	--	--	--	--	--
$E_f(GPa)$	--	--	--	--	--	--	--	--	--	--
$E_1(GPa)$	110.78	90	57.2	119.2	--	--	--	--	104	66.9
$E_2(GPa)$	10.38	90	57.2	24.86	--	--	--	--	104	66.9
$E_3(GPa)$	10.37	--	--	24.86	--	--	--	--	--	--
ν_{12}	0.2	0.21	0.028	0.226	--	--	--	--	0.38	0.073
ν_{21}	0.2	0.21	0.028	--	--	--	--	--	--	--
ν_{13}	0.2	0.21	0.028	0.226	--	--	--	--	--	--
ν_{31}	0.2	0.21	0.028	--	--	--	--	--	--	--
ν_{23}	0.28	--	--	0.403	--	--	--	--	--	--
ν_{32}	0.28	--	--	--	--	--	--	--	--	--
$G_{12}(GPa)$	7.18	6.0	5.4	7.522	--	--	--	--	5.0	5.4
$G_{23}(GPa)$	4.18	--	--	7.264	--	--	--	--	--	--
$G_{13}(GPa)$	6.84	--	--	7.522	--	--	--	--	--	--

Table 3.14 Mechanical properties of C/C composites reported in literature by references [22], [108] to [112], and [140].

Method	Ex	Ex	Ex	Ex	Ex	Ex	Nu	Ex/Nu	Ex	Ex
Fiber Precursor	PAN	PAN	PAN	PAN	PAN	PAN	PAN	PAN	PAN	PAN
Fiber Architecture	J	J	K	L	M	M	M	N	N	O
Reference	[114]	[115]	[22]	[116]	[117]	[117]	[118]	[119]	[140]	[118]
$T_{max}(^{\circ}C)$	--	2000	1100	2527	2550	2550	--	--	2300	--
$\rho (g/cm^3)$	--	1.705	1.4	1.9	1.912	1.912	--	--	1.95	--
$\mathcal{W}_f(wt. \%)$	--	--	60	--	--	--	--	--	--	--
$\mathcal{V}_f(vol. \%)$	25	--	--	48	30	30	43	--	56	43
$\mathcal{V}_p(vol. \%)$	--	--	--	--	--	--	8	--	--	8
$\sigma_T(MPa)$	126	--	--	225	104	--	--	--	750	--
$\sigma_c(MPa)$	--	230.44	--	--	--	78	--	--	--	--
$\sigma_s^{IPSS} (MPa)$	45	--	--	17.1	--	--	--	--	--	--
$\sigma_s^{DNS} (MPa)$	--	--	--	--	--	--	--	--	--	--
$\sigma_f(MPa)$	--	--	100	--	110	110	--	--	--	--
$E_f(GPa)$	--	--	--	--	55	55	--	--	--	--
$E_1(GPa)$	33	4.78	--	41.5	47	29	37.14	11.7	--	26.26
$E_2(GPa)$	22	--	--	40.0	47	29	37.14	11.7	--	26.26
$E_3(GPa)$	--	--	--	46.5	47	29	37.14	92.4	--	46.34
ν_{12}	--	--	--	0.035	--	--	0.05	0.11	--	0.024
ν_{21}	--	--	--	--	--	--	0.05	--	--	--
ν_{13}	--	--	--	0.035	--	--	0.05	--	--	--
ν_{31}	--	--	--	--	--	--	0.05	0.05	--	--
ν_{23}	--	--	--	0.035	--	--	0.05	--	--	0.058
ν_{32}	--	--	--	--	--	--	0.05	--	--	--
$G_{12}(GPa)$	5.8	--	--	2.5	--	--	2.526	9.93	--	2.14
$G_{23}(GPa)$	--	--	--	--	--	--	2.526	--	--	7.19
$G_{13}(GPa)$	--	--	--	2.5	--	--	2.526	8.69	--	2.14

3.4 Conclusion

A review of several papers showed there was a gap in literature for reporting mechanical properties of 3D printed C/C composites. Taking advantage of new experimental and numerical characterization techniques, impulse excitation tests were performed on 50wt.% short carbon fiber-reinforced polyphenylene sulfide-derived 3D printed C/C composites to measure the elastic constant evolutions of E_1 and G_{23} throughout PIP processing and use these measurements to drive Mori-Tanaka homogenization-based numerical predictions so that the remaining elastic constants could be determined. After five heat treatment cycles to 1000°C and five infiltration cycles with phenolic resin, the density, pore volume fraction, E_1 , and G_{23} plateaued to 1.09 g/cm³, 36.12%, 31.98 GPa, and 5.97 GPa, respectively. Comparing the error between several 1st-order Mori-Tanaka predictions with experimental results showed that a simple representative volume element (RVE) with randomly distributed spherically closed pores with the same aspect ratio gave the best results, with predictions of $E_1 = 30.47$ GPa and $G_{23} = 5.57$ GPa. The remaining orthotropic elastic constants were subsequently determined to be $E_2 = 17.85$ GPa, $E_3 = 12.34$ GPa, $G_{13} = 6.64$ GPa, $G_{12} = 9.19$ GPa, $\nu_{12} = 0.26$, $\nu_{13} = 0.25$, and $\nu_{23} = 0.28$. The average tensile and double-notched shear strengths of 12.7 MPa and 11.29 MPa revealed the tensile strength was an order of magnitude weaker than 2D woven C/C, while the double-notched shear strength was approximately the same as felt- and woven- based C/C composites. While the potential for additively manufactured carbon/carbon composites is promising, several areas remain unexplored, including 3D printed C/C composites with favorable fiber-matrix debonding characteristics, densities comparable to those produced by chemical vapor infiltration, and 3D printed C/C composites with continuous fiber reinforcement.

4. CONCLUSIONS AND FUTURE WORK

The goal of this project was aimed at reducing hypersonic technology costs by improving access, lead times, and price to carbon/carbon (C/C) composite hot structures/thermal protection systems, since they are notoriously expensive and slow to produce. The conventional manufacturing methods used for shaping C/C composites into mechanical and thermal load-bearing components including hand layup, filament winding, resin transfer molding, autoclave processing, and textile processing (e.g. braiding, stitching, knitting, weaving, needle-punching) require molds/tooling surfaces to rigidize oriented fibers and achieve near-net shapes, which slows down component designs and increases supply chain costs. The mold-less and scalable nature of extrusion deposition additive manufacturing (EDAM) technology addresses these issues, and the experimental results showed that it could be used to make complex near-net shaped C/C composites. However, several aspects of the manufacturing process were not optimized.

The coupon distortion data revealed that the intumescent behavior of the polymers is intimately related to the fiber orientation distribution in the extruded layers, which was not varied to change the swelling characteristics of the printed geometries. The in-plane anisotropy of the short fibers increases strength in load-critical directions but also increases swelling in directions transverse to the dominant fiber alignment direction. The tradeoff between strength and swelling in the extruded layers means that an optimal fiber orientation distribution may not exist for short fiber systems. To simultaneously maximize strength and minimize swelling of the printed geometries would require hybrid fiber reinforcement in which continuous fibers provide the strength in load-critical directions while short fibers reduce swelling along material directions. Because higher bead aspect ratios reduce the in-plane anisotropy of the short fibers, an optimal bead aspect ratio with hybrid fiber reinforcement exists in which this is possible. Future studies could investigate this to highlight the capability of EDAM for processing fiber-reinforced thermoplastic polymers into C/C composites that not only have better dimensional stability but also have higher mechanical properties than those found in this study. The benefits of hybrid fiber reinforcement may also help dimensionally stabilize polyetherimide (PEI) and polyetheretherketone (PEEK), the highest char yielding polymers investigated in this study, which were initially discarded over polyphenylene sulfide (PPS) because of their intumescent behavior.

The X-ray micro-computed tomography (μCT) data of 50 wt.% short carbon fiber reinforced polyphenylene sulfide (50CF-PPS) after pyrolysis showed that the anisotropy of the porosity was also intimately related to the fiber orientation distribution, since the anisotropy of the reinforcing phase causes anisotropic viscosities and permeabilities in the composite material above its melt temperature. The experimental results by Park and Suh [85] showed that higher bubble stretching ratios were observed in higher viscosity fluids for the same shearing rates, indicating that higher fiber loadings in PPS with more aligned short fibers would result in more needle-like porosity. Their research and the experimental results reported in this study suggests that the interconnectivity of the pore network may change with different fiber loadings and fiber orientation distributions. Future work could include investigating if an optimal fiber loading and fiber orientation distribution exists that improves the interconnectivity and densification process of the porous microstructures. The interconnectivity of the pyrolyzed 50CF-PPS appeared to be high in this study, with a percent closed porosity of only 2.85% after initial pyrolysis processing, but the difference in pore volume fraction estimates between the mass conservation analysis and μCT scans showed the 5 μm resolution used was not able to capture all the porosity in the material, leaving the reader with no definitive answer as to whether the 16-19% porosity not detected during μCT scans after initial pyrolysis processing was open or closed porosity. Future studies should use higher resolutions in order definitively quantify the interconnectivity of the pore network, and different densification methods, such as chemical vapor infiltration, to obtain higher densities.

A literature review of the mechanical properties showed that the 3D printed C/C material was much weaker than 2D woven C/C composites. The 3D printed C/C had a double-notched shear strength (11.29 MPa) within ± 5 MPa of 2D felt- and 2D woven- based C/C, but the tensile strength (12.71 MPa) was an order of magnitude smaller than the tensile strength of 2D woven C/C, owing to the significant amount of porosity (36%) left behind after densification as well as the short fibers used for the reinforcing phase. Although the orthotropic compliance/stiffness tensor was fully populated, the coefficients of thermal expansion and strengths in the other material directions were not experimentally measured. As a result, the viability of 3D printed C/C composites for structural applications will require more research before EDAM can be used to develop 3D printed C/C composite hot structures/thermal protection systems.

APPENDIX A. CHAPTER 1 MATERIAL PROPERTIES AND SCRIPTS

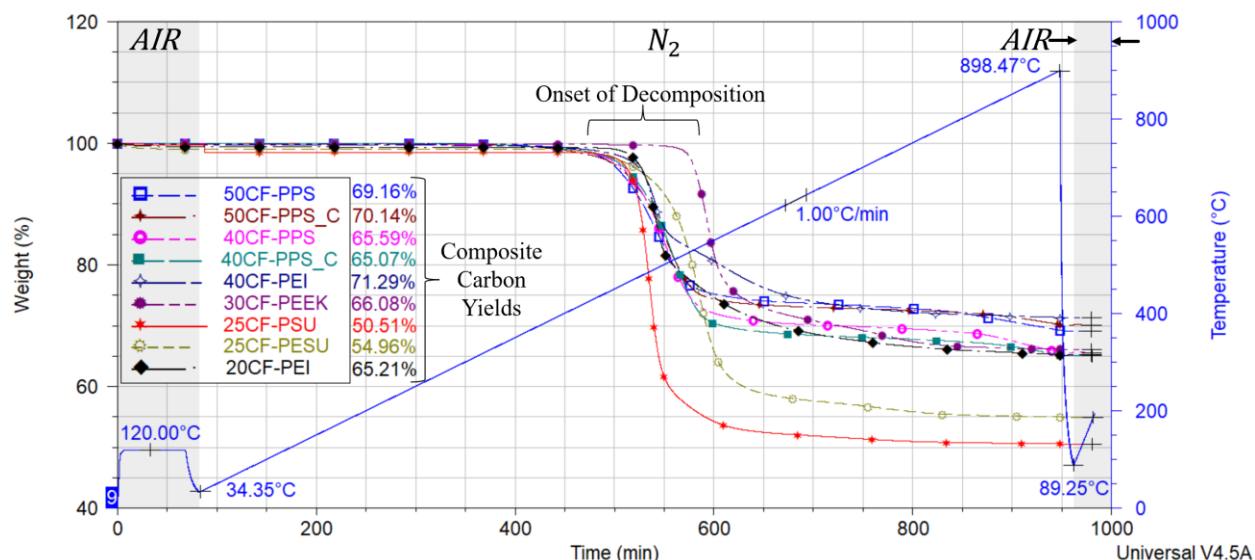


Figure A.1 Fractional weight loss versus time at $1^\circ\text{C}/\text{min}$ showing the composite char yields.

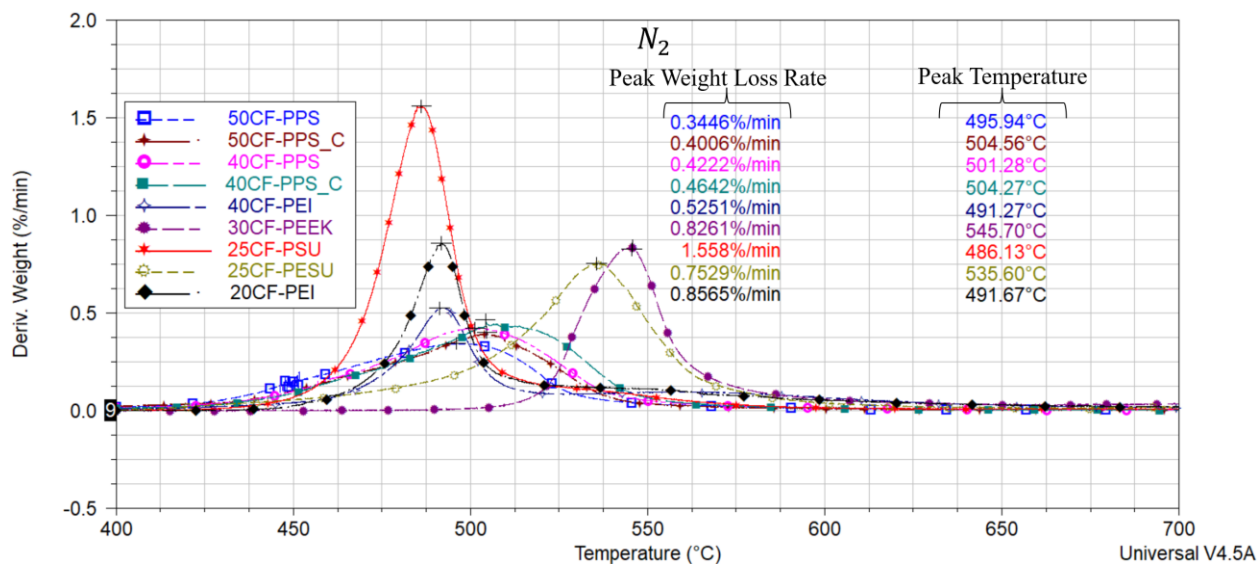


Figure A.2 Fractional weight loss rates versus temperature for the composite pellets tested at $1^\circ\text{C}/\text{min}$ showing the peak weight loss rate and the decomposition temperature at the peak.

APPENDIX B. CHAPTER 2 MATERIAL PROPERTIES AND SCRIPTS

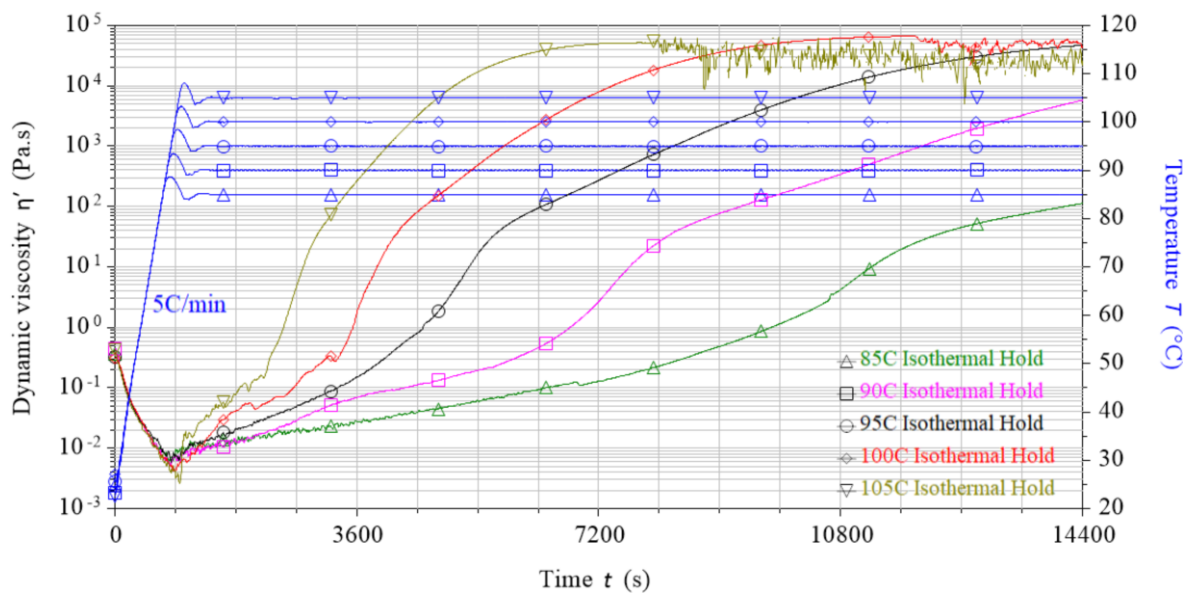


Figure B.1 The temperature dependence of the resol phenolic resin viscosity at various isothermal holds showed that a gel time of 90 min at 105°C suitably increases the dynamic viscosity above 10,000 Pa.s.

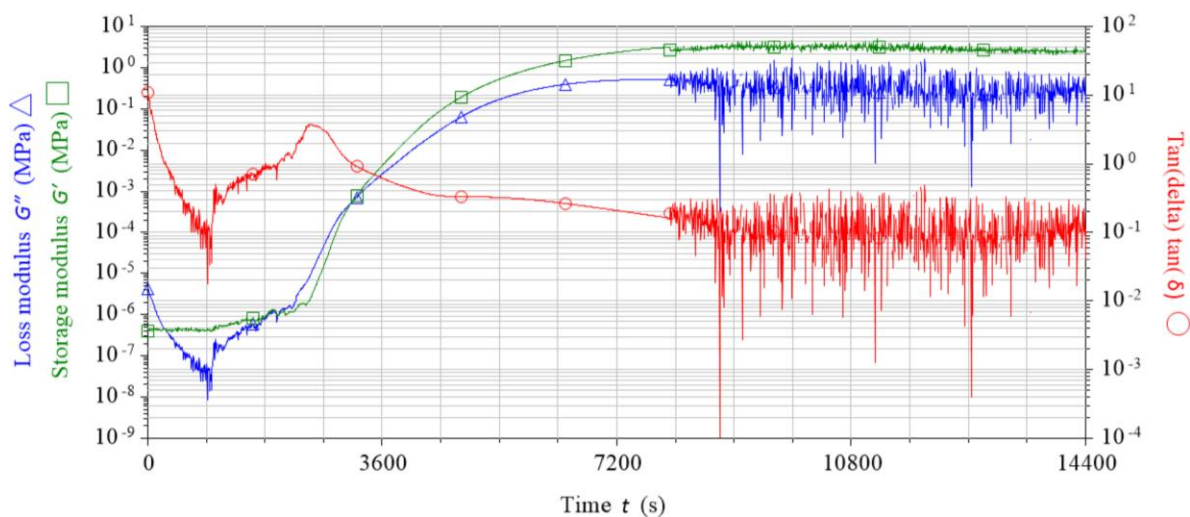


Figure B.2 Storage modulus, loss modulus and tan delta as a function of time for the resol phenolic resin ramped at a rate of 5°C/min from 25°C to 105°C, then dwelled for 4 hrs.

Table B.2 Script developed in MATLAB® 2021a that processes weight data to calculate the density and pore volume fraction evolution during PIP processing. The main script, “DensificationPlots,” calls a function called “PoreVolumeFraction”, which calculates the pore volume fraction at each processing step. The input at the start is 50CF-PPS.

```
clear all;close all;clc;
%% User Input
material = input('What material is being analyzed?:','s');

%% Reading Weight and Volume Data
%Note: Always import even number of rows
WD = xlsread('DensificationData.xlsx',1,'L2:L13'); %weight data (WD)

%% Sorting Weight and Volume Data
%Initialize
W_RTM = zeros(length(WD(:,1))/2, length(WD(1,:)));
W_Py = zeros(length(WD(:,1))/2, length(WD(1,:)));
W_Py2 = zeros(length(WD(:,1))/2, length(WD(1,:)));
Vf2 = zeros(length(WD(:,1))/2, length(WD(1,:)));
Vp2 = zeros(length(WD(:,1))/2, length(WD(1,:)));

for i = 1:length(WD(:,1))/2
    W_RTM(i,:) = WD(2*i-1,:); %[g], matrix of all VARTM weights (as-printed is 1st row)
    W_Py(i,:) = WD(2*i,:); %[g], matrix of all pyrolysis weights

%Pre-pyrolysis volume of X-ray uCT C/C coupon
V_Pr = 49.631; %[cm^3]

%Vector of post-pyrolysis volumes [for PIP cycle 0-5]
V_Py = [64.4437;38.4443;38.4443;38.4443;38.4443;38.4443]; %[cm^3]
end

%% Quantifying Density and Fractional Density
Nsamples = length(WD(1,:)); %number of samples
Ncycles = length(WD(:,1))/2; %number of cycles (includes cycle 0)

%Initialize
rho_act = zeros(Ncycles,Nsamples);
rho_max = zeros(Ncycles,Nsamples);
ratio = zeros(Ncycles,Nsamples);
Wf2 = zeros(1,Nsamples);
Wm2 = zeros(1,Nsamples);
Vp = zeros(Ncycles,Nsamples);

%Assumptions
rhof = 1.78; %[g/cm^3], fiber density
rhom = 1.65; %[g/cm^3], carbon matrix density
rhopf = 1.55; %[g/cm^3], phenolic resin density

for k = 1:Nsamples
    for j = 1:Ncycles
        [Vp(j,k),Wf2(1,k),Wm2(1,k),W_Py2(j+1,k),Vf2(j+1,k),Vp2(j+1,k)] =
        PoreVolumeFraction(j,material,rhof,rhom,...

W_RTM(j,k),W_Py(j,k),W_Py2(j,k),V_Pr(k,1),V_Py(j,k),Wf2(1,k),Wm2(1,k),Vf2(j,k),Vp2(j
,k));
    end
end

W_Py(1,:) = 0.706*W_RTM(1,:);

for k = 1:Nsamples
```



```

        for j = 1:Ncycles
rho_act(j,k) = W_Py(j,k)/V_Py(j,k);
%[g/cm^3], actual density of C/C coupon in the current cycle

rho_max(j,k) = ( W_Py(j,k) + rhom*(Vp(j,1)/100)*V_Py(j,k) )/V_Py(j,k);
%[g/cm^3], max density of C/C coupon in the current cycle
%(assuming no pores)

ratio(j,k) = rho_act(j,k)/rho_max(j,k)*100;
        end
    end

%% Plotting
%Standardize color (C) and linestyle (LS)
C = {'m','b','r','g','c','k','b','g'};
M = {'^','s','d','o','p','h','*'};
LS = {'-','--',':','-.','-.-','-.','-.','-.','.'};
Legend = {Nsamples};
PIPCycles = linspace(0,Ncycles-1,Ncycles); %vector of cycles
PIPCycles1 = [0 1 2 3 4 5 6];
PIPCyclesaxis = {'GS','PIP0','PIP1','PIP2','PIP3','PIP4','PIP5'};

%Adds GS density & pore volume fraction data to PIP cycle data
rho_act_plot = [1.51; rho_act];
Vp_plot = [0; Vp];

%X-ray Micro-Computed Tomography Data
Vp_plot_Xray = [0;40.93;35.51;35.32;30.53;30.98;29.51];

for n = 1:Nsamples
figure(1) %Density
plot(PIPCycles1,rho_act_plot(:,n),'Color',C{6},'Marker',M{n},'Markersize',8,'LineStyle',LS{n},'LineWidth',1.4);
grid on; hold on;
xlabel('Process Step'); ylim([0.6 1.6]);yticks(linspace(0.6,1.6,6));
xticks(PIPCycles1);
xticklabels(PIPCyclesaxis);
ylabel('\rho_a_c_t (g/cm^3)');
title('Density Evolution of C/C CT Coupon');
set(gca,'FontSize',12,'FontName','Times');
grid on; hold on;
end

legend('Mass Conservation Analysis');

for n = 1:Nsamples
figure(2) %Pore Volume Fraction
plot(PIPCycles1,Vp_plot(:,n),'Color',C{6},'Marker',M{n},'Markersize',8,'LineStyle',LS{n},'LineWidth',1.4);
grid on; hold on;
plot(PIPCycles1,Vp_plot_Xray(:,1),'Color',C{7},'Marker',M{5},'Markersize',8,'LineStyle',LS{1},'LineWidth',1.4);
xlabel('Process Step'); ylim([0 60]);yticks(linspace(0,100,11));
xticks(PIPCycles1);
xticklabels(PIPCyclesaxis);
ylabel('V_p (%)');
title('Pore Volume Fraction Evolution of C/C CT Coupon');
set(gca,'FontSize',12,'FontName','Times');
grid on; hold on;
end

```

```
legend('Mass Conservation Analysis','X-ray Micro-Computed Tomography');
```

```
function [Vp,Wf2,Wm2,W_Py2,Vf2,Vp2] = PoreVolumeFraction(j,material,rhof,rhom,...
    W_VARTM,W_Py,W_Py2,V_Pr,V_Py,Wf2,Wm2,Vf2,Vp2)

if j ==1 %this if-statement separates the
%calculation of pore volume fraction (Vp)
%in cycle 0 from all following cycles, since we
%assume that the fibers only lose weight during
%cycle 0 and because the yield of thermoplastic
%polymer (cycle 0) differs from the yield of
%phenolic resin (cycle 1,2,...).

%% Vp for cycle 0
if isequal(material,'65CF-PPS') %(Techmer)
    Wf = 65; %[%], fiber weight fraction
    Wm = 35; %[%], matrix (polymer) weight fraction
    Yc = 84.0; %[%], composite carbon yield
    Ym = 57.2; %[%], matrix (polymer) carbon yield
elseif isequal(material,'50CF-PPS') %(Techmer)
    Wf = 50; %[%], fiber weight fraction
    Wm = 50; %[%], matrix (polymer) weight fraction
%    Yc = (W_Py/W_VARTM)*100; %[%], composite carbon yield
    Yc = 70.6; %[%], composite carbon yield
    Ym = 42.9; %[%], matrix (polymer) carbon yield
elseif isequal(material,'50CF-PPS_C') %(Celanese)
    Wf = 50; %[%], fiber weight fraction
    Wm = 50; %[%], matrix (polymer) weight fraction
    Yc = 66.1; %[%], composite carbon yield
    Ym = 33.9; %[%], matrix (polymer) carbon yield
elseif isequal(material,'40CF-PPS') %(Techmer)
    Wf = 40; %[%], fiber weight fraction
    Wm = 60; %[%], matrix (polymer) weight fraction
    Yc = 68.8; %[%], composite carbon yield
    Ym = 49.1; %[%], matrix (polymer) carbon yield
elseif isequal(material,'40CF-PPS_C') %(Celanese)
    Wf = 40; %[%], fiber weight fraction
    Wm = 60; %[%], matrix (polymer) weight fraction
    Yc = 66.3; %[%], composite carbon yield
    Ym = 44.9; %[%], matrix (polymer) carbon yield
elseif isequal(material,'40CF-PEI') %(Sabic)
    Wf = 40; %[%], fiber weight fraction
    Wm = 60; %[%], matrix (polymer) weight fraction
    Yc = 71.8; %[%], composite carbon yield
    Ym = 54.1; %[%], matrix (polymer) carbon yield
elseif isequal(material,'30CF-PEEK') %(Evonik)
    Wf = 30; %[%], fiber weight fraction
    Wm = 70; %[%], matrix (polymer) weight fraction
    Yc = 64.9; %[%], composite carbon yield
    Ym = 50.6; %[%], matrix (polymer) carbon yield
elseif isequal(material,'25CF-PSU') %(Techmer)
    Wf = 25; %[%], fiber weight fraction
    Wm = 75; %[%], matrix (polymer) weight fraction
    Yc = 51.3; %[%], composite carbon yield
    Ym = 35.6; %[%], matrix (polymer) carbon yield
elseif isequal(material,'25CF-PESU') %(Techmer)
    Wf = 25; %[%], fiber weight fraction
    Wm = 75; %[%], matrix (polymer) weight fraction
    Yc = 54.8; %[%], composite carbon yield
    Ym = 40.3; %[%], matrix (polymer) carbon yield
elseif isequal(material,'20CF-PEI') %(Sabic)
    Wf = 20; %[%], fiber weight fraction
```

```

        Wm = 80; %[%], matrix (polymer) weight fraction
        Yc = 65.2; %[%], composite carbon yield
        Ym = 56.9; %[%], matrix (polymer) carbon yield
    end

    %% Fiber Carbon Yield (%)
    Yf = 98.4; %AS4-GP3K (Hexcel)

    %% As 3D Printed
    Wf1 = (Wf/100)*W_VARTM; %[g], fiber weight in 3D printed samples
    Wm1 = (Wm/100)*W_VARTM; %[g], polymer weight in 3D printed samples
    Vf1 = (Wf1/rhof)/V_Pr; %[%], fiber volume fraction
    Vm1 = 1-Vf1; %[%], polymer matrix volume fraction

    %% After Pyrolysis
    Wf2 = (Yf/100)*Wf1; %[g], fiber weight
    Wm2 = W_VARTM*(Yc/100)-Wf2; %[g], carbonized matrix weight
    %    Wm2 = (Yc/100)*W_VARTM-Wf2; %[g], carbonized matrix weight
    Vf2 = (Wf2/rhof)/V_Py; %[%], fiber volume fraction
    Vm2 = (Wm2/rhom)/V_Py; %[%], carbon matrix volume fraction
    Vp = (1-Vf2-Vm2)*100; %[%], pore volume fraction
    W_Py2 = W_Py; %stores current C/C weight so it can be called
    %in the next cycle to find the phenolic resin weight added
    %see Wpf line below)
    Vf2 = Vf2; %also gets stored for future calcs
    Vp2 = Vp;

elseif j > 1
    %% Vp for cycle 1,2,...
    Wf2 = Vf2*V_Py*rhof; %[g], updates the current fiber weight with fiber volume
    fraction
    Vm2 = 1-Vf2-(Vp2/100); %[%], finds matrix volume fraction
    Wm2 = Vm2*V_Py*rhom; %[g], updates current matrix weight with line above
    Wpf = W_VARTM - W_Py2; %[g], phenolic resin weight added during current cycle
    Ypf = ((W_Py-Wf2-Wm2)/Wpf)*100; %[%], phenolic resin carbon yield
    Vf2 = (Wf2/rhof)/V_Py; %[%], fiber volume fraction
    Vm2 = ((Wm2 + (Ypf/100)*Wpf)/rhom)/V_Py; %[%], new carbon matrix volume fraction
    Vp = (1- Vf2 - Vm2)*100; %[%], new pore volume fraction
    W_Py2 = W_Py;
    Vp2 = Vp;
end
end

```

Table B.3 Matlab 2021 a script used to plot the open and closed pore aspect ratio distributions throughout PIP processing.

```

clc;close all;clear all;

%% Initialize ((%6 bc theres 6 PIP process steps (PIP0 to PIP5)))
C_Matrix = cell(1,6); %matrix for closed pores
O_Matrix = cell(1,6); %matrix for open pores

%%%%% Column 2 = pore number
%%%%% Column 5 = pore volume (um^3)
%%%%% Column 6 = pore aspect ratio (>0)
for i = 1:6 %6 bc theres 6 PIP process steps (PIP0 to PIP5)
C_Matrix{i} = readmatrix(sprintf('PIP%d_ClosedPores.xlsx',i-1));
O_Matrix{i} = readmatrix(sprintf('PIP%d_OpenPores.xlsx',i-1));
end

%% Plotting
C = {'b','g','r','k','c','m','y','b'}; %standardizes color of data
LS = {'-','--',':','-.','-.-','-.-','-.','.'}; %standardizes linestyle of data
M = {'*','s','o','d','p','h','v','x'}; %standardizes marker of data

%% Aspect Ratio (AR = L/D) Evolution
for i = 1:6
figure (1) %Closed Pores
x2 = linspace(0,80,241);
h2 = histogram(1./C_Matrix{i}(:,6),x2,'DisplayStyle','stairs',...
    'EdgeColor',C{1,i},'LineStyle',LS{1,1},'LineWidth',1.2);
set(gca,'yscale','log');
title('Aspect Ratio Evolution for Closed Porosity');
xlabel('Aspect Ratio, AR = L/D'); ylabel('Number of Closed Pores');
ylim([10^-1 1e6]);
xlim([0 80]);
set(gca,'FontSize',12,'FontName','Times');
grid on; hold on;
end

for i = 1:6
figure (2) %Open Pores
x2 = linspace(0,1e5,1e5+1);
h2 = histogram(1./O_Matrix{i}(:,6),x2,'DisplayStyle','stairs',...
    'EdgeColor',C{1,i},'LineStyle',LS{1,1},'LineWidth',1.2);
set(gca,'yscale','log');
set(gca,'xscale','log');
title('Aspect Ratio Evolution for Open Porosity');
xlabel('Aspect Ratio, AR = L/D'); ylabel('Number of Open Pores');
ylim([10^-1 1e6]);
xlim([0 1e4]);
set(gca,'FontSize',12,'FontName','Times');
grid on; hold on;
end

%% Aspect Ratio-Derived Pore Length Evolution
%Initialize
C_ARL = cell(1,6);
O_ARL = cell(1,6);

%Substituting AR = L/D into cylinder volume
%formula and solving for L:
for i = 1:6
C_ARL{i} = ((4./pi).*C_Matrix{i}(:,5).*C_Matrix{i}(:,6)).^(1/3);
O_ARL{i} = ((4./pi).*O_Matrix{i}(:,5).*O_Matrix{i}(:,6)).^(1/3);
end

```

```

end

for i = 1:6
figure (3) % Closed Pores
x1 = linspace(0,1300,1301);
h1 = histogram(C_ARL{i},x1,'DisplayStyle','stairs',...
    'EdgeColor',C{1,i},'LineStyle',LS{1,1},'LineWidth',1.2);
set(gca,'yscale','log');
set(gca,'xscale','log');
title('Aspect Ratio-Derived Length Evolution for Closed Porosity');
xlabel('Aspect Ratio-Derived Length, L ({\mu}m)'); ylabel('Number of Closed Pores');
ylim([10^-1 1e6]);
xlim([3 1e3]);
set(gca,'FontSize',12,'FontName','Times');
grid on; hold on;
end

for i = 1:6
figure (4) %Open Pores
x1 = linspace(0,1300,1301);
h1 = histogram(O_ARL{i},x1,'DisplayStyle','stairs',...
    'EdgeColor',C{1,i},'LineStyle',LS{1,1},'LineWidth',1.2);
set(gca,'yscale','log');
set(gca,'xscale','log');
title('Aspect Ratio-Derived Length Evolution for Open Porosity');
xlabel('Aspect Ratio-Derived Length, L ({\mu}m)');
ylabel('Number of Open Pores');
ylim([10^-1 1e6]);
xlim([3 1e3]);
set(gca,'FontSize',12,'FontName','Times');
grid on; hold on;
end

for i = 1:6
    C_Leg{i} = sprintf('PIP%d,# Closed Pores = %d',i-1,length(C_Matrix{i}(:,2)));
    O_Leg{i} = sprintf('PIP%d,# Open Pores = %d',i-1,length(O_Matrix{i}(:,2)));
end

figure(1)
legend(C_Leg);
figure(3)
legend(C_Leg);

figure(2)
legend(O_Leg);
figure(4)
legend(O_Leg);

```

Table B.4 MATLAB 2021a script used to plot the radial distribution of percent open and percent closed porosity throughout PIP processing.

```

clc;close all;clear all;

%% Reading Data

%Initialize
Vp_C = zeros(6,3); %matrix for closed pores
Vp_O = zeros(6,3); %matrix for open pores

%Table of Pore Volume Fractions vs PIP Process Steps
Matrix = xlsread('Vp_v_Radii.xlsx',1,'B3:D14');

%Separates data in Matrix for open and closed porosity
for i = 1:6 %6 bc theres 6 PIP process steps (PIP0 to PIP5)
    Vp_O(i,:) = Matrix(2*i-1,:); %columns for r/3,2r/3,3r/3
    Vp_C(i,:) = Matrix(2*i,:);
    VpO_total(i,1) = sum(Vp_O(i,:));
    VpC_total(i,1) = sum(Vp_C(i,:));
end

%repeat each column of data twice for stair step plots
Vp_O = [Vp_O(:,1),Vp_O(:,1),Vp_O(:,2),Vp_O(:,2),Vp_O(:,3),Vp_O(:,3)];
Vp_C = [Vp_C(:,1),Vp_C(:,1),Vp_C(:,2),Vp_C(:,2),Vp_C(:,3),Vp_C(:,3)];

%% Plotting
C = {'b','g','r','k','c','m','y','b'}; %standardizes color of data
LS = {'-','--',':','-.','-.-','-.-','-.',':'}; %standardizes linestyle of data
M = {'*','s','o','d','p','h','v','x'}; %standardizes marker of data

Zones = {'R/3', '2R/3', '3R/3'};

for i = 1:6
figure (1) %Closed Pores
x = [0 1 1 2 2 3];
stairs(x,Vp_C(i,:), 'Color',C{i}, 'Marker',M{i}, 'LineStyle',LS{1,i}, 'LineWidth',1.4);
title('Radial Distribution Evolution of Percent Closed Porosity');
xlabel('Radius, R (mm)'); ylabel('Pore Volume Fraction, V_p (%)');
ylim([0 6.75]);
xticks([ 1 2 3]);
xticklabels(Zones)
set(gca, 'FontSize',12, 'FontName', 'Times');
grid on; hold on;
end
% legend('PIP0','PIP1','PIP2','PIP3','PIP4','PIP5');

for i = 1:6
figure (2) %Open Pores
x = [0 1 1 2 2 3];
stairs(x,Vp_O(i,:), 'Color',C{i}, 'Marker',M{i}, 'LineStyle',LS{1,i}, 'LineWidth',1.4);
title('Radial Distribution Evolution of Percent Open Porosity');
xlabel('Radius, R (mm)'); ylabel('Pore Volume Fraction, V_p (%)');
ylim([0 30]);
xticks([ 1 2 3]);
xticklabels(Zones)
set(gca, 'FontSize',12, 'FontName', 'Times');
grid on; hold on;
end

for i = 1:6
    O_Leg{i} = sprintf('PIP%d, Total Vp =%0.2f %%',i-1, VpO_total(i,1));

```

```
        C_Leg{i} = sprintf('PIP%d, Total Vp =%0.2f %%',i-1, VpC_total(i,1));  
    end  
  
    figure(1)  
    legend(C_Leg);  
  
    figure(2)  
    legend(O_Leg);
```

APPENDIX C. CHAPTER 3 MATERIAL PROPERTIES AND SCRIPTS

Table C.1 Script developed in MATLAB® 2021a to calculate the density and pore volume fraction evolutions for the 5 C/C coupons in Figure 3.1 taken through phenolic resin densification. This code is similar to the code in Table B.2. The main script, “DensificationPlots,” calls a function called “PoreVolumeFraction”, which calculates the pore volume fraction at each processing step. The input at the start is 50CF-PPS.

```
clear all; close all; clc;
%% User Input
material = input('What material is being analyzed?:','s');

%% Reading Weight and Volume Data
%Note: Always import even number of rows
WD = xlsread('DensificationData.xlsx',1,'G2:K13'); %weight data (WD)

%% Sorting Weight and Volume Data
%Initialize
W_RTM = zeros(length(WD(:,1))/2, length(WD(1,:)));
W_Py = zeros(length(WD(:,1))/2, length(WD(1,:)));
W_Py2 = zeros(length(WD(:,1))/2, length(WD(1,:)));
Vf2 = zeros(length(WD(:,1))/2, length(WD(1,:)));
Vp2 = zeros(length(WD(:,1))/2, length(WD(1,:)));

for i = 1:length(WD(:,1))/2
W_RTM(i,:) = WD(2*i-1,:); %[g], matrix of all VARTM weights (as-printed is 1st row)
W_Py(i,:) = WD(2*i,:); %[g], matrix of all pyrolysis weights

%vector of all pre-pyrolysis volumes (coupon 1,2,3,4,5)
V_Pr = [49.5247;50.2929;48.8088;49.3658;50.0676];

%vector of all post-pyrolysis volumes
%(columns for coupons 1-5, rows for volume at each PIP cycle (0-5))
V_Py = [64.6182 65.1981 60.6203 63.1733 62.5342;...
        38.7017 39.4263 38.4085 37.3115 37.2799;...
        38.7017 39.4263 38.4085 37.3115 37.2799;...
        38.7017 39.4263 38.4085 37.3115 37.2799;...
        38.7017 39.4263 38.4085 37.3115 37.2799;...
        38.7017 39.4263 38.4085 37.3115 37.2799]; %[cm^3]
end

%% Quantifying Density and Fractional Density
Nsamples = length(WD(1,:)); %number of samples
Ncycles = length(WD(:,1))/2; %number of cycles (includes cycle 0)

%Initialize
rho_act = zeros(Ncycles,Nsamples);
rho_max = zeros(Ncycles,Nsamples);
ratio = zeros(Ncycles,Nsamples);
Wf2 = zeros(1,Nsamples);
Wm2 = zeros(1,Nsamples);
Vp = zeros(Ncycles,Nsamples);

%Assumptions
rhof = 1.78; %[g/cm^3], fiber density
rhom = 1.65; %[g/cm^3], carbon matrix density (1.7-2.6)
rhopf = 1.55; %[g/cm^3], phenolic resin density
```



```

for k = 1:Nsamples
    for j = 1:Ncycles
        [Vp(j,k),Wf2(1,k),Wm2(1,k),W_Py2(j+1,k),Vf2(j+1,k),Vp2(j+1,k)] =
        PoreVolumeFraction(j,material,rhof,rhom,...

W_RTM(j,k),W_Py(j,k),W_Py2(j,k),V_Pr(k,1),V_Py(j,k),Wf2(1,k),Wm2(1,k),Vf2(j,k),Vp2(j
,k));
        end
    end

W_Py(1,:) = 0.706*W_RTM(1,:);

for k = 1:Nsamples
    for j = 1:Ncycles
        rho_act(j,k) = W_Py(j,k)/V_Py(j,k);
        %[g/cm^3], actual density of C/C sample in the current cycle

        rho_max(j,k) = ( W_Py(j,k) + rhom*(Vp(j,1)/100)*V_Py(j,k) )/V_Py(j,k);
        %[g/cm^3], max density of C/C sample in the current cycle
        %(assuming no pores)

        ratio(j,k) = rho_act(j,k)/rho_max(j,k)*100;
        end
    end

%% Plotting
%Standardize color (C) and linestyle (LS)
C = {'m','b','r','g','c','k','b','g'};
M = {'^','s','d','o','p','h','*'};
LS = {'-','--',':','-.','-','-.','-.',':'};
Legend = {Nsamples};
PIPCycles = linspace(0,Ncycles-1,Ncycles); %vector of cycles
PIPCycles1 = [0 1 2 3 4 5 6];
PIPCyclesaxis = {'GS','PIP0','PIP1','PIP2','PIP3','PIP4','PIP5'};
rho_act_plot = [1.51 1.51 1.51 1.51 1.51; rho_act];
ratio_plot = [100 100 100 100 100; ratio];
Vp_plot = [0 0 0 0 0; Vp];

for z = 1:7
    rho_act_plot_avg(1,z) = mean(rho_act_plot(z,:));
    ratio_plot_avg(1,z) = mean(ratio_plot(z,:));
    Vp_plot_avg(1,z) = mean(Vp_plot(z,:));
end

for n = 1:Nsamples
    figure(1) %Density
    plot(PIPCycles1,rho_act_plot(:,n),'Color',C{6},'Marker',M{n},'Markersize',8,'LineSt
yle',LS{n},'LineWidth',1.4);
    xlabel('Process Step'); ylim([0.6 1.6]);yticks(linspace(0.6,1.6,6));
    xticks(PIPCycles1);
    xticklabels(PIPCyclesaxis);
    ylabel('{\rho}_a_c_t (g/cm^3)');
    title('Density Evolution of C/C Composite Coupons');
    set(gca,'FontSize',12,'FontName','Times');
    grid on; hold on;
end
plot(PIPCycles1,rho_act_plot_avg,'Color',C{3},'Marker',M{7},'Markersize',8,'LineStyl
e',LS{1},'LineWidth',1.4);
legend('Coupon 1','Coupon 2','Coupon 3','Coupon 4','Coupon 5','Average');

for n = 1:Nsamples

```

```

figure(2) %Fractional Density
plot(PIPCycles1, ratio_plot(:,n), 'Color', C{6}, 'Marker', M{n}, 'Markersize', 8, 'LineStyle'
e', LS{n}, 'LineWidth', 1.4);
xlabel('Process Step'); ylim([40 100]); yticks(linspace(0,100,11));
xticks(PIPCycles);
xticklabels(PIPCyclesaxis);
ylabel('{\rho}_a_c_t / {\rho}_m_a_x (%)');
title('Fractional Density Evolution of C/C Composite Coupons');
set(gca, 'FontSize', 12, 'FontName', 'Times');
grid on; hold on;
end
plot(PIPCycles1, ratio_plot_avg, 'Color', C{3}, 'Marker', M{7}, 'Markersize', 8, 'LineStyle'
, LS{1}, 'LineWidth', 1.4);
legend('Coupon 1', 'Coupon 2', 'Coupon 3', 'Coupon 4', 'Coupon 5', 'Average');

for n = 1:Nsamples
figure(3) %Pore Volume Fraction
plot(PIPCycles1, Vp_plot(:,n), 'Color', C{6}, 'Marker', M{n}, 'Markersize', 8, 'LineStyle',
LS{n}, 'LineWidth', 1.4);
xlabel('Process Step'); ylim([0 60]); yticks(linspace(0,100,11));
xticks(PIPCycles1);
xticklabels(PIPCyclesaxis);
ylabel('V_p (%)');
title('Pore Volume Fraction Evolution of C/C Composite Coupons');
set(gca, 'FontSize', 12, 'FontName', 'Times');
grid on; hold on;
end
plot(PIPCycles1, Vp_plot_avg, 'Color', C{3}, 'Marker', M{7}, 'Markersize', 8, 'LineStyle', LS
{1}, 'LineWidth', 1.4);
legend('Coupon 1', 'Coupon 2', 'Coupon 3', 'Coupon 4', 'Coupon 5', 'Average');

```

```

function [Vp, Wf2, Wm2, W_Py2, Vf2, Vp2] = PoreVolumeFraction(j, material, rhof, rhom, ...
W_VARTM, W_Py, W_Py2, V_Pr, V_Py, Wf2, Wm2, Vf2, Vp2)

if j ==1 %this if-statement separates the
%calculation of pore volume fraction (Vp)
%in cycle 0 from all following cycles, since we
%assume that the fibers only lose weight during
%cycle 0 and because the yield of thermoplastic
%polymer (cycle 0) differs from the yield of
%phenolic resin (cycle 1,2,...).

%% Vp for cycle 0
if isequal(material, '65CF-PPS') %(Techmer)
Wf = 65; %[%], fiber weight fraction
Wm = 35; %[%], matrix (polymer) weight fraction
Yc = 84.0; %[%], composite carbon yield
Ym = 57.2; %[%], matrix (polymer) carbon yield
elseif isequal(material, '50CF-PPS') %(Techmer)
Wf = 50; %[%], fiber weight fraction
Wm = 50; %[%], matrix (polymer) weight fraction
% Yc = (W_Py/W_VARTM)*100; %[%], composite carbon yield
Yc = 70.6; %[%], composite carbon yield
Ym = 42.9; %[%], matrix (polymer) carbon yield
elseif isequal(material, '50CF-PPS_C') %(Celanese)
Wf = 50; %[%], fiber weight fraction
Wm = 50; %[%], matrix (polymer) weight fraction
Yc = 66.1; %[%], composite carbon yield
Ym = 33.9; %[%], matrix (polymer) carbon yield
elseif isequal(material, '40CF-PPS') %(Techmer)
Wf = 40; %[%], fiber weight fraction

```

```

Wm = 60; %[%], matrix (polymer) weight fraction
Yc = 68.8; %[%], composite carbon yield
Ym = 49.1; %[%], matrix (polymer) carbon yield
elseif isequal(material,'40CF-PPS_C') %(Celanese)
Wf = 40; %[%], fiber weight fraction
Wm = 60; %[%], matrix (polymer) weight fraction
Yc = 66.3; %[%], composite carbon yield
Ym = 44.9; %[%], matrix (polymer) carbon yield
elseif isequal(material,'40CF-PEI') %(Sabic)
Wf = 40; %[%], fiber weight fraction
Wm = 60; %[%], matrix (polymer) weight fraction
Yc = 71.8; %[%], composite carbon yield
Ym = 54.1; %[%], matrix (polymer) carbon yield
elseif isequal(material,'30CF-PEEK') %(Evonik)
Wf = 30; %[%], fiber weight fraction
Wm = 70; %[%], matrix (polymer) weight fraction
Yc = 64.9; %[%], composite carbon yield
Ym = 50.6; %[%], matrix (polymer) carbon yield
elseif isequal(material,'25CF-PSU') %(Techmer)
Wf = 25; %[%], fiber weight fraction
Wm = 75; %[%], matrix (polymer) weight fraction
Yc = 51.3; %[%], composite carbon yield
Ym = 35.6; %[%], matrix (polymer) carbon yield
elseif isequal(material,'25CF-PESU') %(Techmer)
Wf = 25; %[%], fiber weight fraction
Wm = 75; %[%], matrix (polymer) weight fraction
Yc = 54.8; %[%], composite carbon yield
Ym = 40.3; %[%], matrix (polymer) carbon yield
elseif isequal(material,'20CF-PEI') %(Sabic)
Wf = 20; %[%], fiber weight fraction
Wm = 80; %[%], matrix (polymer) weight fraction
Yc = 65.2; %[%], composite carbon yield
Ym = 56.9; %[%], matrix (polymer) carbon yield
end

%% Fiber Carbon Yield (%)
Yf = 98.4; %AS4-GP3K (Hexcel)

%% As 3D Printed
Wf1 = (Wf/100)*W_VARTM; %[g], fiber weight in 3D printed samples
Wm1 = (Wm/100)*W_VARTM; %[g], polymer weight in 3D printed samples
Vf1 = (Wf1/rhof)/V_Pr; %[%], fiber volume fraction
Vm1 = 1-Vf1; %[%], polymer matrix volume fraction

%% After Pyrolysis
Wf2 = (Yf/100)*Wf1; %[g], fiber weight
Wm2 = W_VARTM*(Yc/100)-Wf2; %[g], carbonized matrix weight
% Wm2 = (Yc/100)*W_VARTM-Wf2; %[g], carbonized matrix weight
Vf2 = (Wf2/rhof)/V_Py; %[%], fiber volume fraction
Vm2 = (Wm2/rhom)/V_Py; %[%], carbon matrix volume fraction
Vp = (1-Vf2-Vm2)*100; %[%], pore volume fraction
W_Py2 = W_Py; %stores current C/C weight so it can be called
%in the next cycle to find the phenolic resin weight added
%see Wpf line below
Vf2 = Vf2; %also gets stored for future calcs
Vp2 = Vp;

elseif j > 1
%% Vp for cycle 1,2,...
Wf2 = Vf2*V_Py*rhof; %[g], updates the current fiber weight with fiber volume
fraction
Vm2 = 1-Vf2-(Vp2/100); %[%], finds matrix volume fraction
Wm2 = Vm2*V_Py*rhom; %[g], updates current matrix weight with line above

```

```

Wpf = W_VARTM - W_Py2; %[g], phenolic resin weight added during current cycle
Ypf = ((W_Py-Wf2-Wm2)/Wpf)*100; %[%], phenolic resin carbon yield
Vf2 = (Wf2/rhof)/V_Py; %[%], fiber volume fraction
Vm2 = ((Wm2 + (Ypf/100)*Wpf)/rhom)/V_Py; %[%], new carbon matrix volume fraction
Vp = (1- Vf2 - Vm2)*100; %[%], new pore volume fraction
W_Py2 = W_Py;
Vp2 = Vp;
end
end

```

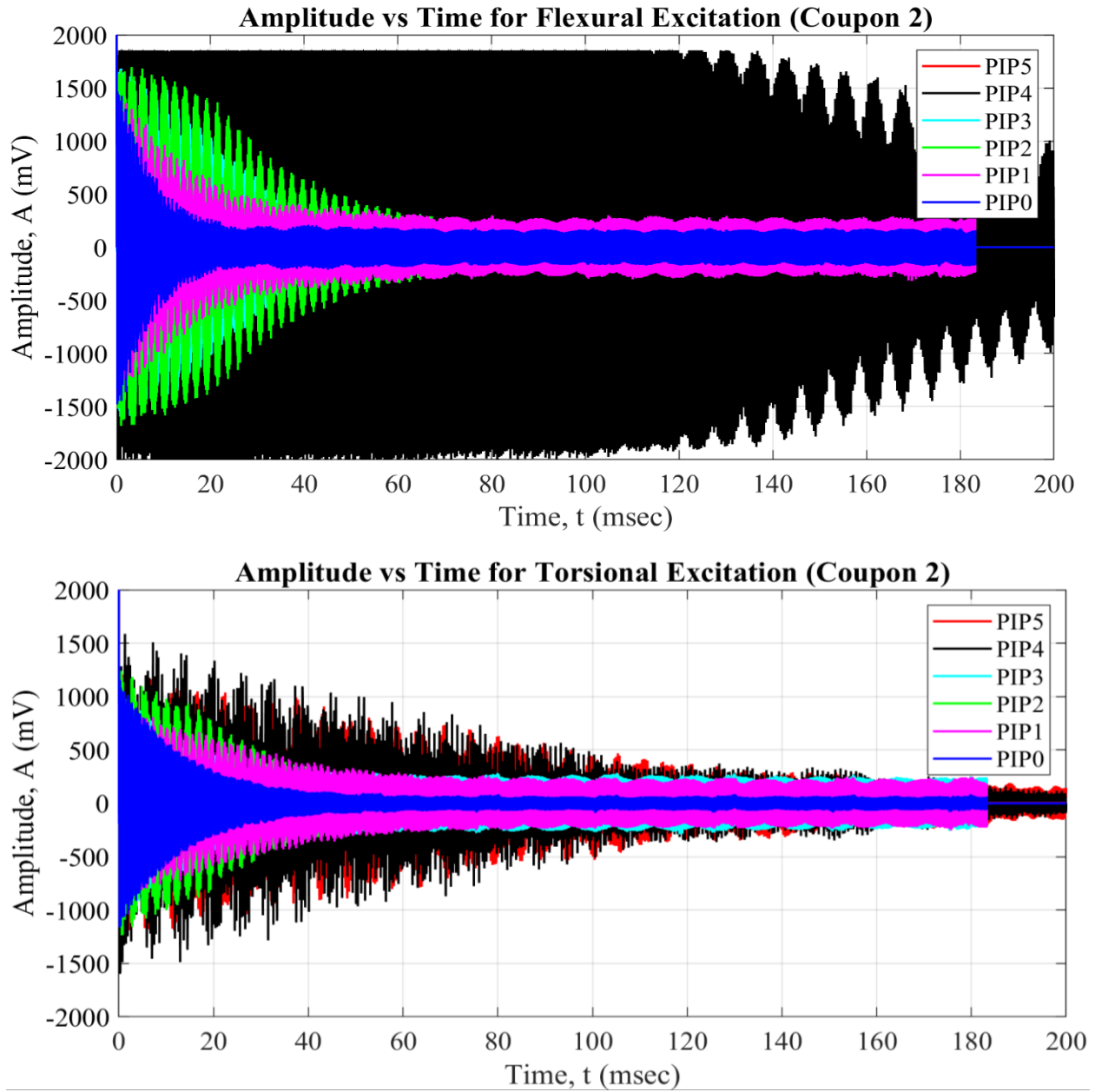


Figure C.1 Amplitude versus time for C/C composite coupons 2.

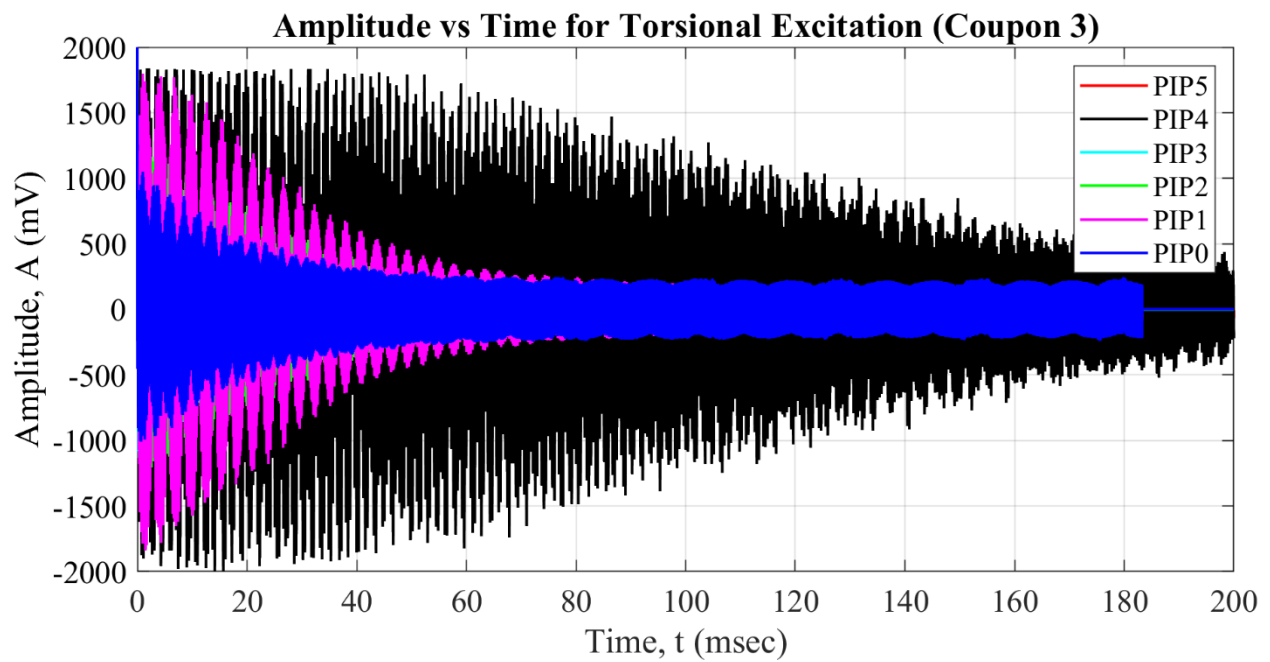
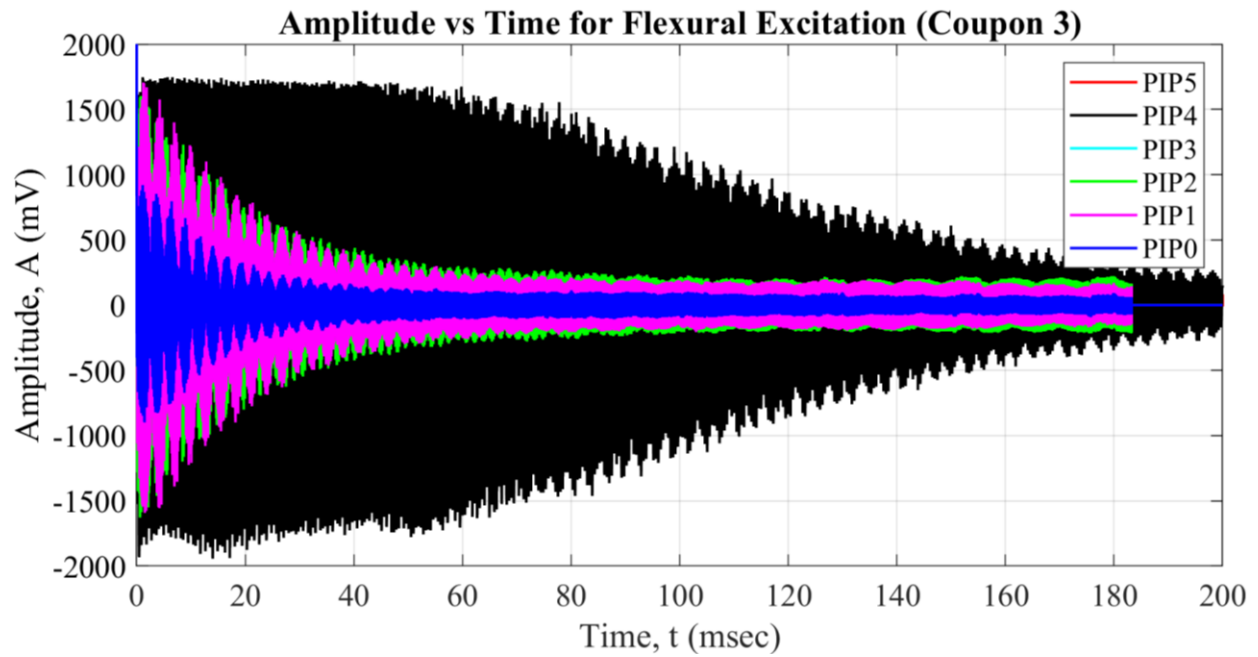


Figure C.2 Amplitude versus time for C/C composite coupons 3.

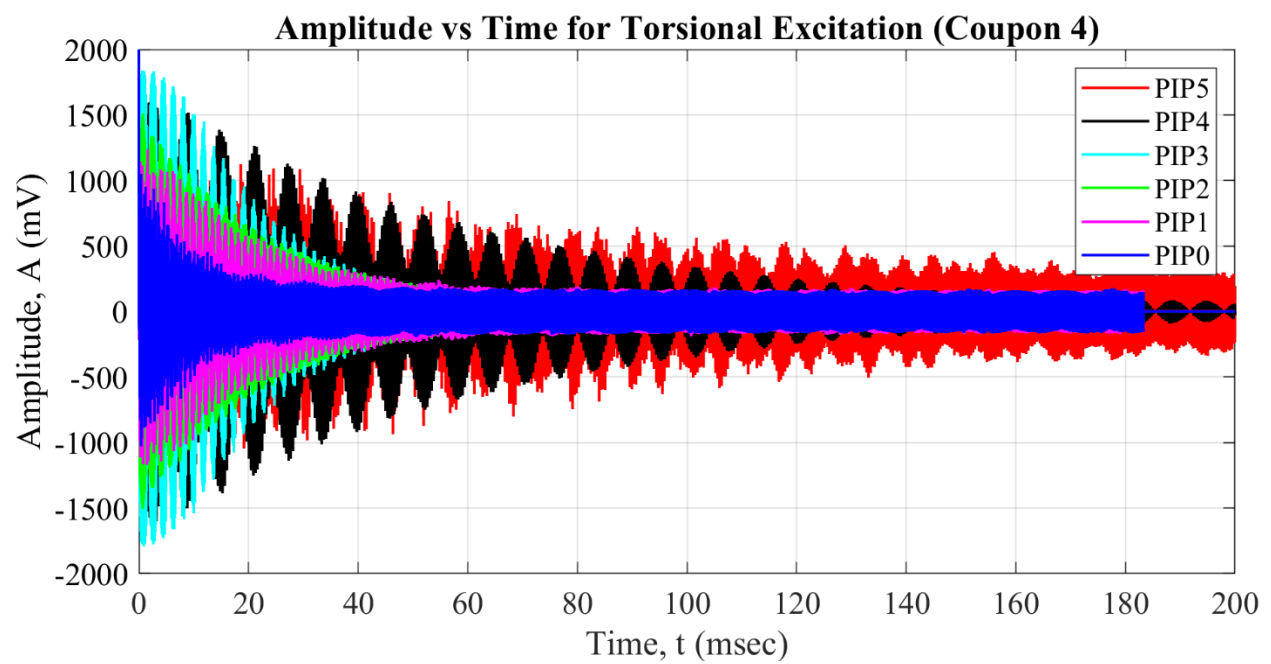


Figure C.3 Amplitude versus time for C/C composite coupons 4.

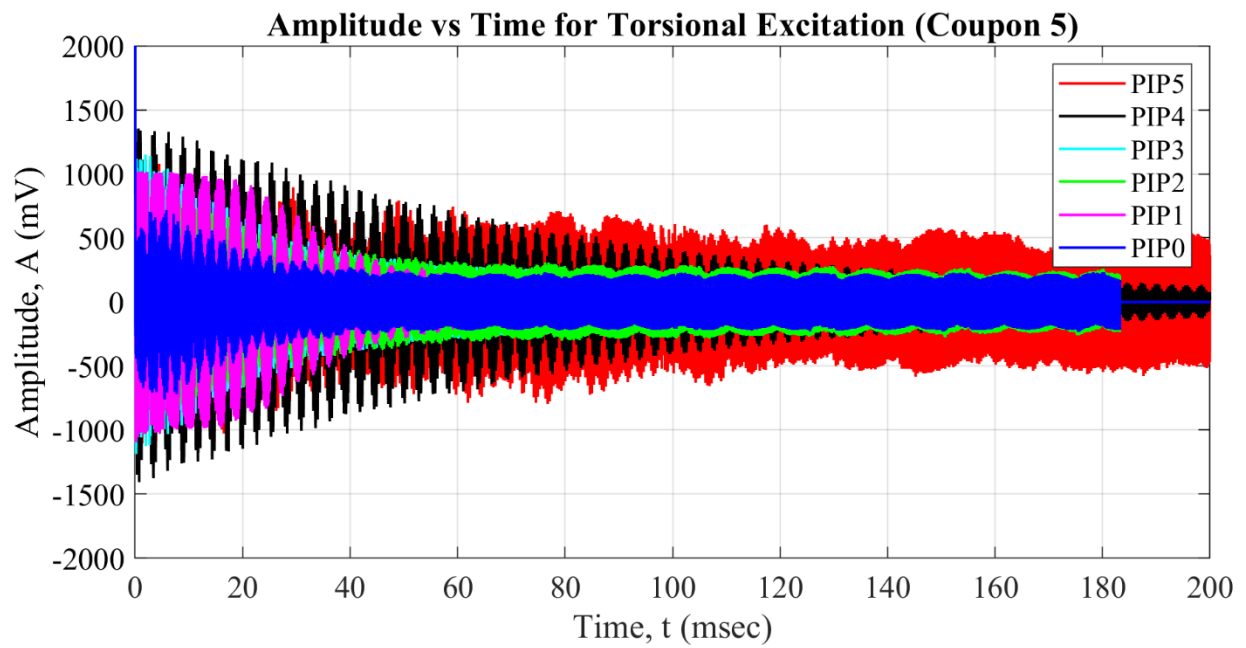
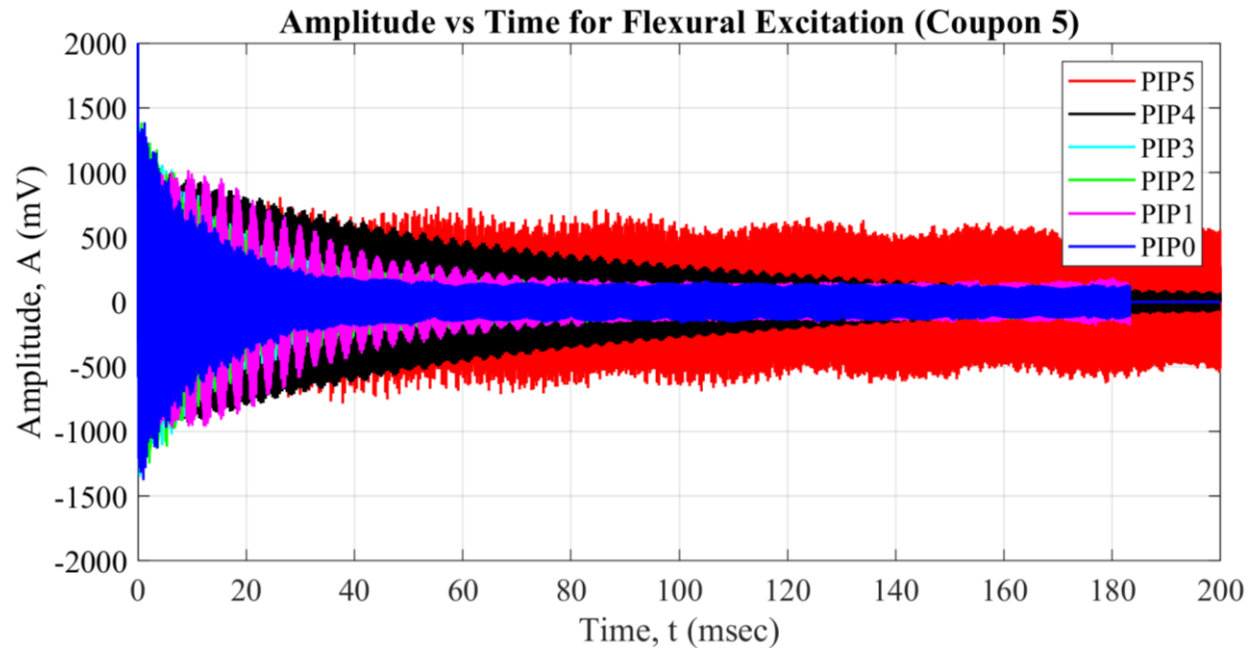


Figure C.4 Amplitude versus time for C/C composite coupons 5.

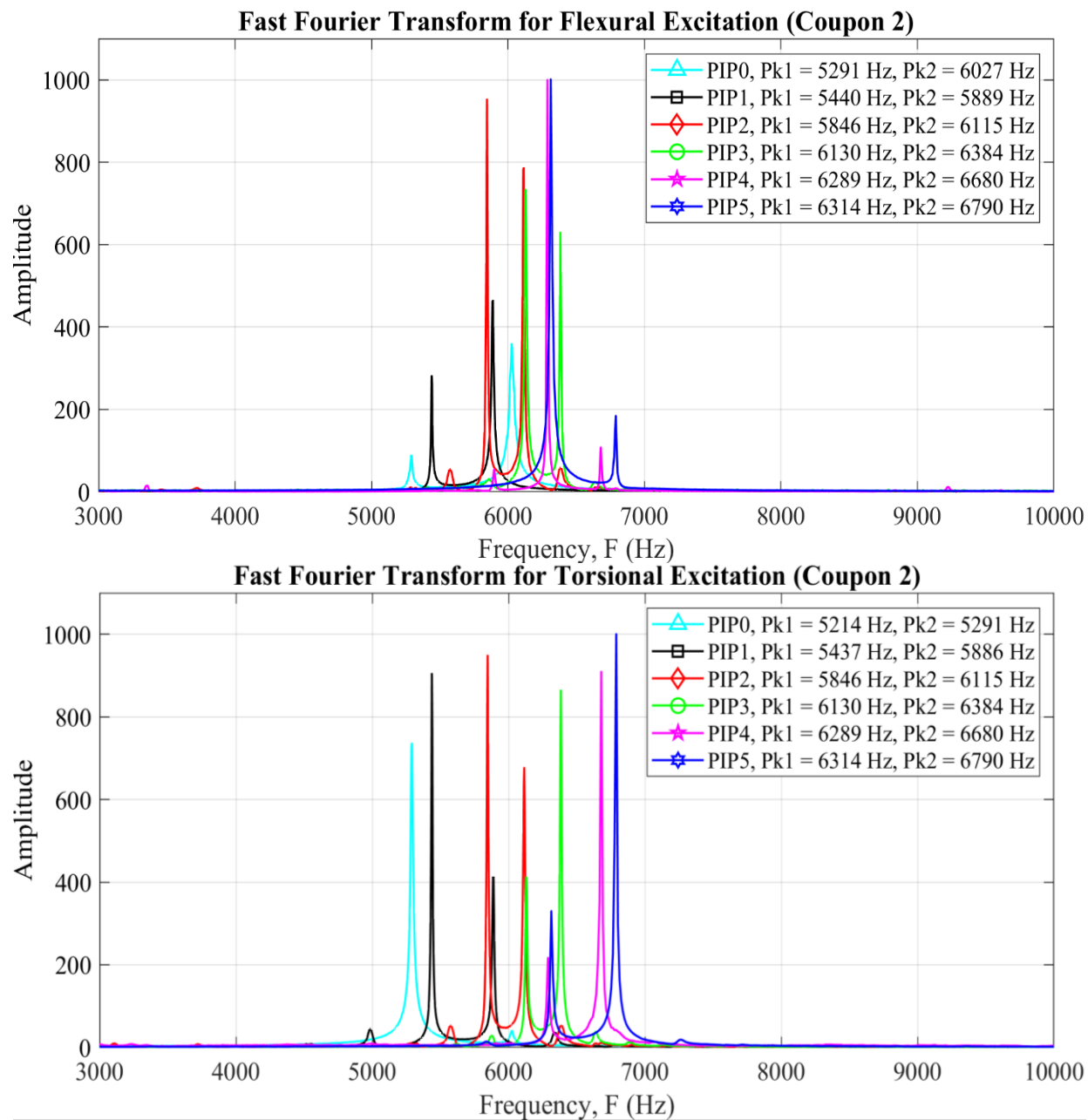


Figure C.5 Fast Fourier transform for C/C composite coupon 2.

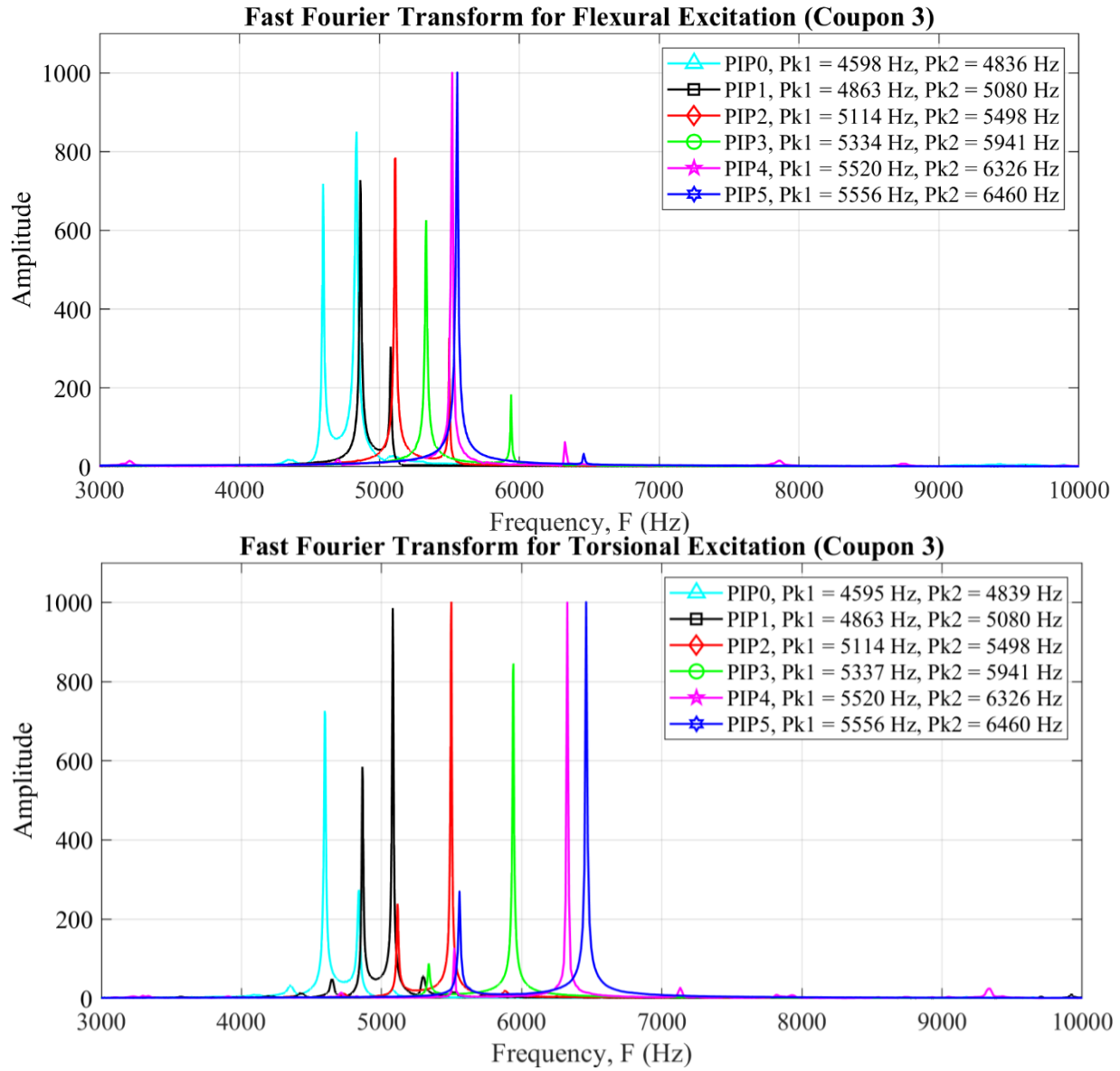


Figure C.6 Fast Fourier transform for C/C composite coupon 3.

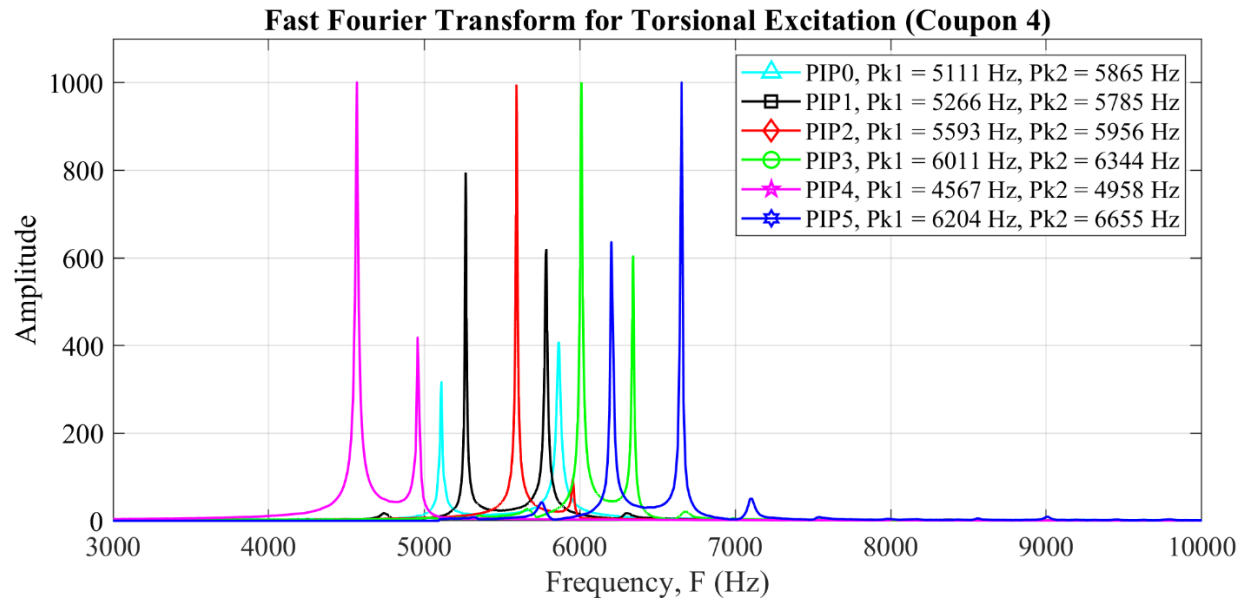


Figure C.7 Fast Fourier transform for C/C composite coupon 4.

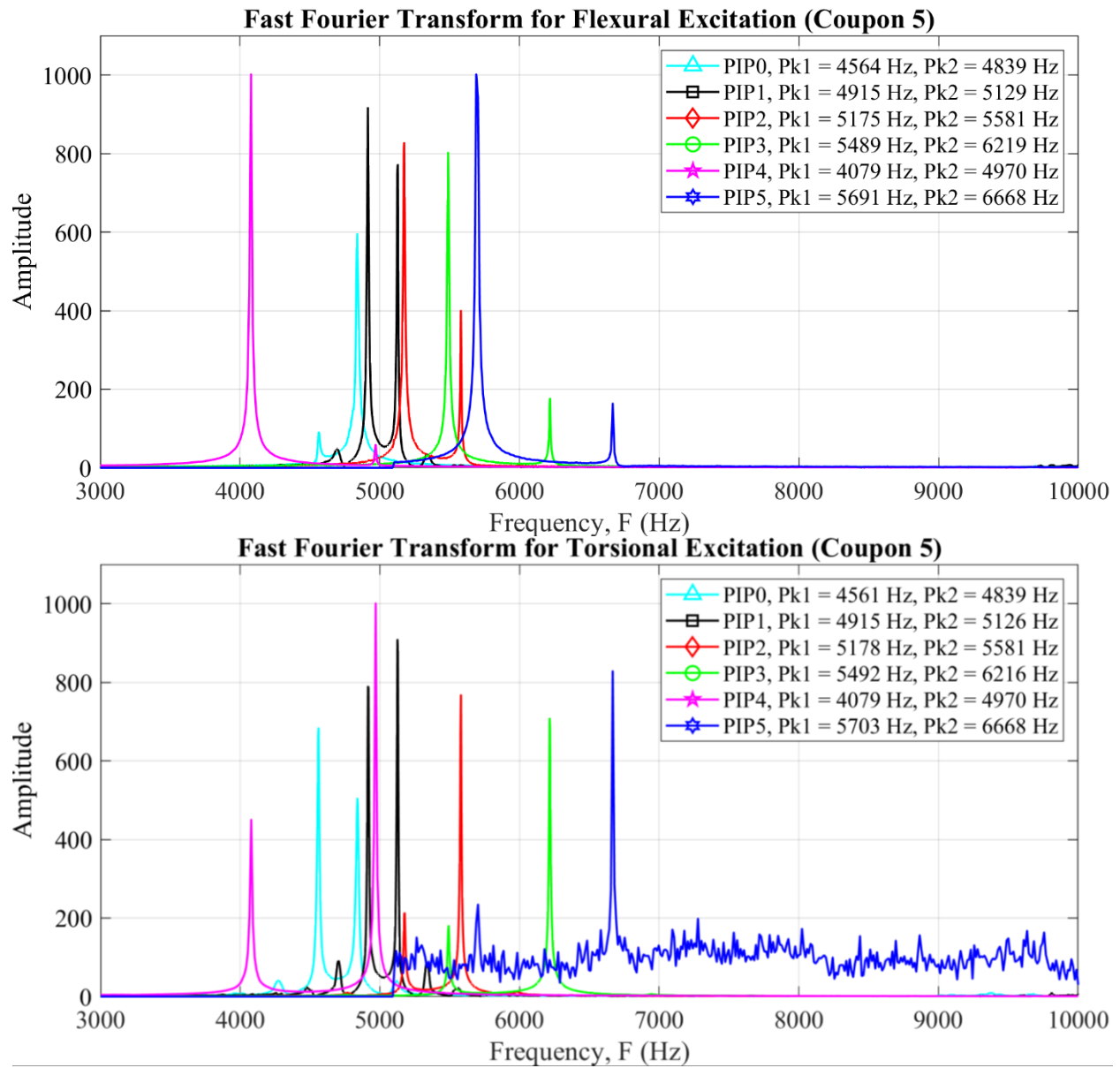


Figure C 8 Fast Fourier transform for C/C composite coupon 5.

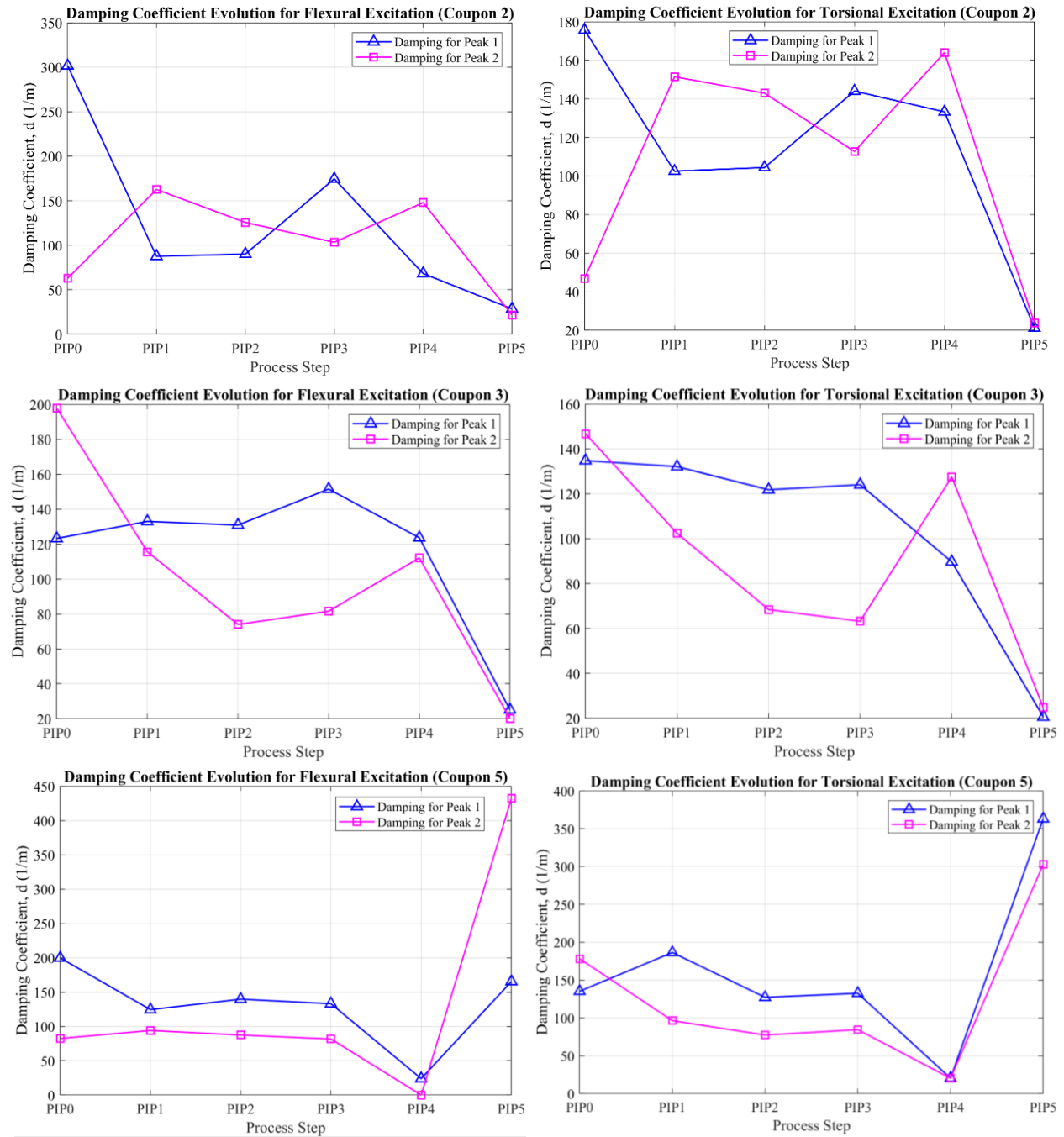


Figure C.9 Damping coefficient evolutions for the first two harmonic frequency peaks in the FFT graphs for C/C composite coupon 2, 3, and 5.

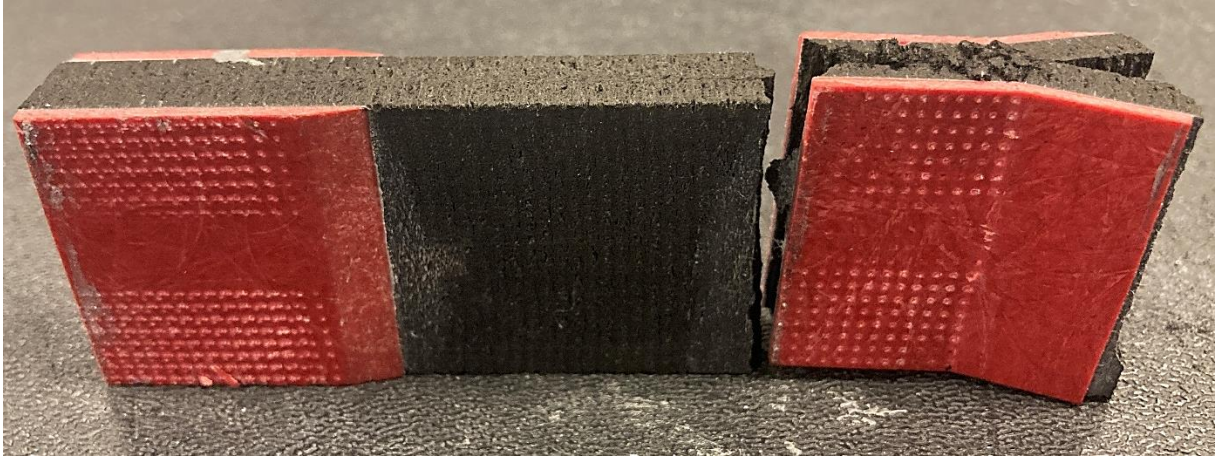


Figure C.10 Damage to the alignment coupon when a lateral grip pressure of 2757.90 *kPa* (400 *psi*) and 3447.38 *kPa* (500 *psi*) were used on the left side and right side, respectively.

Table C.2 Transverse isotropy convention used in this study for PyC (left) vs. the transverse isotropy convention used by Gebert et. al [130] (right).

Constant (<i>GPa</i>)	PyC	Constant (<i>GPa</i>)	PyC [130]
C_{22}	40	C_{11}	40
C_{23}	20	C_{12}	20
C_{12}	13.1	C_{13}	13.1
C_{11}	18.2	C_{33}	18.2
E_1	27.1	E_1	27.1
E_2	12.8	E_3	12.8

$$C = \begin{bmatrix} C_{11} & C_{12} & C_{12} & 0 & 0 & 0 \\ C_{12} & C_{22} & C_{23} & 0 & 0 & 0 \\ C_{12} & C_{23} & C_{22} & 0 & 0 & 0 \\ 0 & 0 & 0 & C_{44} & 0 & 0 \\ 0 & 0 & 0 & 0 & C_{66} & 0 \\ 0 & 0 & 0 & 0 & 0 & C_{66} \end{bmatrix}$$

$$\text{where } C_{44} = \frac{1}{2}(C_{22} - C_{23})$$

$$C = \begin{bmatrix} C_{11} & C_{12} & C_{13} & 0 & 0 & 0 \\ C_{12} & C_{11} & C_{13} & 0 & 0 & 0 \\ C_{13} & C_{13} & C_{33} & 0 & 0 & 0 \\ 0 & 0 & 0 & C_{44} & 0 & 0 \\ 0 & 0 & 0 & 0 & C_{44} & 0 \\ 0 & 0 & 0 & 0 & 0 & C_{66} \end{bmatrix}$$

$$\text{where } C_{66} = \frac{1}{2}(C_{11} - C_{12})$$

Table C.3 Script developed in Mathematica® 13 to calculate the engineering constants for transversely isotropic pyrolytic carbon (PyC) elastic constants reported by Gebert et. al [130]. Values entered with units of *MPa*.

```

ClearAll[E1,E2,v12,v23, G23,v23PyC,v23PyC,G23PyC]

S0 = {{1/E1, -v12/E1, -v12/E1,0,0,0},{-v12/E1,1/E2,-v23/E2,0,0,0},{-v12/E1,-
v23/E2,1/E2,0,0,0},{0,0,0,2*(1+v23)/E2,0,0},{0,0,0,0,1/G12,0},{0,0,0,0,0,1/G12}};
C0 = FullSimplify[Inverse[S0]];

PyC = {E1->12800, E2->27100 };
CPyC = FullSimplify[C0/.PyC];

G23PyC = 10000;

v23PyC = N[Solve[CPyC[[4,4]]==G23PyC, v23]]
nuPyC = {v23->0.355};
v12PyC = N[Solve[(CPyC[[2,2]]/.nuPyC)==40000,v12]]

{{v23->0.355}}
{{v12->-0.213677},{v12->0.213677}}

ClearAll[E1,E2,v12,v23, E2PyG,v12PyG,v23PyG,G23PyG]

PyG = {E1->36500,E2->1020000};
CPyG = FullSimplify[C0/.PyG];

G23PyG = 440000;

v23PyG = N[Solve[CPyG[[4,4]]==G23PyG,v23]]
nuPyG = {v23->0.159};
v12PyG = N[Solve[(CPyG[[1,2]]/.nuPyG)==15000,v12]]

{{v23->0.159091}}
{{v12->-1.22891},{v12->0.0122444}}

```

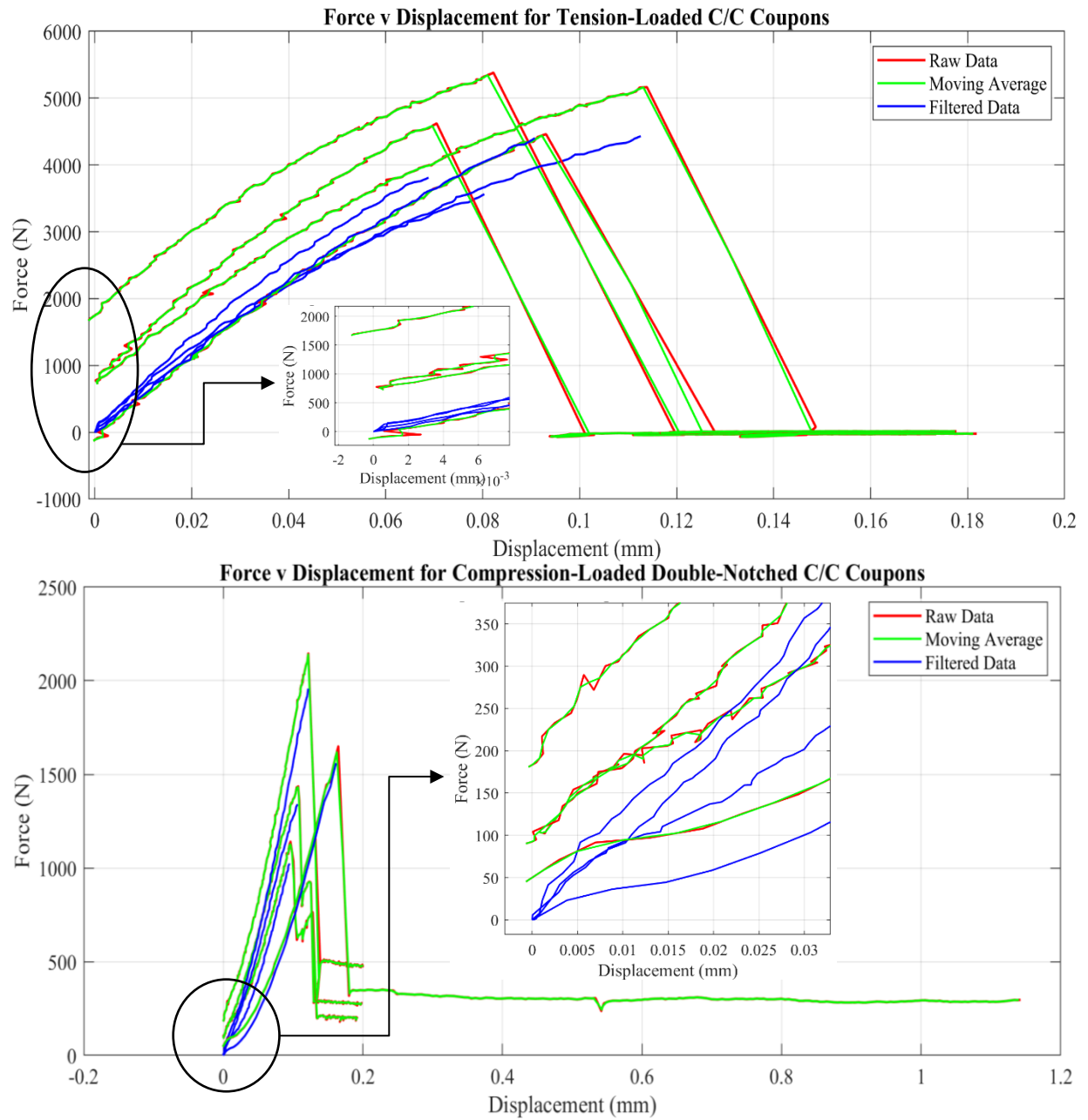


Figure C.11 Raw load vs displacement data, moving average with a window size of 2 used to reduce noise, and the filter used to concatenate only ever-increasing values up to the maximum load value and reset the origin.

Table C.4 Script developed in MATLAB 2021a to produce the results in Figure C.11 and the stress vs strain curves in section 3.3.2. Note: the stress strain curves in section 3.3.2 were obtained using a window size of 1.

```

clc;close all;clear all;

%% Read Data
%Initialize
C_Matrix = cell(1,4); %raw compression data
T_Matrix = cell(1,4); %raw tension data
C_displ = cell(1,4); %averaged compression displacement data
C_Load = cell(1,4); %averaged compression load data
T_displ = cell(1,4); %averaged tension displacement data
T_Load = cell(1,4); %averaged tension load data

%%%%% Column 1 = Displacement (mm)
%%%%% Column 2 = Force (N)
%%%%% Column 4 = strain (mm/mm)
for i = 1:4 %4 bc theres 4 C/C coupons
C_Matrix{i} = readmatrix(sprintf('C13-%d.xlsx',i));
T_Matrix{i} = readmatrix(sprintf('T13-%d.xlsx',i));
end

%% Process Data
%Finds moving average of load & displacement data.
%A small window size (=) was used because there
%wasn't too much noise

WS = 1; %window size

for i = 1:4
    C_displ{i} = movmean(-C_Matrix{i}(:,1),WS); % [mm]
    C_Load{i} = movmean(-C_Matrix{i}(:,2),WS); % [N]
    T_displ{i} = movmean(T_Matrix{i}(:,1),WS); % [mm]
    T_Load{i} = movmean(T_Matrix{i}(:,2),WS); % [N]
end

%Filters through moving average so that
%load and displacement data are ever-increasing

%Initialize. "F" represents filtered data
for k = 1:4
C_LoadF{k} = zeros(length(C_Load{k}),1);
C_displF{k} = zeros(length(C_displ{k}),1);
T_LoadF{k} = zeros(length(T_Load{k}),1);
T_displF{k} = zeros(length(T_displ{k}),1);
end

i = 1;
j = 1;

%while loops add only ever-increasing value to new vectors
for k = 1:4 %for each notched coupon dataset
    while i <= length(C_Load{k})-1
        if C_LoadF{k}(j,1) <= C_Load{k}(i+1,1) && C_displF{k}(j,1) <=
C_displ{k}(i+1,1)
            C_LoadF{k}(j+1,1) = C_Load{k}(i+1,1);
            C_displF{k}(j+1,1) = C_displ{k}(i+1,1);
            i = i+1;
            j = j+1;
        else

```



```

        i=i+1;
    end
end
i = 1;
j = 1;
end
for k = 1:4 %for each tensile coupon dataset
    while i<=length(T_Load{k})-1
        if T_LoadF{k}(j,1) <= T_Load{k}(i+1,1) && T_displF{k}(j,1) <=
T_displ{k}(i+1,1)
            T_LoadF{k}(j+1,1) = T_Load{k}(i+1,1);
            T_displF{k}(j+1,1) = T_displ{k}(i+1,1);
            i = i+1;
            j = j+1;
        else
            i=i+1;
        end
    end
    i = 1;
    j = 1;
end

for k = 1:4 %removes remaining zeros from initialization
C_LoadF{k} = nonzeros(C_LoadF{k}(2:end,1));
C_displF{k} = nonzeros(C_displF{k}(2:end,1));
T_LoadF{k} = nonzeros(T_LoadF{k}(2:end,1));
T_displF{k} = nonzeros(T_displF{k}(2:end,1));
end

%Offset Along X-Axis
for i = 1:4
    if C_displF{i}(1,1) < 0 %shifts data right to x = 0
        C_displF{i}(:,1) = C_displF{i}(:,1) + C_displF{i}(1,1);
    elseif C_displF{i}(1,1) > 0 %shifts data left to x = 0
        C_displF{i}(:,1) = C_displF{i}(:,1) - C_displF{i}(1,1);
    end
    if T_displF{i}(1,1) < 0 %shifts data right to x = 0
        T_displF{i}(:,1) = T_displF{i}(:,1) + T_displF{i}(1,1);
    elseif T_displF{i}(1,1) > 0 %shifts data left to x = 0
        T_displF{i}(:,1) = T_displF{i}(:,1) - T_displF{i}(1,1);
    end
end

%Offset Along Y-Axis
for i = 1:4
    if C_LoadF{i}(1,1) < 0 %shifts data up to y = 0
        C_LoadF{i}(:,1) = C_LoadF{i}(:,1) + C_LoadF{i}(1,1);
    elseif C_LoadF{i}(1,1) > 0 %shifts data down to y = 0
        C_LoadF{i}(:,1) = C_LoadF{i}(:,1) - C_LoadF{i}(1,1);
    end
    if T_LoadF{i}(1,1) < 0 %shifts data up to y = 0
        T_LoadF{i}(:,1) = T_LoadF{i}(:,1) + T_LoadF{i}(1,1);
    elseif T_LoadF{i}(1,1) > 0 %shifts data down to y = 0
        T_LoadF{i}(:,1) = T_LoadF{i}(:,1) - T_LoadF{i}(1,1);
    end
end

for k = 1:4 %removes remaining zeros from initialization
b{k}= find(abs(C_LoadF{k}-50) < 5);
C_LoadF2{k} = C_LoadF{k}(b{k}:end,1)- C_LoadF{k}(b{k},1);
C_displF2{k} = C_displF{k}(b{k}:end,1)- C_displF{k}(b{k},1);

```

```

end

for i = 1:4
    figure(1)
    plot(-C_Matrix{i}(:,1),-C_Matrix{i}(:,2), 'r','LineWidth',1.4);
    hold on; grid on;
    plot(C_displ{i},C_Load{i}, 'g','LineWidth',1.2);
    hold on;
    plot(C_displF{i},C_LoadF{i}, 'b','LineWidth',1.2);
    hold on;
    title('Force v Displacement for Compression-Loaded Double-Notched C/C Coupons');
    xlabel('Displacement (mm)'); ylabel('Force (N)');
    set(gca,'FontSize',12,'FontName','Times');

    figure(2)
    plot(T_Matrix{i}(:,1),T_Matrix{i}(:,2), 'r','LineWidth',1.4);
    hold on; grid on;
    plot(T_displ{i},T_Load{i}, 'g','LineWidth',1.2);
    hold on;
    plot(T_displF{i},T_LoadF{i}, 'b','LineWidth',1.2);
    hold on;
    title('Force v Displacement for Tension-Loaded C/C Coupons');
    xlabel('Displacement (mm)'); ylabel('Force (N)');
    set(gca,'FontSize',12,'FontName','Times');
end

for i = 1:2
    figure(i)
    legend('Raw Data','Moving Average','Filtered Data');
end

%% Cross-sectional areas and lengths (row for each coupon)
C_Area = [127.7367; 128.4662; 128.7372; 121.4014]; %[mm^2], Compressive
C_Length = [79.5266; 79.53; 79.54; 79.13]; %[mm], Compressive
T_Area = [322.423; 322.4078; 321.1272; 318.8089]; %[mm^2], Tensile
T_Length = [101.1666; 101.133; 100.64; 101.2633]; %[mm], Tensile

%% Stress and Strain
for k = 1:4
    C_eps{k} = C_displF2{k}./C_Length(k); %eps = strain
    C_sig{k} = C_LoadF2{k}./C_Area(k); %sig = stress
    T_eps{k} = T_displF{k}./T_Length(k);
    T_sig{k} = T_LoadF{k}./T_Area(k);
end

%% Fracture Load, Ultimate Stress, Young's Modulus, Shear Modulus

for k = 1:4
    C_Pf{k} = max(C_LoadF2{k}); %[N], fracture loads from compression tests
    C_Pf_d{k} = C_displF2{k}(find(C_LoadF2{k} == C_Pf{k},1)); %[mm], displ at fracture
    T_Pf{k} = max(T_LoadF{k}); %[N], fracture loads from tension tests
    T_Pf_d{k} = T_displF{k}(find(T_LoadF{k} == T_Pf{k},1)); %[mm], displ at fracture
    C_eps_ult{k} = max(C_eps{k}); %ultimate strain
    C_sig_ult{k} = max(C_sig{k}); %[MPa], ultimate stress
    T_eps_ult{k} = max(T_eps{k});
    T_sig_ult{k} = max(T_sig{k});

    b_c = find(abs(C_eps{k}-0.2e-3) < 0.00003,1); %end of linear regime
    p = polyfit(C_eps{k}(1:b_c,1),C_sig{k}(1:b_c,1),1); %best fit
    line %Generates the linear
    equation of best fit for the data
end

```

```

f = polyval(p,C_eps{k}(1:b_c,1));
C_eps_y{k} = C_eps{k}(b_c,1); %engineering strain for compression data
C_sig_y{k} = C_sig{k}(b_c,1); %engineering stress for compression data
G13{k} = p(1)/1e3; %G13 from double-notched shear tests

b_t = find(abs(T_eps{k}-0.2e-3) < 0.00001,1); %end of linear regime
q = polyfit(T_eps{k}(1:b_t,1),T_sig{k}(1:b_t,1),1); %best fit
line %Generates the linear
equation of best fit for the data
r = polyval(q,T_eps{k}(1:b_t,1));
T_eps_y{k} = T_eps{k}(b_t,1); %engineering strain for tensile data
T_sig_y{k} = T_sig{k}(b_t,1); %engineering stress for tensile data
E1{k} = q(1)/1e3; %E1 from tensile tests
end

%% Average Values
for k = 1:4
    C_eps_y_1(k) = C_eps_y{k};
    C_sig_y_1(k) = C_sig_y{k};
    T_eps_y_1(k) = T_eps_y{k};
    T_sig_y_1(k) = T_sig_y{k};
    C_eps_ult_1(k) = C_eps_ult{k};
    C_sig_ult_1(k) = C_sig_ult{k};
    T_eps_ult_1(k) = T_eps_ult{k};
    T_sig_ult_1(k) = T_sig_ult{k};
    G13_1(k) = G13{k};
    E1_1(k) = E1{k};
end

C_eps_y_avg = mean(C_eps_y_1);
C_sig_y_avg = mean(C_sig_y_1);
T_eps_y_avg = mean(T_eps_y_1);
T_sig_y_avg = mean(T_sig_y_1);
C_eps_ult_avg = mean(C_eps_ult_1);
C_sig_ult_avg = mean(C_sig_ult_1);
T_eps_ult_avg = mean(T_eps_ult_1);
T_sig_ult_avg = mean(T_sig_ult_1);
G13_avg = mean(G13_1);
E1_avg = mean(E1_1);

%% Plotting
C = {'b','r','g','k','m','b','g'};
M = {'^','s','d','o','p','h','*'};
LS = {'-','--',':','-.','-','-.','-.','.'};

%% Compression-loaded Double-Notched C/C Coupons
for i = 1:4
    figure (3) % Force v displ curve
    plot(C_displF2{i},C_LoadF2{i},...
        'Color',C{i}, 'Marker',M{i}, 'Markersize',8,...
        'MarkerIndices',1:5:length(C_displF2{i}), 'LineStyle',LS{i}, 'LineWidth',1);
    title('Force vs Displacement Curves for Compression Loaded Double-Notched C/C
Coupons');
    xlabel('Displacement, \Delta L (mm)');
    ylabel('Force, P (N)');
    xticks(0:0.01:0.15);
    yticks(0:250:2000);
    set(gca, 'FontSize',12, 'FontName', 'Times');
    grid on; hold on;
end

```

```

for i = 1:4
figure (4) % Stress v strain curve
plot(C_eps{i},C_sig{i},...
      'Color',C{i},'Marker',M{i},'Markersize',8,...
      'MarkerIndices',1:5:length(C_eps{i}),'LineStyle',LS{i},'LineWidth',1);
title('Stress vs Strain Curves for Compression Loaded Double-Notched C/C Coupons');
xlabel('Strain,  $\epsilon$  (mm/mm)','Interpreter','latex');
ylabel('Stress,  $\sigma$  (MPa)');
yticks(0:2:16);
set(gca,'FontSize',12,'FontName','Times');
grid on; hold on;
end

%% C/C Tensile Coupons
for i = 1:4
figure (5) % Force v displ curve
plot(T_displF{i},T_LoadF{i},...
      'Color',C{i},'Marker',M{i},'Markersize',8,...
      'MarkerIndices',1:5:length(T_displF{i}),'LineStyle',LS{i},'LineWidth',1);
title('Force vs Displacement Curves for Tension-Loaded C/C Coupons');
xlabel('Displacement,  $\Delta L$  (mm)');
ylabel('Force, P (N)');
xticks(0:0.01:0.12);
set(gca,'FontSize',12,'FontName','Times');
grid on; hold on;
end

for i = 1:4
figure (6) % Stress v strain curve
plot(T_eps{i},T_sig{i},...
      'Color',C{i},'Marker',M{i},'Markersize',8,...
      'MarkerIndices',1:5:length(T_eps{i}),'LineStyle',LS{i},'LineWidth',1);
title('Stress vs Strain Curves for Tension-Loaded C/C Coupons');
xlabel('Strain,  $\epsilon$  (mm/mm)','Interpreter','latex');
ylabel('Stress,  $\sigma$  (MPa)');
set(gca,'FontSize',12,'FontName','Times');
grid on; hold on;
end

for i = 1:4 %creating legends for the plots
C_Leg_fd{i} = sprintf('Coupon %d, P_f = %0.2f N',i,C_Pf{i});
T_Leg_fd{i} = sprintf('Coupon %d, P_f = %0.2f N',i,T_Pf{i});
C_Leg_se{i} = sprintf('Coupon %d,  $\sigma_S$  = %0.2f MPa',i,C_sig_ult{i});
T_Leg_se{i} = sprintf('Coupon %d,  $\sigma_T$  = %0.2f MPa',i,T_sig_ult{i});
end

figure(3)
legend(C_Leg_fd);

figure(4)
legend(C_Leg_se);

figure(5)
legend(T_Leg_fd);

figure(6)
legend(T_Leg_se);

```

Table C.5 Script developed in MATLAB script used to plot the Mori-Tanaka model results for the 4 different test cases in Table 3.6.

```

clc; clear all; close all;

TC = 4; %# test cases
for zz = 1:TC
    Input1 = 'Digimat-MF Ortho Eng Constants';
    Input2 = sprintf('TestCase%d',zz);

    PIPcycles = [0 1 2 3 4 5 6 7 8 9 10 11];
    PIPcycles1 = [0 1 2 3 4 5 6];
    PIPcyclesaxis = {'GS', 'PIP0', 'PIP1', 'PIP2', 'PIP3', 'PIP4', 'PIP5'};

    %Pore volume fraction evolution of coupons 1-5 (columns)
    %for PIP cycles 0-5 (rows) [calculated with script in Table B.1]
    Vp = [0.00000 0.00000 0.00000 0.00000 0.00000;...
          59.8726 59.6378 58.2244 59.4113 58.5224;...
          46.1368 47.4248 47.4544 47.0632 45.0970;...
          42.3941 43.8277 41.6634 43.4734 39.9761;...
          38.1033 40.6304 37.1347 40.9232 35.2615;...
          36.4277 38.2323 35.1623 39.8349 33.8147;...
          35.8639 37.6328 34.7520 39.2827 33.0506];

    for k = 1:7
        Vp_avg(1,k) = mean(Vp(k,:)); %[vol.%], average pore volume fraction
    end

    %For error bars in plots
    for k = 1:7
        Vp_min(1,k) = Vp_avg(1,k) - min(Vp(k,:));
        Vp_max(1,k) = max(Vp(k,:)) - Vp_avg(1,k);
    end

    %% 50CF-PPS Constants
    Data_50CFPPS = xlsread(Input1,Input2,'B5:B16');
    E1_50CFPPS = Data_50CFPPS(1,1); %[MPa]
    E2_50CFPPS = Data_50CFPPS(2,1); %[MPa]
    E3_50CFPPS = Data_50CFPPS(3,1); %[MPa]
    v12_50CFPPS = Data_50CFPPS(4,1);
    v21_50CFPPS = Data_50CFPPS(5,1);
    v13_50CFPPS = Data_50CFPPS(6,1);
    v31_50CFPPS = Data_50CFPPS(7,1);
    v23_50CFPPS = Data_50CFPPS(8,1);
    v32_50CFPPS = Data_50CFPPS(9,1);
    G12_50CFPPS = Data_50CFPPS(10,1); %[MPa]
    G23_50CFPPS = Data_50CFPPS(11,1); %[MPa]
    G13_50CFPPS = Data_50CFPPS(12,1); %[MPa]

    %% C/C Constants
    Data_CC = xlsread(Input1,Input2,'C5:N16'); %constants

    %C/PyC Constants
    E1_PyC = Data_CC(1,1:2:end-1); %[MPa]
    E2_PyC = Data_CC(2,1:2:end-1); %[MPa]
    E3_PyC = Data_CC(3,1:2:end-1); %[MPa]
    v12_PyC = Data_CC(4,1:2:end-1);
    v21_PyC = Data_CC(5,1:2:end-1);
    v13_PyC = Data_CC(6,1:2:end-1);
    v31_PyC = Data_CC(7,1:2:end-1);
    v23_PyC = Data_CC(8,1:2:end-1);
    v32_PyC = Data_CC(9,1:2:end-1);

```

```

G12_PyC = Data_CC(10,1:2:end-1); %[MPa]
G23_PyC = Data_CC(11,1:2:end-1); %[MPa]
G13_PyC = Data_CC(12,1:2:end-1); %[MPa]

%C/PyG Constants
E1_PyG = Data_CC(1,2:2:end); %[MPa]
E2_PyG = Data_CC(2,2:2:end); %[MPa]
E3_PyG = Data_CC(3,2:2:end); %[MPa]
v12_PyG = Data_CC(4,2:2:end);
v21_PyG = Data_CC(5,2:2:end);
v13_PyG = Data_CC(6,2:2:end);
v31_PyG = Data_CC(7,2:2:end);
v23_PyG = Data_CC(8,2:2:end);
v32_PyG = Data_CC(9,2:2:end);
G12_PyG = Data_CC(10,2:2:end); %[MPa]
G23_PyG = Data_CC(11,2:2:end); %[MPa]
G13_PyG = Data_CC(12,2:2:end); %[MPa]

%Combining 50CF-PPS and C/C (PyC) and 50CF-PPS C/C (PyG) constants into
%one vector (for plotting purposes)

E1_PyCconst = [E1_50CFPPS E1_PyC];
E2_PyCconst = [E1_50CFPPS E2_PyC];
E3_PyCconst = [E3_50CFPPS E3_PyC];
v12_PyCconst = [v12_50CFPPS v12_PyC];
v21_PyCconst = [v21_50CFPPS v21_PyC];
v13_PyCconst = [v13_50CFPPS v13_PyC];
v31_PyCconst = [v31_50CFPPS v31_PyC];
v23_PyCconst = [v23_50CFPPS v23_PyC];
v32_PyCconst = [v32_50CFPPS v32_PyC];
G12_PyCconst = [G12_50CFPPS G12_PyC]; %[MPa]
G23_PyCconst = [G23_50CFPPS G23_PyC]; %[MPa]
G13_PyCconst = [G13_50CFPPS G13_PyC]; %[MPa]

E1_PyGconst = [E1_50CFPPS E1_PyG];
E2_PyGconst = [E1_50CFPPS E2_PyG];
E3_PyGconst = [E3_50CFPPS E3_PyG];
v12_PyGconst = [v12_50CFPPS v12_PyG];
v21_PyGconst = [v21_50CFPPS v21_PyG];
v13_PyGconst = [v13_50CFPPS v13_PyG];
v31_PyGconst = [v31_50CFPPS v31_PyG];
v23_PyGconst = [v23_50CFPPS v23_PyG];
v32_PyGconst = [v32_50CFPPS v32_PyG];
G12_PyGconst = [G12_50CFPPS G12_PyG]; %[MPa]
G23_PyGconst = [G23_50CFPPS G23_PyG]; %[MPa]
G13_PyGconst = [G13_50CFPPS G13_PyG]; %[MPa]

%% Experimentally Measured Values for C/C (Impulse Excitation)
%6mm thick sample results
% E1 = [27.26, 29.25]; %[GPa]
% G23 = [2.88 3.64]; %[GPa]

%11mm thick sample results
%Matrix of Flexural Values. Rows represent green state,
%PIP0, PIP1,... , PIP5 while column values represent
%samples 1-5
E1 = [22.50 22.50 22.50 22.50 22.50;...
      20.00 20.41 13.80 18.30 14.80;...
      21.68 21.49 17.75 21.62 18.83;...
      27.04 26.44 21.68 25.99 22.75;...
      32.39 30.67 25.37 31.30 27.57;...
      34.91 32.78 27.24 32.88 29.48;...
      35.39 33.36 27.79 33.46 29.88]; %[GPa]

```

```

G23 = [3.040 3.040 3.040 3.040 3.040;...
       2.480 2.480 2.480 2.480 2.360;...
       3.272 3.270 2.667 3.215 2.678;...
       4.101 4.030 3.414 3.865 3.546;...
       4.897 4.677 4.734 4.658 4.442;...
       6.244 5.645 5.406 4.893 5.883;...
       6.467 5.887 5.678 5.737 6.110]; %[GPa]

for k = 1:7
    E1_avg(1,k) = mean(E1(k,:)); %[GPa]
    G23_avg(1,k) = mean(G23(k,:)); %[GPa]
end

%For error bars in plots
for k = 1:7
    E1_min(1,k) = E1_avg(1,k) - min(E1(k,:)); %lower bound
    E1_max(1,k) = max(E1(k,:)) - E1_avg(1,k); %upper bound
    G23_min(1,k) = G23_avg(1,k) - min(G23(k,:)); %lower bound
    G23_max(1,k) = max(G23(k,:)) - G23_avg(1,k); %upper bound
end

E3 = [5.186]; %[GPa] (green state or 50CF-PPS)
G12 = [2.79]; %[GPa] (green state or 50CF-PPS)

G13_avg = 4.41; %[GPa], C/C Post PIP5 from double-notched shear tests
G13_min = G13_avg - 3.01; %[GPa], from double-notched shear tests
G13_max = 6.04 - G13_avg; %[GPa], from double-notched shear tests

%% Measuring Total Error Between Predictions and Experimental Result
for i = 1:6
    Err_E1(zz,1) = sum(abs(E1_avg(1,:) - E1_PyCconst(1,:)./1e3));
    Err_G23(zz,1) = sum(abs(G23_avg(1,:) - G23_PyCconst(1,:)./1e3));
end

%% Plotting
%Standardize color (C), marker (M), and linestyle (LS)
C = {'m','b','g','c','k','b','r'};
M = {'^','s','d','o','p','h','*'};
LS = {'--','-',':','-.','-','--','-.',':'};
MS = 8; %marker size
LWS = 1.2; %linewidth size

%% E1 Evolution Results from Impulse Testing
figure(1)
for n = 1:5
    plot(PIPCycles1,E1(:,n),'Color',C{6},'Marker',M{n},'Markersize',8,'LineStyle',LS{n},
        'LineWidth',0.8);
    grid on; hold on;
    xlabel('Process Step');
    xticks(PIPCycles);
    xticklabels(PIPCyclesaxis);
    ylabel('E_1 (GPa)');
    title('Impulse Excitation Evolution of E_1 in C/C Composite Coupons');
    set(gca,'ycolor','k');
    set(gca,'FontSize',12,'FontName','Times');
end
plot(PIPCycles1,E1_avg,'Color',C{3},'Marker',M{7},'Markersize',8,'LineStyle',LS{1},
    'LineWidth',0.8);
grid on; hold on;
legend('Coupon 1','Coupon 2','Coupon 3','Coupon 4','Coupon 5','Average');

```

```

%% G23 Evolution Results from Impulse Testing
figure(2)
for n = 1:5
plot(PIPCycles1,G23(:,n),'Color',C{6},'Marker',M{n},'Markersize',8,'LineStyle',LS{n}
),'LineWidth',0.8);
grid on; hold on;
xlabel('Process Step');
xticks(PIPCycles);
xticklabels(PIPCyclesaxis);
ylabel('G_2_3 (GPa)');
title('Impulse Excitation Evolution of G_2_3 in C/C Composite Coupons');
set(gca,'ycolor','k');
set(gca,'FontSize',12,'FontName','Times');
end
plot(PIPCycles1,G23_avg,'Color',C{3},'Marker',M{7},'Markersize',8,'LineStyle',LS{1},
'LineWidth',0.8);
grid on; hold on;
legend('Coupon 1','Coupon 2','Coupon 3','Coupon 4','Coupon 5','Average');

%% E1 Evolution with Digimat-MF Prediction
figure(3)
yyaxis left
plot(PIPCycles1,E1_PyCconst./1e3,'Color',C{zz},'Marker',M{zz},'Markersize',MS,'LineS
tyle',LS{zz},'LineWidth',LWS);
grid on;hold on;
%
plot(PIPCycles1,E1_PyGconst./1e3,'Color',C{4},'Marker',M{6},'Markersize',MS,'LineSty
le',LS{3},'LineWidth',LWS);
ylabel('E_1 (GPa)');
title('E_1 Evolution with 1^s^t Order Mori-Tanaka Digimat-MF Predictions');

%% G23 Evolution with Digimat-MF Prediction
figure(4)
yyaxis left
plot(PIPCycles1,G23_PyCconst./1e3,'Color',C{zz},'Marker',M{zz},'Markersize',MS,'Line
Style',LS{zz},'LineWidth',LWS);
grid on; hold on;
%
plot(PIPCycles1,G23_PyGconst./1e3,'Color',C{4},'Marker',M{6},'Markersize',MS,'LineSt
yle',LS{3},'LineWidth',LWS);
ylabel('G_2_3 (GPa)');
title('G_2_3 Evolution with 1^s^t Order Mori-Tanaka Digimat-MF Predictions');

%% Digimat-MF Prediction of E2 Evolution
figure(5)
yyaxis left
plot(PIPCycles1,E2_PyCconst./1e3,'Color',C{zz},'Marker',M{zz},'Markersize',MS,'LineS
tyle',LS{zz},'LineWidth',LWS);
grid on; hold on;
%
plot(PIPCycles1,E2_PyGconst./1e3,'Color',C{4},'Marker',M{6},'Markersize',MS,'LineSty
le',LS{3},'LineWidth',LWS);
ylabel('E_2 (GPa)');
title('1^s^t Order Mori-Tanaka Digimat-MF Predictions of E_2 Evolution');

%% Digimat-MF Prediction of E3 Evolution
figure(6)
yyaxis left
plot(PIPCycles1,E3_PyCconst./1e3,'Color',C{zz},'Marker',M{zz},'Markersize',MS,'LineS
tyle',LS{zz},'LineWidth',LWS);
grid on; hold on;

```



```

%
plot(PIPCycles1,E3_PyGconst./1e3,'Color',C{4},'Marker',M{6},'Markersize',MS,'LineStyle',LS{3},'LineWidth',LWS);
ylabel('E_3 (GPa)');
title('1^s^t Order Mori-Tanaka Digimat-MF Predictions of E_3 Evolution');

%% Digimat-MF Prediction of G13 Evolution
figure(7)
yyaxis left
plot(PIPCycles1,G13_PyCconst./1e3,'Color',C{zz},'Marker',M{zz},'Markersize',MS,'LineStyle',LS{zz},'LineWidth',LWS);
grid on; hold on;
%
plot(PIPCycles1,G13_PyGconst./1e3,'Color',C{4},'Marker',M{6},'Markersize',MS,'LineStyle',LS{3},'LineWidth',LWS);
ylabel('G_1_3 (GPa)');
title('1^s^t Order Mori-Tanaka Digimat-MF Predictions of G_1_3 Evolution');

%% Digimat-MF Prediction of G12 Evolution
figure(8)
yyaxis left
plot(PIPCycles1,G12_PyCconst./1e3,'Color',C{zz},'Marker',M{zz},'Markersize',MS,'LineStyle',LS{zz},'LineWidth',LWS);
grid on; hold on;
%
plot(PIPCycles1,G12_PyGconst./1e3,'Color',C{4},'Marker',M{6},'Markersize',MS,'LineStyle',LS{3},'LineWidth',LWS);
ylabel('G_1_2 (GPa)');
title('1^s^t Order Mori-Tanaka Digimat-MF Predictions of G_1_2 Evolution');

%% Digimat-MF Prediction of v12 Evolution
figure(9)
yyaxis left
plot(PIPCycles1,v12_PyCconst,'Color',C{zz},'Marker',M{zz},'Markersize',MS,'LineStyle',LS{zz},'LineWidth',LWS);
grid on; hold on;
%
plot(PIPCycles1,v12_PyGconst,'Color',C{4},'Marker',M{6},'Markersize',MS,'LineStyle',LS{3},'LineWidth',LWS);
ylabel('{\nu}_1_2');
title('1^s^t Order Mori-Tanaka Digimat-MF Prediction of {\nu}_1_2 Evolution');

%% Digimat-MF Prediction of v21 Evolution
figure(10)
yyaxis left
plot(PIPCycles1,v21_PyCconst,'Color',C{zz},'Marker',M{zz},'Markersize',MS,'LineStyle',LS{zz},'LineWidth',LWS);
grid on; hold on;
%
plot(PIPCycles1,v21_PyGconst,'Color',C{4},'Marker',M{6},'Markersize',MS,'LineStyle',LS{3},'LineWidth',LWS);
ylabel('{\nu}_2_1');
title('1^s^t Order Mori-Tanaka Digimat-MF Predictions of {\nu}_2_1 Evolution');

%% Digimat-MF Prediction of v23 Evolution
figure(11)
yyaxis left
plot(PIPCycles1,v23_PyCconst,'Color',C{zz},'Marker',M{zz},'Markersize',MS,'LineStyle',LS{zz},'LineWidth',LWS);
grid on; hold on;
%
plot(PIPCycles1,v23_PyGconst,'Color',C{4},'Marker',M{6},'Markersize',MS,'LineStyle',LS{3},'LineWidth',LWS);

```

```

ylabel('\nu_2_3');
title('1^s^t Order Mori-Tanaka Digimat-MF Predictions of {\nu}_2_3 Evolution');

%% Digimat-MF Prediction of v32 Evolution
figure(12)
yyaxis left
plot(PIPCycles1,v32_PyCconst,'Color',C{zz},'Marker',M{zz},'Markersize',MS,'LineStyle',
'LS{zz}','LineWidth',LWS);
grid on; hold on;
%
plot(PIPCycles1,v32_PyGconst,'Color',C{4},'Marker',M{6},'Markersize',MS,'LineStyle',
LS{3},'LineWidth',LWS);
ylabel('\nu_3_2');
title('1^s^t Order Mori-Tanaka Digimat-MF Predictions of {\nu}_3_2 Evolution');

%% Digimat-MF Prediction of v13 Evolution
figure(13)
yyaxis left
plot(PIPCycles1,v13_PyCconst,'Color',C{zz},'Marker',M{zz},'Markersize',MS,'LineStyle',
'LS{zz}','LineWidth',LWS);
grid on; hold on;
%
plot(PIPCycles1,v13_PyGconst,'Color',C{4},'Marker',M{6},'Markersize',MS,'LineStyle',
LS{3},'LineWidth',LWS);
ylabel('\nu_1_3');
title('1^s^t Order Mori-Tanaka Digimat-MF Predictions of {\nu}_1_3 Evolution');

%% Digimat-MF Prediction of v31 Evolution
figure(14)
yyaxis left
plot(PIPCycles1,v31_PyCconst,'Color',C{zz},'Marker',M{zz},'Markersize',MS,'LineStyle',
'LS{zz}','LineWidth',LWS);
grid on; hold on;
%
plot(PIPCycles1,v31_PyGconst,'Color',C{4},'Marker',M{6},'Markersize',MS,'LineStyle',
LS{3},'LineWidth',LWS);
ylabel('\nu_3_1');
title('1^s^t Order Mori-Tanaka Digimat-MF Predictions of {\nu}_3_1 Evolution');
end

figure(3)
yyaxis left
errorbar(PIPCycles1,E1_avg,E1_min,E1_max,'Color','r','Marker',M{7},'Markersize',MS,'
LineStyle','-','LineWidth',LWS);

figure(4)
yyaxis left
errorbar(PIPCycles1,G23_avg,G23_min,G23_max,'Color','r','Marker',M{7},'Markersize',M
S,'LineStyle','-','LineWidth',LWS);

%Constructing the legends for plots
Leg = cell(1,TC+2);
Leg2 = cell(1,TC+2);
Leg3 = cell(1,TC+1);
for zz = 1:TC
    Leg{zz} = sprintf('C/C (PyC), Test Case #%d',zz);
    Leg2{zz} = sprintf('C/C (PyC), Test Case #%d',zz);
    Leg3{zz} = sprintf('C/C (PyC), Test Case #%d',zz);
end
Leg{TC+1} = sprintf('Impulse Excitation Evolution');
Leg{TC+2} = sprintf('V_p (%)');
Leg2{TC+1} = sprintf('double-notched Shear Test Value');

```

```

Leg2{TC+2} = sprintf('V_p (%%)');
Leg3{TC+1} = sprintf('V_p (%%)');

for i = 3:14
    figure(i)
    yyaxis left
    xlabel('Process Step');
    xticks(PIPCycles);
    xticklabels(PIPCyclesaxis);
    set(gca,'ycolor','k');
    set(gca,'FontSize',12,'FontName','Times');

    yyaxis right

    errorbar(PIPCycles1,Vp_avg,Vp_min,Vp_max,'Color','k','Marker',M{4},'Markersize',MS,'
LineStyle','-','LineWidth',LWS);
    set(gca,'ycolor','k');
    set(gca,'FontSize',12,'FontName','Times');
    ylabel('V_p (%)');
    ylim([0 60]);yticks(linspace(0,100,11));
    hold on;
end

for i = 3:4
    figure(i)
    legend(Leg);
end

for i = 5:14
    figure(i)
    legend(Leg3);
end

```

Table C.6 Orthotropic engineering constants generated by Digimat-MF for test case 1 in Table 3.6 for the 50 wt. % carbon fiber-reinforced polyphenylene sulfide (50CF-PPS) and C/C composite materials.

Material	50CF-PPS	C/C Composite					
PIP Cycle	--	PIP0	PIP1	PIP2	PIP3	PIP4	PIP5
$\nu_p(\%)$	0	59.13	46.64	42.27	38.41	36.69	36.12
$E_1(MPa)$	24935	18994.435	27495.1883	29876.61	31866.416	32732.153	33016.376
$E_2(MPa)$	8484	7557.4365	12414.1869	14004.818	15408.5579	16038.235	16247.746
$E_3(MPa)$	4890	5011.7777	8983.91879	10350.145	11570.5922	12121.506	12305.269
ν_{12}	0.423	0.351492	0.30780863	0.2944818	0.28335298	0.2785834	0.2770206
ν_{21}	0.144	0.1398504	0.13897682	0.1380399	0.13701136	0.1365014	0.1363251
ν_{13}	0.389	0.2883545	0.26286775	0.2569388	0.25252223	0.2507741	0.2502146
ν_{31}	0.076	0.0760838	0.08589076	0.0890113	0.09169	0.0928677	0.0932555
ν_{23}	0.411	0.3220904	0.3031172	0.2986527	0.29542828	0.2941893	0.293808
ν_{32}	0.237	0.213597	0.21936034	0.2207169	0.22184296	0.2223448	0.2225162
$G_{12}(MPa)$	5057	4282.8387	6834.3357	7666.9478	8405.48037	8737.4399	8847.9915
$G_{23}(MPa)$	2232	2262.9554	3968.0965	4553.3194	5076.65753	5312.9317	5391.7076
$G_{13}(MPa)$	2958	2843.009	4970.42597	5720.4965	6401.22904	6712.3104	6816.168

Table C.7 Orthotropic engineering constants generated by Digimat-MF for test case 2 in Table 3.6 for the 50 wt. % carbon fiber-reinforced polyphenylene sulfide (50CF-PPS) and C/C composite materials.

Material	50CF-PPS	C/C Composite					
PIP Cycle	--	PIP0	PIP1	PIP2	PIP3	PIP4	PIP5
$\nu_p(\%)$	0	59.13	46.64	42.27	38.41	36.69	36.12
$E_1(MPa)$	22326.9106	17189.81	25160.3975	27440.865	29362.5393	30202.356	30478.513
$E_2(MPa)$	9988.0144	8605.1114	13823.2286	15502.674	16977.6404	17637.306	17856.824
$E_3(MPa)$	4920.2913	5028.9163	9014.69395	10384.863	11609.0086	12161.603	12345.984
ν_{12}	0.3919	0.3356998	0.29742106	0.2851929	0.27478345	0.2702718	0.2687839
ν_{21}	0.1753	0.1680492	0.16340438	0.1611193	0.15888185	0.157831	0.1574758
ν_{13}	0.389	0.2887716	0.26458674	0.2590939	0.25507238	0.2535005	0.2529991
ν_{31}	0.0857	0.0844808	0.09479852	0.0980528	0.10084746	0.1020772	0.1024828
ν_{23}	0.4108	0.3187677	0.29829145	0.2935431	0.29011392	0.2887933	0.2883877
ν_{32}	0.2024	0.1862912	0.19452808	0.1966374	0.19837474	0.1991341	0.1993876
$G_{12}(MPa)$	5471.0581	4560.5874	7174.11579	8012.1785	8750.43752	9081.8273	9192.0213
$G_{23}(MPa)$	2336.94	2344.7758	4103.91103	4709.4283	5252.10084	5497.5261	5579.4231
$G_{13}(MPa)$	2876.8699	2777.392	4854.36893	5584.4083	6246.09619	6547.5021	6648.4941

Table C.8 Orthotropic engineering constants generated by Digimat-MF for test case 3 in Table 3.6 for the 50 wt. % carbon fiber-reinforced polyphenylene sulfide (50CF-PPS) and C/C composite materials.

Material	50CF-PPS	C/C Composite					
PIP Cycle	--	PIP0	PIP1	PIP2	PIP3	PIP4	PIP5
$\nu_p(\%)$	0	59.13	46.64	42.27	38.41	36.69	36.12
$E_1(MPa)$	22326.9106	32657.327	34816.517	36004.897	37171.9575	37724.461	37911.817
$E_2(MPa)$	9988.0144	10853.756	12617.9781	13544.813	14461.1069	14897.579	15046.192
$E_3(MPa)$	4920.2913	10853.756	12617.9781	13544.813	14461.1069	14897.579	15046.192
ν_{12}	0.3919	0.2417263	0.24243785	0.2391805	0.23617947	0.2348687	0.2344391
ν_{21}	0.1753	0.0803384	0.08786277	0.0899782	0.09188153	0.0927508	0.0930426
ν_{13}	0.389	0.2417263	0.24243785	0.2391805	0.23617947	0.2348687	0.2344391
ν_{31}	0.0857	0.0803384	0.08786277	0.0899782	0.09188153	0.0927508	0.0930426
ν_{23}	0.4108	0.188291	0.22413314	0.2319414	0.23779844	0.2401639	0.2409196
ν_{32}	0.2024	0.188291	0.22413314	0.2319414	0.23779844	0.2401639	0.2409196
$G_{12}(MPa)$	5471.0581	9845.4268	9879.47046	10191.187	10537.5188	10710.193	10769.711
$G_{23}(MPa)$	2336.94	4567.2528	5151.45271	5494.5055	5838.39327	6003.1216	6059.1372
$G_{13}(MPa)$	2876.8699	9845.4268	9879.47046	10191.187	10537.5188	10710.193	10769.711

Table C.9 Orthotropic engineering constants generated by Digimat-MF for test case 4 in Table 3.6 for the 50 wt. % carbon fiber-reinforced polyphenylene sulfide (50CF-PPS) and C/C composite materials.

Material	50CF-PPS	C/C Composite					
PIP Cycle	--	PIP0	PIP1	PIP2	PIP3	PIP4	PIP5
$\nu_p(\%)$	0	59.13	46.64	42.27	38.41	36.69	36.12
$E_1(MPa)$	22326.9106	29447.275	31234.3828	32323.755	33410.1767	33928.208	34104.086
$E_2(MPa)$	9988.0144	12606.048	14247.6527	15167.602	16084.6697	16522.917	16672.224
$E_3(MPa)$	4920.2913	12606.048	14247.6527	15167.602	16084.6697	16522.917	16672.224
ν_{12}	0.3919	0.2077535	0.22158296	0.2215696	0.22100498	0.2206657	0.2205443
ν_{21}	0.1753	0.0889369	0.1010757	0.1039694	0.10639848	0.1074634	0.1078159
ν_{13}	0.389	0.2077535	0.22158296	0.2215696	0.22100498	0.2206657	0.2205443
ν_{31}	0.0857	0.0889369	0.1010757	0.1039694	0.10639848	0.1074634	0.1078159
ν_{23}	0.4108	0.1724381	0.20536567	0.2125284	0.21796336	0.2201844	0.2208903
ν_{32}	0.2024	0.1724381	0.20536567	0.2125284	0.21796336	0.2201844	0.2208903
$G_{12}(MPa)$	5471.0581	9429.5144	9609.84048	9942.3345	10301.844	10478.995	10539.962
$G_{23}(MPa)$	2336.94	5376.3441	5908.07042	6251.9537	6600.22441	6767.7315	6825.0068
$G_{13}(MPa)$	2876.8699	9429.5144	9609.84048	9942.3345	10301.844	10478.995	10539.962

REFERENCES

- [1] T.H. Squire, J. Marschall, Material property requirements for analysis and design of UHTC components in hypersonic applications, *J Eur Ceram Soc* 30 (2010) 2239–2251. <https://doi.org/10.1016/J.JEURCERAMSOC.2010.01.026>.
- [2] S.D. Kasen, *Thermal Management at Hypersonic Leading Edges*, 2013.
- [3] D.M. Van Wie, D.G. Drewry, D.E. King, C.M. Hudson, *ULTRA-HIGH TEMPERATURE CERAMICS The hypersonic environment: Required operating conditions and design challenges*, 2004. <https://doi.org/10.1023/B:JMSC.0000041688.68135.8b>.
- [4] J.J. Bertin, R.M. Cummings, *CRITICAL HYPERSONIC AEROTHERMODYNAMIC PHENOMENA*, *Annu Rev Fluid Mech* 38 (2006) 129–157. <https://doi.org/10.1146/annurev.fluid.38.050304.092041>.
- [5] O. Uyanna, H. Najafi, Thermal protection systems for space vehicles: A review on technology development, current challenges and future prospects, *Acta Astronaut* 176 (2020) 341–356. <https://doi.org/10.1016/J.ACTAASTRO.2020.06.047>.
- [6] D. Glass, Ceramic Matrix Composite (CMC) Thermal Protection Systems (TPS) and Hot Structures for Hypersonic Vehicles, in: *15th AIAA International Space Planes and Hypersonic Systems and Technologies Conference*, American Institute of Aeronautics and Astronautics, Reston, Virginia, 2008. <https://doi.org/10.2514/6.2008-2682>.
- [7] C.L. Tracy, D. Wright, Modeling the Performance of Hypersonic Boost-Glide Missiles, *Science & Global Security* 28 (2020) 135–170. <https://doi.org/10.1080/08929882.2020.1864945>.
- [8] E. Fitzer, L.M. Manocha, *Carbon Reinforcements and Carbon/Carbon Composites*, 1st ed., Springer Berlin Heidelberg, Berlin, Heidelberg, 1998. <https://doi.org/10.1007/978-3-642-58745-0>.
- [9] N.P. Bansal, J. Lamon, *CERAMIC MATRIX COMPOSITES MATERIALS, MODELING AND TECHNOLOGY* Edited by, 2015. <http://www.wiley.com/go/permission.www.wiley.com>.
- [10] C. Scarponi, Carbon–carbon composites in aerospace engineering, *Advanced Composite Materials for Aerospace Engineering* (2016) 385–412. <https://doi.org/10.1016/B978-0-08-100037-3.00013-4>.
- [11] P. Morgan, *Carbon Fibers and Their Composites*, 1st ed., CRC Press, Boca Raton, 2005. <https://doi.org/10.1201/9781420028744>.

- [12] G. Savage, Carbon-Carbon Composites, 1st ed., Springer Netherlands, Dordrecht, 1993. <https://doi.org/10.1007/978-94-011-1586-5>.
- [13] R. Zaldivar, A. Martinez, R. Elhessen, H. Kim, J. Severino, V. Arredondo, P. Adams, G. Ferrelli, The effect of heat-treatment temperature (HTT) on the carbon matrix development of both polyarylacetylene-and phenolic-derived carbon–Carbon (C/C) composites, *J Compos Mater* (2023). <https://doi.org/10.1177/00219983231191165>.
- [14] E.I. Borrego, S. Athukorale, S. Gorla, A.K. Duckworth, M. Baker, J. Rosales, W.W. Johnson, S. Kundu, H. Toghiani, B. Farajidizaji, C.U. Pittman, D.W. Smith, High carbon yielding and melt processable bis-ortho-diynylarene (BODA)-derived resins for rapid processing of dense carbon/carbon composites, *Compos B Eng* 242 (2022) 110080. <https://doi.org/10.1016/J.COMPOSITESB.2022.110080>.
- [15] A. McIlhagger, E. Archer, R. McIlhagger, Manufacturing processes for composite materials and components for aerospace applications, *Polymer Composites in the Aerospace Industry* (2020) 59–81. <https://doi.org/10.1016/B978-0-08-102679-3.00003-4>.
- [16] R. Kamiya, B.A. Cheeseman, P. Popper, T.W. Chou, Some recent advances in the fabrication and design of three-dimensional textile preforms: a review, *Compos Sci Technol* 60 (2000) 33–47. [https://doi.org/10.1016/S0266-3538\(99\)00093-7](https://doi.org/10.1016/S0266-3538(99)00093-7).
- [17] X. Chen, L.W. Taylor, L.-J. Tsai, An overview on fabrication of three-dimensional woven textile preforms for composites, (n.d.). <https://doi.org/10.1177/0040517510392471>.
- [18] Y. Liu, T.W. Chou, Additive manufacturing of multidirectional preforms and composites: from three-dimensional to four-dimensional, *Mater Today Adv* 5 (2020) 100045. <https://doi.org/10.1016/J.MTADV.2019.100045>.
- [19] M. Attaran, The rise of 3-D printing: The advantages of additive manufacturing over traditional manufacturing, *Bus Horiz* 60 (2017) 677–688. <https://doi.org/10.1016/J.BUSHOR.2017.05.011>.
- [20] T. Pereira, J. V. Kennedy, J. Potgieter, A comparison of traditional manufacturing vs additive manufacturing, the best method for the job, *Procedia Manuf* 30 (2019) 11–18. <https://doi.org/10.1016/J.PROMFG.2019.02.003>.
- [21] J. Sun, D. Ye, J. Zou, X. Chen, Y. Wang, J. Yuan, H. Liang, H. Qu, J. Binner, J. Bai, A review on additive manufacturing of ceramic matrix composites, *J Mater Sci Technol* 138 (2023) 1–16. <https://doi.org/10.1016/J.JMST.2022.06.039>.
- [22] X. Yi, Z.J. Tan, W.J. Yu, J. Li, B.J. Li, B.Y. Huang, J. Liao, Three dimensional printing of carbon/carbon composites by selective laser sintering, *Carbon N Y* 96 (2016) 603–607. <https://doi.org/10.1016/J.CARBON.2015.09.110>.

- [23] W. Zhu, H. Fu, Z. Xu, R. Liu, P. Jiang, X. Shao, Y. Shi, C. Yan, Fabrication and characterization of carbon fiber reinforced SiC ceramic matrix composites based on 3D printing technology, *J Eur Ceram Soc* 38 (2018) 4604–4613. <https://doi.org/10.1016/J.JEURCERAMSOC.2018.06.022>.
- [24] X. Chen, J. Yin, X. Liu, B. Pei, J. Huang, X. Peng, A. Xia, L. Huang, Z. Huang, Effect of laser power on mechanical properties of SiC composites rapidly fabricated by selective laser sintering and direct liquid silicon infiltration, *Ceram Int* 48 (2022) 19123–19131. <https://doi.org/10.1016/J.CERAMINT.2022.03.203>.
- [25] Z. Chen, Z. Li, J. Li, C. Liu, C. Lao, Y. Fu, C. Liu, Y. Li, P. Wang, Y. He, 3D printing of ceramics: A review, *J Eur Ceram Soc* 39 (2019) 661–687. <https://doi.org/10.1016/J.JEURCERAMSOC.2018.11.013>.
- [26] H. Zhang, Y. Yang, K. Hu, B. Liu, M. Liu, Z. Huang, Stereolithography-based additive manufacturing of lightweight and high-strength Cf/SiC ceramics, *Addit Manuf* 34 (2020) 101199. <https://doi.org/10.1016/J.ADDMA.2020.101199>.
- [27] T. Schlotthauer, D. Nolan, P. Middendorf, Influence of short carbon and glass fibers on the curing behavior and accuracy of photopolymers used in stereolithography, *Addit Manuf* 42 (2021) 102005. <https://doi.org/10.1016/J.ADDMA.2021.102005>.
- [28] D.H.-J.A. Lukaszewicz, C. Ward, K.D. Potter, The engineering aspects of automated prepreg layup: History, present and future, *Compos B Eng* 43 (2012) 997–1009. <https://doi.org/10.1016/j.compositesb.2011.12.003>.
- [29] A. Brasington, C. Sacco, J. Halbritter, R. Wehbe, R. Harik, Automated fiber placement: A review of history, current technologies, and future paths forward, *Composites Part C: Open Access* 6 (2021) 100182. <https://doi.org/10.1016/J.JCOMC.2021.100182>.
- [30] M.A.S.R. Saadi, A. Maguire, N.T. Pottackal, M.S.H. Thakur, M.Md. Ikram, A.J. Hart, P.M. Ajayan, M.M. Rahman, Direct Ink Writing: A 3D Printing Technology for Diverse Materials, *Advanced Materials* 34 (2022) 2108855. <https://doi.org/10.1002/adma.202108855>.
- [31] W. Wang, L. Zhang, X. Dong, J. Wu, Q. Zhou, S. Li, C. Shen, W. Liu, G. Wang, R. He, Additive manufacturing of fiber reinforced ceramic matrix composites: Advances, challenges, and prospects, *Ceram Int* 48 (2022) 19542–19556. <https://doi.org/10.1016/J.CERAMINT.2022.04.146>.
- [32] P. Pibulchinda, E. Barocio, A.J. Favaloro, R.B. Pipes, Influence of printing conditions on the extrudate shape and fiber orientation in extrusion deposition additive manufacturing, *Compos B Eng* 261 (2023) 110793. <https://doi.org/10.1016/J.COMPOSITESB.2023.110793>.
- [33] D.A. Rau, M.J. Bortner, C.B. Williams, A rheology roadmap for evaluating the printability of material extrusion inks, *Addit Manuf* 75 (2023) 103745. <https://doi.org/10.1016/J.ADDMA.2023.103745>.

- [34] A. Shahzad, I. Lazoglu, Direct ink writing (DIW) of structural and functional ceramics: Recent achievements and future challenges, *Compos B Eng* 225 (2021) 109249. <https://doi.org/10.1016/J.COMPOSITESB.2021.109249>.
- [35] B. Brenken, E. Barocio, A. Favaloro, V. Kunc, R.B. Pipes, Fused filament fabrication of fiber-reinforced polymers: A review, *Addit Manuf* 21 (2018) 1–16. <https://doi.org/10.1016/J.ADDMA.2018.01.002>.
- [36] Sylvie Beland, *High Performance Thermoplastics and Their Resin Composites*, 1st ed., Noyes Data Corporation, 1990. <https://www.sciencedirect.com/book/9780815512783/high-performance-thermoplastic-resins-and-their-composites#book-description>.
- [37] B. Brenken, E. Barocio, A. Favaloro, V. Kunc, R.B. Pipes, Development and validation of extrusion deposition additive manufacturing process simulations, *Addit Manuf* 25 (2019) 218–226. <https://doi.org/10.1016/J.ADDMA.2018.10.041>.
- [38] A. Wedgewood, P. Pibulchinda, E. Vaca, C. Hill, M. Bogdanor, *Materials Development and Advanced Process Simulation for Additive Manufacturing with Fiber-Reinforced Thermoplastics*, Golden, CO (United States), 2021. <https://doi.org/10.2172/1769016>.
- [39] G. Franchin, L. Wahl, P. Colombo, Direct ink writing of ceramic matrix composite structures, *Journal of the American Ceramic Society* 100 (2017) 4397–4401. <https://doi.org/10.1111/jace.15045>.
- [40] Z. Lu, Y. Xia, K. Miao, S. Li, L. Zhu, H. Nan, J. Cao, D. Li, Microstructure control of highly oriented short carbon fibres in SiC matrix composites fabricated by direct ink writing, *Ceram Int* 45 (2019) 17262–17267. <https://doi.org/10.1016/J.CERAMINT.2019.05.283>.
- [41] E.B. Vaca, FUSION BONDING OF FIBER REINFORCED SEMI-CRYSTALLINE POLYMERS IN EXTRUSION DEPOSITION ADDITIVE MANUFACTURING, 2018. <https://doi.org/10.25394/PGS.7434068.v1>.
- [42] B.P. Heller, D.E. Smith, D.A. Jack, Planar deposition flow modeling of fiber filled composites in large area additive manufacturing, *Addit Manuf* 25 (2019) 227–238. <https://doi.org/10.1016/J.ADDMA.2018.10.031>.
- [43] H.L. Tekinalp, V. Kunc, G.M. Velez-Garcia, C.E. Duty, L.J. Love, A.K. Naskar, C.A. Blue, S. Ozcan, Highly oriented carbon fiber–polymer composites via additive manufacturing, *Compos Sci Technol* 105 (2014) 144–150. <https://doi.org/10.1016/J.COMPSCITECH.2014.10.009>.
- [44] H. Wu, M. Sulkis, J. Driver, A. Saade-Castillo, A. Thompson, J.H. Koo, Multi-functional ULTEMTM1010 composite filaments for additive manufacturing using Fused Filament Fabrication (FFF), *Addit Manuf* 24 (2018) 298–306. <https://doi.org/10.1016/J.ADDMA.2018.10.014>.

- [45] H. Wu, A. Kafi, C. Yee, O. Atak, J.H. Langston, R. Reber, J. Misasi, S. Kim, W.P. Fahy, S. Bateman, J.H. Koo, Ablation Performances of Additively Manufactured High-Temperature Thermoplastic Polymers, in: AIAA Scitech 2020 Forum, American Institute of Aeronautics and Astronautics, Reston, Virginia, 2020. <https://doi.org/10.2514/6.2020-1125>.
- [46] H. Wu, S.D. Kim, C.M. Yee, W.P. Fahy, Z. August, Z. Liu, J.H. Koo, Ablation Performance of 3D Printed Continuous Carbon Fiber-Reinforced PEEK, in: AIAA Scitech 2021 Forum, American Institute of Aeronautics and Astronautics, Reston, Virginia, 2021. <https://doi.org/10.2514/6.2021-0535>.
- [47] A.J. Thomas, E. Barocio, V. Kapre, P. Pibulchinda, F.N. Nguyen, R.B. Pipes, Relationship between flow-controlled fiber orientation and spring-in deformation in extrusion deposition additive manufacturing, in: 2022 International Solid Freeform Fabrication Symposium, 2022. <http://dx.doi.org/10.26153/tsw/44204> (accessed September 29, 2023).
- [48] E. Barocio, V. Kapre, P. Pibulchinda, M. Ramirez, A. Franc, J. Susnjara, Material Characterization for Large Scale Additive Manufacturing (AM), West Lafayette, 2022. <http://www.osti.gov/scitech/>.
- [49] A.J. Thomas, E. Barocio, R.B. Pipes, A machine learning approach to determine the elastic properties of printed fiber-reinforced polymers, *Compos Sci Technol* 220 (2022) 109293. <https://doi.org/10.1016/J.COMPSCITECH.2022.109293>.
- [50] C. Y, V. B, D. N, D. E, Isothermal and anisothermal decomposition of carbon fibres polyphenylene sulfide composites for fire behavior analysis, *Fire Saf J* 109 (2019). <https://doi.org/10.1016/j.firesaf.2019.102868>.
- [51] L.H. Perng, Thermal decomposition characteristics of poly(phenylene sul@de) by stepwise Py-GC/MS and TG/MS techniques, 2000. [https://doi.org/10.1016/S0141-3910\(00\)00077-X](https://doi.org/10.1016/S0141-3910(00)00077-X).
- [52] P. Patel, T.R. Hull, R.W. McCabe, D. Flath, J. Grasmeder, M. Percy, Mechanism of thermal decomposition of poly(ether ether ketone) (PEEK) from a review of decomposition studies, *Polym Degrad Stab* 95 (2010) 709–718. <https://doi.org/10.1016/j.polymdegradstab.2010.01.024>.
- [53] C.J. Tsai, L.H. Perng, Y.C. Ling, A Study of Thermal Degradation of Poly(aryl-ether-ether-ketone) Using Stepwise Pyrolysis/Gas Chromatography/Mass Spectrometry, 1997. [https://doi.org/10.1002/\(SICI\)1097-0231\(199712\)11:18<1987::AID-RCM100>3.0.CO;2-Q](https://doi.org/10.1002/(SICI)1097-0231(199712)11:18<1987::AID-RCM100>3.0.CO;2-Q).
- [54] G. Molnár, A. Botvay, L. Pöpl, K. Torkos, J. Borossay, Á. Máthé, T. Török, Thermal degradation of chemically modified polysulfones, *Polym Degrad Stab* 89 (2005) 410–417. <https://doi.org/10.1016/J.POLYMDEGRADSTAB.2005.01.031>.

- [55] L.H. Perng, Thermal Degradation Mechanism of Poly(arylene sulfone)s by Stepwise Py-GC/MS, 2000. [https://doi.org/10.1002/\(SICI\)1099-0518\(20000201\)38:3<583::AID-POLA23>3.0.CO;2-6](https://doi.org/10.1002/(SICI)1099-0518(20000201)38:3<583::AID-POLA23>3.0.CO;2-6).
- [56] S. Carroccio, C. Puglisi, G. Montaudo, Thermal degradation mechanisms of polyetherimide investigated by direct pyrolysis mass spectrometry, 1999. [https://doi.org/10.1002/\(sici\)1521-3935\(19991001\)200:10<2345::aid-macp2345>3.0.co;2-t](https://doi.org/10.1002/(sici)1521-3935(19991001)200:10<2345::aid-macp2345>3.0.co;2-t).
- [57] L.-H. Perng, Thermal decomposition characteristics of poly(ether imide) by TG/MS, *Journal of Polymer Research* 7 (2000). <https://doi.org/10.1007/s10965-006-0119-7>.
- [58] Y. Carpier, A. Alia, B. Vieille, F. Barbe, Experiments based analysis of thermal decomposition kinetics model. Case of carbon fibers PolyPhenylene Sulfide composites, *Polym Degrad Stab* 186 (2021) 109525. <https://doi.org/10.1016/J.POLYMDEGRADSTAB.2021.109525>.
- [59] F. Hache, M. Delichatsios, T. Fateh, J. Zhang, Comparison of methods for thermal analysis: Application to PEEK and a composite PEEK+CF, *J Fire Sci* 33 (2015) 232–246. <https://doi.org/10.1177/0734904115584154>.
- [60] P. Tadini, N. Grange, K. Chetehouna, N. Gascoin, S. Senave, I. Reynaud, Thermal degradation analysis of innovative PEKK-based carbon composites for high-temperature aeronautical components, *Aerosp Sci Technol* 65 (2017) 106–116. <https://doi.org/10.1016/j.ast.2017.02.011>.
- [61] J. Li, S.I. Stoliarov, Measurement of kinetics and thermodynamics of the thermal degradation for charring polymers, *Polym Degrad Stab* 106 (2014) 2–15. <https://doi.org/10.1016/J.POLYMDEGRADSTAB.2013.09.022>.
- [62] R. Banerjee, S. Sinha Ray, R. Banerjee, S.S. Ray, Foamability and Special Applications of Microcellular Thermoplastic Polymers: A Review on Recent Advances and Future Direction, (2020). <https://doi.org/10.1002/mame.202000366>.
- [63] John D. Buckley, Dan D. Edie, *Carbon-Carbon Materials and Composites*, Illustrated, Noyes Publications, Park Ridge, 1993.
- [64] T.M. Besmann, B.W. Sheldon, R.A. Lowden, D.P. Stinton, Vapor-Phase Fabrication and Properties of Continuous-Filament Ceramic Composites, *Science* (1979) 253 (1991) 1104–1109. <https://doi.org/10.1126/science.253.5024.1104>.
- [65] W.G. Zhang, K.J. Huttinger, Densification of a 2D carbon fiber preform by isothermal, isobaric CVI: Kinetics and carbon microstructure, *Carbon N Y* 41 (2003) 2325–2337. [https://doi.org/10.1016/S0008-6223\(03\)00284-7](https://doi.org/10.1016/S0008-6223(03)00284-7).
- [66] K.L. Choy, Chemical vapour deposition of coatings, *Prog Mater Sci* 48 (2003) 57–170. [https://doi.org/10.1016/S0079-6425\(01\)00009-3](https://doi.org/10.1016/S0079-6425(01)00009-3).

- [67] B. Fathollahi, P.C. Chau, J.L. White, Injection and stabilization of mesophase pitch in the fabrication of carbon–carbon composites. Part I. Injection process, *Carbon N Y* 43 (2005) 125–133. <https://doi.org/10.1016/J.CARBON.2004.08.030>.
- [68] B. Fathollahi, P.C. Chau, J.L. White, Injection and stabilization of mesophase pitch in the fabrication of carbon–carbon composites: Part II. Stabilization process, *Carbon N Y* 43 (2005) 135–141. <https://doi.org/10.1016/j.carbon.2004.08.031>.
- [69] K.M. Chioujones, W. Ho, B. Fathollahi, P.C. Chau, P.G. Wapner, W.P. Hoffman, Microstructural analysis of in situ mesophase transformation in the fabrication of carbon–carbon composites, *Carbon N Y* 44 (2006) 284–292. <https://doi.org/10.1016/J.CARBON.2005.07.026>.
- [70] T. Hosomura, H. Okamoto, Effects of pressure carbonization in the C/C composite process, *Materials Science and Engineering: A* 143 (1991) 223–229. [https://doi.org/10.1016/0921-5093\(91\)90741-5](https://doi.org/10.1016/0921-5093(91)90741-5).
- [71] D. Cho, Y.S. Ahn, J.Y. Lee, Effect of Resin Impregnation Methods at the Early Stage of Densification on the Impregnation Efficiency, Microstructure, and Thermal Stability of Carbon-Carbon Composites, *J Appl Polym Sci* 85 (2002) 183–192. <https://doi.org/10.1002/app.10595>.
- [72] X. Shen, X. Liu, S. Dong, L. Gong, RVE model with shape and position defects for predicting mechanical properties of 3D braided CVI-SiCf/SiC composites, *Compos Struct* 195 (2018) 325–334. <https://doi.org/10.1016/J.COMPSTRUCT.2018.04.074>.
- [73] U. Santhosh, J. Ahmad, G. Ojard, I. Smyth, Y. Gowayed, G. Jefferson, Effect of porosity on the nonlinear and time-dependent behavior of Ceramic Matrix Composites, *Compos B Eng* 184 (2020) 107658. <https://doi.org/10.1016/J.COMPOSITESB.2019.107658>.
- [74] N. Douarche, D. Rouby, G. Peix, J.M. Jouin, Relations between X-ray tomography, density and mechanical properties in carbon–carbon composites, *Carbon N Y* 39 (2001) 1455–1465. [https://doi.org/10.1016/S0008-6223\(00\)00196-2](https://doi.org/10.1016/S0008-6223(00)00196-2).
- [75] J. Martín-Herrero, C. Germain, Microstructure reconstruction of fibrous C/C composites from X-ray microtomography, *Carbon N Y* 45 (2007) 1242–1253. <https://doi.org/10.1016/J.CARBON.2007.01.021>.
- [76] O. Coindreau, G.L. Vignoles, Assessment of Geometrical and Transport Properties of a Fibrous C/C Composite Preform Using x-ray Computerized Micro-tomography: Part I. Image Acquisition and Geometrical Properties, *J Mater Res* 20 (2005) 2328–2339. <https://doi.org/10.1557/jmr.2005.0311>.
- [77] E. Weber, M. Fernandez, P. Wapner, W. Hoffman, Comparison of X-ray microtomography measurements of densities and porosity principally to values measured by mercury porosimetry for carbon–carbon composites, *Carbon N Y* 48 (2010) 2151–2158. <https://doi.org/10.1016/J.CARBON.2009.11.047>.

- [78] B. Drach, A. Drach, I. Tuskrov, Characterization and Statistical Modeling of Irregular Porosity in Carbon/Carbon Composites Based on X-ray Microtomography Data, Wiley Online Library (2013).
- [79] H.A. Bale, A. Haboub, A.A. MacDowell, J.R. Nasiatka, D.Y. Parkinson, B.N. Cox, D.B. Marshall, R.O. Ritchie, Real-time quantitative imaging of failure events in materials under load at temperatures above 1,600 °C, *Nat Mater* 12 (2013) 40–46. <https://doi.org/10.1038/nmat3497>.
- [80] N.M. Larson, F.W. Zok, In-situ 3D visualization of composite microstructure during polymer-to-ceramic conversion, *Acta Mater* 144 (2018) 579–589. <https://doi.org/10.1016/J.ACTAMAT.2017.10.054>.
- [81] N.M. Larson, C. Cuellar, F.W. Zok, X-ray computed tomography of microstructure evolution during matrix impregnation and curing in unidirectional fiber beds, *Compos Part A Appl Sci Manuf* 117 (2019) 243–259. <https://doi.org/10.1016/J.COMPOSITESA.2018.11.021>.
- [82] P.J. Creveling, J. Fisher, N. Lebaron, M.W. Czabaj, 4D Imaging of ceramic matrix composites during polymer infiltration and pyrolysis, *Acta Mater* 201 (2020) 547–560. <https://doi.org/10.1016/j.actamat.2020.10.036>.
- [83] T.-H. Ko, W.-S. Kuo, Y.-H. Chang, Microstructural changes of phenolic resin during pyrolysis, *J Appl Polym Sci* 81 (2001) 1084–1089. <https://doi.org/10.1002/app.1530>.
- [84] H. Zhang, E. López-Honorato, P. Xiao, Fluidized bed chemical vapor deposition of pyrolytic carbon-III. Relationship between microstructure and mechanical properties, *Carbon N Y* 91 (2015) 346–357. <https://doi.org/10.1016/J.CARBON.2015.05.009>.
- [85] C.B. Park, N.P. Suh, Rapid Polymer/Gas Solution Formation for Continuous Production of Microcellular Plastics, *J Manuf Sci Eng* 118 (1996) 639–645. <https://doi.org/10.1115/1.2831079>.
- [86] S.S. Ray, R. Banerjee, *Foamability of Thermoplastic Polymeric Materials*, Elsevier, 2021. <https://doi.org/10.1016/B978-0-323-90767-5.00011-X>.
- [87] L. Jin, K. Zhang, T. Xu, T. Zeng, S. Cheng, The fabrication and mechanical properties of SiC/SiC composites prepared by SLS combined with PIP, *Ceram Int* 44 (2018) 20992–20999. <https://doi.org/10.1016/J.CERAMINT.2018.08.134>.
- [88] H. Zhang, Y. Yang, K. Hu, B. Liu, M. Liu, Z. Huang, Stereolithography-based additive manufacturing of lightweight and high-strength Cf/SiC ceramics, *Addit Manuf* 34 (2020) 101199. <https://doi.org/10.1016/J.ADDMA.2020.101199>.
- [89] W. Wang, X. Bai, L. Zhang, S. Jing, C. Shen, R. He, Additive manufacturing of Csf/SiC composites with high fiber content by direct ink writing and liquid silicon infiltration, *Ceram Int* 48 (2022) 3895–3903. <https://doi.org/10.1016/J.CERAMINT.2021.10.176>.

- [90] R. Chen, A. Bratten, J. Rittenhouse, M. Leu, H. Wen, Additive manufacturing of high mechanical strength continuous C_f/SiC composites using a 3D extrusion technique and polycarbosilane-coated carbon fibers, *Journal of the American Ceramic Society* 106 (2023) 4028–4037. <https://doi.org/10.1111/jace.19079>.
- [91] W. Zhu, H. Fu, Z. Xu, R. Liu, P. Jiang, X. Shao, Y. Shi, C. Yan, Fabrication and characterization of carbon fiber reinforced SiC ceramic matrix composites based on 3D printing technology, *J Eur Ceram Soc* 38 (2018) 4604–4613. <https://doi.org/10.1016/J.JEURCERAMSOC.2018.06.022>.
- [92] W. Freudenberg, F. Wich, N. Langhof, S. Schafföner, Additive manufacturing of carbon fiber reinforced ceramic matrix composites based on fused filament fabrication, *J Eur Ceram Soc* 42 (2022) 1822–1828. <https://doi.org/10.1016/J.JEURCERAMSOC.2021.12.005>.
- [93] Y. Liu, Y. Cheng, D. Ma, N. Hu, W. Han, D. Liu, S. Wu, Y. An, A. Wang, Continuous carbon fiber reinforced ZrB₂-SiC composites fabricated by direct ink writing combined with low-temperature hot-pressing, *J Eur Ceram Soc* 42 (2022) 3699–3707. <https://doi.org/10.1016/J.JEURCERAMSOC.2022.03.045>.
- [94] J.W. Kemp, A.A. Diaz, E.C. Malek, B.P. Croom, Z.D. Apostolov, S.R. Kalidindi, B.G. Compton, L.M. Rueschhoff, Direct ink writing of ZrB₂-SiC chopped fiber ceramic composites, *Addit Manuf* 44 (2021) 102049. <https://doi.org/10.1016/J.ADDMA.2021.102049>.
- [95] D.W. McKee, Oxidation behavior and protection of carbon/carbon composites, *Carbon N Y* 25 (1987) 551–557. [https://doi.org/10.1016/0008-6223\(87\)90197-7](https://doi.org/10.1016/0008-6223(87)90197-7).
- [96] S. V. Ushakov, A. Navrotsky, Experimental Approaches to the Thermodynamics of Ceramics Above 1500°C, *Journal of the American Ceramic Society* 95 (2012) 1463–1482. <https://doi.org/10.1111/j.1551-2916.2012.05102.x>.
- [97] E.L. Corral, R.E. Loehman, Ultra-High-Temperature Ceramic Coatings for Oxidation Protection of Carbon–Carbon Composites, *Journal of the American Ceramic Society* 91 (2008) 1495–1502. <https://doi.org/10.1111/j.1551-2916.2008.02331.x>.
- [98] X. Jin, X. Fan, C. Lu, T. Wang, Advances in oxidation and ablation resistance of high and ultra-high temperature ceramics modified or coated carbon/carbon composites, *J Eur Ceram Soc* 38 (2018) 1–28. <https://doi.org/10.1016/J.JEURCERAMSOC.2017.08.013>.
- [99] B. Reznik, M. Guellali, D. Gerthsen, R. Oberacker, M.J. Hoffmann, Microstructure and mechanical properties of carbon–carbon composites with multilayered pyrocarbon matrix, *Mater Lett* 52 (2002) 14–19. [https://doi.org/10.1016/S0167-577X\(01\)00357-3](https://doi.org/10.1016/S0167-577X(01)00357-3).
- [100] A. Bussiba, M. Kupiec, R. Piat, T. Böhlke, Fracture characterization of C/C composites under various stress modes by monitoring both mechanical and acoustic responses, *Carbon N Y* 46 (2008) 618–630. <https://doi.org/10.1016/J.CARBON.2008.01.020>.

- [101] X. Wu, R. Luo, Mechanical properties investigation of carbon/carbon composites fabricated by a fast densification process, *Mater Des* 32 (2011) 2361–2364. <https://doi.org/10.1016/J.MATDES.2010.11.061>.
- [102] X. Chao, L. Qi, J. Cheng, W. Tian, S. Zhang, H. Li, Numerical evaluation of the effect of pores on effective elastic properties of carbon/carbon composites, *Compos Struct* 196 (2018) 108–116. <https://doi.org/10.1016/J.COMPSTRUCT.2018.05.014>.
- [103] L.R. Bradley, C.R. Bowen, B. McEnaney, D.C. Johnson, Shear properties of a carbon/carbon composite with non-woven felt and continuous fibre reinforcement layers, *Carbon N Y* 45 (2007) 2178–2187. <https://doi.org/10.1016/J.CARBON.2007.06.072>.
- [104] K.F. Yan, C.Y. Zhang, S.R. Qiao, D. Han, M. Li, In-plane shear strength of a carbon/carbon composite at different loading rates and temperatures, *Materials Science and Engineering: A* 528 (2011) 1458–1462. <https://doi.org/10.1016/J.MSEA.2010.10.047>.
- [105] K.F. Yan, C.Y. Zhang, S.R. Qiao, C.Z. Song, D. Han, M. Li, Measurement of In-Plane Shear Strength of Carbon/Carbon Composites by Compression of Double-Notched Specimens, *J Mater Eng Perform* 21 (2012) 62–68. <https://doi.org/10.1007/s11665-010-9823-x>.
- [106] X. Li, Y. Yan, Y. Tan, F. Guo, Y. Hong, Z. Tian, Experimental and numerical investigations of the interlaminar shear properties of carbon/carbon composites, *J Appl Polym Sci* 134 (2017). <https://doi.org/10.1002/app.44783>.
- [107] J. Chłopek, S. Błżewicz, Effect of processing variables on the properties of carbon-carbon composites, *Carbon N Y* 29 (1991) 127–131. [https://doi.org/10.1016/0008-6223\(91\)90063-O](https://doi.org/10.1016/0008-6223(91)90063-O).
- [108] J. Neumeister, S. Jansson, F. Leckie, The effect of fiber architecture on the mechanical properties of carbon/carbon fiber composites, *Acta Mater* 44 (1996) 573–585. [https://doi.org/10.1016/1359-6454\(95\)00184-0](https://doi.org/10.1016/1359-6454(95)00184-0).
- [109] V.N.M. Manchiraju, A.R. Bhagat, V.K. Dwivedi, Estimation of Elastic Constants Using Numerical Methods and Their Validation Through Experimental Results for Unidirectional Carbon/Carbon Composite Materials, *MAPAN* 38 (2023) 923–937. <https://doi.org/10.1007/s12647-023-00669-3>.
- [110] M.S. Aly-Hassan, H. Hatta, S. Wakayama, M. Watanabe, K. Miyagawa, Comparison of 2D and 3D carbon/carbon composites with respect to damage and fracture resistance, *Carbon N Y* 41 (2003) 1069–1078. [https://doi.org/10.1016/S0008-6223\(02\)00442-6](https://doi.org/10.1016/S0008-6223(02)00442-6).
- [111] X. Chao, L. Qi, W. Tian, X. Hou, W.J. Ma, H. Li, Numerical evaluation of the influence of porosity on bending properties of 2D carbon/carbon composites, *Compos B Eng* 136 (2018) 72–80. <https://doi.org/10.1016/J.COMPOSITESB.2017.10.027>.

- [112] K. Anand, V. Gupta, The effect of processing conditions on the compressive and shear strength of 2-D carbon-carbon laminates, *Carbon N Y* 33 (1995) 739–748. [https://doi.org/10.1016/0008-6223\(95\)00015-6](https://doi.org/10.1016/0008-6223(95)00015-6).
- [113] G.L. Vignoles, Y. Aspa, M. Quintard, Modelling of carbon–carbon composite ablation in rocket nozzles, *Compos Sci Technol* 70 (2010) 1303–1311. <https://doi.org/10.1016/J.COMPSCITECH.2010.04.002>.
- [114] O. Siron, J. Pailhes, J. Lamon, Modelling of the stress/strain behaviour of a carbon/carbon composite with a 2.5 dimensional fibre architecture under tensile and shear loads at room temperature, *Compos Sci Technol* 59 (1999) 1–12. [https://doi.org/10.1016/S0266-3538\(97\)00241-8](https://doi.org/10.1016/S0266-3538(97)00241-8).
- [115] D. sen Li, G. Luo, Q. qian Yao, N. Jiang, L. Jiang, High temperature compression properties and failure mechanism of 3D needle-punched carbon/carbon composites, *Materials Science and Engineering: A* 621 (2015) 105–110. <https://doi.org/10.1016/J.MSEA.2014.10.060>.
- [116] H. Hatta, K. Taniguchi, Y. Kogo, Compressive strength of three-dimensionally reinforced carbon/carbon composite, *Carbon N Y* 43 (2005) 351–358. <https://doi.org/10.1016/J.CARBON.2004.09.026>.
- [117] H. Weisshaus, S. Kenig, A. Sivegmann, Effect of materials and processing on the mechanical properties of C/C composites, *Carbon N Y* 29 (1991) 1203–1220. [https://doi.org/10.1016/0008-6223\(91\)90038-K](https://doi.org/10.1016/0008-6223(91)90038-K).
- [118] M.V. Rao, P. Mahajan, R.K. Mittal, Effect of architecture on mechanical properties of carbon/carbon composites, *Compos Struct* 83 (2008) 131–142. <https://doi.org/10.1016/J.COMPSTRUCT.2007.04.003>.
- [119] R.M. Jones, Modeling Nonlinear Deformation of Carbon-Carbon Composite Materials, *AIAA Journal* 18 (1980) 995–1001. <https://doi.org/10.2514/3.50844>.
- [120] T. Lauwagie, Vibration-Based Methods for the Identification of the Elastic Properties of Layered Materials, Katholieke Universiteit Leuven, 2005. https://kuleuven.limo.libis.be/discovery/fulldisplay?docid=lirias1747291&context=SearchWebhook&vid=32KUL_KUL:Lirias&search_scope=lirias_profile&tab=LIRIAS&adaptor=SearchWebhook&lang=en (accessed July 9, 2023).
- [121] T. Lauwagie, K. Lambrinou, H. Sol, W. Heylen, Resonant-Based Identification of the Poisson's Ratio of Orthotropic Materials, *Exp Mech* 50 (2010) 437–447. <https://doi.org/10.1007/s11340-009-9250-9>.
- [122] J.A. Ogilvy, H.M. Merklinger, Theory of Wave Scattering from Random Rough Surfaces, *J Acoust Soc Am* 90 (1991) 3382–3382. <https://doi.org/10.1121/1.401410>.

- [123] S.G. Haslinger, M.J.S. Lowe, P. Huthwaite, R. V. Craster, F. Shi, Elastic shear wave scattering by randomly rough surfaces, *J Mech Phys Solids* 137 (2020) 103852. <https://doi.org/10.1016/j.jmps.2019.103852>.
- [124] E. Lara-Curzio, D. Bowers, M.K. Ferber, The interlaminar tensile and shear behavior of a unidirectional C/C composite, *Journal of Nuclear Materials* 230 (1996) 226–232. [https://doi.org/10.1016/0022-3115\(96\)80018-3](https://doi.org/10.1016/0022-3115(96)80018-3).
- [125] T. Mori, K. Tanaka, Average stress in matrix and average elastic energy of materials with misfitting inclusions, *Acta Metallurgica* 21 (1973) 571–574. [https://doi.org/10.1016/0001-6160\(73\)90064-3](https://doi.org/10.1016/0001-6160(73)90064-3).
- [126] O. Pierard, C. Friebel, I. Doghri, Mean-field homogenization of multi-phase thermo-elastic composites: a general framework and its validation, *Compos Sci Technol* 64 (2004) 1587–1603. <https://doi.org/10.1016/J.COMPSCITECH.2003.11.009>.
- [127] F. Tanaka, T. Ishikawa, M. Tane, A comprehensive review of the elastic constants of carbon fibers: implications for design and manufacturing of high-performance composite materials, *Advanced Composite Materials* (2023) 1–21. <https://doi.org/10.1080/09243046.2023.2245210>.
- [128] A.J. Thomas, E. Barocio, I. Billionis, R.B. Pipes, Bayesian inference of fiber orientation and polymer properties in short fiber-reinforced polymer composites, *Compos Sci Technol* 228 (2022) 109630. <https://doi.org/10.1016/J.COMPSCITECH.2022.109630>.
- [129] T.S. Gross, K. Nguyen, M. Buck, N. Timoshchuk, I.I. Tsukrov, B. Reznik, R. Piat, T. Böhlke, Tension–compression anisotropy of in-plane elastic modulus for pyrolytic carbon, *Carbon N Y* 49 (2011) 2145–2147. <https://doi.org/10.1016/J.CARBON.2011.01.012>.
- [130] J.M. Gebert, B. Reznik, R. Piat, B. Viering, K. Weidenmann, A. Wanner, O. Deutschmann, Elastic constants of high-texture pyrolytic carbon measured by ultrasound phase spectroscopy, *Carbon N Y* 48 (2010) 3647–3650. <https://doi.org/10.1016/J.CARBON.2010.06.002>.
- [131] P. Yeole, A.A. Hassen, S. Kim, J. Lindahl, V. Kunc, A. Franc, U. Vaidya, Mechanical Characterization of High-Temperature Carbon Fiber-Polyphenylene Sulfide Composites for Large Area Extrusion Deposition Additive Manufacturing, *Addit Manuf* 34 (2020) 101255. <https://doi.org/10.1016/J.ADDMA.2020.101255>.
- [132] F. Pernot, P. Etienne, F. Boschet, L. Datas, Weibull Parameters and the Tensile Strength of Porous Phosphate Glass-Ceramics, *Journal of the American Ceramic Society* 82 (1999) 641–648. <https://doi.org/10.1111/j.1151-2916.1999.tb01812.x>.
- [133] E. Rezaei, G. Bianchi, S. Gianella, A. Ortona, On the nonlinear mechanical behavior of macroporous cellular ceramics under bending, *J Eur Ceram Soc* 34 (2014) 2133–2141. <https://doi.org/10.1016/j.jeurceramsoc.2014.02.034>.

- [134] M. Sakai, R. Matsuyama, T. Miyajima, The pull-out and failure of a fiber bundle in a carbon fiber reinforced carbon matrix composite, *Carbon N Y* 38 (2000) 2123–2131. [https://doi.org/10.1016/S0008-6223\(00\)00067-1](https://doi.org/10.1016/S0008-6223(00)00067-1).
- [135] K. Fujita, H. Sakai, N. Iwashita, Y. Sawada, Influence of heat treatment temperature on interfacial shear strength of C/C, *Compos Part A Appl Sci Manuf* 30 (1999) 497–501. [https://doi.org/10.1016/S1359-835X\(98\)00140-7](https://doi.org/10.1016/S1359-835X(98)00140-7).
- [136] S. Ozcan, J. Tezcan, B. Gurung, P. Filip, The effect of heat treatment temperature on the interfacial shear strength of C/C composites, *J Mater Sci* 46 (2011) 38–46. <https://doi.org/10.1007/s10853-010-4793-9>.
- [137] A. Oya, K. Arai, K. Fujita, Carbonization and graphitization of poly-p-phenylene sulphide (PPS) film, *J Mater Sci* 29 (1994) 4477–4480. <https://doi.org/10.1007/BF00376269>.
- [138] J. Kim, S.J. Heo, D. Lee, B.W. Im, T.H. Kim, S.G. Kim, B.C. Ku, Highly strong carbon fibers through synergistic carbonization process of sulfonated poly(p-phenylene sulfide) and carbon nanotube, *Carbon N Y* 219 (2024) 118814. <https://doi.org/10.1016/J.CARBON.2024.118814>.
- [139] X. Qin, Y. Lu, H. Xiao, Y. Wen, T. Yu, A comparison of the effect of graphitization on microstructures and properties of polyacrylonitrile and mesophase pitch-based carbon fibers, *Carbon N Y* 50 (2012) 4459–4469. <https://doi.org/10.1016/J.CARBON.2012.05.024>.
- [140] H. Hatta, K. Goto, S. Ikegaki, I. Kawahara, M.S. Aly-Hassan, H. Hamada, Tensile strength and fiber/matrix interfacial properties of 2D- and 3D-carbon/carbon composites, *J Eur Ceram Soc* 25 (2005) 535–542. <https://doi.org/10.1016/J.JEURCERAMSOC.2004.02.014>.

PUBLICATION

Romero, E.S., Barocio, E. & Trice, R.W. Evaluating Extrusion Deposited Additively Manufactured Fiber-Reinforced Thermoplastic Polymers as Carbon/Carbon Preforms. *Applied Composite Materials* (2023). <https://doi.org/10.1007/s10443-023-10176-y>